

Kinetics and Modulation of the Viral Ion Channel Vpu from HIV-1

A Thesis submitted to the Board of the Mathematical, Physical and
Life Sciences Division in partial fulfilment of the requirements for the
Degree of Doctor of Philosophy at the University of Oxford



Peter J. Judge

Merton College

Trinity Term 2008

Abstract

Vpu is a 9 kDa integral membrane protein encoded by the genome of HIV-1 to enhance the rate of virus particle release from infected T_h cells.

Transmembrane currents are observed when a peptide corresponding to the N-terminal 32 amino acids is reconstituted into black lipid membranes. Discrete channel opening events are recorded, whose frequency and duration increases with the applied voltage. A main conductance state of 17.5 pS is observed, with a principal subconductance state of 13.5 pS. Other conductance states are present, however transitions between conductance states are rare. Substitution of residue Ser24 with alanine produces a mutant which is unable to conduct ions. The full length Vpu protein was expressed in *E. coli* and purified by affinity chromatography and HPLC. Transmembrane currents were also observed when the protein was reconstituted into black lipid membranes, with a main conductance state of 17 pS and a principal subconductance state of 12 pS.

The inhibition of Vpu channel activity by the amiloride derivative HMA was investigated using a combination of computational and experimental techniques. The frequency of channel openings decreases with increasing concentrations HMA up to 100 μ M, although channel openings were never observed to be completely blocked. The high octanol/water partition coefficient of the drug ($\log(P) = 2.3$) suggests that HMA is capable of binding non-specifically to the lipid bilayer. HMA (and its homologues DMA and amiloride) were observed to partition into a model membrane from the aqueous phase during a series of equilibrium molecular dynamics (MD) simulations. The simulations predict that the drugs straddle the membrane region between the phospholipid headgroups and the acyl chains and that a strong electrostatic interaction is formed between the positively charged guanidium group of HMA and the negatively charged lipid phosphate groups.

¹H MAS NOESY NMR was used to verify the predicted membrane location of HMA. 2D spectra of DMPC vesicles containing HMA at a total lipid to drug molar ratio of 7:1 were acquired at ¹H frequencies of 500 MHz and 600 MHz. Cross-peaks are observed between the -NH₂ resonances from the drug and the lipid choline and glycerol ¹H resonances, indicating that these groups lie less than 5 Å apart. The drug was demonstrated to preferentially interact with the negatively charged lipid DMPG over DMPC by ³¹P MAS NMR.

Previous docking experiments have identified both the Vpu channel lumen and residue Trp23 on the outside of the Vpu oligomer as potential binding sites for HMA. Equilibrium MD simulations showed that when HMA was bound to the lipid-accessible side chain of Trp23, a local distortion of the lipid bilayer around the Vpu helix was induced, allowing water molecules to penetrate into the region around the Val25 side chain. The simulations suggest that HMA inhibits Vpu channel activity by altering the conformations of neighbouring lipid molecules. However no interaction between the drug and the protein was observed by ¹³C-¹⁵N REDOR NMR.

List of Publications

T. Mehnert, A. Routh, **P. J. Judge**, Y. H. Lam, D. Fischer, A. Watts, W. B Fischer (2008) Biophysical Characterisation of Vpu from HIV-1 Suggests a Channel-Pore Dualism *Proteins* **70** 1488-1497

J. Krüger, G. Patargias, H. Martay, T. Mehnert, A. Routh, **P. J. Judge**, Y. H. Lam, D. Fischer, A. Watts, W. B. Fischer (2008) Self-Assembly of Viral Ion Channel Forming Proteins *Proceedings of the IX. Linz Winter Workshop 2007* 31-35

T. Mehnert, Y. H. Lam, **P. J. Judge**, A. Routh, D. Fischer, A. Watts, W. B. Fischer (2007) Towards a Mechanism of Function of the Viral Ion Channel Vpu from HIV-1 *Journal of Biomolecular Structure and Dynamics* **24** 589-596

W. B. Fischer, **P. J. Judge** (2005) Viral Ion Channels *BioForum Europe* **4** 45-47

Acknowledgements

This research was funded by a Medical Research Council Doctoral Training Award, through the Bionanotechnology Interdisciplinary Research Collaboration.

Most graduate students are only lucky enough to benefit from the inspiration and guidance of one supervisor, however I have had the good fortune to work with two. Dr Wolfgang Fischer first introduced me to viral ion channels in as long ago as June 2003 and closely supervised the first two years of doctoral research. Professor Anthony Watts took up the challenge of taming my maverick instincts and for guiding me through the second half of my research.

I have been fortunate during my time as a DPhil student to visit four other laboratories and to perform experiments at each. Initial NOESY experiments were performed at the Frankfurt Biozentrum in the laboratory of Prof. Clemens Glaubitz, under the expert tutelage of Dr Jakob Lopez. Raman spectroscopy was performed at the Central Laser Facility of the Rutherford Appleton Laboratory under the supervision of Dr Andrew Ward. Dr Jens Krüger introduced me to the exciting new features of Gromacs 3.3.1 in Wolfgang Fischer's lab in Taipei. REDOR experiments were performed at the Karlsruhe Forschungszentrum in the laboratory of Prof. Anne Ulrich, under the supervision of Dr Stephan Grage.

I am also grateful to several researchers from other laboratories who have either sent material for me to work with or performed experiments on my behalf. Prof Strebel (NIAID, Bethesda) provided the anti-Vpu antibodies and to Prof Gage (ANU, Canberra) sent the p2GEX plasmid. Dr Marco Casarotto and Mr Matt Rosenberg provided the labelled HMA and Vpu for the REDOR study. Dr David Harvey and Dr Robin Antrobus (Glycobiology, Oxford) performed Mass Spectrometry on purified and unpurified peptides. Dr Richard Ferguson (Inorganic Chemistry, Oxford) acquired the solution NMR spectra of HMA. I also thank Dr Tim Claridge (Chemistry, Oxford) for helpful discussions.

I would like to thank my friends and colleagues in the lab in Oxford. Dr Thomas Mehnert was responsible for training me in BLM recordings and Dr George Patargias, who introduced a sceptical experimentalist to molecular dynamics simulations. Dr Tracy Lam taught me the mysteries of the peptide synthesiser and the HPLC apparatus. Dr Krisztina Varga for demystifying solid state Nuclear Magnetic Resonance. Five undergraduate students have worked with me on this project at different times: Andrea, Deeba, Jochen, James and Danny, all of whom made their marks on the lab in their

very different ways! Thank you also to Helen, Pete H, Julia, Marcella, Olivia, Satita and the rest of the Watts lab for working alongside me and keeping me focussed on my experiments. I also thank Pete F for his diligent work both at RAL and at Oxford and Liz, who has guided me through the murky waters of Oxford Administration and tolerated my sense of humour for the last four years!

I thank my friends at Merton for providing distractions from my labwork. Finally I thank Mum and John for their love and encouragement and Sophie for her love, support and advice.

Contents

Abstract	i
List of Publications	ii
Acknowledgements	iii
Abbreviations	xi
1 Introduction	1
1.1 Biological Membranes	1
1.2 Ion Channels	2
1.3 Viral Ion Channels	3
1.4 Human Immunodeficiency Virus (HIV)	6
1.5 The Vpu protein of HIV-1	7
1.5.1 Mechanism of enhancement of HIV-1 release from infected cells	9
1.5.2 Structure of Vpu	11
1.5.3 Inhibition of <i>in vitro</i> ion channel activity of Vpu	12
1.6 Examples of other viral ion channels	13
1.6.1 M2 from Influenza A	13
1.6.2 p7 from Hepatitis C	16
1.6.3 6K from Alphavirus	17
1.7 Inhibition of eukaryotic ion channel activity	18
1.7.1 General Anaesthetics	18
1.7.2 The Meyer-Overton Rule	18
1.7.3 Inhibitors of nAChRs	19
1.7.3.1 Tetracaine and procaine	21
1.7.3.2 Quinacrine	22
1.7.3.3 Halothane	23
1.8 Aims of the thesis	23
2 Channel Recording of Vpu₁₋₃₂	26
2.1 Introduction	26

2.1.1	Black Lipid Membranes	26
2.1.2	Previous electrophysiological studies of viral ion channels . .	28
2.1.3	Previous electrophysiological studies of Vpu	30
2.1.3.1	Amiloride	31
2.1.3.2	HMA and DMA	31
2.1.4	Channel Kinetics	33
2.2	Materials and Methods	34
2.2.1	Peptide synthesis	34
2.2.2	Channel Recording	35
2.2.3	Data Processing	36
2.3	Results	37
2.3.1	Vpu ₁₋₃₂ synthesis and purification	37
2.3.2	Vpu ₁₋₃₂ channel traces	38
2.3.3	Conductance histogram	39
2.3.4	I/V Curves for Main and Subconductance States	39
2.3.5	Variation of rate constants with applied voltage	40
2.3.6	Vpu ₁₋₃₂ S24A Mutant Channel Traces	43
2.3.7	Inhibition of <i>in vitro</i> channel activity	43
2.4	Discussion	47
2.4.1	Models for Vpu channel opening and closing	48
2.4.1.1	Semi-permanent bundle models	48
2.4.1.2	Rapid equilibrium models	51
2.4.2	Comparison of inhibition data with previously published work	51
2.5	Conclusion	54
3	Channel Recordings of Vpu₁₋₈₂	55
3.1	Introduction	55
3.1.1	Glutathione- <i>S</i> -transferase fusion proteins	55
3.1.2	Aims of this study	56
3.2	Materials and Methods	56
3.2.1	Data Processing	58
3.3	Results	58
3.3.1	Vpu ₁₋₈₂ expression and purification	58
3.3.2	Channel recording of Vpu ₁₋₈₂ reconstituted into black lipid membranes	59
3.3.3	Conductance histogram	62
3.3.4	I/V Curves for Main and Subconductance States	63
3.3.5	Variation of rate constants with applied voltage	64
3.4	Discussion	66
3.4.1	Origin of the principal subconductance state	66
3.5	Conclusion	68
4	Molecular Dynamics Simulations	69
4.1	Introduction	69

4.1.1	Simulations of lipids and membrane proteins	70
4.1.2	Simulation studies of the TM domain of Vpu	71
4.1.2.1	TM domain monomer structure	71
4.1.2.2	Oligomeric structure	72
4.1.2.3	Mode of inhibition of ion flux	73
4.1.3	Localisation of lipid-soluble molecules in model membranes by MD simulation	74
4.1.4	Force-field calculations	75
4.1.5	Force fields	78
4.1.6	Timestep	79
4.1.7	Periodic boundary of the simulation box	79
4.1.8	Maintenance of constant temperature and pressure	80
4.1.9	Long range non-bonded interactions	81
4.1.10	Aims of this study	83
4.2	Materials and methods	84
4.3	Results and Discussion	86
4.3.1	Location of HMA within a model membrane	86
4.3.1.1	Interaction between HMA and the phospholipid head groups	91
4.3.1.2	Membrane location of DMA and amiloride	94
4.3.1.3	Discussion	96
4.3.2	Insertion of HMA into membrane	97
4.3.2.1	Stage 1 - diffusion through the aqueous phase	98
4.3.2.2	Stage 2 - vertical position in bilayer	99
4.3.2.3	Stage 3 - reorientation to lie flat on membrane surface	100
4.3.2.4	Stage 4 - reorientation continues	103
4.3.2.5	Stage 5	103
4.3.2.6	Movement of HMA from the core of the bilayer to lipid headgroup region	105
4.3.2.7	Conclusion	106
4.3.3	Location of abietic acid within a model membrane	107
4.3.3.1	Conclusion	110
4.3.4	Interaction between HMA and Vpu	111
4.3.4.1	Generation of starting structures	111
4.3.4.2	Differences in the interactions of the drugs and Trp23	112
4.3.4.3	Affect of HMA binding on Tyr30	113
4.3.4.4	Affect of HMA binding on helix secondary structure	115
4.4	Discussion	116
4.4.1	Interaction of drugs with model membrane	116
4.4.2	Interaction of drugs with Trp23	117
4.4.3	Evaluation of proposed mechanisms of inhibition	118
4.5	Conclusion	120

5	Spectroscopic studies of the location of HMA in model membranes	122
5.1	Introduction	122
5.1.1	The Nuclear Overhauser Effect (NOE)	122
5.1.1.1	A 1D NOE experiment	123
5.1.2	Nuclear Overhauser Effect Spectroscopy (NOESY)	124
5.1.2.1	Pulse sequence	124
5.1.2.2	NOE development during (τ_m)	125
5.1.2.3	Phase Cycling	127
5.1.2.4	Time-Proportional Phase Incrementation (TPPI)	127
5.1.3	Raman Spectroscopy	129
5.1.4	Aims of this study	132
5.2	Materials and Methods	133
5.2.1	Determination of the partition coefficient of HMA	133
5.2.2	NOESY spectra	133
	Sample preparation	133
	^1H MAS NOESY measurements	133
	Data processing	134
5.2.3	MAS ^{31}P measurements	134
	Sample preparation	134
5.2.4	Raman spectroscopy	136
	Sample preparation	136
	Equipment and instrumentation	136
5.3	Results and discussion	137
5.3.1	Octanol-water partition coefficient	137
5.3.1.1	Results	137
5.3.2	^1H MAS NOESY	138
5.3.2.1	Assignment of HMA ^1H chemical shifts	138
5.3.2.2	Assignment of DMPC ^1H chemical shifts	138
5.3.2.3	2D MAS NOESY spectrum of DMPC:HMA 7:1	140
	CH_3 and CH_2 spectral region	140
	Lipid headgroup spectral region	143
5.3.3	Comparison of MAS NOESY spectra acquired at 600 MHz and 500 MHz	144
5.3.4	Comparison of DMPC only and DMPC:HMA 7:1 at 500 MHz	146
5.3.5	^1H MAS NOESY spectra of DMA and amiloride in DMPC	147
5.3.6	Substitution of DMPC by chain-deuterated DMPC	148
5.3.7	Discussion	149
5.4	HMA-lipid interactions by ^{31}P MAS NMR	152
5.4.0.1	Chemical shift perturbation	152
5.4.0.2	DMPG:DMPC 2:1 model membrane	153
5.4.0.3	Discussion	153
5.4.1	Raman Spectroscopy	156
5.4.1.1	Conclusion	158

5.5	Conclusion	160
6	REDOR Spectroscopy	162
6.1	Introduction	162
6.1.1	Applications	162
6.1.2	Outline of pulse sequence	163
6.1.3	Cross polarisation	164
6.1.4	Proton decoupling	165
6.1.5	REDOR pulses	165
6.1.6	Aims of this study	169
6.2	Materials and methods	170
6.2.1	Sample preparation	170
6.2.2	^1H - ^{13}C cross polarisation experiments	170
6.2.3	REDOR experiments	171
6.3	Results	172
6.3.1	Cross polarisation	172
6.3.2	REDOR spectra	173
6.4	Discussion	175
6.5	Conclusion	176
7	Conclusions and future work	177
7.1	Vpu channel kinetics	177
7.2	Inhibition of channel activity by HMA	179
7.3	Conclusion	183
A	List of Viral Ion Channels	184
B	General Methods	185
B.1	Solid Phase Peptide Synthesis	185
B.2	Heat shock transformation of competent cells	187
B.3	SDS PAGE	187
B.4	Basic principles of solid state NMR	188
B.4.1	Magic Angle Spinning	191
B.5	Raman Spectroscopy	193
B.5.1	Apparatus	193
B.5.2	Calibration	193
C	Media and buffer compositions	195
C.1	Growth media	195
	Luria-Betani (LB) liquid media	195
	Luria-Betani (LB) agar	195
	SOC medium	195
C.2	SDS PAGE	195
	2x sample buffer	195

	Tris-Glycine SDS running buffer	195
	Tris-Glycine transfer buffer	195
C.3	V _{pu1-82} purification buffers	196
	PBS buffer	196
	Buffer I	196
	Buffer II	196
	Buffer III	196
	GHB Buffer	196
	TCB Buffer	196
C.4	HPLC Buffers	196
	Buffer A	196
	Buffer B	196

Bibliography

Abbreviations

ACN	Acetonitrile
AHSV	African horse sickness virus
AIDS	Acquired Immunodeficiency Syndrome
bp	base pairs
BtV	Bluetongue virus
CCD	Charge-coupled device
CD	Circular dichroism
CP	Cross polarisation
DCM	Dichloromethane
DMA	5-(N-N-dimethyl)amiloride
DMF	Dimethylformamide
DMPC	1,2-dimyristoyl- <i>sn</i> -glycero-3-phosphatidylcholine
DNA	Deoxyribonucleic acid
DOPC	1,2-dioleoyl- <i>sn</i> -glycero-3-phosphocholine
DTT	Dithiothreitol
EDT	Ethane dithiol
EDTA	Ethylenediaminetetraacetic acid
ENaC	Epithelial Na ⁺ Channel
ER	Endoplasmic reticulum
FID	Free induction decay
Fmoc	9-fluorenylmethoxycarbonyl
GABA	γ -aminobutanic acid
GBV-B	GB Virus B
gp	glycoprotein
GST	Glutathione- <i>S</i> -transferase enzyme
HAART	Highly active anti-retroviral therapy

HBTU	2-(H-Bezotriazole-1-yl)-1,1,3,3-tetramethyluronium hexafluorophosphate
HCV	Hepatitis C Virus
HEPES	N-(2-Hydroxyethyl)-piperazine-N-(2-ethanesulfonic acid)
HIV-1	Human Immunodeficiency Virus 1
HIV-2	Human Immunodeficiency Virus 2
HMA	5-(N-N-hexamethylene)amiloride
HOBt	N-Hydroxybenzotriazole
HPLC	High Performance Liquid Chromatography
IPTG	Isopropyl- β -D-thiogalactopyranoside
kbp	Kilo base pairs
LB	Luria-Bertani medium
MALDI	Matrix-assisted Laser Desorption/Ionization
MAS	Magic angle spinning
MD	Molecular dynamics
MDM	Monocyte-derived macrophages
MWCO	Molecular weight cut off
MS	Mass Spectrometry
nAChR	Nicotinic acetylcholine receptor
NARTI	Nucleoside analogue reverse transcriptase inhibitor
NCA	Noncompetitive antagonist
NDSB 256	Dimethyl benzyl ammonium propane sulphonate
NMR	Nuclear Magnetic Resonance
NNRTI	Non-nucleoside reverse transcriptase inhibitor
NOE	Nuclear Overhauser Effect
PAGE	Polyacrylamide Gel Electrophoresis
PBS	Phosphate Buffered Saline solution
PME	Particle-mesh Ewald
POPC	1-palmitoyl-2-oleoyl- <i>sn</i> -glycero-3-phosphocholine
POPE	1-palmitoyl-2-oleoyl- <i>sn</i> -glycero-3-phosphoethanolamine
POPS	1-palmitoyl-2-oleoyl- <i>sn</i> -glycero-3-phosphoserine
PyBOP	Benzotriazole-1-yl-oxy-tris-pyrrolidino-phosphonium hexafluorophosphate
RDF	Radial distribution function

REDOR	Rotational Echo Double Resonance
RMSD	Root mean square deviation
RNA	Ribonucleic acid
RT	Reverse transcriptase
SARS	Severe acute respiratory syndrome
SDS	Sodium dodecyl sulphate
SFV	Semliki Forest Virus
ssNMR	Solid state Nuclear Magnetic Resonance
TASK	TWIK-related Acid Sensitive K ⁺ channel
TCB	Thrombin Cleavage Buffer
TFA	2,2,2-trifluoroacetic acid
TFE	2,2,2-trifluoroethanol
TIS	Triisopropylsilane
TM	Transmembrane
UNAIDS	United Nations Programme on HIV/AIDS
UV	Ultraviolet
Vpu₁₋₃₂	Truncated Virus Protein U (the first 32 amino acids)
Vpu₁₋₈₂	Full length wild type Virus Protein U
WHO	World Health Organization

Chapter 1

Introduction

1.1 Biological Membranes

The evolution of the cell membrane enabled the transition from surface-based to compartmentalised life [1, 2], allowing the metabolic reactions required for growth and reproduction to proceed more efficiently within an enclosed volume [3]. The bilayer structures formed by the spontaneous association of phospholipid molecules, define the boundaries of cells and subcellular compartments, providing a unique amphipathic environment, in which peptides may fold, proteins self assemble and organic molecules accumulate (figure 1.1) [4]. Although most measure less than 3 nm across, cell membranes effectively contain metabolic processes, since the change in free energy as a hydrophilic species is moved from an aqueous environment (dielectric constant $\varepsilon = 80$) into the hydrophobic interior ($\varepsilon = 2$), is highly unfavourable [5]. The integrity of phospholipid bilayers is such that all known organisms use either an H^+ or Na^+ transmembrane gradient to store free energy and to drive the production of ATP [6, 7].

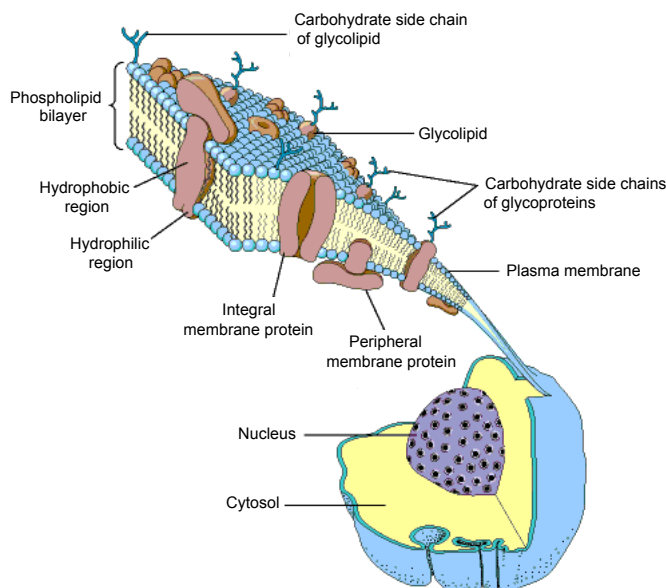


FIGURE 1.1: *Schematic structure of a typical mammalian cell membrane* reproduced from [8] after the Singer-Nicholson Fluid Mosaic model [4]. Phospholipids are arranged so that the polar headgroups are exposed to the aqueous cytosol and extracellular fluid. The non-polar acyl chains self-associate in the hydrophobic core of the membrane. Proteins are either embedded in the phospholipid bilayer or attached peripherally.

1.2 Ion Channels

Although some hydrophilic species (e.g. O_2 gas) are able to cross cell membranes unaided [9], most water-soluble molecules require specialised transport proteins embedded in the membrane to facilitate their passage. Proteins which require an energy source (e.g. ATP or a transmembrane potential) to move substances across the membrane against an electrochemical gradient are classified as active transporters, while the remaining types of transport protein which do not require an additional source of energy, are classified by substrate. Some 3.0% of the open reading frames identified in the human genome encode transport proteins, of which 43.3% are ion channels, proteins which create hydrophilic pores through the membrane to enable the passage of charged species down their electrochemical gradient [10, 11]. In general, ion channels are selective for a particular ion or class

of ions and are able to conduct charges rapidly at rates of $> 10^6 \text{ s}^{-1}$ [11]. Most ion channels are able to open and/or close in response to an external stimulus such as ligand binding or changes in osmotic pressure or transmembrane potential [12, 13]. Since ion channel dysfunction is implicated in the pathophysiology of many chronic human diseases, these proteins are the focus of intense pharmacological research [14]. Approximately one third of all commercially available drugs are thought to target ion channels, yet the structures of these proteins and the mechanisms of action of pharmaceutical compounds are largely unknown [15].

1.3 Viral Ion Channels

Viral ion channels are short, highly hydrophobic integral membrane proteins, typically under 100 amino acid residues in length [16]. The insertion of these proteins into host cell membranes, followed by the oligomerisation of the transmembrane domains, results in the formation of a channel with hydrophilic residues forming the pore lining face of the channel and the hydrophobic residues facing the phospholipid bilayer. Their small size means that they are ideal models for more complex ion channel proteins.

Despite the considerable variation in sequence between the ion channels of different viruses, there are some common features: all are homo-oligomers with an oligomeric state of between four (M2 from Influenza A) and seven (p7 from Hepatitis C Virus) [17, 18]. Some, including Vpu from HIV-1 are type I integral membrane proteins, and are expressed with an N-terminal secretory signal peptide which is removed post translation. Others, including M2 and NB from Influenza A and B respectively, are type III integral membrane proteins which carry an uncleaved N-terminal signal peptide. M2 and the related BM2 channel from Influenza B, are unusual among viral ion channels in that they are highly

selective for H⁺ ions. Most viral ion channels exhibit only a weak cation selectivity [16]. A list of viral proteins which have been identified as ion channels is given in Appendix A.

The amino acids with β -branched side chains (isoleucine and valine) are commonly found at the interfaces between transmembrane α helices in a variety of proteins. Since these side chains have restricted rotational freedom in the monomer, the entropic penalty of oligomerisation is reduced. These side chains are particularly common in viral ion channels (50% of the residues in the transmembrane domain of Vpu from HIV-1 are either Val or Ile) and they are predicted to lie at the interfaces between adjacent monomers [19]. The relative weakness of the intermolecular bonds between the transmembrane helices suggests that the oligomeric form of these proteins is relatively short-lived and in dynamic equilibrium with monomeric forms.

Like other classes of integral membrane protein, the transmembrane helices of viral ion channels commonly contain residues with aromatic side chains [16, 20]. Residues of this type are commonly found near the N-terminal and C-terminal ends of the transmembrane domain, where they form an aromatic belt to anchor the protein in the membrane [20]. Most viral ion channels have few hydrophilic residues lining the pore itself (mostly serine and threonine, see figure 1.2) which results in lower conductances than are observed for most prokaryotic and eukaryotic channels. Basic residues are commonly found at both ends of each transmembrane α helix and several viral ion channels have arginine and lysine-rich sequences on the C-terminal side of the transmembrane region. It has been proposed that these residues contribute to membrane destabilisation by acting like a detergent [21, 22], although given the ratio of protein to lipid in a cell surface membrane, it is questionable whether this effect is significant *in vivo*.

There has been some debate as to the classification of viral ion channel proteins,

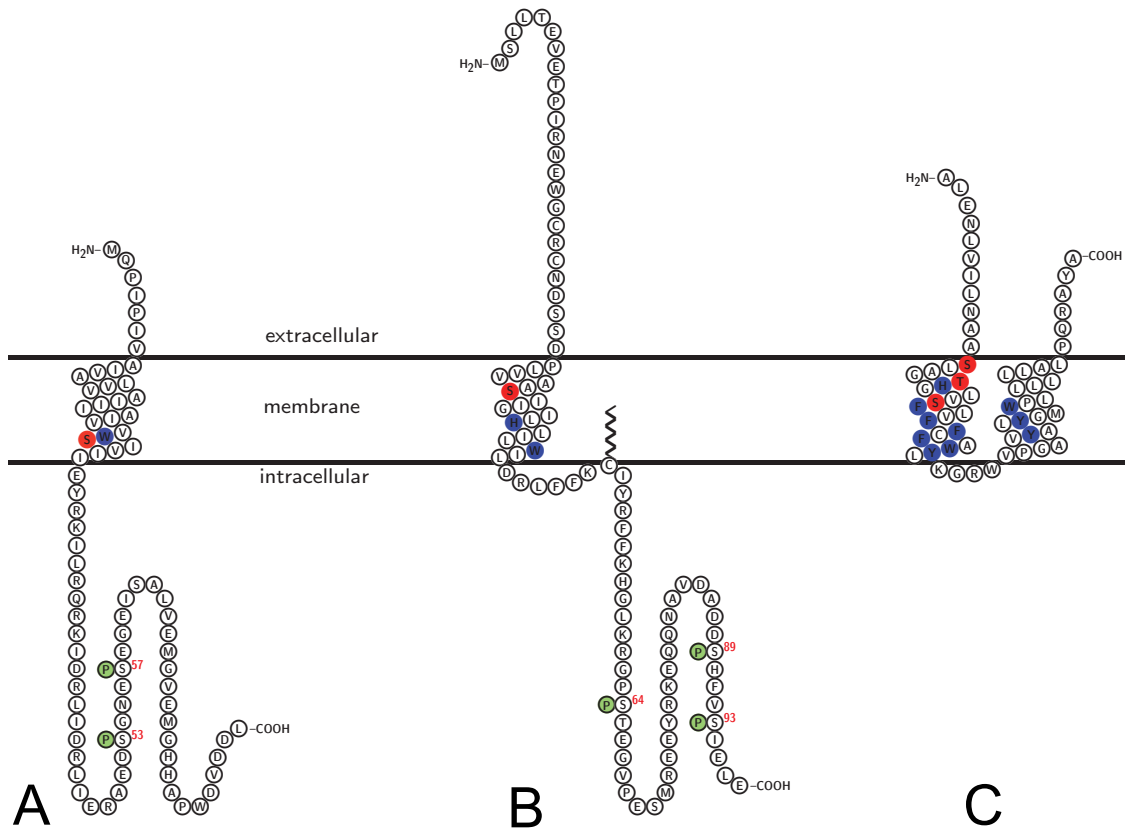


FIGURE 1.2: *Topology diagrams for three viral ion channel monomers* **A**: Vpu from HIV-1 (SWSSProt Entry Code P05919) **B**: M2 from Influenza A (P03491) and **C**: p7 from Hepatitis C virus (P27958). p7 is unusual among viral ion channels, because each monomer has two transmembrane helices [23]. The figures were prepared using the `TeXtopo` package for \LaTeX [24]. Hydrophilic TM residues are shaded red, aromatic TM residues are shaded blue. The putative phosphorylation and palmitoylation sites for Vpu and M2 are also shown.

with some arguing that they should not be designated as ion channels unless they can be shown to be selective for a specific ion and their gating can be regulated [21]. The term *viroporin* has been suggested for those proteins which enhance the permeability of membranes, but are unable to fulfil these criteria [21]. The majority of the literature published in the field uses the term viral ion channel indiscriminately and this term will be used exclusively in this thesis.

1.4 Human Immunodeficiency Virus (HIV)

HIV infection in humans has reached pandemic proportions. In January 2006, the Joint United Nations Programme on HIV/AIDS (UNAIDS) and the World Health Organisation (WHO) estimated that AIDS has killed more than 25 million people worldwide since 1981, and that 0.6% of the global population is infected by HIV [25]. The virus may cause a progressive decline in CD4⁺ T lymphocyte cell counts in humans and lead to the opportunist infections characteristic of acquired immunodeficiency syndrome (AIDS) [26–28]. However an estimated 10% of HIV positive individuals do not develop AIDS within 15 years of the initial infection [29].

HIV is a member of the *Lentivirus* genus of retroviruses, which are best known as agents of slow disease, persisting indefinitely in their hosts and replicating continuously during the course of a lifelong infection [30]. Disease in *Lentivirus*-infected organisms may be primary (directly induced by the virus) or secondary (caused by opportunist pathogens which proliferate unchecked as a result of the loss of T_h lymphocyte function). Unlike other retroviruses, lentiviruses replicate efficiently in non-dividing, terminally differentiated cells both *in vitro* and *in vivo* [31, 32].

Two distinct species of HIV infect humans (HIV-1 and HIV-2). HIV-1 is more virulent, is easily transmitted and is thought to have originated from wild chimpanzees in southern Cameroon, before transferring to humans in around 1930 [33–35], although a recent study has dated the emergence of the human virus to *circa* 1900 [36]. HIV-2 is largely confined to West Africa, where it is believed to have originated in the Sooty Mangabey monkey [37]. HIV-1 is classified into three distantly related groups (M, N and O) and Group M, which is responsible for the global HIV pandemic, is further classified into nine subtypes or lineages (A, B, C, D, F, G, H, J and K) [38]. There is an uneven geographical distribution of HIV-1 subtypes: Subtype C accounts for around 50% of all HIV-1 infections worldwide,

but is largely absent from North America and Europe; Subtype B is responsible for 12% of global HIV-1 infections, but is the dominant form in the developed world (see Table 1.1) [39, 40].

Region	New HIV-1 Infections in 2000 ($\times 10^3$)	Percentage of HIV-1 env subtypes			
		A	B	C	D
Southern Africa	1680	1.08	4.03	94.22	0.00
West Africa	850	79.91	0.99	1.72	2.71
East Africa (excluding Ethiopia)	700	56.32	2.44	7.16	32.71
Central Africa	260	56.32	2.44	7.16	5.78
Ethiopia	350	0.00	2.50	95.00	2.50
North Africa and Middle East	80	44.00	40.00	4.00	4.00
West Europe	30	6.72	84.49	1.76	0.52
East Europe and Central Asia	250	55.97	36.01	3.73	1.87
East Asia and Pacific	130	4.76	82.14	0.00	1.19
Southeast Asia	230	0.16	32.34	0.63	0.00
Indian Subcontinent	550	0.00	80.71	1.61	0.00
Latin America and Caribbean	210	0.00	80.71	1.61	0.32
North America	45	0.00	96.49	0.00	0.00
Worldwide	5365	26.70	12.30	47.20	5.30

TABLE 1.1: Percentage of HIV-1 subtypes A to D by world region (adapted from [39]). Subtypes F, G, H, J and K accounted for the remaining 8.5% of new HIV-1 infections worldwide in 2000.

1.5 The Vpu protein of HIV-1

In addition to the enzymes and structural proteins common to all retroviruses, the genome of HIV-1 also encodes four accessory proteins, lacking enzymic activity, which are not essential for successful reproduction in $CD4^+$ T lymphocyte cell lines. The four proteins (Nef, Vpr, Vif and Vpu) are responsible for manipulating the metabolic processes of host cells to increase the rate of viral replication [41].

Vpu is a 9 kDa, monotopic integral membrane protein found in the membranes of infected cells but not in the virus particles themselves [42]. The protein has two roles *in vivo*: It enhances the release of newly formed virus particles from the cell

surface [43, 44], and is responsible for targetting newly-synthesised CD4 receptor to the degradation pathway [45, 46]. The two functions are associated with separate domains of the protein [47]. The cytoplasmic helices bind the cytoplasmic tail of CD4 and promote the recruitment of β -TrCP and Skp1p, which target CD4 for ubiquitination and proteasomal degradation. In cells infected by HIV-1 carrying a Vpu mutant from which the C-terminal cytoplasmic helices have been deleted, CD4 is able to reach the endoplasmic reticulum (ER). Once in the ER, CD4 binds to the viral coat protein gp160 and prevents it from being correctly incorporated into the capsid [48, 49].

The transmembrane domain of Vpu is able to oligomerise within bilayers to form ion-conducting pores which are responsible for enhancing the rate at which viral release occurs, by altering the transmembrane potential. This mechanism is currently in dispute (see Section 1.5.1) and critics suggest that this is an *in vitro* effect, which is not replicated *in vivo*.

There is considerable variation between Vpu sequences from different HIV-1 subtypes (see figure 1.3). The subtype B protein (studied in this thesis) is localised predominantly in the Golgi body of infected cells [44, 50, 51], although it has been detected in complex with CD4 at the cell surface in HeLa cells [52]. The second cytoplasmic α helical domain of the subtype B Vpu includes the signal sequence for the retention of the protein in the Golgi body [42]. In contrast, subtype C Vpu lacks this signal sequence and is not retained within the intracellular membranes of the host cell, and is instead transported efficiently to the cell membrane. Subtype C Vpu has been shown by flow cytometry to downregulate the expression of CD4 at the cell surface less efficiently than the subtype B protein [53].

The *Vpu* gene is absent from both HIV-2 and simian immunodeficiency virus (SIV) genomes, although one isolate of the HIV-2 Env envelope protein appears to be able to enhance virus particle release [55, 56]. This activity requires both the

Subtype	Isolate	Sequence
B	H2	MQPIP-----I V A I VA L V V AI I I A IV V W S I V L I E Y R K L R Q R K I D R L I D R L I E R A E D S G N E S E G E I S A L V E M G V E M G H A F W D V D D L
B	RH	MQSLE-----I L A I VA L V V AI I L A IV V W T I V G I E I R K T L R Q K I D R L I D R L I E R A E D S G N E S D G D E E L S A L - V E M G H A F W D V D D L
B	WE	MQS L Q-----I L A I VA L V V AI I L A IV V W S I V L I E Y R K L R Q R K I D R L I D R L I E R A E D S G N E S E G D Q E E L S A L - V E M G H A F W D I D D L
C	ET	M V D L L A K V D Y R I V I V A F I V A L I I A IV V W T I A Y I E Y R K L L R Q R I D R L I K R T E R A E D S G N E S D G D T E E L S T M - V D M G N L R L L D V N D L
C	92	M L E L I G R I D Y R L G V G A L I V A L I I V I V W T I A Y I E Y R K L V R Q R I D W L V K R I K E R A E D S G N E S G D T E E L E T M - V D M G H L R L L D G N D L
C	BW	M I N F L A K V D Y R L G V G A L I V A F I I A IV V W I I A Y I E Y R K L L R Q R K I D R L I R K I E R A E D S G N E S D G D I E E L S A M - V D V G H L R L L D V

FIGURE 1.3: *ClustalW* alignment of the sequences of *Vpu* from isolates of HIV-1 subtypes B and C [54]. Subtype B, Isolate H2 is studied in this thesis. The C-terminal 13 residues of Subtype B *Vpu* are responsible for the retention of the protein in the Golgi body [42]. The WS/TIxxIEYRK motif at the C-terminal end of the putative transmembrane domain and the RAEDSGNES phosphorylation motif between the two cytoplasmic helices are highly conserved.

cytoplasmic tail and ectodomain of the protein. The membrane-spanning domain of the HIV-2 Env protein appears to be less important for this process, suggesting that the mechanism is not analogous to that of *Vpu* in HIV-1 [57].

1.5.1 Mechanism of enhancement of HIV-1 release from infected cells

The mechanism by which the transmembrane domain of *Vpu* enhances virus particle release from the cell surface membrane is disputed. There are two competing hypotheses: that *Vpu* interacts with host proteins to down-regulate their activity [58]; or that *Vpu* forms ion channels within the host cell membranes, to alter the transmembrane electrochemical potential [59].

The extent to which *Vpu* is able to enhance the rate of virus particle release from cultured cell lines *in vitro* is dependent on cell type. African green monkey epithelial cells (Cos-7) are able to produce new virus particles efficiently when infected with an infectious molecular clone of HIV-1 from which the *Vpu* gene has been deleted. However human epithelial HeLa cells are only able to produce new virions when infected by a molecular clone containing the *Vpu* gene. In their 2003 paper, Varthakavi *et al.* argued that *Vpu* was required by the HIV-1 virus to

overcome a dominant host cell restriction to assembly, which is present in human cell lines [58].

Vpu has been shown to interact *in vivo* with a number of mammalian proteins. In their 2004 paper, Hsu *et al.* showed that Vpu is homologous to the first part of the mammalian TASK1 K⁺ channel and that Vpu was able to bind to TASK1 channels at the cell membrane and inhibit expression [60]. The authors suggested that Vpu might be able to modify the TASK1 protein by forming a hetero-oligomeric structure. (The peptide MiRP1 modifies the mammalian HERG pore-forming protein to produce a potassium channel, with a substantially altered gating from the original homotetrameric protein [61].) Earlier voltage clamp experiments showed that when Vpu is expressed in *Xenopus* oocytes, ion flux through the endogenous K⁺ channels in the membrane is inhibited [62]. It is questionable whether this effect is likely to be able to account for the increase in virus particle release from the cell surface membrane, given that the K⁺ ion potential is close to equilibrium in most mammalian cells [5]. The expression level of TASK1 in T_h lymphocytes is also unclear. In a recent paper by Neil *et al.*, tetherin, a previously unidentified membrane-associated protein, was shown to have the ability to prevent HIV-1 virus budding from the cell surface membrane, and was disrupted in an expression system in which Vpu was present [63].

More recently, *in vivo* experiments involving the construction of a chimaeric gene consisting of the transmembrane helix of the M2 ion channel from Influenza A and the cytoplasmic domain of Vpu, have been used to produce evidence in support of the ion channel hypothesis. The chimeric *Vpu* gene was substituted for the wild type gene in the genome of a pathogenic simian human immunodeficiency virus SHIV_{KU-1bMC33}, and the resulting virus was fully functional and able to reproduce when injected into pig-tailed macaques [64]. Electron microscopy of C8166 cells, infected by the virus carrying the chimaeric gene, showed that the viral infection was sensitive to rimantidine, a well-characterised inhibitor of the

M2 channel [64]. A similar effect was observed, when the A19H mutation, which produces the WxxxH motif also present in M2, was introduced into a wild type *Vpu* gene; virus particles again accumulated at the cell surface membrane when infected C8166 cells were treated with rimantidine [65].

1.5.2 Structure of Vpu

Vpu from HIV-1 subtype B has 82 amino acids and three α helices, of which one spans the phospholipid bilayer, while the others lie on the cytoplasmic surface of the membrane [59]. The cytoplasmic portion has two potential phosphorylation sites at residues Ser52 and Ser57 [66].

The structure of the transmembrane (TM) domain of wild type Vpu has been resolved by solid state NMR and has been shown to be a kinked α helix tilted at an angle of 12° to the bilayer normal [67]. The transmembrane domain of the rimantidine-sensitive A19H mutant is an ideal straight helix, which has tilt angle of 41° (greater than that of the wild type helix) in C14 phospholipid bilayers [68].

Simulation studies suggest that three residues, Trp23, Ser24 and Arg31, are important for ion conduction (see figure 1.4) [69]. Current models indicate that in the pentameric and hexameric bundles, the serine residues face the interior of the pore and that the tryptophan residues are at the lipid-protein interface. Ser24 is thought to stabilise the ions as they cross the membrane; Trp23 is thought to anchor the peptide in the bilayer and Arg31 is thought to form a salt bridge clamp to residues Tyr30 and Glu29, which stabilises the bundle [70].

Vpu is believed to form pentameric assemblies *in vivo* (figure 1.4) and the transmembrane (TM) helices form multimeric ion-conducting pores, which enhance the rate of budding and release of new viral particles. Mutations in the transmembrane domain which abrogate *in vitro* channel activity result in a reduced viral

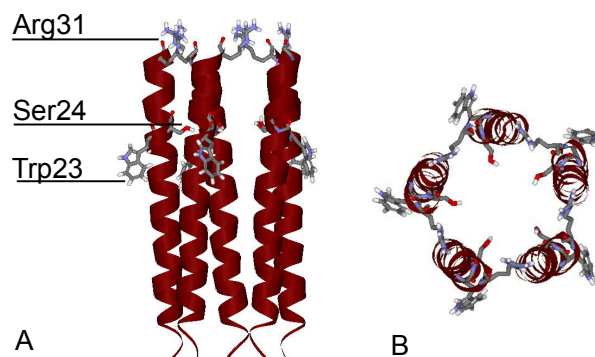


FIGURE 1.4: *Model of a pentameric bundle of Vpu₁₋₃₂ after [69]. A: side view B: view from N terminus. The model was drawn with DS ViewerPro (Accelrys Inc.). For clarity the lipid bilayer and water molecules are omitted.*

release rate [71, 72]. A truncated Vpu peptide, (Vpu₁₋₃₂, the TM domain), has been shown to be sufficient to enhance virus particle release without degrading CD4. Vpu is therefore a potential drug target and investigations into its activity have wide-reaching implications for the development of AIDS therapies [73].

1.5.3 Inhibition of *in vitro* ion channel activity of Vpu

Amiloride is a well characterised inhibitor of transmembrane ion transport, which inhibits the multimeric ENaC Na⁺ channels of the urinary epithelia and is used therapeutically as a diuretic [74]. It has also been shown to inhibit a number of eukaryotic Na⁺/H⁺ antiporters and Na⁺/Ca²⁺ exchangers [75].

Two amiloride derivatives, HMA and DMA (see figure 1.5), have been found to inhibit the *in vitro* channel activity of Vpu₁₋₃₂ reconstituted into black lipid membranes at concentrations of 100 μ M and 125 μ M respectively. An HMA concentration of 10 μ M was also found to inhibit the budding of new virus-like particles from the plasma membranes of HeLa cells expressing HIV-1 Gag and Vpu proteins [73]. *In silico* docking simulations of both charged and uncharged forms of both HMA and amiloride to monomeric and multimeric forms of Vpu₁₋₃₂ suggest that HMA inhibits Vpu by occluding the pentameric channel [76, 77].

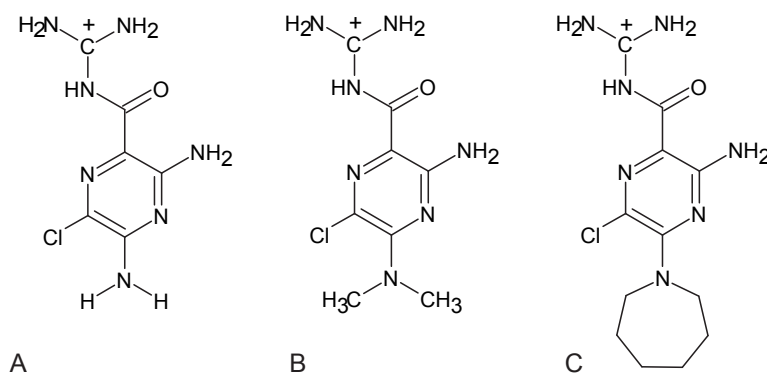


FIGURE 1.5: *Structural formulae of amiloride and derivatives at physiological pH* **A**: amiloride, **B**: DMA and **C**: HMA. The positive charge on the guanidinium moiety is stabilised by resonance.

Both HMA and DMA have been shown to inhibit the replication of HIV-1 in cultured human blood monocyte-derived macrophages (MDM cells) at micromolar concentrations. An HMA concentration of 10 μM was effective at suppressing the accumulation of viral DNA and RNA in cultured MDM cells over a period of ten days. HMA concentrations above 30 μM were found to be toxic to HeLa cells [78].

1.6 Examples of other viral ion channels

1.6.1 M2 from Influenza A

The M2 proton channel from Influenza A is a homotetrameric type III integral membrane protein of 97 amino acids, essential for viral replication [79]. The homotetramer is stabilised by disulphide bridges between the N-termini of neighbouring helices, although these bonds are not essential for ion flux [79]. M2 is active at two stages of the Influenza life cycle. It promotes viral uncoating after the virion has been engulfed by the host cell [80] and is found in the internal membranes of the host, where it is thought to influence the pH balance between the

acidic lumen of the trans Golgi network and the cytoplasm, preventing the premature conformational change of the viral envelope glycoprotein hemagglutinin [81]. Unlike most other viral ion channels, M2 is detectable as a minor component of the viral membrane [17].

M2 is highly selective for H^+ ions and the selectivity is dependent on the presence of the histidine residue of the HxxxW motif in the transmembrane part of the channel. Substitution of this residue by gly, thr, ser, ala or glu, results in the loss of specificity, allowing mutants to transport the larger cations Na^+ and K^+ [82]. The ion selectivity of the H37G, H37S and H37T mutants was partially restored in the presence of 50 mM imidazole at pH 5.5 [83].

The specific activity of M2 is low ($10^5 H^+ s^{-1}$ at pH 5.7) and the conductance decreases further in D_2O by an amount greater than the molecular weight ratio of H_2O and D_2O , indicating that the bulk transport of H_3O^+ is not involved in the mechanism of ion flux. Two mechanisms for H^+ ion conduction have been proposed: a *histidine/proton shuttle* mechanism, supported by energy minimisation simulations, in which the imadazole ring of His37 serves as a relay, binding H^+ on one side of the channel and releasing it to the other membrane face [84, 85]. An alternative, *transient proton wire* hypothesis, supported by the results of molecular dynamics (MD) simulations, allows the rapid transfer of H^+ ions along a network of hydrogen-bonded water molecules [86, 87].

The antiviral drugs amantadine and rimantidine inhibit ion flux through the channel and are routinely prescribed as antiviral drugs against community outbreaks of Influenza A infection [88]. Four rimantidine molecules have been shown by solid state NMR to bind to four equivalent sides on the lipid-accessible faces of the tetramer, near residue Trp41, stabilising the closed conformation of the pore. The amine headgroup of rimantidine is in close contact with the polar sidechains of

Asp44 and Arg45 and the molecule creates a “polar patch” in a highly hydrophobic region of the protein (see figure 1.6) [89].

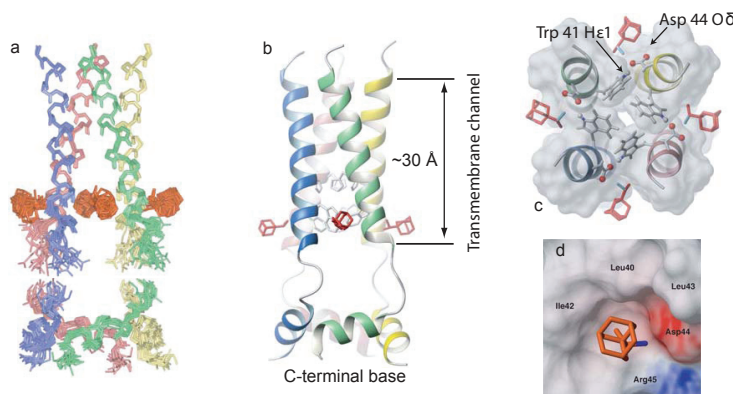


FIGURE 1.6: *Solution state NMR structure of the M2 channel in the presence of the inhibitor rimantidine* reproduced from [89]. (Protein Data Bank accession code 2RLF.) **a**: An ensemble of 15 low energy structures derived from NMR restraints. **b**: Ribbon representation of a typical structure from the ensemble shown in **a**, showing the left handed packing of the amphipathic helices, the side chains of His37 and Trp41 and the drug rimantidine (coloured red). **c**: Close up view of C-terminal side of channel showing the Trp41 gate and its stabilisation by Asp44 of the adjacent helix. **d**: Surface representation of the rimantidine binding pocket showing the residues which form the “polar patch”.

The crystal structure of M2 in the presence of amantidine has been solved to 3.5 Å resolution. An region of electron density in the C-terminal mouth of the channel was suggested by the authors to indicate the binding site of the drug and that this data supports the inhibition of the channel by occlusion [90].

Although the solution state NMR and crystal structures for M2 differ in the location of the amantidine binding site, their structures are broadly similar. Both structures show the highly conserved residues His37 and Trp41 pointing into the centre of the pore. The NMR structure appears to represent the closed state of the channel, and the TM α helices are sufficiently close together, that the four Trp41 residues occlude the lumen [89]. The X-ray crystal structure has been suggested to represent the the open conformation and the helices are splayed further apart

at the C termini, widening the pore at the level of the Trp41 residues [90, 91]. Mutations found in adamantane-resistant strains of Influenza A would appear to map to the region proposed as the adamantane binding site in the crystal structure [92], although the same residues are shown in the solution state NMR structure to be important for inter-helix interactions and substitution of these residues may reduce the stability of the closed state relative to the open state [89]. The mechanism proposed in [89] is also supported by the fact that inactivation of the channel occurs more rapidly at low pH, when the channel is open [93].

BM2 is a homotetrameric proton channel from the closely related virus, Influenza B. The only significant homology to M2 is the HxxxW motif of the transmembrane spanning region [17]. The genome of Influenza B encodes a second viral ion channel, NB, which is not essential for viral replication *in vitro* [94].

1.6.2 p7 from Hepatitis C

p7 is a type III integral membrane protein, which forms cation-selective ion channels in the internal membranes of cells infected by Hepatitis C [95]. The exact role of p7 in the viral life cycle is unclear, however the protein is essential for virus infectivity [96]. Unlike most other viral ion channels, each monomer has two transmembrane helices, resulting in the orientation of both the N and C termini towards the extracellular side of the membrane, (figure 1.2). Transmission electron microscopy of GST-FLAG-p7 fusion proteins reconstituted into unilamellar phosphatidic acid and phosphatidyl choline lipid vesicles, suggest that p7 is heptameric [18]. *Ab initio* model building *in silico*, found that a hexameric channel was most plausible and suggested that the His17 residues formed a ring lining the inside of the channel [97].

Proteins related to p7 have been found in two other members of the *Flaviviridae* family: The p13-C protein from GB Virus B is essential for viral replication *in*

vivo and forms cation-selective ion channels in black lipid membranes [98, 99]. Although *in vitro* channel activity is completely inhibited in the presence of 10 μM amantidine, the *in vivo* replication of the virus in marmoset hepatocyte cell lines was not affected at amantidine concentrations of up to 100 μM [99]. A p7 protein, essential for viral replication *in vivo*, is also present in the related Bovine Viral Diarrhoea Virus [100].

1.6.3 6K from Alphavirus

The 6K protein is encoded by the genomes of three members of the *Alphavirus* family and is expressed in the internal membranes of host cells, but is largely excluded from the viral membrane. The proteins are not essential for viral replication, however total deletion of the *6K* gene in Semliki Forest Virus (SFV) reduces the rate of *in vitro* viral replication to between 2% and 50% of the wild type virus, depending on the host cell type [101]. A partial deletion of the *6K* gene in Sindbis Virus resulted in a 300 fold decrease in the rate of virus particle release, which was partially abrogated by the introduction of the *Vpu* gene from HIV-1 [102]. Inducible expression of the SFV 6K protein in *E. coli* cells enhanced the permeability of the bacterial membrane [103], and when Sindbis Virus 6K protein was expressed in *Xenopus* oocytes, endogenous transmembrane currents were found to be increased [104].

Melton *et al.* observed *in vitro* cation-selective channel activity when recombinant BFV and Ross River Virus 6K proteins were reconstituted into black lipid membranes; a range of rapidly fluctuating conductances of between 40 pS and 800 pS was observed [105]. The N-terminal domains of the 6K proteins are rich in aromatic residues [22]. It has been suggested that the protein is unstructured in this region and destabilises the membrane around the channel mouth thus enhancing membrane permeability [21, 22]. It is possible that this mechanism is responsible

for the rapid fluctuations in conductance observed by Melton *et al.*, rather than a rapid switching between oligomerisation states.

1.7 Inhibition of eukaryotic ion channel activity

The channel architecture, gating and regulator mechanisms of the n-acetyl choline receptor are described in this section, in order to place the mechanisms of inhibition of viral ion channels into the wider context of ion channel modulation.

1.7.1 General Anaesthetics

A wide variety of exogenous compounds are capable of modulating the activity of mammalian ion channels. The most clinically important of these are the general anaesthetics, a diverse group of hydrophobic drugs, which are routinely administered to patients before surgery. Chemical agents which induce a state of general anaesthesia include the inert gas xenon and simple compounds such as nitrous oxide (N_2O) and chloroform [106].

1.7.2 The Meyer-Overton Rule

The Meyer-Overton rule relates the critical concentration at which a state of anaesthesia is induced (ED_{50}) by a given molecule to its octanol/water partition coefficient (P) (see equation 1.1) [107, 108].

$$ED_{50} \propto \frac{1}{P} \quad (1.1)$$

Some volatile compounds, which are homologues of well characterised general anaesthetics and which are predicted by the Meyer-Overton rule to be general

anaesthetics, have no anaesthetic potency. In many homologous series, anaesthetic potency is increased by adding successive methylene groups up to a *cutoff* point, beyond which there is a complete loss of anaesthetic potency [109]. The primary alcohols comprise a homologous series of anaesthetics which exhibits this trend. The anaesthetic potency of compounds in the series increases from methanol to decanol, after which the potency decreases dramatically. Tridecanol ($C_{13}H_{27}OH$) and higher homologues are completely devoid of anaesthetic activity [110, 111].

Substitution of functional groups of anaesthetic molecules can also alter anaesthetic potency contrary to the Meyer-Overton rule. For example, substitution of fluorine by larger halogens increases anaesthetic potency and the molecular size at which the cutoff occurs, however polyhalogenation of monofluorinated anaesthetics produces compounds which induce transient tremors and convulsions in tadpoles [112].

1.7.3 Inhibitors of nAChRs

Neural nicotinic acetylcholine receptors (nAChRs) are pentameric ligand-gated ion channels consisting of five homologous subunits arranged around a central pore with the composition $\alpha_2\beta\gamma\delta$ and $\alpha_2\beta\epsilon\delta$ in embryonic and adult neuronal muscle tissue respectively [113]. The channels are located in the postsynaptic membrane and in the presynaptic and preterminal areas of interneurons [114], and when activated, stimulate the release of neurotransmitters including GABA, glutamate, acetylcholine, dopamine and norepinephrine [115].

nAChRs may exist in three or more interconvertible states. In a model proposed by Dilger in 2002, the three states, resting (R), channel-open (R^*) and desensitised (D), spontaneously interconvert in the absence of agonist. Exposure of the receptor to agonists initially increases the probability of the R^* state, however prolonged exposure results in the stabilisation of the receptor in the D state [116].

Agonist-induced activation of nAChRs is noncompetitively inhibited by a structurally diverse group of exogenous and endogenous compounds. Noncompetitive antagonists (NCAs) inhibit by one or more different molecular mechanisms [117]:

1. An open-channel blocking mechanism in which the NCAs bind within the lumen of the pore, blocking the passage of ions.
2. Binding to and stabilising D or R states.
3. Increasing the rate of transition from R* to D states.

nAChRs are also sensitive to the lipid composition of the membrane in which they are located. The functional properties affected by the lipid environment include the processes of channel gating, opening and closing and the kinetics of desensitisation [118, 119]. Electron spin resonance (ESR) was first used to identify the presence of a lipid annulus of negatively charged lipids, steroids and fatty acids, surrounding the protein [120, 121]. The annular lipids are restricted in motion both around and perpendicular to their long axes and exhibit rotational correlation times which are typically 50-100 times greater than those of lipids in a fluid bilayer [122]. Water penetrates this region to a lesser degree than the bulk bilayer lipid, making the region more hydrophobic [123]. There are also discrete lipid binding sites on the surface of the nAChR, but distant from the interface of the annular lipid, initially identified as crevices in the first low resolution electron micrographs of the receptor (see figure 1.7) [124].

Given the complex nature of the interactions between the nAChR and lipophilic species, there are a number of potential ways in which hydrophobic drugs could inhibit ion flux through the channel. It has been suggested that drug-induced perturbations in bulk membrane properties may alter protein function, although binding sites for some lipophilic drugs have been identified [127]. Such drugs could directly influence membrane protein activity by disrupting the formation of lipid

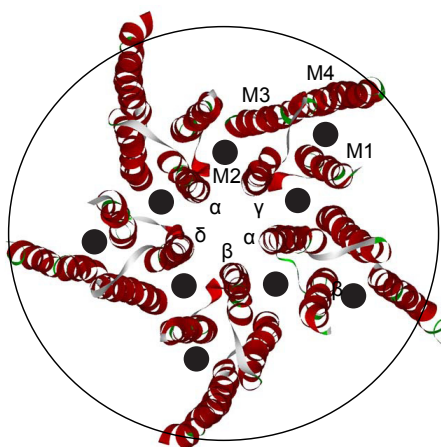


FIGURE 1.7: *Molecular model of the closed (resting) AChR pore from Torpedo* modified from [117]. Coordinates were taken from the Protein Data Bank with accession code 1OED [125]. The model was drawn with DS ViewerPro (Accelrys Inc.). The perimeter of the AChR is surrounded by 42 ± 7 lipid molecules, (the annular lipid domain, represented by the large circle) [126]. The small filled circles between helices represent the possible locations of non-annular lipids. The transmembrane helices of the γ subunit are labelled.

rafts and the association of proteins with rafts [128, 129]. Alternatively a channel blocker could bind directly to the lumen of the channel, thus preventing ion flux.

1.7.3.1 Tetracaine and procaine

The local anaesthetic tetracaine (figure 1.8A) has been shown by photoaffinity labelling studies to bind between the rings of valine and isoleucine in the centre of the channel, thus inhibiting ion flux. The benzene ring is positioned at the valine ring (position 9) with the N-butyl chain interacting with the hydrophobic residues at positions 12 and 13 [130]. Tetracaine has also been shown to partition into unilamellar phosphatidylcholine vesicles and to affect the pressure- and temperature-dependent phase behaviour of DMPC [131–133]. Procaine (figure 1.8B), a related compound, lacks the butyl group on the *N*-aryl moiety and interacts with the resting *Torpedo* nAChR with 1000-fold lower affinity than tetracaine, suggesting

that the interaction between the butylammonium group of the drug and the hydrophobic residues at positions 12 and 13 contributes to the stabilisation of the drug at this point (figure 1.9) [134].

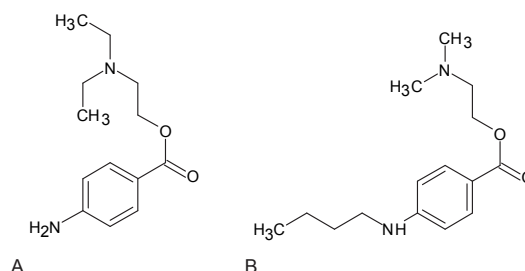


FIGURE 1.8: *Structures of inhibitors of the Torpedo nAChR* **A**: tetracaine **B**: procaine.

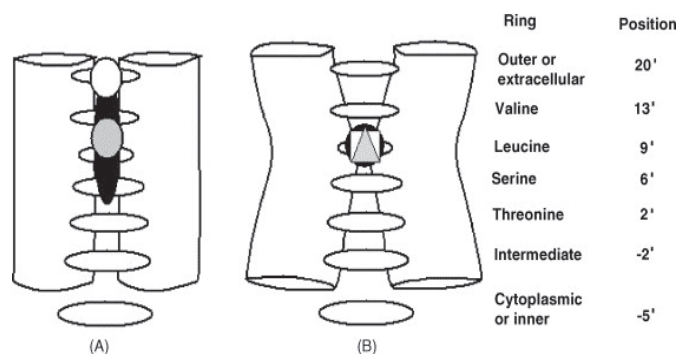


FIGURE 1.9: *Cartoons of the Torpedo nAChR reproduced from [117]* **A**: resting state **B**: closed state. In the resting state the tetracaine binding domain (black elongated ellipse) is located between positions 5 and 20

1.7.3.2 Quinacrine

Quinacrine is a potent, fluorescent NCA of nAChR. FRET measurements performed with the lipophilic acceptors 5-(*N*-dodecanoylamino)eosin and *N*-(3-sulphopropyl)-4-(*p*-didecylaminostyryl)pyridinium suggest that the quinacrine binding site is located less than 10 Å from the lipid bilayer [135], (the centre of the channel is approximately 20 Å from the phospholipids) [136]. Quinacrine fluorescence

was also quenched by nitroxide-labelled phospholipids, suggesting that the spin-labelled phospholipids are accessible to the drug binding site [137, 138]. Photo-labelling experiments with an azide derivative of quinacrine, suggest that the drug binding site is adjacent to Arg209 and Pro211 of the δ M1 transmembrane domain at the lipid-water interface. However further fluorescence quenching experiments using the fatty acid analogue spin-labelled-stearate, have suggested that the drug binding site is buried approximately 7 Å below the lipid-water interface, in the interior of the bilayer and that the quinacrine binding site is in intimate contact with a non-annular lipid molecule [139, 140]. Cys residues introduced into the pore-lining M2 transmembrane helix were protected from reaction with 2-aminoethyl methanesulphonate by quinacrine binding, suggesting that structural changes involving complete closure of the pore are induced on drug binding [141].

1.7.3.3 Halothane

Halothane (2-chloro-2-bromo-1,1,1-trifluoroethane) is a clinically important volatile anaesthetic which inhibits ion conduction by nAChRs with an IC_{50} of 0.1 mM for neuronal subtypes and 0.8 mM for muscle subtypes [142]. Tyr228, located on the M1 helix of subunit δ , was identified as a binding site for halothane in photo-labelling studies. The δ Tyr228 sidechain projects into a water-accessible pocket between the δ M1 and δ M3 helices, access to which appears to be increased in the D state relative to the R* state [143].

1.8 Aims of the thesis

The primary aim of the thesis is to further the knowledge of the kinetics and inhibition of the ion channel activity of Vpu from the subtype B isolate of HIV-1, using a combination of experimental and computational techniques.

The transmembrane domain (Vpu₁₋₃₂) has been synthesised by solid phase peptide synthesis, purified and black lipid membranes and ion channel currents recorded (Chapter 2). The channel activity of the S24A (Vpu₁₋₃₂) mutant is characterised and the inhibitory action of the amiloride derivatives HMA and DMA is examined. The full length protein (Vpu₁₋₈₂) has been expressed as a fusion with glutathione-*S*-transferase, purified by affinity chromatography and reconstituted into black lipid membranes (Chapter 3). The kinetics of the transmembrane domain and the full length protein are compared.

The mode of inhibition of Vpu by HMA has been investigated using MD simulations (Chapter 4). The insertion of drug molecules into a model POPC membrane will be followed and the equilibrium position of the drug in the membrane has been determined. Binding sites for the drug on the exterior of the Vpu bundle have also been explored.

The predictions made by MD simulation have been tested using MAS NMR spectroscopy. The equilibrium location of HMA in a lipid bilayer has been determined by ¹H NOESY and 1D ³¹P spectroscopy (Chapter 6) and evidence for a direct interaction between the drug and residue Trp23 has been sought by ¹³C ¹⁵N REDOR (Chapter 7). The effect of the addition of HMA to DMPC membranes on lipid dynamics has been examined by Raman Spectroscopy.

Chapter 6 introduces the theory of REDOR NMR spectroscopy and its application to determining the nature of the interaction between HMA and Vpu. HMA labelled with ¹³C and Vpu₁₋₃₂ labelled at the backbone nitrogen atom of residue Trp23 ¹⁵N have been synthesised and are used to determine whether any evidence for an interaction exists.

Chapter 7 draws together the main findings of the thesis and suggests future directions to more fully understand the ion channel function of Vpu and the mechanism of inhibition by HMA.

ff

Chapter 2

Channel Recording of Vpu_{1–32}

SUMMARY

A peptide corresponding to the transmembrane domain of Vpu from HIV-1 (Vpu_{1–32}) has been synthesised by solid phase peptide synthesis. Vpu_{1–32} was reconstituted into black lipid membranes, and channel activity was observed. The main conductance state observed has a conductance of 17.5 pS and a principal subconductance state of 13.5 pS. The mean length of individual channel openings is independent of the applied voltage, however the channel open rate increases with the magnitude of the applied voltage. The inhibitor HMA and DMA were found to reduce the probability of channel openings occurring at concentrations up to 100 μ M, however channel activity was not completely abolished. A peptide corresponding to the transmembrane domain of the Vpu_{1–32} S24A mutant was synthesised and reconstituted into black lipid membranes. Channels formed by the mutant peptide were only observed at applied voltages of ± 120 mV, suggesting that the Ser24 residue is important in stabilising ions as they cross the membrane.

2.1 Introduction

2.1.1 Black Lipid Membranes

Black Lipid Membranes (BLMs) are free standing planar lipid films up to 4 nm thick, spread across an aperture of between 0.5 mm and 2.5 mm in diameter, separating two buffer solutions. Like naturally occurring cell membranes, BLMs have a high capacitance of around 0.5 μ F/cm² and resistivities of > 1 M Ω cm² [144]. Electrodes placed in the buffer solutions either side of the membrane may be used

to measure changes in membrane capacitance which correspond to channel and pore formation events.

Two different methods are commonly used to prepare BLMs, both of which require the lipid to first be dissolved in an organic solvent (typically decane). The first method requires the lipid/solvent mixture to be then be brushed across the aperture to form the membrane. In the second method, the lipids are spread across the surface of the buffer on either side of the membrane and the buffer level is lowered below the hole and then raised above it to form the membrane. The second method allows an asymmetrical membrane to be formed if lipid mixtures of different compositions are applied to the buffers either side of the septum. This technique has been used to create an environment which mimics that of the outer membrane of Gram negative bacteria [145]. Whichever method is used, there is the potential for organic solvent to be present in the membrane along with the phospholipids, although BLMs formed using the second technique are generally considered to have with a lower solvent content [146].

Proteins and peptides may be added to BLMs in a variety of different ways. The most straightforward is to pretreat the area immediately surrounding the aperture with the peptide or protein of interest, dissolved in organic solvent, before lipids and buffer solutions are added. The peptide may also be added directly to the buffer solutions, or be reconstituted into vesicles, which are added to the buffer solution either side of the membrane. A transmembrane voltage may be applied or Ca²⁺ ions added to stimulate fusion of the vesicle with the BLM [147].

A major limitation of channel recording experiments, is the intrinsic lack of mechanical long term stability of BLMs, which have a typical half life of a few hours [146]. BLMs are unable to tolerate large fluctuations in surface tension, and hydrodynamic pressure changes caused by evaporation from the chambers may cause the membrane to rupture. Attempts have been made to increase the

stability of BLMs by tethering them to solid supports, however the capacitance and resistance of the membranes is significantly lower than unsupported membranes, and the incorporation of larger membrane proteins (with more than two transmembrane helices) is more difficult in these systems [146, 148, 149].

2.1.2 Previous electrophysiological studies of viral ion channels

In vitro electrophysiological studies of the ion channel activity of viral membrane proteins have largely used chemically synthesised peptides corresponding to their transmembrane domains reconstituted into BLMs. In general, the traces of the channel recordings show rapid fluctuations in current over relatively short time scales. The channels are ohmic conductors of ion flux (*i.e.* the measured current is proportional to the applied transmembrane voltage).

A number of compounds have been identified as inhibitors of viral ion channel activity, most of which are amphipathic molecules and which are capable of partitioning into phospholipid membranes [150]. The most well characterised viral ion channel inhibitor is amantidine, which inhibits the M2 H⁺ channel and is routinely prescribed for community outbreaks of Influenza A [88]. The related compound rimantidine also inhibits the M2 channel [89]. A group of iminosugar derivatives (modified by the addition of a hydrocarbon chain of between four and nine carbons in length) has been shown to prevent ion flux through the p7 channel from HCV [151]. The amiloride derivative HMA, has been shown to inhibit the viral ion channel activity of Vpu from HIV-1 [73].

The quality of channel data appears to be important for the identification of inhibitors of viral ion channels. For example, in their 2003 paper, Griffin *et al.* identified amantadine, as an inhibitor of the Hepatitis C Virus (HCV) p7 protein by *in vitro* channel recordings [23]. The authors reconstituted a p7-GST fusion

protein into black lipid membranes and observed rapidly fluctuating channel currents, which were completely inhibited by the addition of amantadine on both sides of the membrane to a final concentration of $1 \mu\text{M}$ (see figure 2.1). A more recent study with a similar system, in which a HCV p7 was reconstituted into black lipid membranes has cast doubt on this finding [151]. In a randomised, double blind, placebo-controlled trial, the addition of amantadine to the standard anti-HCV therapy of interferon γ -2b and ribavirin, had no effect on patient outcomes [152].

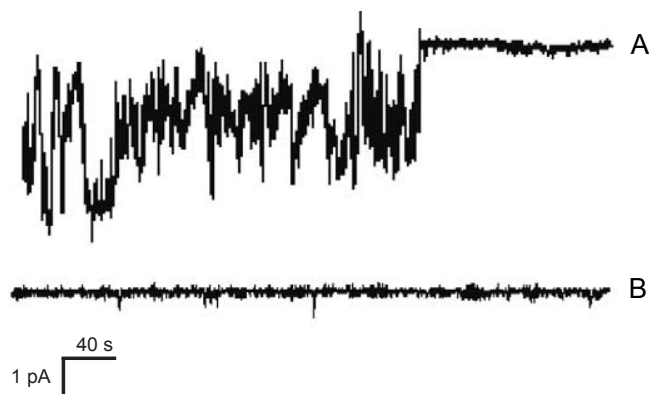


FIGURE 2.1: Channel traces for the p7 protein from Hepatitis C reconstituted into black lipid membranes under an applied voltage of 120 mV (reproduced from [23]) A: rapidly fluctuating conductance in the absence of amantadine. B: transmembrane currents abolished 10 s after addition of amantadine to a final concentration of $1 \mu\text{M}$ to both sides of the bilayer. The time and current scales for both traces are identical.

Similarly, amantidine was found to inhibit the rapid flickering channel activity of the p13 ion channel protein of GB virus B (GBVB) in black lipid membranes, although this was not found to inhibit the reproduction of the virus in an *in vitro* cell culture assay [99].

Given the contradictory results of the BLM assay and the *in vivo* cell culture assays, it is possible that the rapid fluctuations in conductance observed, do not represent channel activity, but instead represent the imperfect insertion of the ion channel peptide into the membrane, resulting in a *leaky* membrane. It has been proposed that some proteins which have been characterised as viral ion channels,

contribute to membrane destabilisation by acting like a detergent and that the inhibition of this activity may have been incorrectly characterised as the inhibition of ion channel activity [21].

2.1.3 Previous electrophysiological studies of Vpu

Channel recordings of covalently linked tetrameric and pentameric assemblies of a variant of the subtype C isolate of Vpu have been obtained. Both the pentameric and tetrameric forms were able to conduct ions and exhibited conductances of 76 pS and 45 pS respectively. The two conductances correspond to those observed when the monomeric form is reconstituted into black lipid membranes, suggesting that this isolate has two oligomeric states which are in dynamic equilibrium with one another. The recordings in that study were performed with at KCl concentration of 500 mM, however in this thesis a lower concentration of 300 mM was used [153]. The higher solute concentration may partially explain why higher conductances were reported in [153] than in this thesis.

Vpu ion channel activity has also been observed in previous electrophysiological studies which use the same isolate as that in this thesis. Unlike the recordings reported in [153], channel openings are not discrete and the transmembrane currents rapidly fluctuate [59]. The same study has also found that the channel was weakly cation selective and that black lipid membranes into which Vpu₁₋₃₂ had been reconstituted were five times more permeable to Na⁺ than Cl⁻. The same authors later reported that Vpu₁₋₃₂ channel activity also inhibited by 125 μ M DMA or 100 μ M HMA administered as a single application [73].

2.1.3.1 Amiloride

Amiloride (figure 1.5) is a well-characterised reversible inhibitor of ion transport. It inhibits the multimeric ENaC Na⁺ channels of the urinary epithelia and is used therapeutically as a diuretic. A putative binding site with the sequence WYRFHY has been identified on an extracellular loop of the α subunit of ENaC, which is thought to lie in close proximity to the channel pore. A similar sequence on the extracellular loop of the γ subunit and other domains both within the pore and the second membrane-spanning domain have also been implicated in amiloride binding [74, 154]. Structural modelling suggests that the positively-charged guanidinium group of Amiloride penetrates into the pore of the channel while the pyrazine group interacts with the outer mouth [155]. The tricyclic antidepressant Amitriptyline has also been found to inhibit ENaC channel activity at higher concentrations, and is thought also though to bind in the same region [156]. Amiloride and its derivatives also inhibit a number of eukaryotic Na⁺/H⁺ antiporters and Na⁺/Ca²⁺ exchangers [75].

2.1.3.2 HMA and DMA

Two Amiloride derivatives, HMA and DMA (figure 1.5), have been found to completely inhibit Vpu channel activity at concentrations of 50 μ M and 125 μ M respectively and were also found to inhibit the budding of new virus particles from the plasma membrane [73]. Docking simulations of charged and uncharged forms of both HMA and Amiloride to monomeric and multimeric forms of Vpu₁₋₃₂ have been performed. The ligands are predicted to bind to residue Trp23 of the monomer interacting through their π molecular orbitals, however in the tetrameric and pentameric bundles both ligands are observed forming a strong interaction with the ring of Ser24 residues at the narrowest part of the pore. The ligand

binds both to the outside of the pore if an interaction with the Trp residue can be achieved and the inside of the hexameric bundles [76].

HMA (but not amiloride) has also been shown to inhibit ion conduction by the E protein viral ion channel from the coronaviruses SARS and Mouse Hepatitis Virus (MHV) in a dose-dependent manner [157]. The traces shown in figure 2.2 demonstrate that the rapidly fluctuating transmembrane currents are inhibited by the addition of HMA to one side of the membrane. The same paper also reported that HMA was able to inhibit replication of HCoV229E in *in vitro* cell cultures with an EC_{50} of 1.34 μM , a concentration considerably below that required for a complete block of the reconstituted E protein.

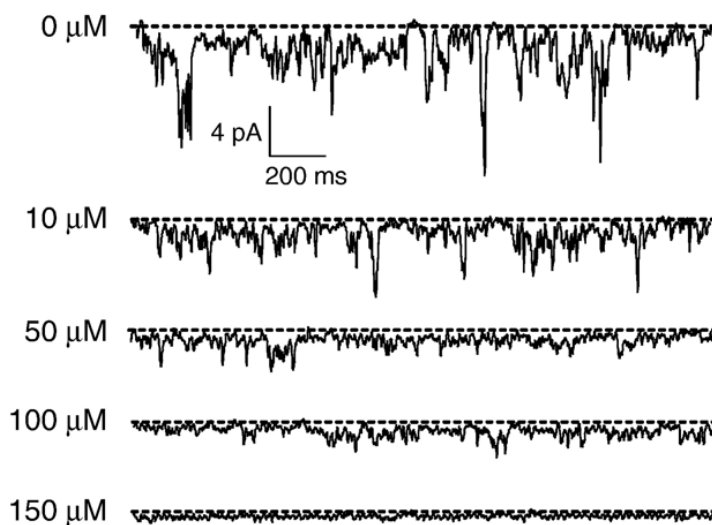


FIGURE 2.2: *Channel traces for the E protein from HCoV-229E reconstituted into black lipid membranes under an applied voltage of -50 mV (reproduced from [157])* The traces show a rapid variation in transmembrane currents, which decreases with successive additions (from 10 μM to 150 μM) of HMA to the cis chamber of the BLM apparatus. The time and current scales for the traces are identical.

It has also been suggested that HMA inhibits the p7 channel from HCV [158].

2.1.4 Channel Kinetics

The conductance of a channel (G) is related to the applied voltage (V) and transmembrane current (I) by equation 2.1.

$$G = \frac{I}{V} \quad (2.1)$$

The SI unit of conductance is siemens (S). Ion channels typically have conductances of between 10 pS and 100 pS, although large channels such as the nuclear pore complex may exhibit conductances in the nS range [11, 159]. A range of conductances may be observed for a single channel and the most frequently observed conductance level is designated the *main conductance state*. *Subconductance* and/or *superconductance* states may also be observed. A main conductance state of 27 pS has been measured for the mouse γ -aminobutyric acid A receptor Cl⁻ channel has been measured using the patch-clamp technique and a principal subconductance state of 16 pS has also been identified [160].

Figure 2.3 shows a typical channel trace of Vpu₁₋₃₂. Square shaped channel openings are observed. The main conductance state is identified by the green line and the principal subconductance state by the orange line. The base level of conductance, corresponding to the closed state, is denoted by the blue line. The duration of an individual channel opening is defined as the open time (t_O). The time period immediately preceding a given channel opening, is defined as the closed time (t_C).

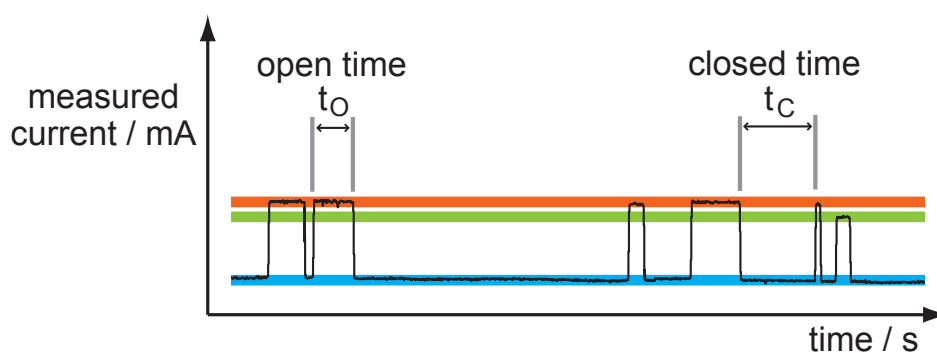


FIGURE 2.3: Trace of channels formed by Vpu_{1-32} reconstituted into black lipid membranes, under an applied voltage of 60 mV. The main conductance state is identified by the green line and the principal subconductance state by the orange line. The closed state in which no current flows through the channel is identified by the blue line.

2.2 Materials and Methods

2.2.1 Peptide synthesis

A peptide corresponding to the TM domain of Vpu was synthesised by continuous flow solid phase peptide synthesis using an automated peptide synthesiser (Pioneer, Perspective Biosystems). Novasyn Fmoc-PAL-PEG-PS resin, to which the first amino acid (lysine) had already been added, was used as a solid support and deprotection was performed with a 20% solution of piperidine in *N,N*-dimethylformamide (DMF). Coupling was performed with a threefold excess of PyBOP, HOBt and HBTU and a fourfold excess of Fmoc-protected amino acids (Novabiochem, Merck Biosciences). (See also Appendix B.1.)

Vpu_{1-32} sequence: MQPIPIVAIV¹⁰ ALVVAIHIAI²⁰ VVWSIVHIEY³⁰ RK

Vpu_{1-32} S24A seq: MQPIPIVAIV¹⁰ ALVVAIHIAI²⁰ VVWAIHIEY³⁰ RK

After synthesis the resin was washed with DCM, methanol and diethyl ether and dried for 24 hours in a desiccator under vacuum. The resin was suspended in

10 ml cleavage solution (94% TFA, 2.5% H₂O, 2.5% EDT, 1.5% TIS) and was agitated for two hours. The resin was washed with TFA and concentrated to 1 ml. 40 ml diethyl ether was added the product was centrifuged at 5000 g at 4 °C for 15 min. The resulting pellet was lyophilised and resuspended in a 1:1 TFE:chloroform mixture prior to purification by HPLC.

2.2.2 Channel Recording

Two different lipid mixtures were used: 1:4 w/w POPE (1-palmitoyl-2-oleoyl-sn-glycero-3-phosphoethanolamine) : DOPC (1,2-dioleoyl-sn-glycero-3-phosphocholine); 7:2:1 POPE : POPC (1-palmitoyl-2-oleoyl-sn-glycero-3-phosphocholine): POPS (1-palmitoyl-2-oleoyl-sn-glycero-3-phosphoserine) (Avanti Polar Lipids, Alabaster, US). Lipid mixtures were dissolved in chloroform, dried under N₂ gas and resuspended in n-decane at 20.0 mg/ml.

A Delrin cup chamber system was used for channel recordings with an aperture diameter of 150 μ m. Lipid suspension was brushed across the aperture and each chamber was filled with 1 ml buffer (300 mM KCl, 5 mM K⁺-HEPES, pH 7.0). Ag electrodes coated with AgCl were used to contact the buffer solution. The level of the *cis* bath was raised and lowered until a bilayer was formed. Experiments were performed at 24 \pm 2 °C and the *cis* bath was held at the desired voltage, while the *trans* bath was connected to earth. The current response was recorded using an Axopatch 700A system with a headstage CV-7B from (Axon Instruments) (see figure 2.4) and data were filtered with a Bessel-8-pole lowpass filter at 10 Hz. The apparatus was enclosed in a Faraday cage to reduce electrical interference. Data obtained from more than twenty discrete experiments is presented in this chapter.

To monitor the effect of HMA, DMA and amiloride on the channel activity of Vpu₁₋₃₂, 10 mM aqueous solutions of the drugs were added in stages to both *cis* and *trans* sides of the membrane, to a final concentration of 100 μ M. Channels

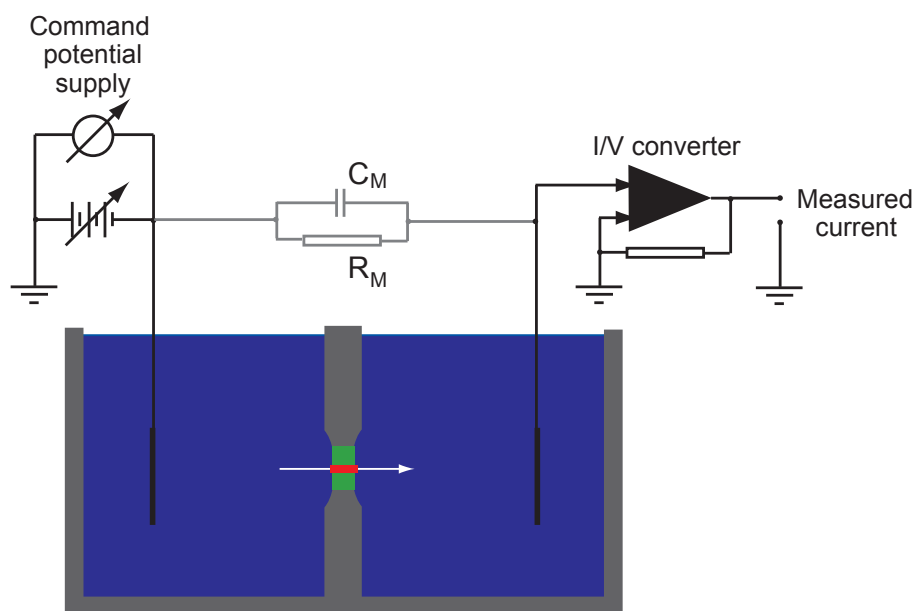


FIGURE 2.4: *Diagram of the bilayer rig* The electrical properties of the membrane may be approximated by a resistor and capacitor in parallel (shown here in grey).

openings were recorded for five minutes between additions of the drug, at voltages of between -80 mV and 80 mV. Data obtained from eight discrete experiments is presented in this chapter.

2.2.3 Data Processing

Raw data were processed and analysed using the ClampFit program (Axon Instruments). Manual baseline correction was used. Individual channel openings were identified and classified into conductance levels using the software. The mean open times for the different states and the rate constants for channel opening were also calculated.

2.3 Results

2.3.1 Vpu₁₋₃₂ synthesis and purification

A peptide corresponding to the transmembrane domain of Vpu (Vpu₁₋₃₂) was synthesised by solid phase peptide synthesis and purified by HPLC. The MALDI mass spectrum of the HPLC fraction is shown in figure 2.5.

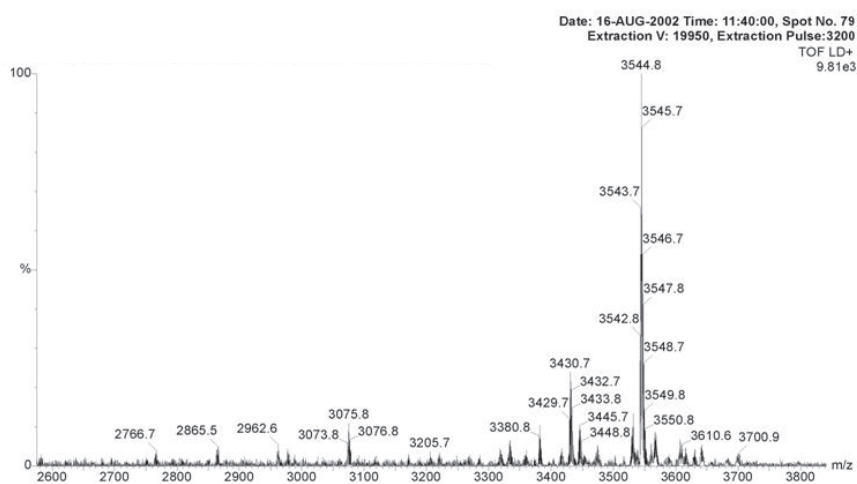


FIGURE 2.5: *MALDI mass spectrum of Vpu₁₋₃₂ acquired by Dr David Harvey (Glycobiology, Oxford). The expected molecular weight of Vpu₁₋₃₂ is 3545 Da.*

A peptide corresponding to transmembrane domain of the S24A mutant of Vpu was synthesised and purified by a coworker.

2.3.2 Vpu₁₋₃₂ channel traces

Figure 2.6 shows the channel traces for Vpu₁₋₃₂ acquired at a range of applied voltages. Initial visual inspection shows that the frequency of channel openings increases with applied voltage.

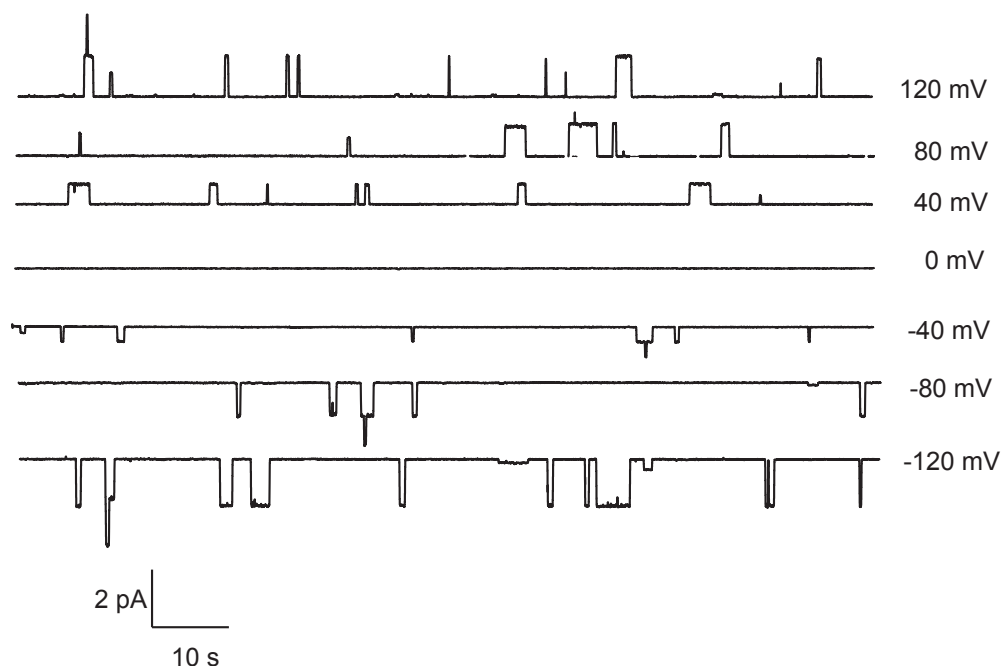


FIGURE 2.6: *Channel trace for Vpu₁₋₃₂ recorded at +80 mV, approximately five hours after the initial formation of the black lipid membrane. At least four channels appear to be active in the membrane.*

In general the number of channels in the black lipid membrane increased over time, as peptide adhering to the sides of the buffer cells diffuses into the membrane. Figure 2.7 shows a trace of Vpu₁₋₃₂ channel openings, recorded approximately five hours after the initial formation of the black lipid membrane containing the peptide. In practice, complex channel recordings such as these proved difficult to analyse, since it was not possible to accurately calculate rate constants if the number of individual channels was unknown.

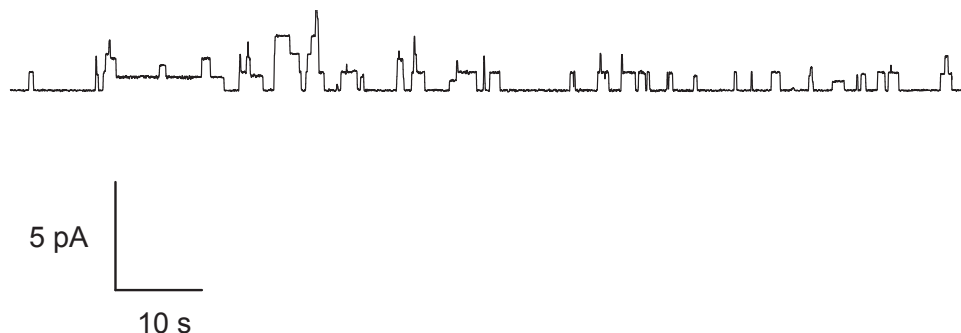


FIGURE 2.7: *Channel trace for Vpu₁₋₃₂ recorded at +80 mV, approximately five hours after the initial formation of the black lipid membrane. At least four channels appear to be active in the membrane.*

2.3.3 Conductance histogram

Figure 2.8 shows the normalised conductance histogram for channel recordings of Vpu₁₋₃₂. The histograms allows two distinct conductance states to be identified. The main conductance state is clearly visible with a conductance of 17.5 pS, accompanied by a main subconductance state at 13.5 pS. The normalised frequency of the closed state has been truncated at 0.33. Additional subconductance states are also visible. A secondary subconductance state occurs at 11 pS and channels may open with a conductance in the range from 3 pS to 8.75 pS. Subconductance states have not previously been identified in channel recordings with Vpu₁₋₃₂. The origin of the different conductance states will be discussed in detail in section 2.4.1, however the presence of multiple conductance states may suggest that the protein is able to access different conformations or that the channel is able to conduct different ions.

2.3.4 I/V Curves for Main and Subconductance States

Figure 2.9 plots the channel currents for the main conductance state and principal subconductance state against applied voltage. The conductance of each state may

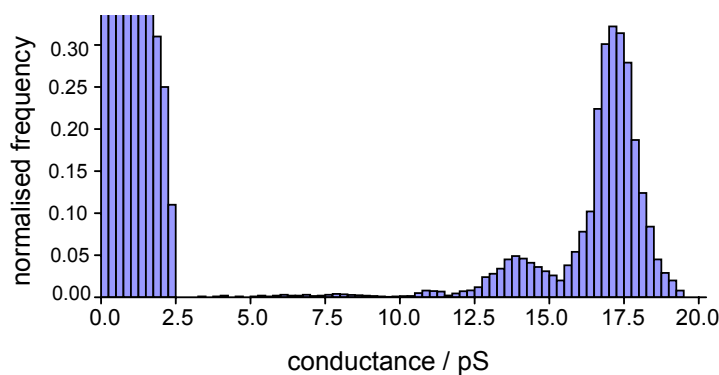


FIGURE 2.8: *Conductance histogram for Vpu_{1-32}* The frequency of the closed state is truncated at a normalised frequency of 0.33.

be calculated as the reciprocal of the gradient. The readings for both states fit a straight line, demonstrating that the channels obey Ohm's Law and that there is no rectification of the transmembrane currents.

The data presented would appear to agree with the simplicity of the suggested channel architecture, and given the limited number of hydrophilic groups which are able to line the pore, it is not surprising that the channel adheres to Ohm's Law.

2.3.5 Variation of rate constants with applied voltage

Figure 2.10 shows the mean open time for individual channel openings which occur within the conductance ranges identified as being the main conductance state and the principal subconductance state. The duration of individual channel openings does not vary with the applied voltage. The mean length of the channel openings across all voltages is 0.50 ± 0.04 s for the main conductance state. The principal subconductance state appears to be less stable, with a mean open time of 0.46 ± 0.05 s. These data indicate that the conformation change which occurs to close the channel is independent of the applied voltages.

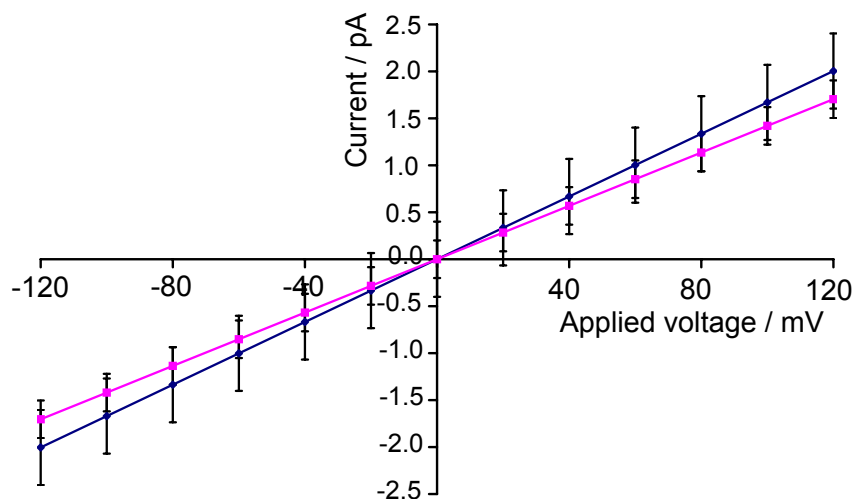


FIGURE 2.9: Graph showing channel currents for Vpu_{1-32} at different applied voltages. Linear best fit lines for the main conductance state and principal subconductance state are shown and other conductance states are omitted for clarity.

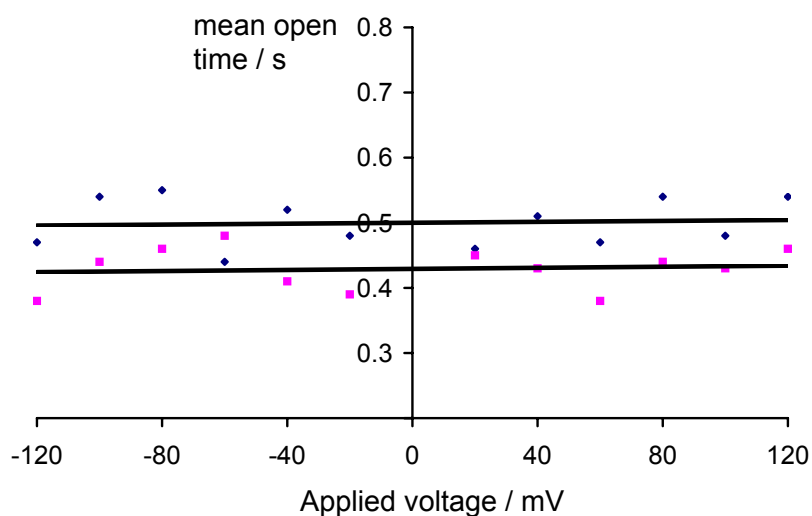


FIGURE 2.10: Graph showing the variation of the open time duration of channels formed by Vpu_{1-32} at different applied voltages. Linear best fit lines for the main conductance state and principal subconductance state are shown and other conductance states are omitted for clarity.

Figure 2.11 shows the variation of the rate at which individual channel openings occur at different applied voltages. The channel opening rate constant, k_{+i} , decreases with the decreasing magnitude of the applied voltage, indicating that channel openings become rarer at voltages close to 0 mV.

The graph appears to be symmetrical in the y axis, suggesting that the behaviour of the channel is not dependent on the applied voltage. However a previously published study, which also presented some of the data from this thesis, identified an asymmetrical increase in the channel open rate at increasing voltage [161]. A close inspection of the data reveals that the asymmetry of the open rates becomes apparent at applied voltages above ± 100 mV. No channel recordings were performed for this thesis at applied voltages greater than ± 120 mv.

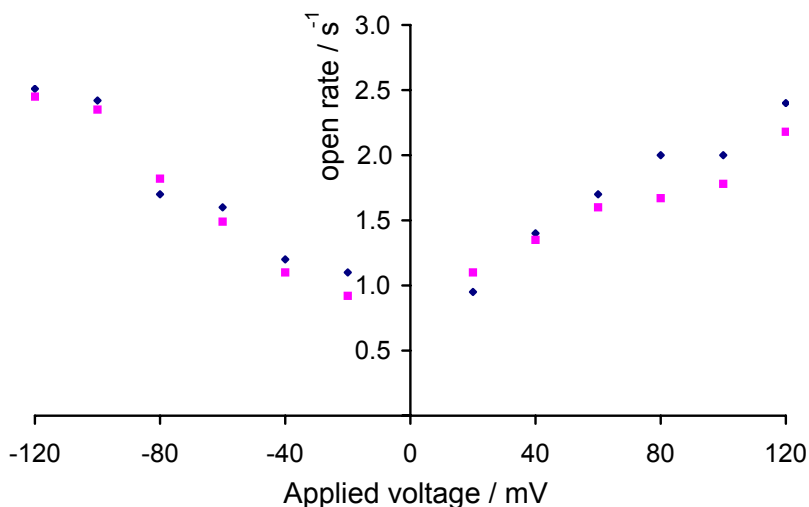


FIGURE 2.11: *Graph showing the variation of the open rate duration of channels formed by Vpu_{1-32} at different applied voltages. Linear best fit lines for the main conductance state and principal subconductance state are shown and other conductance states are omitted for clarity.*

2.3.6 Vpu₁₋₃₂ S24A Mutant Channel Traces

A peptide corresponding to the S24A mutant of Vpu₁₋₃₂ was also reconstituted into black lipid membranes. Channel openings were observed only at applied voltages of ± 120 mV and occurred rarely (approximately one channel opening every five minutes). Figure 2.12 shows a channel opening event recorded at -120 mV. The conductance of the channel is higher than those obtained for the wild type channel. The trace was deliberately left unfiltered to show that the black lipid membrane itself appears to remain intact and that the irregular shape of the channel opening is not caused by a local distortion of the black lipid membrane.

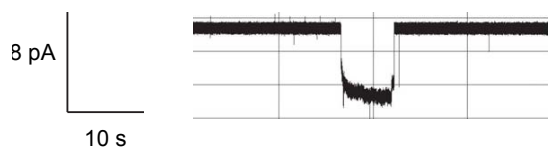


FIGURE 2.12: *Channel trace for the S24A mutant of Vpu₁₋₃₂ recorded at an applied voltage of -120 mV. The trace was left unfiltered to show the lack of destabilisation of the black lipid membrane.*

2.3.7 Inhibition of *in vitro* channel activity

The effect of the addition of HMA, DMA and amiloride on the kinetics of Vpu₁₋₃₂ *in vitro* channel activity was studied using wild type Vpu₁₋₃₂ peptide reconstituted into black lipid membranes. Figure 2.13 shows the channel traces of Vpu₁₋₃₂ from HIV-1 with increasing HMA. An initial visual inspection of the traces shows that as the HMA concentration increases, the channel activity of Vpu decreases, however contrary to the 2002 study of Ewart *et al* [73], it was not possible to achieve a complete block of all channel activity. At concentrations above 100 μ M, the black lipid membrane became unstable.

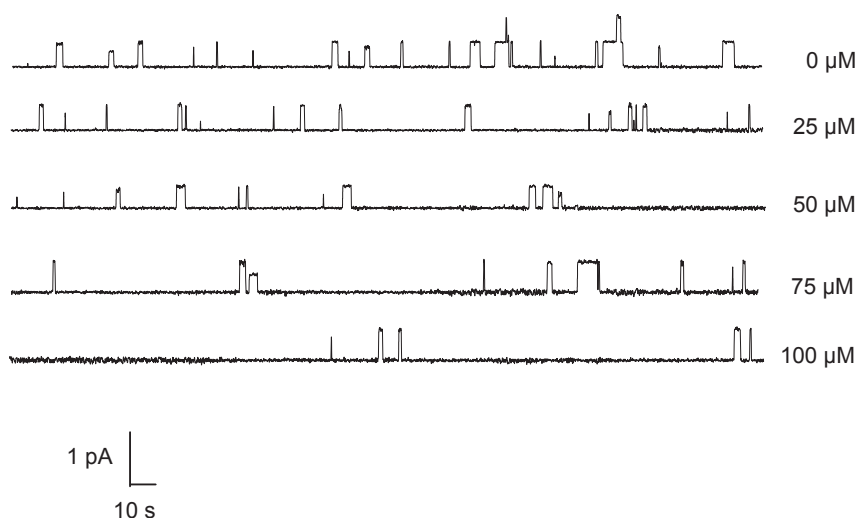


FIGURE 2.13: Channel traces for Vpu_{1-32} recorded at an applied voltage of 60 mV at increasing HMA concentrations. The experiment was repeated at a range of positive and negative applied voltages, however only the 60 mV trace is shown for illustrative purposes.

Figure 2.14 shows the effect of the addition of DMA on the channel activity of Vpu_{1-32} . As has been observed in previous studies, DMA decreases the channel activity of the peptide, however it is not able to achieve a complete inhibition of the channels at concentrations up to 100 μM [73].

Figure 2.15 shows the effect of the addition of amiloride on the channel activity of Vpu_{1-32} . An initial visual inspection suggests that the addition of the drug has little effect on the channel activity of the peptide and multiple channel openings are observed at all concentrations of amiloride.

The channel recordings of Vpu_{1-32} were analysed to determine the effect of the addition of HMA, DMA and amiloride on both the mean open times and open rates. Figure 2.16 clearly shows that the mean open time is reduced by both HMA and DMA, although no effect was observed for amiloride. At 100 μM HMA the mean channel open time is approximately one third of the value at 0 μM HMA.

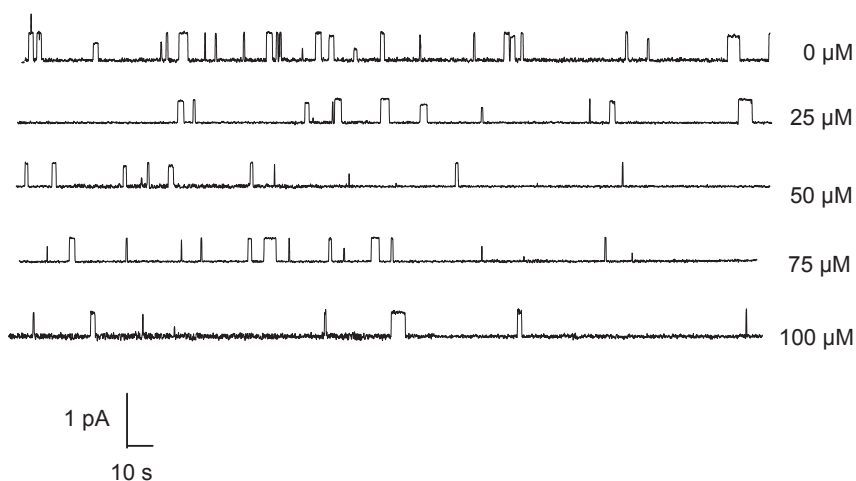


FIGURE 2.14: Channel traces for Vpu_{1-32} recorded at an applied voltage of 60 mV at increasing DMA concentrations. The increasing instability of the bilayer at high drug concentrations can clearly be seen in the bottom trace.

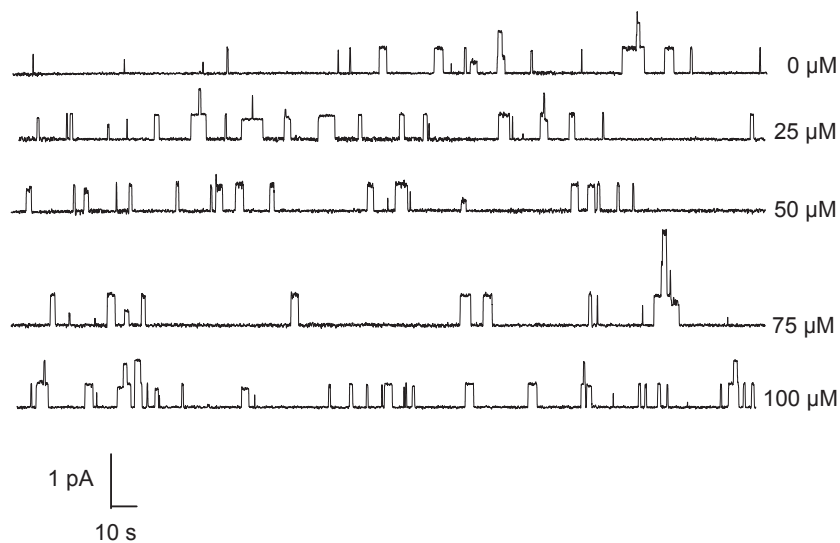


FIGURE 2.15: Channel traces for Vpu_{1-32} recorded at an applied voltage of 60 mV at increasing amiloride concentrations.

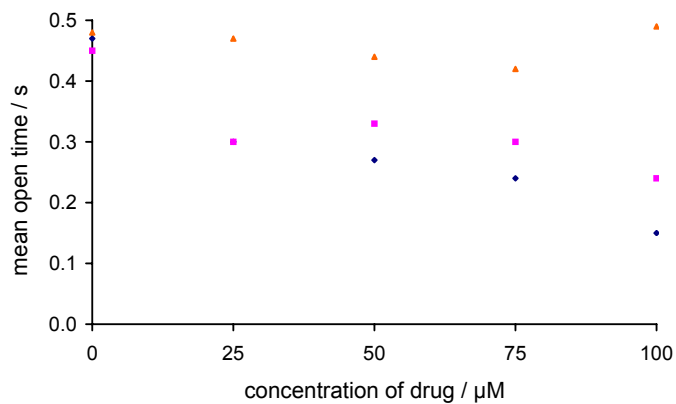


FIGURE 2.16: *Variation of mean open time for the main conductance state of $V_{pu_{1-32}}$ against concentration of drug across all applied voltages. Amiloride (orange triangles), DMA (magenta squares), HMA (blue diamonds).*

Insufficient data was collected to allow an analysis of the effect of HMA, DMA and amiloride on the mean open time of the principal subconductance state. Insufficient data was collected to enable an analysis of the effect of increasing drug concentration on open rate.

2.4 Discussion

When reconstituted in black lipid membranes, peptides corresponding to the transmembrane (TM) domain of Vpu₁₋₃₂ form ion channels which permit the flow of ions across the membrane under an applied voltage. Discrete channel openings are observed and more than one channel may open in the membrane at any one time. The probability of a channel opening event occurring increases with applied voltage, although the rate of channel closure appears to be independent of the applied voltage. A notable property of the channels is the presence of multiple conductance states, which has not been observed previously for the subtype B isolate of Vpu [59, 73]. Transitions between conductance states are rare, and once a channel has opened, the current through it remains constant until it closes.

The main conductance state of 17.5 pS is considerably lower than that reported for the covalently bound tetrameric and pentameric assemblies reported in [153]. The subtype B isolate of Vpu used in [153] includes the deletion of a residue at the N-terminus, and the substitution of a glutamate residue for Pro5. The higher conductances reported may therefore reflect a more hydrophilic N-terminus, which could provide additional stabilisation for ions flowing through the pore.

Mutation of residue Ser24 to an alanine residue resulted in the disappearance of ion channel activity. Occasional openings were observed, and from the regularity of their shape, it is probable that these are not caused by disruption to the membrane. Ser24 is the only hydrophilic side chain in the centre of the transmembrane region, which could provide stabilisation for ions passing through the pore, and its absence would give rise to a highly hydrophobic channel lining. The severely reduced frequency of channel openings compared to the wild type transmembrane peptide may reflect a higher activation energy for the process of creating a hydrophilic channel through the membrane.

2.4.1 Models for Vpu channel opening and closing

Any model which attempts to account for character of the channels formed by Vpu₁₋₃₂ must be consistent with the observations reported above: specifically the model must be able to account for the presence of subconductance states in the channel recordings and the fact that transitions between states are comparatively rare. Models for peptide ion channel gating generally fall into two classes - those that envisage an oligomeric pore which remains intact on a timescale of minutes and in which concerted motions of the monomers result in different conformational states which correspond to the different conductance states (see section 2.4.1.1). Alternative models which assume a more rapid equilibrium between monomeric and multimeric states and that channel opening and closing events correspond to association and dissociation of the Vpu bundle (see section 2.4.1.2).

2.4.1.1 Semi-permanent bundle models

The *helices-kink-to-open* model envisages a closed form of the Vpu ion channel in which the monomers are arranged symmetrically around a central pore, however the individual helices are kinked close to the centre of the bilayer such that the lumen is too narrow for ions to pass (figure 2.17A). A straightening of the helices, possibly induced by the binding of an ion in the mouth of the channel, causes the pore to open (figure 2.17B). The kink is then restored by the lateral pressure imposed by the bilayer on the bundle [161]. The model is supported by some experimental evidence; the structure of the α helical TM domain has been shown to be kinked by both solid state NMR and molecular dynamics simulations at residues Ile17 and Ser24 respectively [67, 162].

The *helices-kink-to-open* model has been used to explain the asymmetric voltage dependence with respect to $V = 0$ mV of the open rates as observed by Mehnert *et al.* in their 2007 paper [161]. As a kinked TM helix straightens, the C=O and

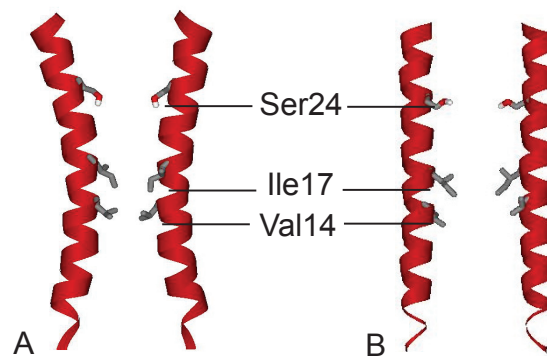


FIGURE 2.17: Indicative diagram of helices-kink-to-open model for the pentameric form of Vpu_{1-32} after [161] and [67]. For clarity only two of the five helices are shown. A: closed state with all five Trp23 residues pointing towards the channel lumen. B: open state with the Ser24 residues pointing towards the channel lumen (after each monomer has rotated by 120°). The diagram was drawn using DS ViewerPro (Accelrys Inc.)

N-H bonds take up a more parallel alignment to the helix axis and the overall helix dipole-moment increases. If the vector of an electric field is parallel to the dipole-moment a stretched helix becomes energetically more favorable than the kinked conformation whereas an anti-parallel orientation favours the kinked form in a voltage-dependent manner. The trends observed by Mehnert *et al.* were not confirmed by this study (which uses an identical peptide) and closer inspection of the published data suggests that the effect is only apparent at applied voltages of above 100 mV [161].

The *helices-kink-to-open* model is able to explain the existence of the subconductance states, since each conductance state would correspond to a stable oligomeric conformation. The model is however unable to explain why transitions between conductance states are so rare, since the activation energy for the straightening or kinking of the helices is likely to be so low, that the channel would switch between open and closed state (and between conductance states) more rapidly than is observed in the channel recording.

The helix-kink model has been suggested to explain the multiple conductance

states observed in recordings of channels formed by gramicidin dimers. The transitions between the states have been attributed to small orientational changes of carbonyl groups within the lumen of the pore [163, 164].

The *helices-rotate-to-open* model in which a concerted rotation of the helices within the bundle to open the pore as also been proposed. Such pore open models envisage a that in the closed state, the monomers are oriented so the Trp23 side chains point towards the lumen, occluding the channel (figure 2.18A), while in the main open state the monomers are rotated by 120° to allow the Ser24 side chains to face the pore (figure 2.18B). Subconductance states may be explained by the incomplete rotation of all of the helices or by rotation of only a few helices [70]. The energetic barrier to rotation is high, since adjacent helical faces are predicted to move in opposing directions and the side chains of β -branched aliphatic amino acids would interlock to stabilise the oligomeric structure. The energy required to separate the helices sufficiently so that the large Trp23 side chains can be moved from inside the pore to facing the phospholipid acyl chains is unlikely to be fully compensated for by ion binding at the mouth of the channel.

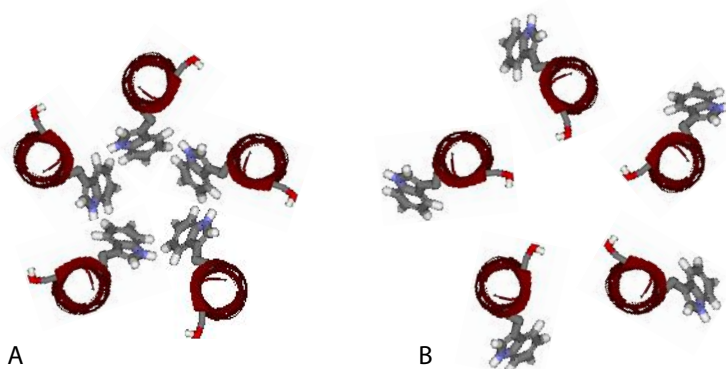


FIGURE 2.18: *Indicative diagram of the helices-rotate-to-open model for the pentameric form of Vpu₁₋₃₂ after [70]* A: closed state with all five Trp23 residues pointing towards the channel lumen. B: open state with the Ser24 residues pointing towards the channel lumen (after each monomer has rotated by 120°).

The diagram was drawn using DS ViewerPro (Accelrys Inc.)

2.4.1.2 Rapid equilibrium models

An alternative model may be envisaged, in which the monomeric and pentameric states of the protein are in a more rapid equilibrium than that assumed by the models in the previous section. In this model, ion flow is permitted to occur when the Vpu₁₋₃₂ pentamer is intact and a channel closure event corresponds to the disassociation of the oligomer. The presence of multiple conductance states may be explained by the formation of non-symmetrical oligomers, which be less able to stabilise an ion as it passes across the membrane. The different conductance states may also reflect a different oligomeric state for the peptide. Transitions between conductance states are not observed, since interconversion between conformer is not possible unless the pentamer dissociates.

Some evidence for this model has been provided by channel recordings of template-assisted synthetic peptides of an alternative isolate of subtype B Vpu (discussed in section 2.1.3). Two conductance states are observed for the alternative isolate, and these correspond to the tetrameric and pentameric Vpu channels [153]. Alamethicin, a well characterised peptaibol, also exhibits channel activity when reconstituted into BLMs. Multiple conductance states are observed, which have been shown to correlate to different oligomerisation states of the peptaibol in the membrane, although unlike the observations reported for Vpu₁₋₃₂, transitions between conductance states are common [165, 166].

2.4.2 Comparison of inhibition data with previously published work

The inhibition data presented in this chapter show that the addition of HMA to both sides of the membrane results in a decrease in the probability of a channel being in an open state and a decrease therefore in the channel opening rate.

Previous studies have indicated that HMA is able to completely block the Vpu channel [73], however a complete block of channel activity was not observed. Both DMA and HMA were able to reduce the mean channel open time for both the main conductance state and the principal subconductance state, and the channel opening rates were also decreased with increasing drug concentration.

The concentrations at which HMA and DMA were shown to be effective at reducing channel activity are significantly higher than indicated by previous studies. In their 2002 paper, Ewart *et al.* observed a complete inhibition of Vpu₁₋₃₂ channel activity after the addition of 100 μM HMA or 125 μM to both sides of the black lipid membrane [73]. The channel openings inhibited by HMA and DMA in that study are similar to those shown in figure 2.1, and may represent a destabilisation of the membrane by the peptide, rather than true channel openings. The data from the study would appear to be inconsistent with the 2004 study by Ewart *et al.* in which an HMA concentration of 10 μM was found to suppress the accumulation of viral DNA and RNA in cultured monocyte-derived macrophages. Together with the data presented in this chapter, it would appear that although HMA does inhibit the *in vitro* channel activity of Vpu, the drug may also affect other essential pathways in the HIV-1 replication cycle [78].

Adamantane has been identified as an inhibitor of the p7 ion channel from Hepatitis C Virus (HCV) by electrophysiological studies of the protein reconstituted into Black Lipid Membranes. Channel traces show that adamantane is able to block the rapidly flickering currents through the membrane at a concentration of 10 μM [23]. A more recent study by Steinmann *et al.* which combined BLM channel recording with *in vitro* cell culture assays, showed that adamantane did not affect p7 ion channel activity at any concentration [151].

In a similar study, adamantane was found to inhibit the rapidly flickering ion channel openings of the p7 channel from GB virus B, but did not inhibit the

replication of the virus in an *in vitro* cell culture [99].

Together the findings of these experiments suggest that electrophysiological studies which identify inhibitors of viral ion channel activity should be treated with some caution. Transmembrane currents with rapidly fluctuating conductances may not represent true ion channel openings, but may indicate leakage across the membrane induced by the imperfect insertion of the peptides into the membrane. It is suggested that many of the amphipathic drugs are able to prevent the leakage of ions across the membrane, and it is this ability which may have previously been misidentified as inhibition of channel activity [21].

Steinmann *et al.* also identified three iminosugar derivatives which inhibit both the replication of p7 in *in vitro* cell culture assays and the regularly shaped channel openings as observed in bilayer recording experiments. The ability to inhibit ion channel activity increased with increasing hydrophobicity and there appears to be no significant difference in the inhibitory potential of *NN-DNJ* and its stereoisomer *NN-DGJ* [151].

The findings of Steinmann *et al.* are consistent with the results presented in this chapter. The inhibitory potential of the members of the amiloride series increases with increasing hydrophobicity and the probability of a the channel being in an open state decreases with addition of the increasing concentrations of the drugs [151]. The data do not however throw any light on the mechanism of inhibition, and the possible alternatives will be explored in Chapters 4 and 5.

2.5 Conclusion

A peptide corresponding to the transmembrane domain of Vpu from HIV-1 was synthesised by solid phase peptide synthesis and was reconstituted into black lipid membranes containing DOPC:POPE 4:1 . Channel openings were observed when a transmembrane voltage was applied and the channel open probability increased with increasing voltage. Vpu₁₋₃₂ forms channels which are ohmic conductors of ion flux, and no rectification was detected. The channel openings have a characteristic square shape. Substitution of residue Ser24 by alanine abolished ion channel activity, suggesting that this residue may have a role in stabilising the charge of the ions as they pass through the pore or in allowing the channel to open and fill with water.

Two amiloride derivatives HMA and DMA have previously been identified as inhibitors of Vpu [73]. The results presented in this chapter show that both molecules are able to decrease the channel open probability, but cannot completely block channel activity even at concentrations of 100 μ M. A concentration of 100 μ M reduced the mean open time of the Vpu₁₋₃₂ channel to approximately one third of the value in the absence of the drug.

The findings presented in this chapter contradict earlier studies in which HMA was shown to block channel openings which were characterised by rapid flickering [73]. The concentration of HMA at which an inhibitory effect is observed is considerably higher than the concentration found to be toxic to HeLa cells, suggesting that HMA itself is unlikely to be included as a constituent of a future anti-AIDS therapy. [78].

Chapter 3

Channel Recordings of Vpu₁₋₈₂

SUMMARY

The full length Vpu₁₋₈₂ protein has been expressed as a fusion with Glutathione-*S*-transferase in *E. coli* BL21 cells. The protein was purified by affinity chromatography and cleaved with thrombin to yield Vpu₁₋₈₂ alone. Vpu₁₋₈₂ was reconstituted into black lipid membranes and channel openings were observed under applied voltages of between -120 mV and 120 mV. The channel openings are similar in character to those recorded for Vpu₁₋₃₂ with a main conductance state of 17 pS. The probability of the channel existing in an open state increases with increasing voltage. A more extensive range of conductance states is observed for the full length protein than for Vpu₁₋₃₂, which may indicate an increase in the number of stable conformations of the oligomer. The position of the principal subconductance state is shifted to 12 pS (for Vpu₁₋₈₂) from 13.5 (for Vpu₁₋₃₂), which may reflect changes in the conformation of the C-terminal end of the helix, caused by the presence of the additional cytoplasmic helices. The study confirms that channel activity of the full length Vpu protein may be detected *in vitro*.

3.1 Introduction

3.1.1 Glutathione-*S*-transferase fusion proteins

Glutathione-*S*-transferase (GST) is a 26 kDa soluble enzyme, commonly used to assist the purification of peptides and proteins expressed recombinantly in *E. coli*. The expression system requires the construction of a pGex plasmid, which contains a fused gene consisting of the *GST* gene sequence from *Schistosoma japonicum*, a

short linker sequence containing a cleavage enzyme recognition site and finally the gene of interest followed by the appropriate transcription and translation termination sequences [167]. The plasmid also includes a gene for resistance to ampicillin. Once the cell pellet containing the expressed protein has been collected, it is then purified by affinity chromatography, using a column consisting of glutathione-tagged Sepharose beads. The linker between the protein of interest and GST may then be cleaved with a protease such as thrombin or TeV [168].

3.1.2 Aims of this study

The primary aim of this chapter was to express full length Vpu₁₋₈₂ as a fusion protein with GST in BL21 *E. coli* cells. The fusion protein has been purified by affinity chromatography and cleaved using thrombin. The purified protein was reconstituted into black lipid membranes and channel currents will be observed. The conductance and kinetics of the Vpu₁₋₈₂ channel are compared to the data presented in Chapter 2 for Vpu₁₋₃₂.

3.2 Materials and Methods

The pGex-Vpu plasmid containing a gene fusion between GST and Vpu was provided by Prof P. Gage (Australia National University, Canberra) (figure 3.1). The pGex-Vpu plasmid was inserted into competent BL21 cells (Invitrogen) by heat shock transformation (see Appendix B.2) [167]. Cells were grown in 3000 ml LB medium containing 50 $\mu\text{g}/\text{ml}$ ampicillin and the turbidity of the culture was followed at 600 nm. Cells were induced by adding IPTG to a final concentration of 0.5 mM when $0.45 < A_{600} < 0.55$. After four hours cells were harvested by centrifugation at 6000 g for 30 min at 4 °C. (For buffer compositions see Appendix B.)

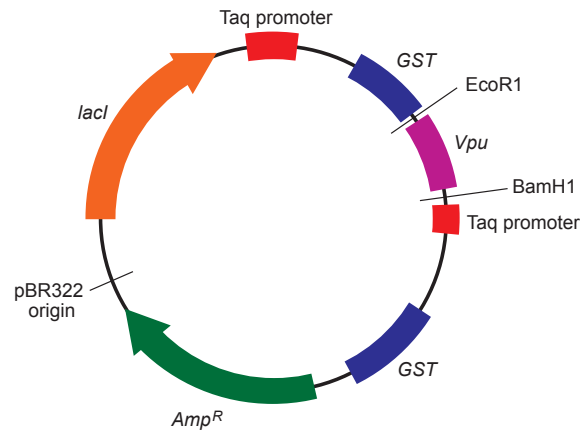


FIGURE 3.1: *Map of the pGex-Vpu plasmid, showing the position of the gene for the GST-Vpu fusion protein in relation to the origin of replication and other genes encoded by the plasmid.*

Cells were washed with PBS buffer and were resuspended in 15 ml Buffer I. 200 μ l of 50 mg/ml lysozyme solution and 5 μ l DNase I were added followed by 15 ml Buffer II. The mixture was incubated at room temperature for 30 minutes, sonicated for 5x 30 s duty cycle 60% (MSE sonicator) and then centrifuged at 17000 g for 30 min at 4 $^{\circ}$ C.

The supernatant was discarded and the pellet resuspended in 15 ml buffer III and sonicated for 5x 30s duty cycle 60% (MSE sonicator) and then centrifuged at 19000 g for 30 min at 4 $^{\circ}$ C.

The pelleted inclusion bodies were washed with GHB buffer until white and then diluted 1 in 10 into cold refolding buffer (50 mM Tris/HCl, 0.2 M NaCl, mM DTT, 1 M NDSB 256) at 4 $^{\circ}$ C and the solution was slowly agitated overnight. The solution was concentrated using a 10 kDa centrifuge concentrator (Amicron) and dialysed into pH 7.5 Thrombin Cleavage Buffer (TCB).

The protein was applied to a GSTrap column (Amersham biosciences) and washed with TCB pH 7.5. The protein was eluted using TCB + 10 mM reduced glutathione and then concentrated to 1 ml and dialysed overnight into TCB pH 6.5.

Cleavage of the GST-Vpu fusion protein was carried out overnight at room temperature using 2 units bovine thrombin (Sigma).

The solution was then lyophilised and resolubilised in 500 ml TFE and then sonicated for 10 minutes on a bath sonicator. 500 ml buffer B was then added. The protein was purified by HPLC using a semiprep C4 column (Hichrom) and a gradient of 80% buffer A 20% buffer B to 20% buffer A and 80% buffer B over the course of one hour. (For buffer compositions see Appendix C.4.) The solvents were removed by evaporation and lyophilising and the purified Vpu was resolubilised in TFE to a concentration of 1 mg/ml. Although reconstitution of the protein with a variety of different solvents and detergents was attempted, stable bilayers containing the protein could only be successfully produced using TFE. TFE is known to promote the formation of secondary structure in proteins and peptides [169].

3.2.1 Data Processing

Data were processed using the protocols described in section 2.2.3.

3.3 Results

3.3.1 Vpu₁₋₈₂ expression and purification

The GST-Vpu₁₋₈₂ fusion protein was expressed in BL21 *E. coli* cells, transfected with the pGex-Vpu plasmid. The protein forms inclusion bodies in the bacterial cells, which may be refolded using NDSB 256 to give a soluble protein with a high α helical content (see figure 3.2).

Figure 3.3 shows the Western blot of the initial stages of expression and purification from induction of the protein expression to cleavage of the protein with thrombin.

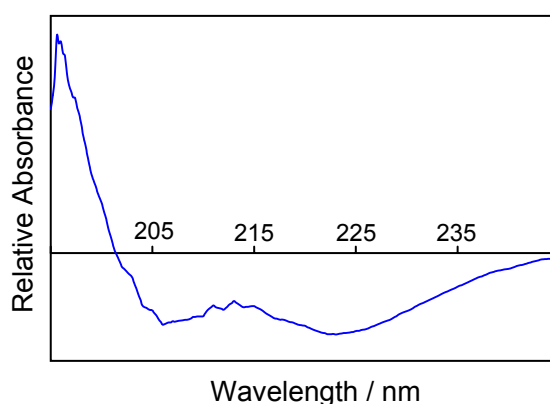


FIGURE 3.2: *Circular Dichroism spectrum for the purified, refolded GST-Vpu fusion protein.* The spectrum shows that the fusion protein has a high α helical content and that the GST moiety has been refolded, making the protein suitable for further purification by GSTrap affinity chromatography.

The fusion protein has a molecular weight of 35 kDa and Vpu₁₋₈₂ has a molecular weight of 9 kDa. Both the cleaved and uncleaved forms of the protein are visible in lane 9 of the Western blot.

The cleavage reaction mixture was subsequently purified by HPLC. Figure 3.4 shows an silver-stained SDS PAGE gel of the purified Vpu₁₋₃₂ showing the absence of the fusion protein and a band at 9 kDa corresponding to the purified Vpu₁₋₈₂.

3.3.2 Channel recording of Vpu₁₋₈₂ reconstituted into black lipid membranes

The solvent used for the HPLC purification was removed by evaporation under a stream of nitrogen gas. The protein was then reconstituted into black lipid membranes and transmembrane currents were measured. Figure 3.5 shows the channel traces for Vpu₁₋₈₂. An initial visual inspection shows that the current passing through the channel increases and the rate of channel openings also increase with

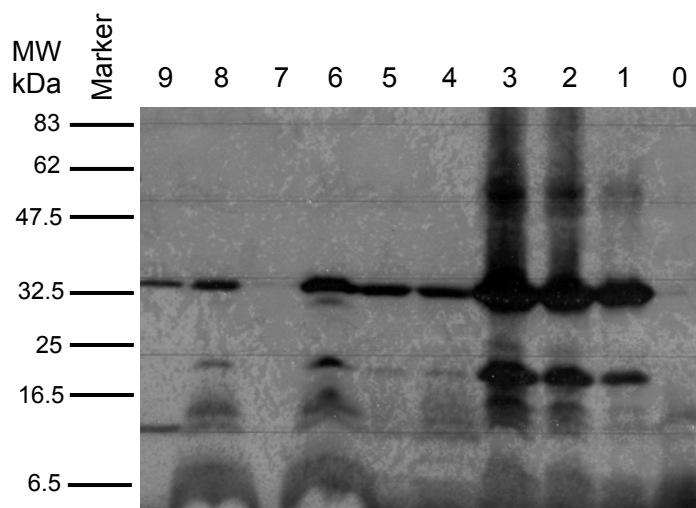


FIGURE 3.3: *Western blot showing the stages of the Vpu₁₋₈₂ purification protocol, using an anti-vpu antibody provided by Prof. K. Strebel (Bethesda, MD). Uninduced cells (lane 0), induced cells after one hour (lane 1), induced cells after two hours (lane 2), induced cells after four hours (lane 3), insoluble protein fraction (lane 4), insoluble protein fraction after removal of membrane proteins (lane 5), refolded proteins prior to GSTrap chromatography (lane 6), GSTrap column wash (lane 7), GSTrap column elute (lane 8) and cleavage reaction product (lane 9).*

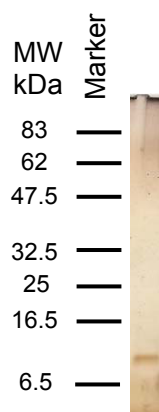


FIGURE 3.4: *Silver stained SDS PAGE of the purified Vpu₁₋₈₂.*

applied voltage. As was observed for channels formed of the Vpu₁₋₃₂ peptide, the channel openings take the form of square waves.

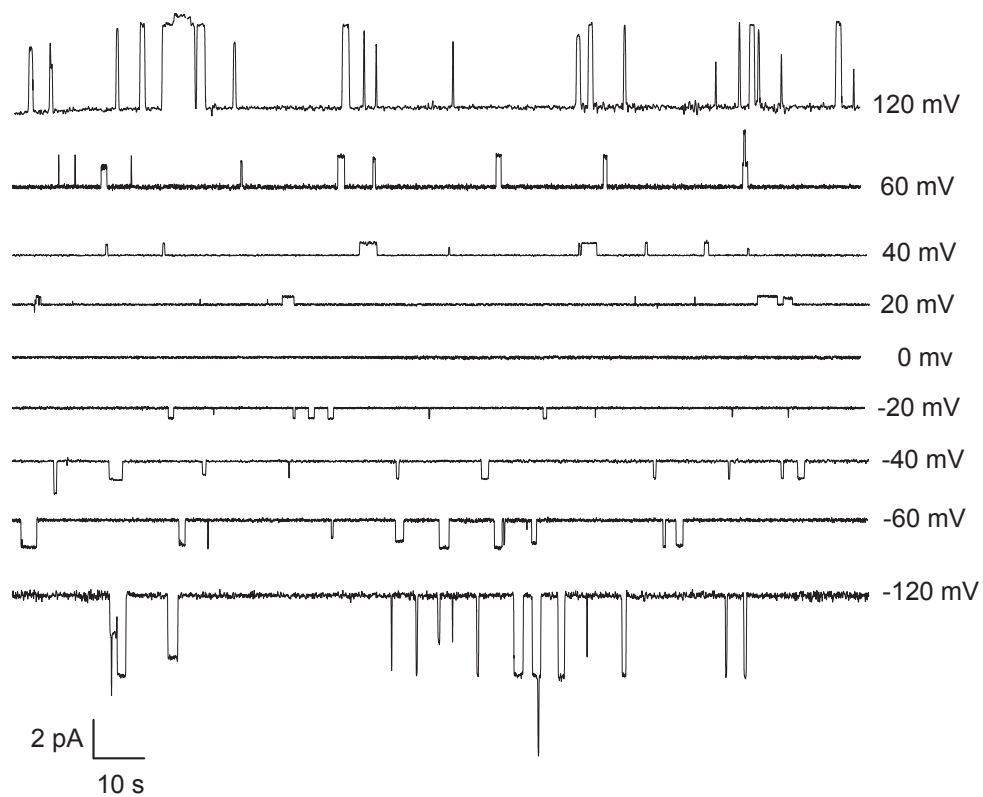


FIGURE 3.5: *Channel recording traces for Vpu₁₋₈₂ acquired at applied voltages of between +120 mV and -120 mV.*

3.3.3 Conductance histogram

Figure 3.6 shows the normalised conductance histogram for channel recordings of Vpu₁₋₈₂. The histogram allows two distinct conductance states to be identified. The main conductance state is clearly visible with a conductance of 17 pS, accompanied by a main subconductance state at 12 pS. The normalised frequency of the closed state has been truncated at 0.33. Additional subconductance states are also visible. A secondary subconductance state occurs at 11.5 pS and channels may open with a conductance in the range from 3 pS to 8.75 pS. Subconductance states have not previously been identified in channel recordings with Vpu₁₋₃₂. The origin of the different conductance states will be discussed in detail in section 2.4.1, however the presence of multiple conductance states may suggest that the protein is able to access different conformations or that the channel is able to conduct different ions.

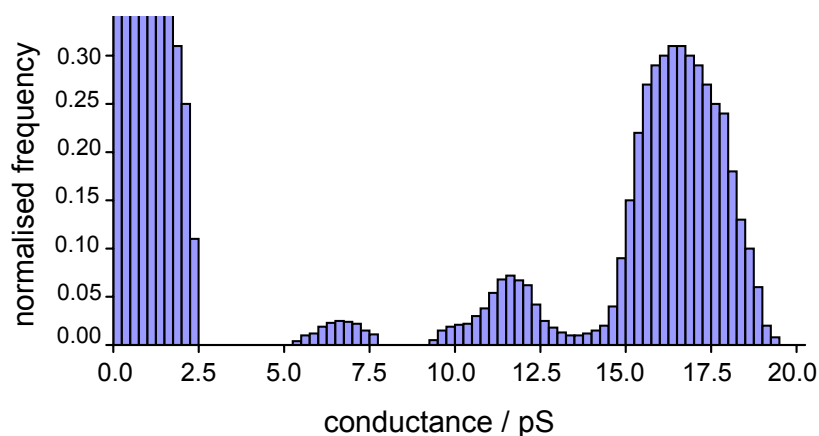


FIGURE 3.6: *Conductance histogram for Vpu₁₋₃₂* The frequency of the closed state is truncated at a normalised frequency of 0.33.

3.3.4 I/V Curves for Main and Subconductance States

Figure 3.7 plots the channel currents for the main conductance state and principal subconductance state against applied voltage. The conductance of each state is given by the gradient. The readings for both states fit a straight line, demonstrating that the channels obey Ohm's Law and that there is no rectification of the transmembrane currents.

The data presented would appear to agree with the simplicity of the suggested channel architecture, and given the limited number of hydrophilic groups which are able to line the pore, it is not surprising that the channel adheres to Ohm's Law.

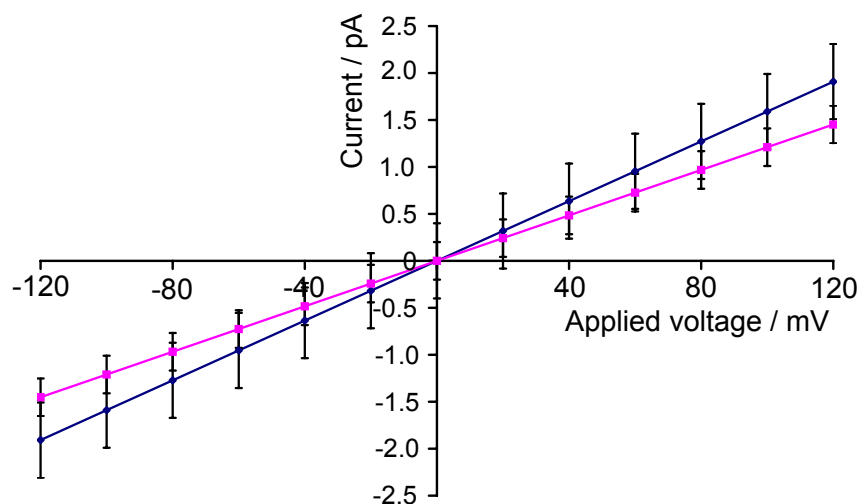


FIGURE 3.7: *Graph showing channel currents for $V_{pu_{1-82}}$ at different applied voltages. Linear best fit lines for the main conductance state and principal subconductance state are shown and other conductance states are omitted for clarity.*

3.3.5 Variation of rate constants with applied voltage

Figure 3.8 shows the mean open time for individual channel openings which occur within the conductance ranges identified as being the main conductance state and the principal subconductance state. The duration of individual channel openings does not vary with the applied voltage. The mean length of the channel openings across all voltages is 0.46 ± 0.04 s for the main conductance state. The principal subconductance state appears to be less stable, with a mean open time of 0.43 ± 0.06 s. These data indicate that the conformation change which occurs to close the channel is independent of the applied voltages.

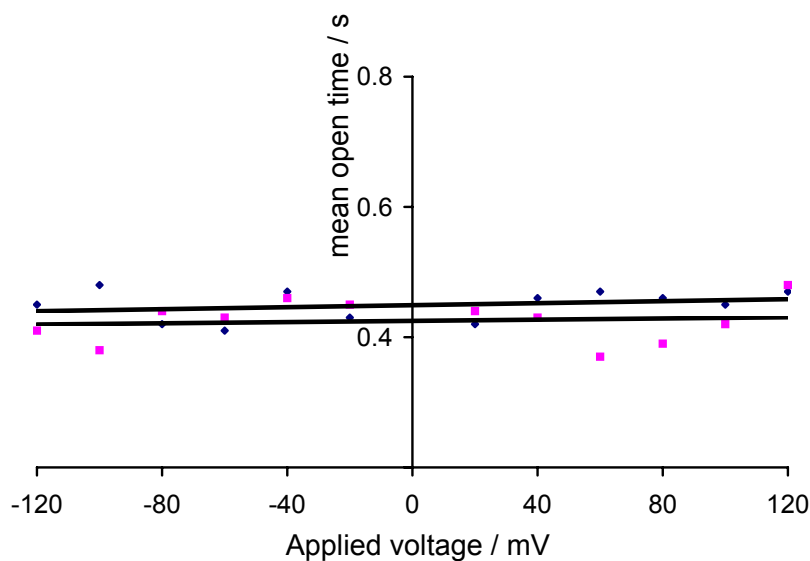


FIGURE 3.8: *Graph showing the variation of the open time duration of channels formed by $V_{pu_{1-82}}$ at different applied voltages. Linear best fit lines for the main conductance state and principal subconductance state are shown and other conductance states are omitted for clarity.*

Figure 3.9 shows the variation of the rate at which individual channel openings occur at different applied voltages. The channel opening rate constant, k_{+i} , decreases with the decreasing magnitude of the applied voltage, indicating that channel openings become rarer at voltages close to 0 mV. Like the similar data presented

for $V_{pu_{1-32}}$, the graph appears to be symmetrical around the y axis, suggesting that the conformational changes which occur to allow ions to pass through the channel are not influenced by the polarity of the applied voltage.

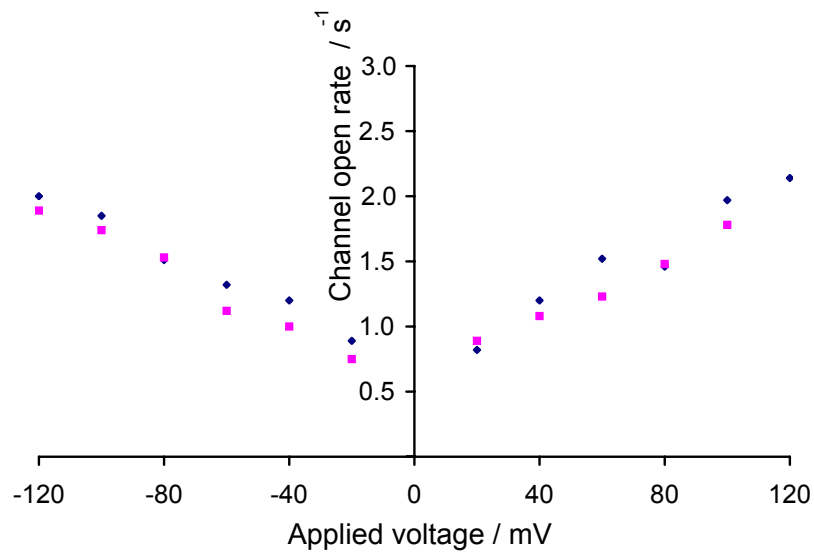


FIGURE 3.9: Graph showing the variation of the open rate duration of channels formed by $V_{pu_{1-32}}$ at different applied voltages. Linear best fit lines for the main conductance state and principal subconductance state are shown and other conductance states are omitted for clarity.

3.4 Discussion

Vpu₁₋₈₂ was successfully expressed as a fusion with GST, purified and cleaved to leave a pure product. The protein was subsequently reconstituted into black lipid membranes and channel currents were observed. Channel openings become more numerous as the applied voltage increases and a number of different conductance states is observed. The main conductance state is visible at 17 pS, a similar value to that recorded for Vpu₁₋₃₂ (see section 2.3.3).

3.4.1 Origin of the principal subconductance state

The major significant difference between the conductance at which the main subconductance state occurs, which is substantially reduced relative to the Vpu₁₋₃₂ peptide channels. Some models for channel functioning discussed in section 2.4.1 , and the most plausible explanation for the existence of the first subconductance state is that it corresponds to the flow of Cl⁻ ions through the channel, instead of Na⁺ ions, which give rise to the main conductance state.

If this is correct, then this might explain why subconductance states are not observed in channel recordings by the Opella lab, because their N terminus is different and is more negatively charged, which might then repel Cl⁻.

The first cytosolic helix of Vpu has been shown by solid state NMR to lie on the surface of the lipid bilayer and includes the residues from Lys32 to Ala52 [170]. In the full length protein, the linker region between the first cytosolic helix and the transmembrane helix must make a 90° to allow the TM α helix to enter the bilayer parallel to the membrane normal. The requirement for the sharp turn in the protein structure must order the residues in the linker region and bend them backwards away from the C-terminal mouth of the oligomeric channel. Given this

arrangement, it is perhaps surprising that the tilt and structure of the transmembrane helix is unaffected relative to that of Vpu₁₋₃₂ [67]. The reorientation of the C-terminal mouth of the channel, would be expected to reduce the stability of Cl⁻ ions passing through the channel and therefore reduce the Cl⁻ conductance.

3.5 Conclusion

Vpu₁₋₈₂ has been expressed as a fusion protein with Glutathione-*S*-transferase in BL21 *E. coli* cells. The protein was refolded and purified by GSTrap affinity chromatography and cleaved using bovine thrombin. Vpu₁₋₈₂ was separated from the cleavage mixture by HPLC and solubilised in 2,2,2-trifluoroethanol to promote an α helical secondary structure. The protein was then reconstituted into Black Lipid Membranes and transmembrane channel currents were observed.

The channel openings observed bear considerable resemblance to those obtained using Vpu₁₋₃₂ peptide. Square channel openings are observed which open at a variety of different conductance states. A key difference in the profile of the conductance histogram profile is the position of the main subconductance state, which is positioned at 12 pS instead of 13.5 pS in the peptide channel recordings. One possibility is that the main subconductance state corresponds to the flow of Cl⁻ ions through the channel and that the structural changes at the C-terminal mouth of the channel which are induced by the presence of the two additional cytoplasmic helices result a reduced ability to stabilise a negatively charged ion.

Chapter 4

Molecular Dynamics Simulations

SUMMARY

The interaction between drugs of the amiloride family and a model POPC bilayer has been probed by MD simulation. All three drugs are able to insert into model membranes of POPC and remain in the bilayer over the course of a 10 ns simulation. The positively charged guanidinium groups of the drugs form a strong electrostatic interaction with the lipid phosphate groups, which appears to restrict the motion of the headgroups within a 0.8 nm radius of the drug (section 4.3.1.1). The presence of the drug in the membrane, pulls the neighbouring lipids towards the centre of the bilayer, allowing water to penetrate further into the membrane than into bulk lipid. Control simulations were performed with both charged and uncharged models of the toxin abietic acid, which is known to partition into membranes and whose bilayer location and orientation has been determined by solid state NMR. The interaction between HMA and a single Vpu₁₋₃₂ helix was also investigated. HMA remains bound to the Trp23 sidechain over the course of a series of 5 ns simulations, at a distance from the aromatic ring of Trp23, which would be consistent with a π bond stacking interaction. Amiloride does not remain bound to the Trp23 side chain.

4.1 Introduction

Molecular dynamics (MD) simulation has become an important computational method for understanding the interrelationship between the structure and function of biological macromolecules [171–173]. It enables the motion of a thermodynamic ensemble of complex molecules to be modelled, by approximating the physical laws which govern a dynamic system. The study of larger and more complex

systems has become possible as a result of recent advances in the speed and capacity of computer hardware and the development of faster and more accurate software algorithms. The timescales available have increased to the point where it is possible to simulate mesoscopic processes, such as vesicle fusion, with atomic resolution [174]. Coarse-grained simulations allow more complex processes, such as the assembly of a lipid bilayer around a membrane protein and helix dimerisation, to be followed over simulation periods of up to 1 μ s [175, 176]. Since the accuracy of the calculations employed is deliberately compromised to reduce the computational burden, MD simulations can never replace laboratory experiments, however the combination of the two approaches often provides greater insight into a biochemical problem than experiment alone.

4.1.1 Simulations of lipids and membrane proteins

Membrane proteins provide a considerable challenge to developers of simulation software. Globular protein simulations are routinely performed by placing the protein of interest in an empty box and applying a forcefield which implicitly accounts for solvation effects. The presence of a phospholipid bilayer, whose physical properties differ dramatically from bulk water, requires an alternative approach to be used for membrane proteins. A number of different approaches have been used to simulate a membrane environment, including the use of membrane-mimic potentials, simplified and coarse grain bilayer models, and simulations in explicitly modelled lipid bilayers. The explicit bilayer models are generally considered the most successful, since the methodology makes no assumptions about the dielectric properties of the system and allows the simulation of bilayers containing more than one lipid type [177, 178].

Molecular dynamics has been most successfully applied to the small number of membrane proteins for which high resolution structural information is available.

However MD simulations must be used in combination with other computational techniques, such as homology modelling or *ab initio* structure prediction, to generate suitable starting structures for membrane proteins for which a high resolution structure is not available. The earliest simulations of this type attempted to study the dynamics of single transmembrane α helices, to evaluate sequence-based secondary structure predictions and the roles of specific amino acids (such as aromatic and proline residues) within a transmembrane domain [179, 180]. The oligomeric state of several pore-forming peptides has been investigated by simulating *ab initio* peptide bundles of alamethicin, gramicidin, Vpu_{1–32} and δ M2 of the nicotinic acetylcholine receptor [16, 181–184].

4.1.2 Simulation studies of the TM domain of Vpu

Low resolution structural information for Vpu from a variety of experimental techniques (including solution and solid state NMR, CD and FTIR spectroscopy) indicates that Vpu has a single transmembrane α helix and two cytoplasmic α helices, one of which is positioned on the surface of the membrane [47, 185–190]. Given the lack of a high resolution structure for the transmembrane helix, most MD simulations of the transmembrane domain of Vpu begin by fitting sections of the primary protein sequence to an ideal α helix, which is then embedded in a model phospholipid bilayer. In general, the simulations of Vpu have sought to characterise the behaviour of TM monomers in a model membrane and the mode of inhibition of ion flux by HMA.

4.1.2.1 TM domain monomer structure

Analysis of PISA wheel solid state NMR spectra and dipolar waves obtained from aligned samples of Vpu_{2–30} reconstituted into DMPC:DMPG (9:1) bilayers, indicates that residues 8 to 25 inclusive can be successfully modelled to an α helix,

which is embedded in the membrane with an average helix tilt of 13° relative to the bilayer normal, and that there is a 3° kink at residue Ile17 [67]. The Vpu TM helix is able to adjust to decreases in bilayer thickness by increasing the tilt angle, although contrary to expectations, the kink angle simultaneously decreases [67, 191]. A recent simulation study of the Vpu_{1–32} helix embedded in a variety of model membranes showed that the helix tilt angle does increase in response to a decrease in bilayer thickness, but that kink observed in the region of Ser24 and Ile20 also increases, contrary to the experimental data (figure 4.1). The study also appears to contradict X-ray and reflectivity data, from which a hydrophobic mismatch between the peptide and bilayer has been inferred [192].

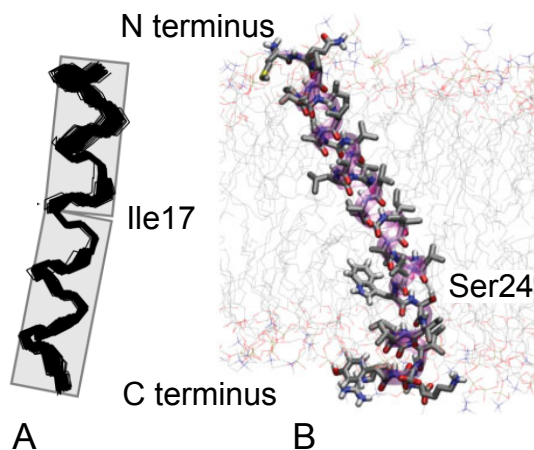


FIGURE 4.1: *Comparison of TM Vpu monomers from simulation and ssNMR*
A: Superposition of 100 calculated backbone structures for Vpu_{2–30} as determined by solid state NMR data (reproduced from [67]). **B:** Vpu_{1–32} after 10 ns simulation in DPPC showing position of kink at residue Ser24 (reproduced from [162]).

4.1.2.2 Oligomeric structure

There is little experimental evidence available for the structure of the oligomeric Vpu protein. Becker *et al.* used template-assisted solid phase peptide synthesis to show that both tetrameric and pentameric assemblies of Vpu_{2–32} were capable of conducting ions when reconstituted into black lipid membranes [153], and the

research reported in Chapter 2 has showed that an S24A mutant of Vpu₁₋₃₂ was unable to conduct ions, suggesting that residue Ser24 is essential for ion transport [193]. Models of the pentameric and tetrameric protein have been generated using *in silico* docking, based on the assumption that the all of the helices have the same topology and are arranged symmetrically around the channel lumen. Residue Ser24 is generally shown facing the pore, and it has been suggested that it helps to stabilise the ion as it passes through the membrane. Ser24 is highly conserved between HIV-1 subtypes (see figure 1.3). Alternative models have been proposed in which Ser24 faces the membrane and a ring of Trp23 residues lines the channel lumen [70]. Steered MD simulations have also been performed, in which single monovalent ions are pulled through Vpu₁₋₃₂ tetramers and pentamers. These simulations favour a pentameric structure in which the Ser24 residues face the pore [69].

4.1.2.3 Mode of inhibition of ion flux

Simulation studies of the mode of inhibition of Vpu by HMA have focused primarily on the binding of the drug within the lumen of a pentameric channel and the blocking of ion flux by occlusion [76, 77]. The *in silico* docking program AUTODOCK 2.0, which uses a Monte-Carlo algorithm to dock a flexible ligand to an inflexible protein target in the absence of solvent or lipid, was used to identify binding sites for HMA and amiloride for both monomeric and pentameric Vpu₁₋₃₂ [76]. A binding site within the channel lumen was identified as the most likely binding site for HMA (figure 4.2) in which the positively charged guanidinium group of HMA is positioned between two adjacent α helices of the pentamer and a hydrogen bond is formed between Ser24 of a third monomer and the drug. The same paper also identified residue Trp23 as a potential binding site for HMA, based on π bond stacking interactions between the aromatic rings [76].

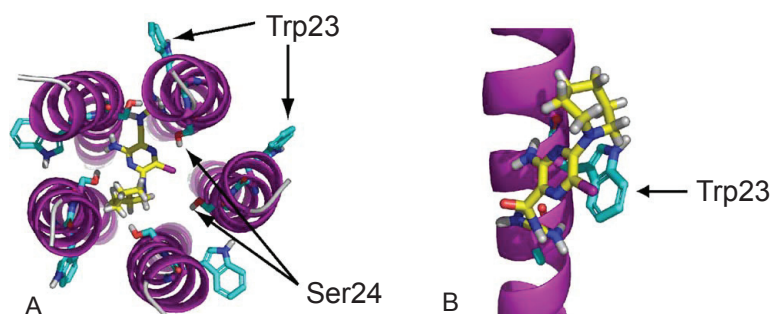


FIGURE 4.2: *Results of docking simulations reproduced from [76]* **A**: Pentameric bundle of Vpu₂₋₃₃ with Trp23 and Ser24 in stick modus viewed from C termini. The lowest energy conformation of HMA⁺ (CPK colour code in greyscale). **B**: Close up view of the lowest energy conformation of HMA⁺ with monomeric Vpu₂₋₃₃. Pictures generated with PyMOL.

The *in silico* docking approach employed by the authors has a number of disadvantages: both lipid and water are absent from the simulations; the bonds of the extended conjugated system of the drug are assumed to be able to rotate fully and binding sites within the channel lumen are automatically favoured by the program owing to non-specific contacts with other helices. Given the nature of the extended delocalised electron system over much of the molecule, it is unlikely that HMA would be as flexible as the AUTODOCK algorithm assumes. The results do not satisfactorily explain why HMA inhibits ion flow and amiloride does not, since both molecules are predicted to bind within the channel and there appears to be little difference in the calculated binding constants for the two drugs [76].

4.1.3 Localisation of lipid-soluble molecules in model membranes by MD simulation

The membrane locations of a number of drugs and other ligands have been investigated by MD simulations. A one dimensional Potential of Mean Force for adamantane, the inhibitor of the M2 H⁺ channel from Influenza A, across a POPC bilayer was determined by umbrella sampling. Both protonated and neutral forms of the drug are located preferentially within the lipid headgroup region of the bilayer and

there appears to be a large barrier to movement across the centre of the membrane for the protonated form [194]. The membrane location of the drug has also been determined experimentally by solid state NMR. A change in the orientation of the lipid headgroup in the presence of adamantane was observed by a change in the anisotropy of the ^{31}P chemical shielding and ^{14}N quadrupolar interactions [150].

The membrane location of the steroid hormone cortisone has also been investigated by MD simulation. Cortisone molecules were observed spontaneously inserting into POPC bilayers over the course of a 25 ns simulation. Select electrostatic interactions between the steroid and the lipid headgroups were found to drive the insertion of the molecule into the membrane [195].

The Potential of Mean Force method has been used to investigate the location of tryptophan and benzene in a POPC bilayer. Three separate binding sites for indole rings were identified: at the lipid-water interface near the glycerol moieties; adjacent to the choline moiety and in the centre of the hydrocarbon core of membrane. The simulations showed that electrostatic interactions appeared to be important in determining the location of tryptophan, including hydrogen bonding to the lipid headgroups and cation- π interactions [196].

4.1.4 Force-field calculations

The calculations performed as part of an MD simulation use classical inter-atomic potential energy functions to generate atom trajectories and velocities. The Born-Oppenheimer assumption states that rapid fluctuations in the electronic structure may be ignored, since these motions are fast relative to the motions of the atoms as a whole. Electrons can therefore be assumed to be able to adapt instantaneously to changes in the positions of atom nuclei and the physical attractions, such as those originating from changes in the electronic structure (such as polarisability) can be represented in terms of an effective inter-atomic potential, using functions

dependent only on the positions of the constituent nuclei. The spectrum of energy states is therefore described as a continuum rather than as a series of discrete steps and Newton's Laws of Motion are used to describe the simulation system [197, 198]. Atoms are treated as a set of point fractional charges connected by bonds represented as harmonic oscillators.

The total energy of the system is given by E_{total}

$$E_{total} = E_{non-bonded} + E_{bonds} + E_{angles} + E_{dihedrals} + E_{impropers} \quad (4.1)$$

Each component will be described in the following section. Each component of E_{total} is calculated for the interaction between each pair of atoms (i and j). The non-bonded energy ($E_{non-bonded}$) is given by:

$$E_{non-bonded} = E_{LJ} + E_{electrostatic} \quad (4.2)$$

Interactions between non-bonded atoms are represented by $E_{electrostatic}$ (the electrostatic interactions) and E_{LJ} (the Lennard-Jones atom pair interactions). r_{ij} is the distance between the atoms, q_i and q_j the charges on the atoms, A_{ij} and B_{ij} are Lennard-Jones parameters specific to that pair, and ϵ_0 is the permittivity of free space.

$$E_{electrostatic} = \sum_{i < j} \frac{q_i q_j}{4\pi\epsilon_0 r_{ij}} \quad (4.3)$$

$$E_{LJ} = \sum_{i < j} \left(\frac{A_{ij}}{r_{ij}^{12}} - \frac{B_{ij}}{r_{ij}^6} \right) \quad (4.4)$$

The interactions between pairs of bonded atoms are responsible for preserving the integrity of individual molecules within the simulation system. E_{bonds} describes the

interactions for each bond, where κ_{ij}^b is the force constant for a bond of equilibrium length b_{ij}^0 between atoms i and j , separated by the distance r_{ij} (See figure 4.3).

$$E_{bonds} = \sum_{i,j} \frac{1}{2} \kappa_{ij}^b (r_{ij} - b_{ij}^0)^2 \quad (4.5)$$

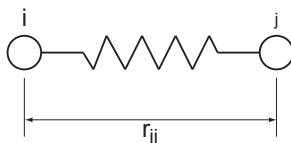


FIGURE 4.3: Approximation of a pair of bonded atoms by point charges (i and j) connected by harmonic oscillator of length r_{ij}

E_{angles} describes the energy of the angle between two bonds, where κ_{ijk}^θ is the force constant for a bond of equilibrium angle θ_{ijk}^0 between atoms i , j and k , separated by an angle θ_{ijk} . (See figure 4.4.)

$$E_{angles} = \sum_{i,j,k} \frac{1}{2} \kappa_{ijk}^\theta (\theta_{ijk} - \theta_{ijk}^0)^2 \quad (4.6)$$

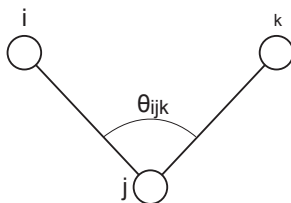


FIGURE 4.4: Approximation of three bonded atoms by point charges (i , j and k) connected by harmonic oscillators with an angle θ_{ijk} between them

$E_{dihedrals}$ describes the energy of the dihedral angle between two planes, as defined by four atoms (i , j , k and l) where κ_{ijkl}^ϕ is the force constant for a dihedral of equilibrium angle ϕ_{ijkl}^0 and n_{ijkl} is the periodicity of the rotation (e.g. $n = 3$ for ethane and $n = 2$ for ethene). (See figure 4.5.)

$$E_{dihedrals} = \sum_{i,j,k,l} \frac{1}{2} \kappa_{ijkl}^{\phi} (1 + \cos(n_{ijkl}(\phi_{ijkl} - \phi_{ijkl}^0))) \quad (4.7)$$

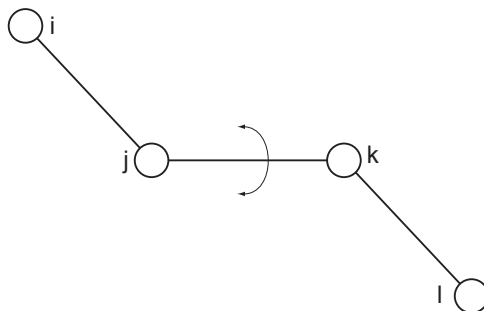


FIGURE 4.5: Approximation of four bonded atoms by point charges (i , j , k and l) connected by harmonic oscillators with an angle between the planes ijk and jkl of ϕ_{ijkl}

$E_{impropers}$ is used to maintain molecular chirality and planarity by preventing rotation around a bond between atoms. Like $E_{dihedrals}$, it is defined by four bonded atoms (i , j , k and l) where κ_{ijkl}^{ω} is the force constant required to maintain the improper dihedral at the equilibrium angle ω_{ijkl}^0 .

$$E_{impropers} = \sum_{i,j,k,l} \frac{1}{2} \kappa_{ijkl}^{\omega} (\omega_{ijkl} - \omega_{ijkl}^0)^2 \quad (4.8)$$

4.1.5 Force fields

The total energy of the simulation system is defined by the forcefield, which describes the system using the equations from section 4.1.4 and contains predefined parameters including equilibrium bond lengths, force constants and atomic charges. The potential energy functions and parameters used vary between different MD simulation programs. The simulations performed for this thesis use the GROMOS forcefield as part of the GROMACS simulation software [199]. The

GROMOS forcefield employs a united-atom approach, in which non-polar hydrogen atoms are not treated explicitly, but are instead included within the description of the associated carbon atoms, which are assigned larger van der Waals radii, reducing the computational cost of the model [200].

4.1.6 Timestep

The motion of every atom within the simulation system simultaneously affects, and is dependent on, the motion of the surrounding atoms. As a result the equations of motion are coupled and it is not possible to obtain an exact solution for large systems. The timestep between successive calculations is therefore chosen to be sufficiently small that the motion of a given particle neither influences nor is dependent on the motion of any other particle. During this period, the motion of each atom is assumed to be driven by a constant force. The length of the timestep is chosen to be sufficiently large that fast atomic vibrations can be ignored, but sufficiently slow that bond stretching vibrations can be followed. The timestep used in this study was 2 fs (10^{-15} s).

4.1.7 Periodic boundary of the simulation box

A typical MD simulation system consists of a cubic or rectangular simulation box containing a finite set of atoms. The edges of the box are not defined as boundaries or with a hard wall effect (e.g. a vacuum), but instead a periodic boundary condition is used so that the simulation box is replicated through space to form an infinite lattice (see figure 4.6).

Each copy of the box is surrounded in three dimensions by an identical copy of the system and any molecule which moves out of the box, simply re-enters on the opposite side. The distance at which the non-bonded interactions are cut off is set

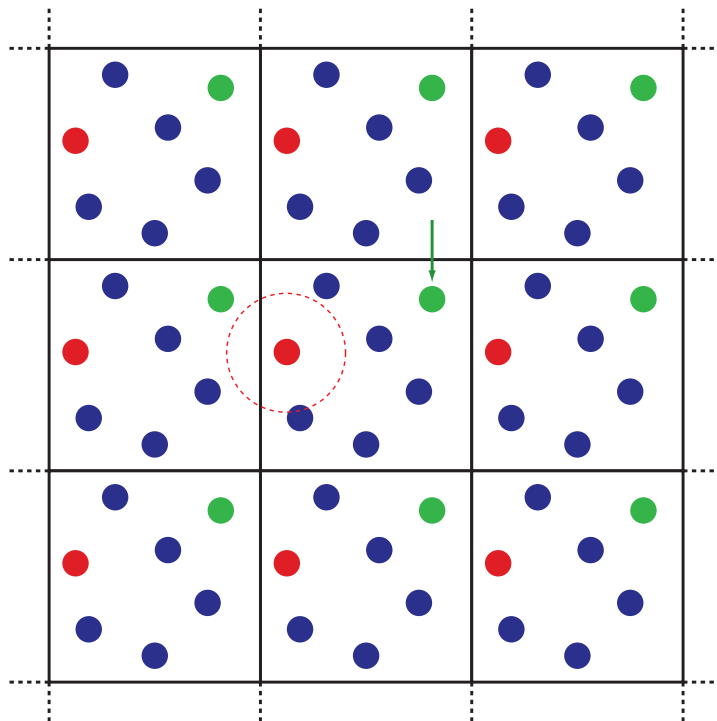


FIGURE 4.6: *Indicative two dimensional slice of a periodic system* The green arrow and particle indicate that as a particle crosses the boundary on one side of the box, it re-enters on the opposite side. The red circle and particle indicate the cut-off boundary for non-bonded interactions.

to less than half the width of the box, so that interactions between particles are only considered once within the system.

4.1.8 Maintenance of constant temperature and pressure

In a molecular dynamics simulation, the *ensemble* is defined as the set of atoms and the associated thermodynamic parameters. In a standard simulation, both the number of particles and the temperature of the system are kept constant and the simulation is performed either at constant volume (a canonical ensemble) or constant pressure (isothermal-isobaric or NPT ensemble). The NPT ensemble was used for the work in this thesis, since it is considered to produce a more realistic representation of membrane systems, in which the pressure applied by the membrane on the protein is an important factor in maintaining protein stability [201].

The temperature and pressure of the simulation must be regulated to prevent drift from the initial values caused by errors in integration, equilibration and heating from frictional forces. The Berendsen thermostat and barostat are commonly used regulatory mechanisms which scale the velocities and coordinates of particles in the system, whilst ensuring that local minor fluctuations in temperature can still occur [202]. During production runs, it is often necessary to couple individual parts of the system (e.g. protein, solvent, lipid) to different external baths to prevent the temperature of one component changing while the overall temperature of the system remains constant.

4.1.9 Long range non-bonded interactions

The non-bonded interactions in the system (electrostatic and van der Waals interactions) must be considered over larger distances than the bonded interactions and pose a significant computational challenge, since the number of non-bonded terms increases as a function of the number of atoms. Given that the average simulation contains tens of thousands of atoms, it is not feasible to calculate the interactions for each pair of atoms in the system.

Van der Waals forces may be repulsive at short interatomic distances (owing to the Pauli repulsion of overlapping electron clouds) and attractive at longer distances (owing to the interactions between instantaneous and induced dipoles within electron clouds). Forcefields include potential functions which implicitly implement quantum effects within a classical simulation. The Lennard-Jones and Buckingham potentials are used to describe pairwise interactions and are typically truncated with a cut-off [203].

A cut-off approach may also be used to calculate the electrostatic interactions, requiring Coulomb's law to be calculated for every pair of charged atoms within a given distance. The distance should include as many interactions as possible

while not being computationally too expensive, and the optimum radius has been fiercely debated [204]. Smoothing functions can be used to reduce artefacts caused by the truncation of the interactions, however cut-off methods are intrinsically time inefficient unless they are combined with neighbour list algorithms to identify pairs of atoms to be considered in the calculation.

The most accurate method for calculating $E_{electrostatic}$ is to solve the Poisson equation iteratively, however this is not possible for large systems such as those encountered in MD simulations. Ewald summation methods based on particle-particle (PPPM) and particle-mesh (PME) algorithms are now commonly used instead [205].

4.1.10 Aims of this study

The mode of inhibition of Vpu by HMA has previously been studied using *in silico* docking simulations, which predict that the amilorides bind to the lumen of the pentameric pore, occluding the channel. As discussed in section 4.1.2.3, the algorithms used in such simulations are implicitly biased to favour a binding site in the centre of the pore. Given the highly hydrophobic nature of the amiloride series, it is plausible that the drugs may be able to partition into the membrane, diffusing laterally within the lipid headgroups and binding to either the monomeric or oligomeric form of the protein. This aim of this study is to determine the ability of members of the amiloride series to partition into the lipid bilayer and the equilibrium binding position for the drug in the membrane. Abietic acid, a toxin secreted by conifers as a defence against fungal pathogens, has been demonstrated to partition into bilayers by solid state NMR, will also be simulated to act as a control [206]. The study will consider binding sites on the protein, for which the drugs are in intimate contact with both the lipid and the peptide. The study will aim to observe differences in the drug-lipid and drug-protein interactions between HMA, which inhibits Vpu and amiloride, which does not [73]. A similar mechanism has been proposed for inhibition of the M2 H⁺ channel from Influenza A by rimantadine, which has been shown to bind to a site on the outside of the channel near residues Asp44 and Arg55 [89].

Molecular dynamics (MD) simulations have been used extensively to investigate the interaction of small molecules with model bilayers. The general anaesthetic halothane, has been observed to partition into a DOPC bilayer and to bind to the Tyr277 residue of the α and δ subunits of the *Torpedo* nicotinic acetylcholine receptor [207]. The inhibitor of the M2 channel from Influenza A, amantadine, was shown to bind to the bilayer and this was subsequently proved experimentally by solid state NMR [150].

4.2 Materials and methods

The protonated structures of amiloride (3,5-diamino-6-chloro-N-(diaminomethylene)-pyrazinecarboxamide), HMA (5-(N,N-hexamethylene) amiloride) and DMA (N,N-dimethylene amiloride) were generated with DS Viewer Pro (Accelrys) and the topology files for the GROMOS43a2 forcefield were generated using the PRODRG server [208]. The drug molecules were then placed in a simulation box with a membrane of 128 POPC molecules. The starting heights for each simulation are shown in figure 4.7.

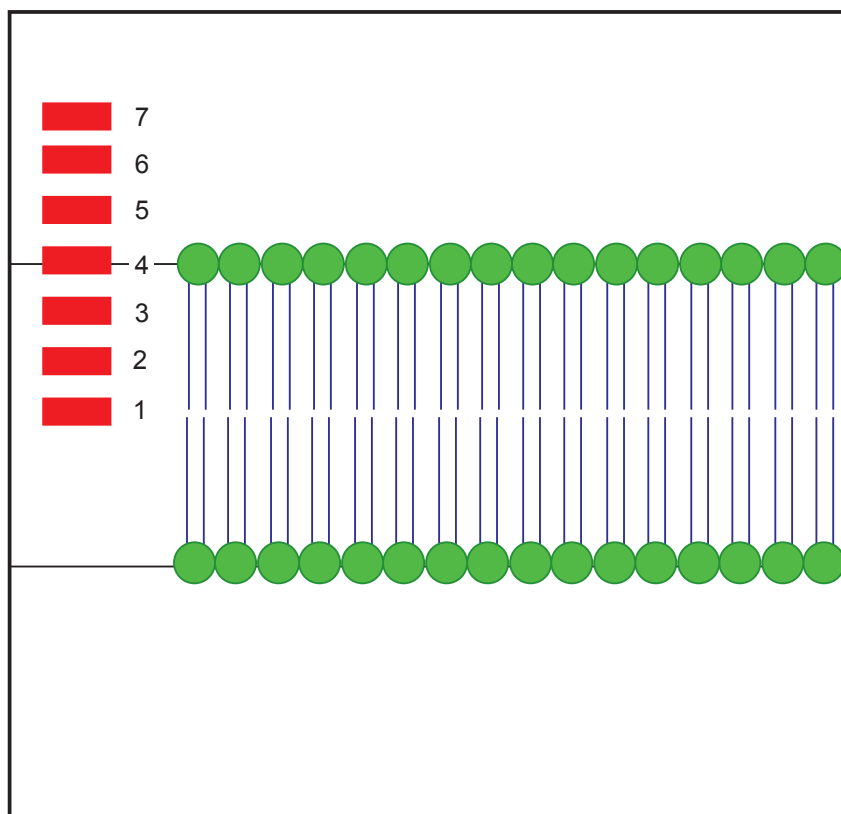


FIGURE 4.7: *Diagram indicating the starting positions of HMA-flex and HMA-stiff in the simulation cell. Seven simulations were performed with both HMA-stiff and HMA-flex. Three simulations were performed with both DMA and amiloride with the starting positions corresponding to numbers 1, 4 and 7.*

Monomeric and pentameric Vpu₁₋₃₂ proteins were generated *in silico* using the program X PLOR 3.1, based on a protocol described in detail elsewhere [69, 209]. This protocol generates ideal α helices (each helix having the sequence MQPIPIVAIV ALLVV AIIIAI VVWSI VIIEY RK) based on a simulated annealing protocol with short molecular dynamics (MD) simulations. The monomeric helix was placed in a bilayer of 210 1-palmitoyl-2-oleoyl-*sn*-glycerol-3-phosphatidylcholine (POPC) lipid molecules in which a hole had already been generated by removing enough lipids to avoid overlap with the helix [184]. The pentameric bundle was placed in a bilayer of 128 POPC molecules in a similar fashion. The systems were solvated by adding water.

Simulations were carried out using GROMACS v3.2.1 and v3.3.1 [200]. Simulations were run at 300 K in an isothermal-isobaric ensemble. Periodic boundaries were present and a Berendsen temperature and pressure coupling was chosen to keep these parameters constant [202]. Long-range electrostatics were calculated by the particle-mesh Ewald (PME) method for the unrestrained simulation and by the cut-off method for the 800 ns simulation. Lennard-Jones and short-range Coulombic interactions were cut off at 1.1 and 0.9 nm respectively. Bond lengths were constrained using the LINCS algorithm [210]. The simple point charge water model was used to describe the water in the simulation box [211], and the particle-mesh Ewald method was used to model the electrostatic interactions in the system. Simulations were performed on a Dell Precision 330 with a Pentium IV 1.5 GHz processor and at the Oxford Supercomputer Centre.

4.3 Results and Discussion

4.3.1 Location of HMA within a model membrane

Equilibrium MD simulations of HMA embedded in a POPC bilayer were performed using Gromacs 3.2.1 and 3.3.1 [199]. Since the extent of the delocalised electron system in the molecule is unclear, two different forms of the molecule were used: one which assumed a minimal aromatic system and was highly flexible (HMA-flex), and one which assumed the stabilisation of the positive charge on the guanidium group by the delocalised electron system (HMA-stiff).

Figure 4.8 shows the bonds which were permitted to rotate in each model. The guanidium moiety was assumed to be planar in both models [212], (see figure 4.9 for resonance structures). By analogy with phenylamine (aniline), the pK_a of the $-NH_2$ group attached to the six-membered aromatic ring is likely to be greater than 9, implying that the group is positively charged in fewer than 1% of HMA molecules at physiological pH (see figure 4.10 for resonance structures) [213], although the apparent pK_a is liable to change on insertion into the membrane [132]. The seven-membered hexamethylene ring was assumed, by analogy with cycloheptane (C_7H_{14}), to be fully flexible in both the HMA-flex and HMA-stiff models [214].

HMA-flex and HMA-stiff were initially subjected to a 1 ns equilibrium MD simulation in water to verify that the parameters had been appropriately assigned (data not shown). Each structure was then placed into a simulation system containing water and a POPC bilayer of 128 lipids. Both HMA-stiff and HMA-flex were initially placed at the height of the phospholipid headgroups, approximately 3.5 nm from the centre of the bilayer.

Figure 4.11 shows snapshots of both HMA-stiff and HMA-flex embedded in the lipid membrane. An initial visual inspection shows that both forms of the drug are

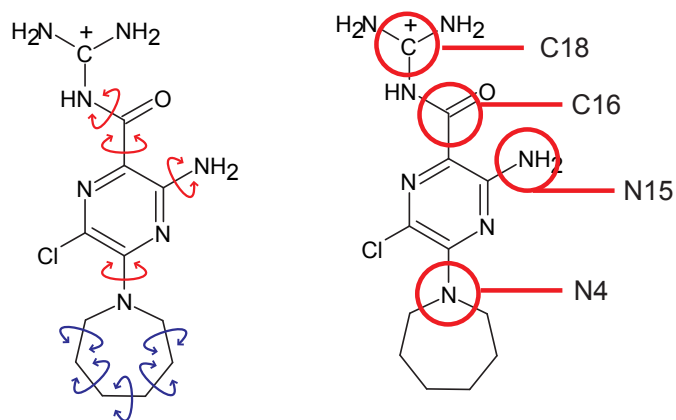


FIGURE 4.8: *Left: Diagram indicating the bonds allowed to flex and rotate in HMA-flex (blue and red) and HMA-stiff (blue only). Right: key to numbered atoms of HMA.*

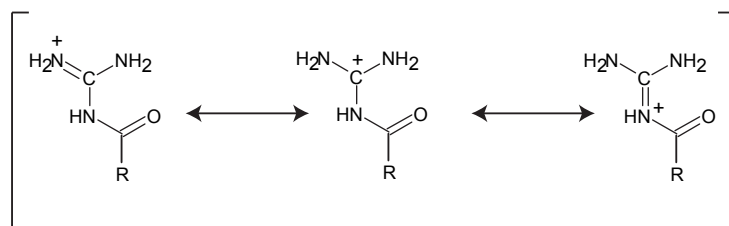


FIGURE 4.9: *Resonance structures of the guanidium group of HMA after [212].*

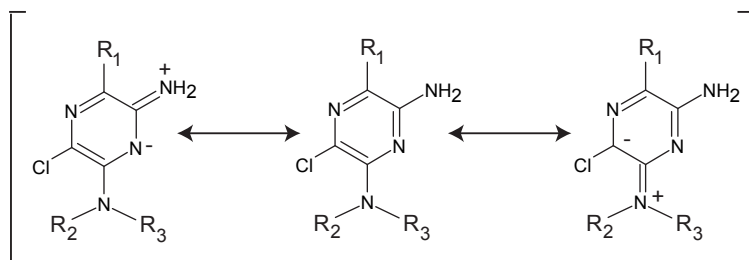


FIGURE 4.10: *Some resonance structures for the six-membered aromatic ring of HMA showing the origin of the planarity of the N4 and N15 atoms.*

located close to the lipid headgroups and that the orientation of the drug depends on the parameter set used.

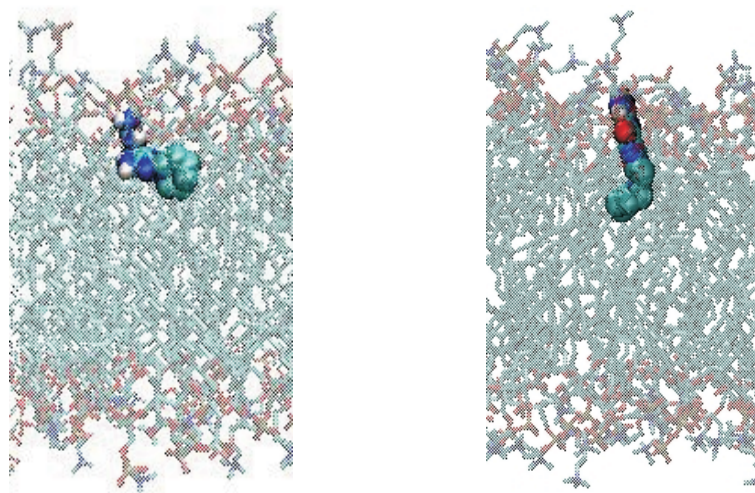


FIGURE 4.11: *Snapshot of HMA-flex (left) and HMA-stiff (right) after 10 ns simulation time. The guanidinium groups of the drug models reside in approximately the same location, however the orientations of the main part of the molecule differ.*

Figure 4.12 shows the positions of the both HMA-stiff and HMA-flex within the membrane after 10 ns. An initial visual inspection reveals that, although both models remain close to the distribution of specific atoms within the HMA-flex and POPC simulation. The central atom of the guanidinium headgroup (C18) is located at the level of the central oxygen atom of the glycerol backbone (O14). The N4 atom of HMA (attached directly to the six-membered aromatic ring) has considerable flexibility in its position and its height in the simulation cell can vary between 0.4 nm and 1.8 nm from the centre of the bilayer.

Figure 4.13 shows the distribution of specific atoms within the HMA-stiff and POPC simulation. The C18 atom of the drug lies in an identical position to that in the HMA-flex simulation, however the position of the N4 atom is markedly different. The N4 atom lies closer to the centre of the bilayer in the HMA-stiff simulations and the standard deviation of the vertical height is approximately half that of the HMA-flex simulations.

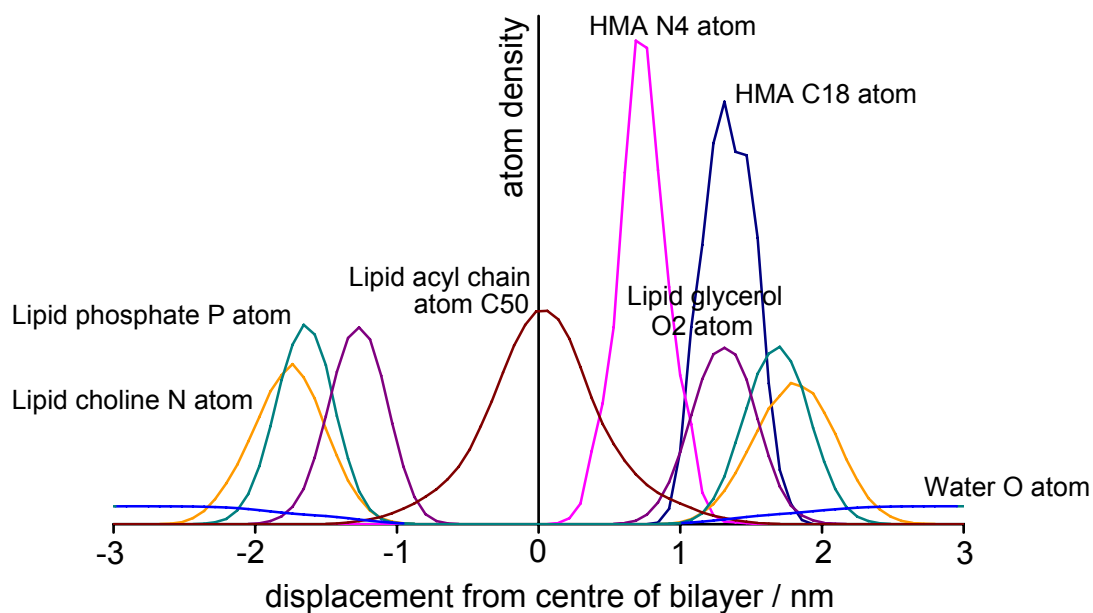


FIGURE 4.12: Density profile for specific HMA and lipid atoms across the membrane for the HMA-stiff simulation.

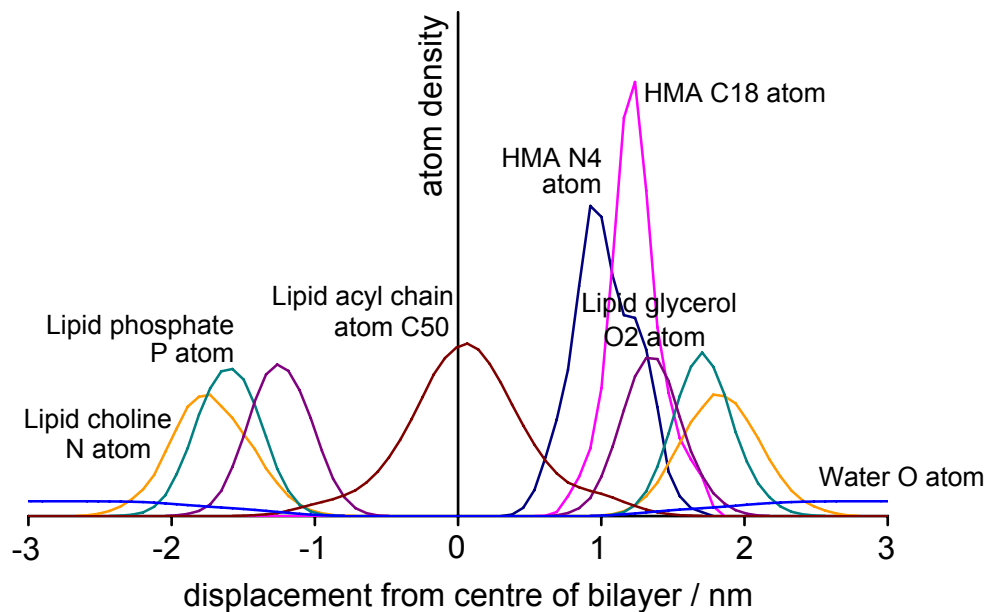


FIGURE 4.13: Density profile for specific HMA and lipid atoms across the membrane for the HMA-flex simulation.

The angle of the drug in the membrane is therefore dependent on the parameter set used. Figure 4.15 shows the histogram of the angles of the vector NC (defined in figure 4.14) to the plane of the bilayer over the final 5 ns of both the HMA-flex and HMA-stiff simulations. At the end of the HMA-flex simulation, the drug lies at a shallow angle of around 15° to the plane of the bilayer, whereas in contrast, HMA-stiff lies perpendicular to the plane of the bilayer.

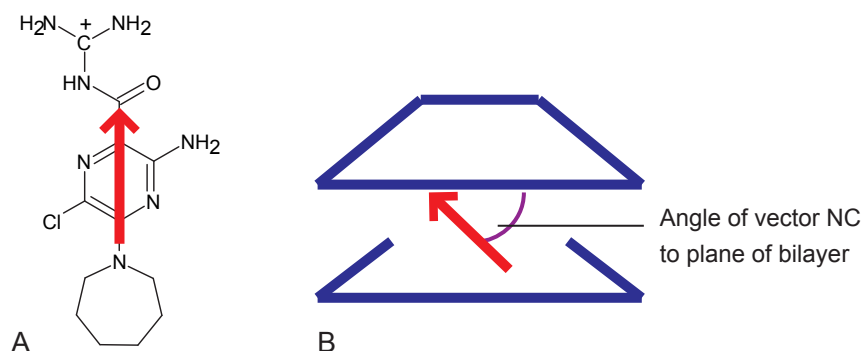


FIGURE 4.14: Definition of angle of vector NC to the plane of the bilayer.

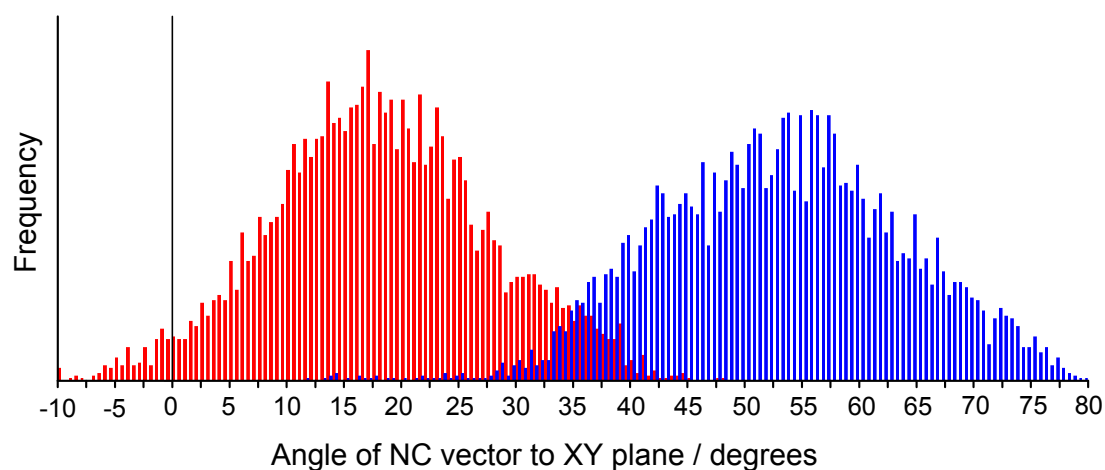


FIGURE 4.15: Histogram of the angle formed between the vector NC and the plane of the lipid bilayer HMA-flex (red) and HMA-stiff (blue).

4.3.1.1 Interaction between HMA and the phospholipid head groups

The guanidium group of HMA carries a positive charge which is stabilised by resonance in both the HMA-stiff and HMA-flex models, and therefore has the potential to interact with the polarisable and negatively charged lipid phosphate groups [215]. Figure 4.16 shows the radial distribution function of water and lipid groups around the central carbon atom of the HMA-stiff guanidium moiety over the course of a 10 ns simulation, in which HMA was located in the lipid headgroup region of a POPC model membrane. The height of the phosphate peak less than 0.5 nm away from the guanidium carbon suggests that the interaction between two species is highly durable. A similar radial distribution is also observed in simulations with the HMA-flex parameters (data not shown).

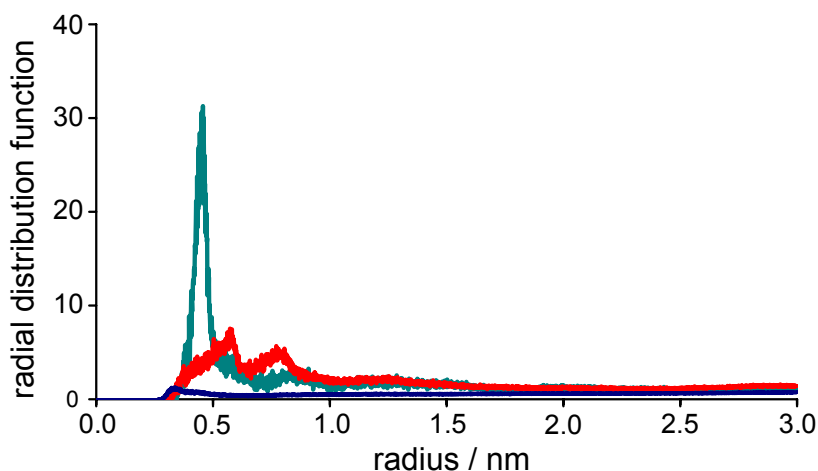


FIGURE 4.16: *Interaction between lipid phosphate groups and HMA guanidium group* lipid phosphate group (green), water O atoms (blue), glycerol backbone O2 atom (red).

The general anaesthetic tetracaine has been shown to partition into DMPC and DPPC membranes (see also section 1.7.3.1). The molecule is positioned so that the tertiary amino group is located at the level of the lipid phosphate groups in both the positively charged and neutral forms. It has been suggested that ionic

and hydrophobic interactions between drug and lipid molecules are responsible for determining the extent of partitioning of tetracaine into the membrane [111, 132].

Given the height of the C18 group within the simulation cell, it would be reasonable to expect the guanidium group to interact with the glycerol backbone. (The positively charged melittin peptide has been shown by neutron diffraction studies to be located at the level of the glycerol backbone when inserted into a phospholipid membrane [216].) The radial distribution function in figure 4.16 shows that the interaction between the two groups is weak and transient. The strong interaction between the HMA C18 atom and the lipid phosphate groups appears to distort the bilayer, pulling the neighbouring lipid headgroups towards the centre of the membrane and creating a local depression around the drug in the leaflet.

Figure 4.17 shows the interaction between two lipid phosphate groups and the HMA guanidium group during the HMA-stiff simulation. Between 0 ns and 0.8 ns, both lipids are free to diffuse laterally within the membrane before binding to HMA on opposite sides of the molecule. The first lipid (blue) remains loosely bound to the phosphate for 2 ns, while the second lipid (green) diffuses away again, before returning to bind again to HMA for 3 ns. During the remainder of the simulation, the close binding exchanges between these two lipid groups.

HMA also affects the motion of the phospholipid within 1 nm of the drug, by restricting its freedom of movement. Figure 4.18 shows the histogram of the angles adopted by the intramolecular vector linking the phosphate atom of the lipid phosphate group with the nitrogen atom of the choline moiety to the XY plane of the bilayer.

A previous study found that amantadine induced a similar decrease in the motions of the lipid headgroups [150]. The distribution of headgroup dipole angles from the bulk lipid observed here are in good agreement with those from previous studies [217].

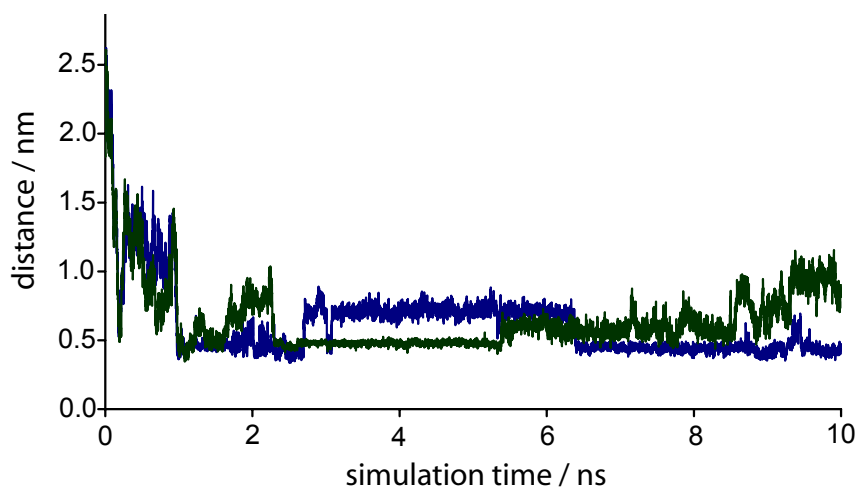


FIGURE 4.17: *Interaction between lipid phosphate groups and HMA guanidinium group* lipid phosphate group (green), water O atoms (blue), glycerol backbone (red).

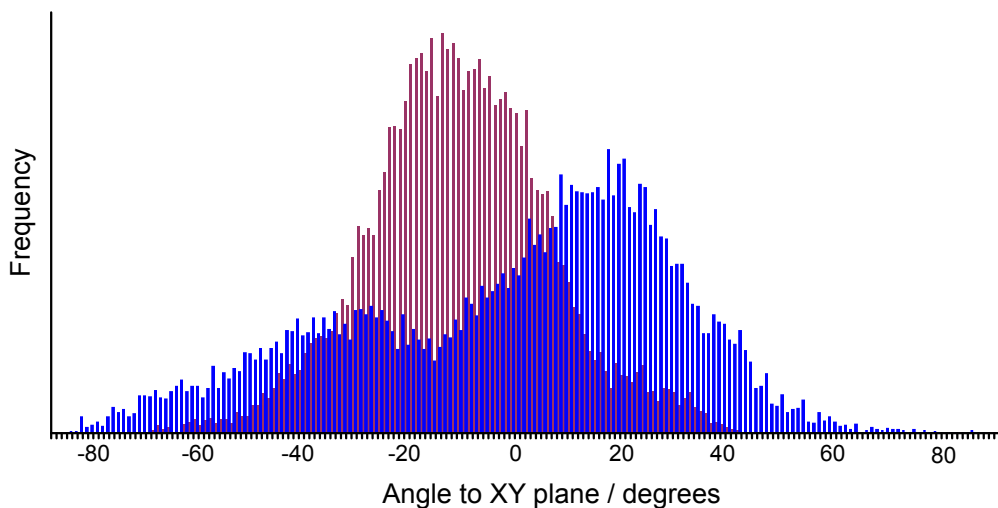


FIGURE 4.18: *Histogram of the angles adopted by the vector connecting the choline N and phosphate P atoms* When HMA is absent (blue), when HMA is present (red). Angles greater than 0° imply that the choline group is positioned above the phosphate and angles less than 0° imply that the choline group lies further towards the centre of the bilayer than the phosphate group

4.3.1.2 Membrane location of DMA and amiloride

The membrane locations of DMA and amiloride were also determined using equilibrium MD simulations with Gromacs 3.2.1 [199]. The parameter files for DMA and amiloride were generated using the PRODRG server [208], so that all of the single bonds within both molecules were unable to rotate. Each molecule was inserted into a POPC bilayer of 128 lipids, parallel to the plane of the membrane at the level of the phospholipid headgroups, and subjected to a 10 ns equilibrium MD simulation. Figure 4.19 shows the structures of the amiloride and DMA and indicates the positions of labelled atoms.

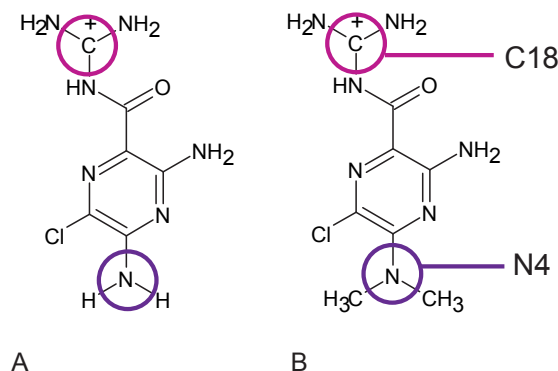


FIGURE 4.19: Structures of amiloride (A) and DMA (B). Atoms C18 and N4 are indicated.

Figure 4.20 shows snapshots of amiloride and DMA at the end of the simulation. Both molecules adopt a similar location within the membrane to the HMA-stiff model discussed above.

The density profiles for specific atoms of amiloride and DMA are shown in figures 4.21 and 4.22 respectively. Since amiloride is a smaller molecule than DMA, it is expected that the motion of the molecule would be more influenced by the motion of the surrounding lipid. As a result although the mean heights of the C18

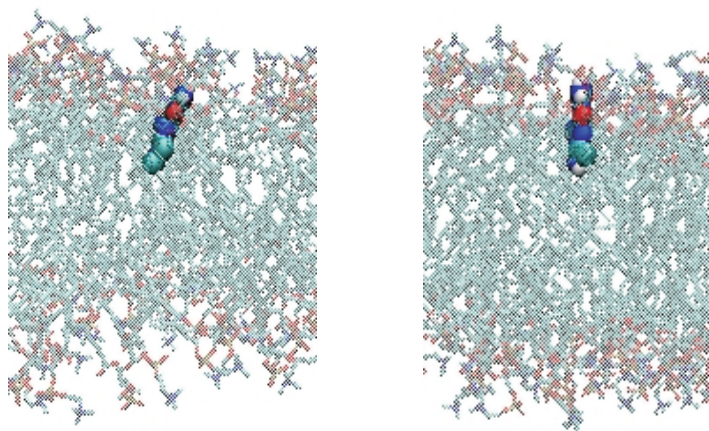


FIGURE 4.20: Snapshots of DMA (left) and amiloride (right) embedded in the POPC bilayer after a 10 ns simulation.

and N4 atoms of both DMA and amiloride are similar, the standard deviations of both parameters are greater for amiloride than DMA.

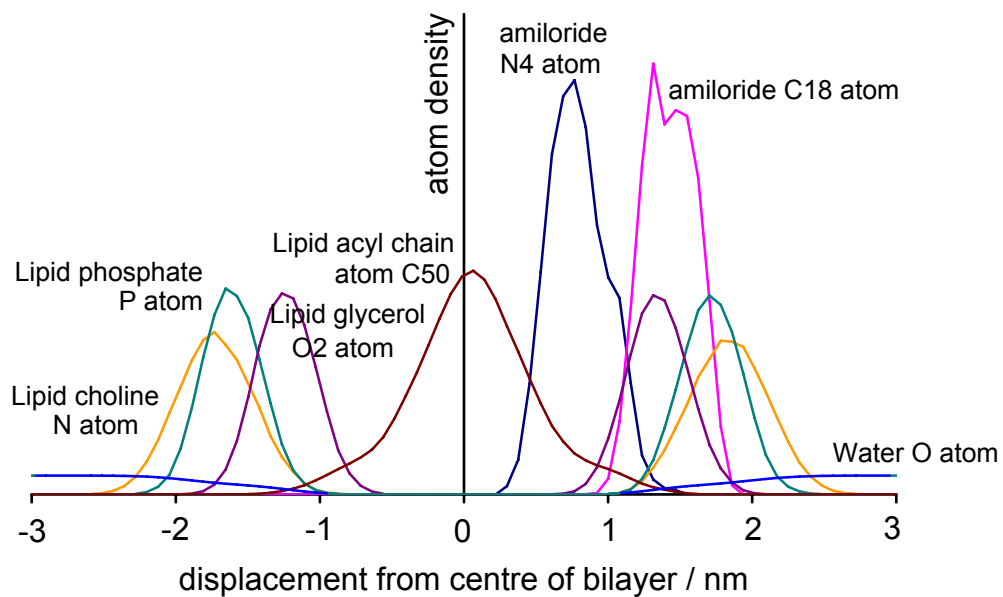
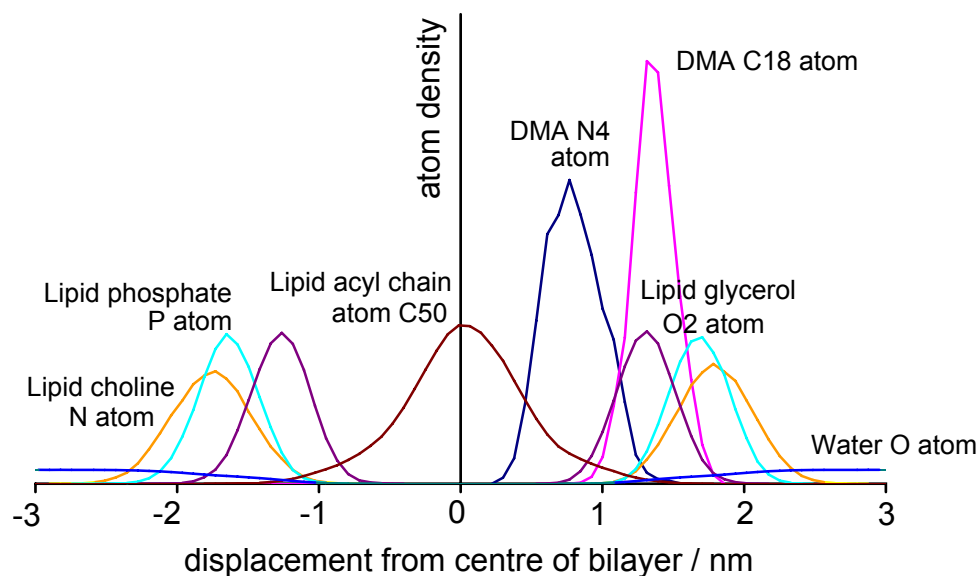


FIGURE 4.21: Density profile for amiloride

FIGURE 4.22: *Density profile for DMA*

4.3.1.3 Discussion

The simulations conducted here show that HMA, amiloride and DMA are able to remain in a model phospholipid bilayer during the course of a 10 ns simulation. There appears to be relatively little difference in the depth of penetration of the drugs into the membrane, despite the presence of the hexamethylene ring attached to the N4 atom of HMA, which might be expected to pull the molecule deeper into the bilayer than the other two molecules.

There is some evidence that the larger size of HMA enables it to resist the motions of the surrounding phospholipids than either amiloride or DMA. Comparison of the standard deviations of the C18 and N4 atom heights in figures 4.12, 4.21 and 4.22 shows that the position of HMA fluctuates less than that of DMA or amiloride within the model membrane, and suggests that HMA might be more effective at regulating the fluidity of the bilayer. Since the differences in the membrane location and between the three drugs are small, it seems unlikely that HMA specifically inhibits Vpu channel activity by altering the biophysical properties

(including order and dynamics) of the bulk lipid, whereas DMA and amiloride do not.

4.3.2 Insertion of HMA into membrane

HMA has been demonstrated above, to be able to reside in a model membrane throughout the course of a 10 ns simulation. The insertion of the drug into the bilayer was followed using a further series of equilibrium MD simulations. Based on the analysis of a series of repeated simulations involving of both HMA-stiff and HMA-flex into the membrane, the insertion process may be thought of as having five distinct stages. The time taken for each stage is highly variable and the process may pause on the boundary between stages.

Figure 4.23 shows the progress of a molecule of HMA-stiff into the membrane, from its initial position above the bilayer, over a 10 ns simulation. The mean positions of the choline nitrogen, phosphorus, glycerol O2 and acyl chain CH₃ groups is shown. The z positions of the HMA N4 and C18 atoms are traced against simulation time. An initial inspection of the figure shows that the first group to interact with the membrane, is the C18 atom, positioned in the centre of the HMA guanidium group, and that for the majority of the simulation time, the molecule is inverted relative to the equilibrium position described in section 4.3.1.

For the remainder of this section, the insertion of a HMA-stiff molecule into the membrane will be followed from its initial height 3.5 nm above the surface of the membrane (corresponding to position 7 in figure 4.7). The simulation lasts for 10 ns and the five stages of the insertion are spread over the entire duration. Other simulations which have been performed have achieved total insertion of the molecule within 2 ns.

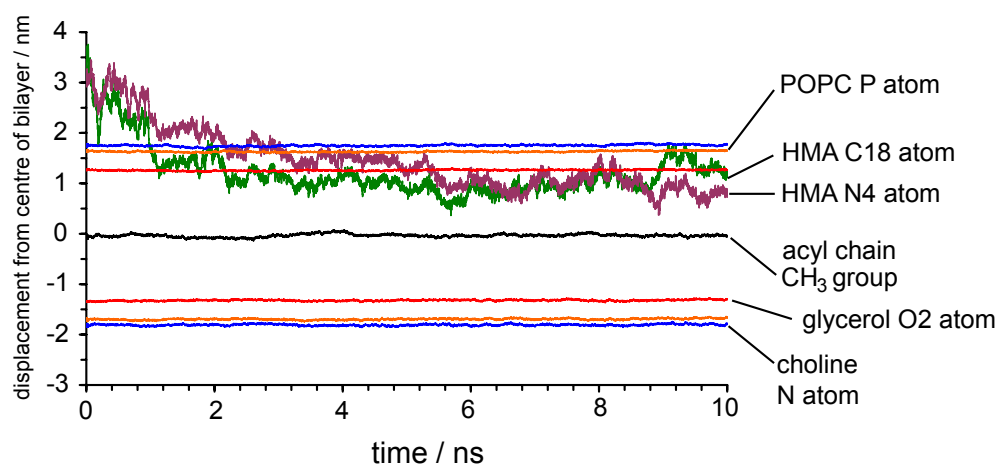


FIGURE 4.23: Progress of an HMA-flex molecule into a POPC bilayer over the course of a 10 ns simulation. The heights of the N4 and C18 atoms of the drug are plotted against simulation time. The mean heights of specific lipid atoms are also plotted.

4.3.2.1 Stage 1 - diffusion through the aqueous phase

The first stage of the insertion process is the random diffusion of the drug molecule from its original starting position through the aqueous phase until it reaches the surface of the membrane. The length of this stage of the simulation may vary considerably. In one simulation in which HMA-stiff was placed 3.5 nm above the surface of the bilayer, the molecule remained at least 1 nm from the surface of the membrane for the entire duration of the 10 ns simulation. In another simulation in which the same HMA model was placed 3.0 nm above the surface of the bilayer, the molecule made contact with the membrane within 250 ps. (The two simulations differed only the initial seed numbers, which are used by Gromacs to generate random numbers to be used in the simulation algorithms [200].)

Figure 4.24 shows the progress of a HMA-stiff molecule towards the surface of the bilayer from its starting height of 3.5 ns above the membrane. The drug begins by moving away from the nearest membrane surface and crosses the boundary with the adjacent cell in the periodic system. The first stage ends with the formation of

an electrostatic interaction between the N15 -NH₂ of HMA (which carries a partial positive charge) and the negatively charged phosphate group of a neighbouring lipid (see figure 4.25).

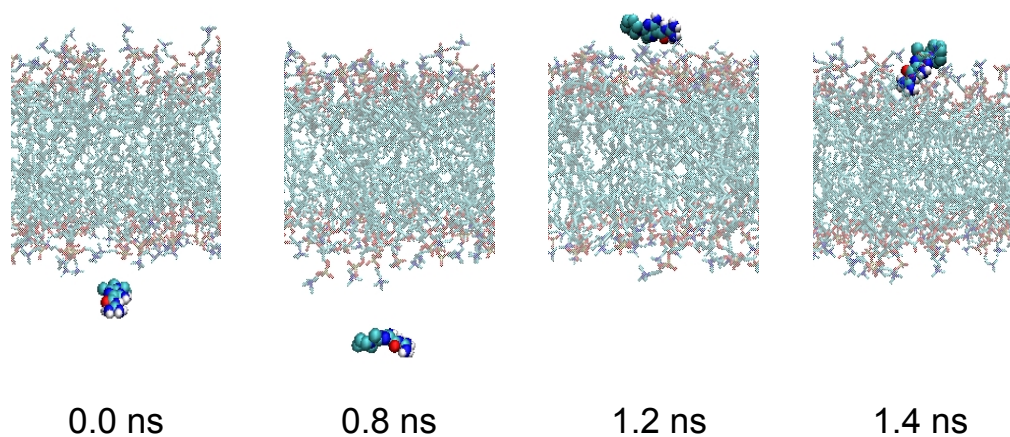


FIGURE 4.24: *Initial diffusion of HMA through the aqueous phase above the bilayer.* During the first 0.8 ns the drug diffuses away from the membrane leaflet closest to it. Between 0.8 ns and 1.2 ns the HMA molecule crosses the lower boundary of the simulation box and reappears above the membrane.

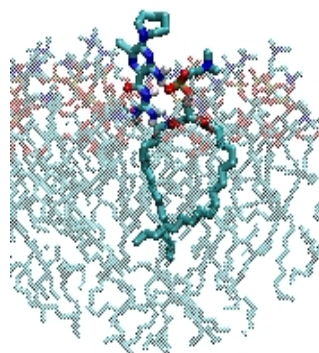


FIGURE 4.25: *Formation of the electrostatic interaction between the N15 -NH₂ group of HMA and the phosphate group of a neighbouring lipid after 1.2 ns*

4.3.2.2 Stage 2 - vertical position in bilayer

The HMA-stiff molecule remains in a ‘head-down’ position, with its long axis at an angle of 90° to the plane of the membrane and is then pulled downwards towards

the centre of the bilayer, by the random vertical motions of the lipid molecule attached to the N15 -NH₂ group of the drug. Figure 4.26 shows the snapshots of HMA as it enters the bilayer. The figure shows that the drug molecule has considerable freedom to rotate around its long axis.

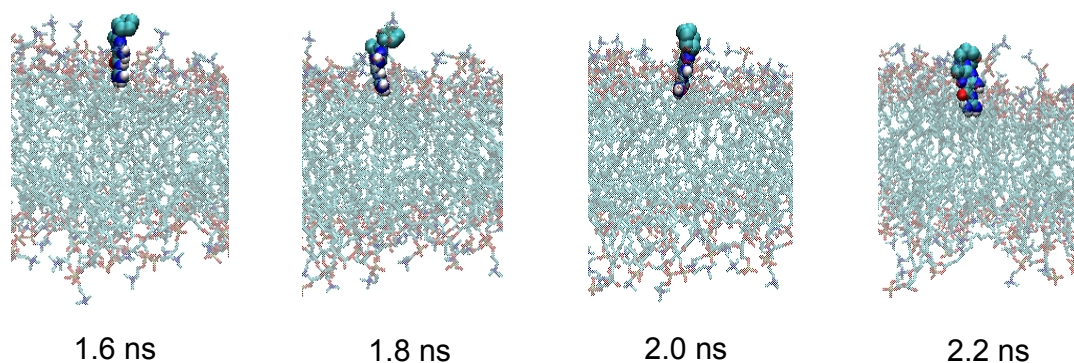


FIGURE 4.26: *Initial diffusion of HMA through the aqueous phase above the bilayer* Between 0.8 ns and 1.2 ns the HMA molecule crosses the lower boundary of the simulation box and reappears above the membrane.

Despite the proximity of the lipid headgroups to the guanidium group of the drug, the electrostatic interaction observed in section 4.3.1 does not form. Figure 4.27 shows the radial distribution function for the lipid phosphate groups around the C18 guanidium carbon atom for the duration of Stage 2. As the guanidium headgroup inserts into the membrane, it brings with it a population of water molecules, which appear to screen the lipid phosphate groups from the positive charge and prevent any interaction occurring. (Compare this diagram to figure 4.16, which clearly shows a strong interaction between C18 of HMA and the phosphate group of a neighbouring lipid.)

4.3.2.3 Stage 3 - reorientation to lie flat on membrane surface

Stage 2 ends once an electrostatic interaction forms between the C18 guanidium carbon and the phosphate group of a neighbouring lipid molecule. Throughout

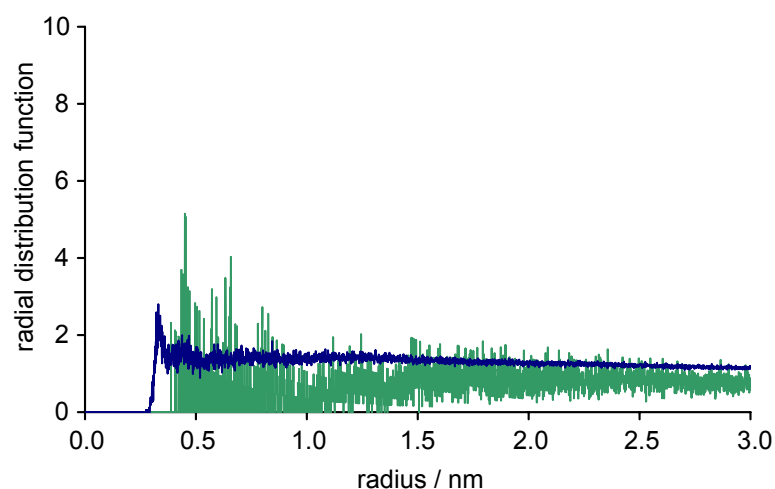


FIGURE 4.27: Radial distribution function showing the interaction between lipid phosphate groups and HMA guanidinium group for the duration of Stage 2. Lipid phosphate group (shown in green) and water O atoms (blue).

Stage 3 therefore, the drug is bound to two lipid molecules: one bound to the positively charged guanidinium carbon atom (Lipid 1) and the other to the N15 -NH₂ group (Lipid 2). Figure 4.28 shows snapshots of the simulation during Stage 3 as the drug molecule inserts further into the bilayer and twists to lie parallel to the plane of the membrane. The reorientation of the drug occurs as a result of the opposing motions of the two lipid molecules, which combine to create a turning force. As Lipid 2 moves towards the centre of the membrane, Lipid 1 moves away from it. As this process occurs, the HMA-stiff molecule twists to prevent Lipid 2 from being trapped underneath the molecule. The third stage of the insertion process ends as the drug molecule lies flat just below the surface of the bilayer.

Figure 4.29 shows the radial distribution function for water and phosphate around C18 throughout the simulation. When compared to figure 4.27, it is clear that an interaction between the lipid phosphate and the C18 atom of HMA occurs in Stage 3, which is absent in Stage 2.

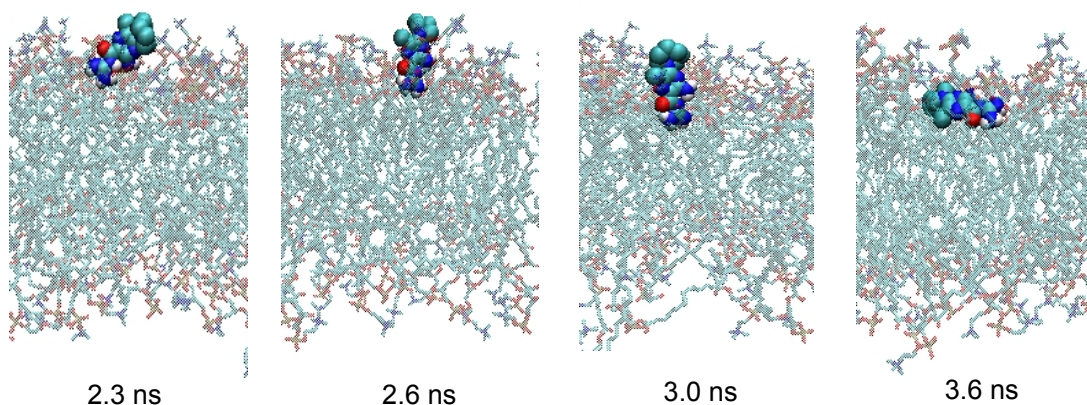


FIGURE 4.28: Snapshots of the insertion of HMA into the POPC bilayer during Stage 3. There is considerable lateral motion of the molecule during this period, however the two lipid phosphate groups remain attached to the drug throughout.

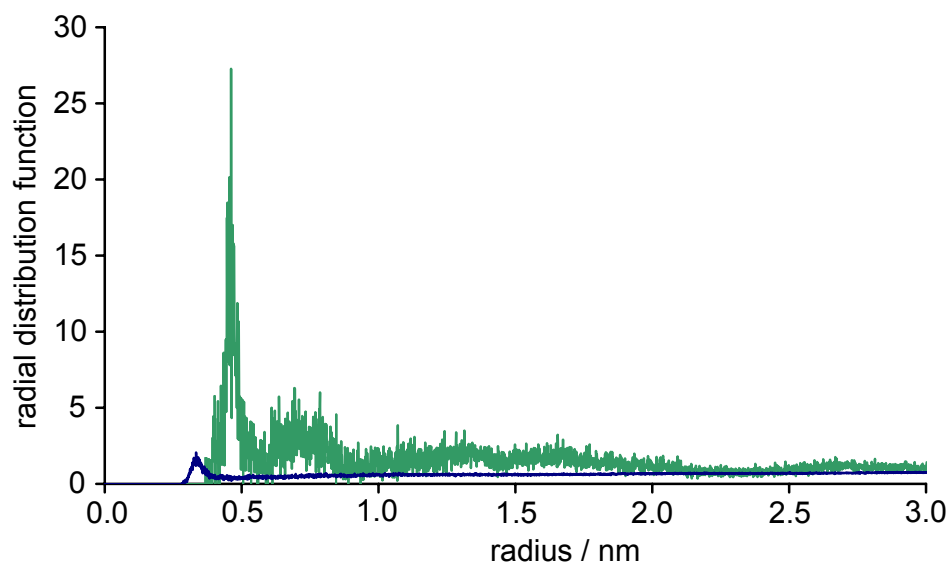


FIGURE 4.29: Interaction between lipid phosphate groups and HMA guanidinium group for the duration of Stage 3. Lipid phosphate group (green) and water O atoms (blue).

4.3.2.4 Stage 4 - reorientation continues

At the end of Stage 3, the HMA molecule lies parallel to the surface of the membrane and is bound to both Lipids 1 and 2. Figure 4.30 shows snapshots of the progress of the drug into the membrane throughout Stage 4.

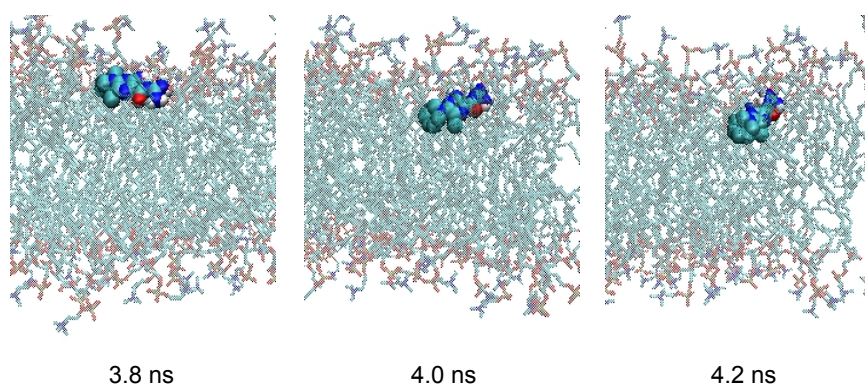


FIGURE 4.30: *Snapshots of the insertion of HMA into the POPC bilayer during Stage 4* There is considerable lateral motion of the molecule during this period, however the two lipid phosphate groups remain attached to the drug throughout.

Figure 4.31 shows the radial distribution function around the HMA guanidinium group carbon atom for the duration of Stage 4. The figure clearly shows that the electrostatic interaction between the drug and Lipid 1 is transient. The final reorientation therefore occurs with only Lipid 2 permanently attached to the drug.

4.3.2.5 Stage 5

Stage 5 is the final stage reached by all of the simulations which involve a drug inserting into the membrane from the aqueous phase, however it is not the same as the conformation described in section 4.3.1. At the start of Stage 5, the electrostatic interaction between the C18 of the drug and the lipid phosphate reforms (see figure 4.32), however the other electrostatic interaction also remains present.

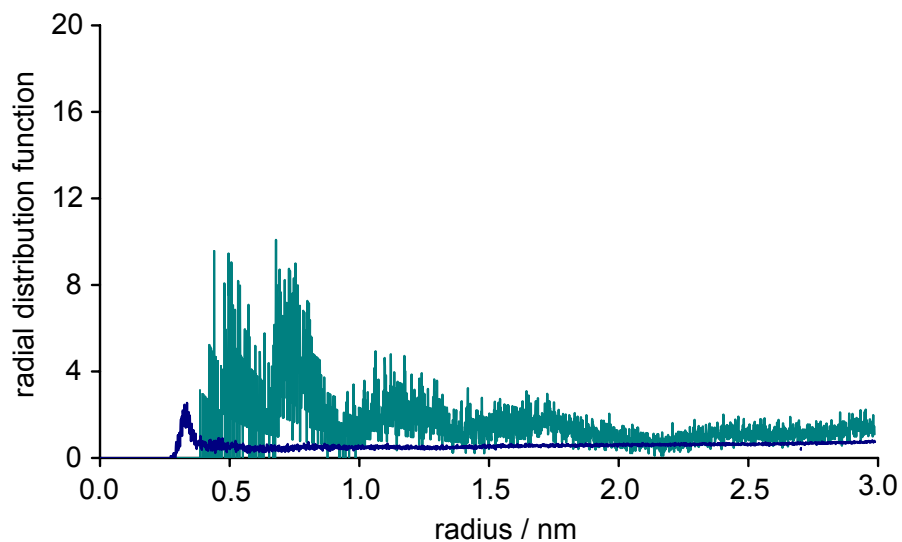


FIGURE 4.31: *Interaction between lipid phosphate groups and HMA guanidium group for the duration of Stage 4* lipid phosphate group (green) and water O atoms (blue).

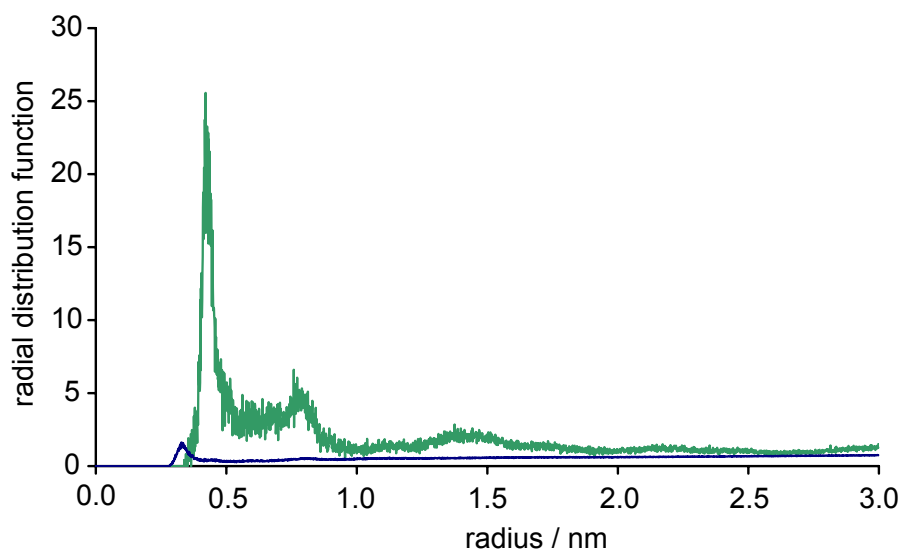


FIGURE 4.32: *Interaction between lipid phosphate groups and HMA guanidium group for the duration of Stage 5* lipid phosphate group (green) and water O atoms (blue). The interaction persists through the remainder of the simulation.

It is not clear whether Stage 5 represents the final stage of the insertion process, or whether it is simply an intermediate before the HMA establishes the orientation described in section 4.3.1.

Figure 4.33 shows the density profile of specific atoms across the membrane for the duration of Stage 5, which reveals a more oblique angle for the drug than that in figure 4.12.

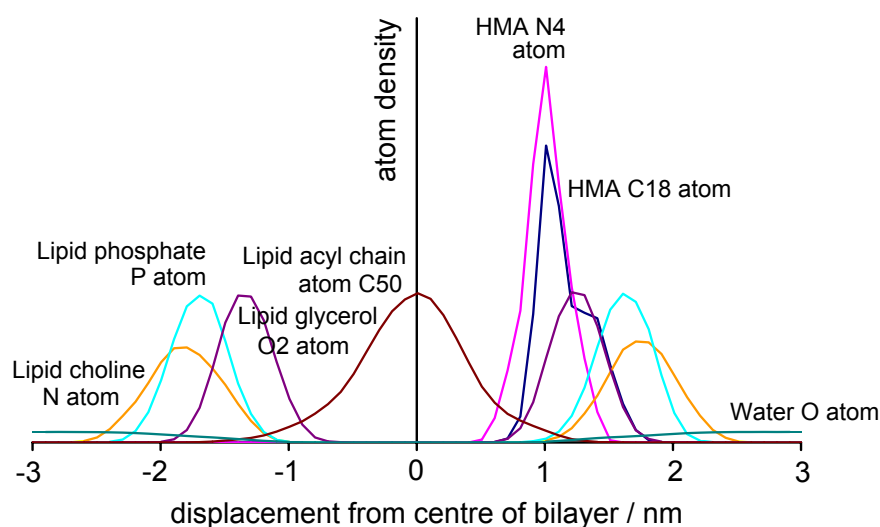


FIGURE 4.33: *Interaction between lipid phosphate groups and HMA guanidium group for the duration of Stage 5 lipid phosphate group (green) and water O atoms (blue). The interaction persists through the remainder of the simulation.*

4.3.2.6 Movement of HMA from the core of the bilayer to lipid headgroup region

Simulations of 10 ns were also performed with both HMA-stiff and HMA-flex models in which the drug was initially positioned in the core of the bilayer, in the region occupied by the lipid acyl chains. Drug molecules placed within this region moved towards the lipid headgroup region, eventually adopting the position described in section 4.3.1. Figure 4.34 shows the progress of an HMA-stiff molecule from

the centre of the membrane to the lipid headgroup region over the course of the simulation. The lateral motion of the lipid acyl chains appears to be responsible for driving the drug from its initial starting position. No inversion of the orientation of the drug is observed in any of the simulations with either HMA-flex or HMA-stiff.

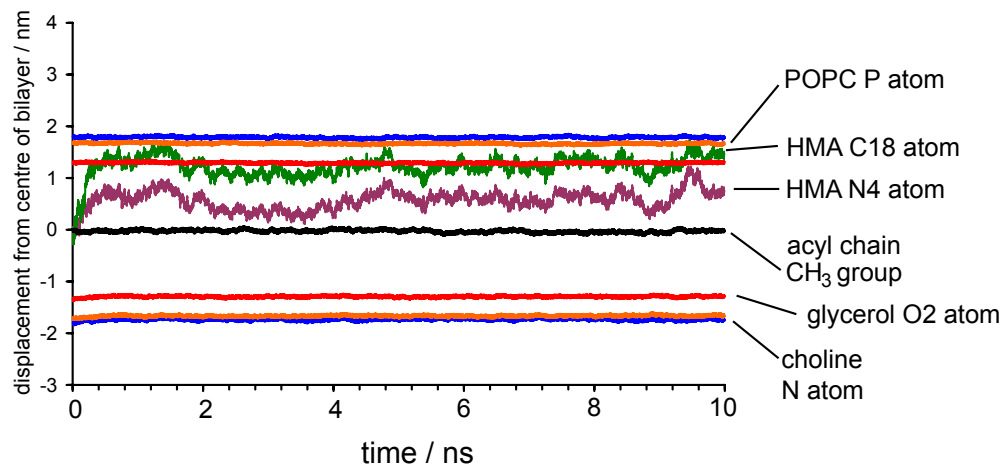


FIGURE 4.34: Progress of an HMA-stiff molecule from the hydrophobic interior of a POPC bilayer to the lipid headgroup region over the course of a 10 ns simulation. The heights of the N4 and C18 atoms of the drug are plotted against simulation time. The mean heights of specific lipid atoms are also plotted.

4.3.2.7 Conclusion

The simulations presented show that HMA, is able to insert into a phospholipid bilayer from the aqueous phase to reside within the lipid headgroup region. Contrary to initial expectations, the first part of HMA-stiff molecule to make contact with the phospholipid bilayer is the positively charged guanidium group rather than the hydrophobic hexamethylene ring. The strong electrostatic interaction between the negatively charged lipid phosphate group and the N15 -NH₂ HMA, persists throughout the remainder of the simulation and the drug is therefore unable to adopt a position at 90° to the plane of the membrane, observed in the

earlier simulations and instead lies tilted at an angle of approximately 60° . Surprisingly, the interaction between the C18 guanidium carbon and the lipid phosphate groups, which was identified in section 4.3.1, does not form until Stage 3 and is then broken during Stage 4. A combination of forces appear to work together to draw the molecule into the bilayer from its initial position in the aqueous phase.

When an HMA molecule is placed in the hydrophobic interior of the bilayer, it also moves to reside in the lipid headgroup region. The driving force for this process appears to be the lateral motion of the lipid acyl chains. The final orientation adopted by the drug is similar to that described in section 4.3.1.

4.3.3 Location of abietic acid within a model membrane

To assess the validity of the predictions of the simulations described above, a series of simulations was performed to determine the membrane location and orientation of abietic acid, a major component of the oleoresin produced by several species of conifer as a defensive secretion against insect and fungal pathogen attack [218]. Abietic acid is thought to act as a neurotoxin by initiating membrane depolarisation and may induce chronic and acute lung disease in humans [219, 220]. Its location within a model membrane of egg yolk lipid has previously been determined by solid state NMR [206]. The molecule has a single carboxylic acid group, which is the only polar part of the molecule and a system of three interconnected non-aromatic carbon rings, which form the hydrophobic part of the molecule. ^{13}C spin-lattice relaxation times suggest that all carbon atoms within the molecule lie within 1.0 nm of the membrane surface [206]. Abietic acid was chosen as a control for this series of experiments, because it has the opposite charge to HMA and because the long axis of the molecule lies almost parallel to the plane of the membrane, unlike the HMA-stiff model, which lies perpendicular to the plane of the membrane.

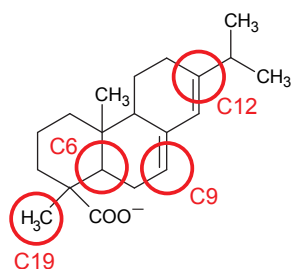


FIGURE 4.35: *Structural formula of abietate (the negatively charged form)*. The atom numbering is consistent with that in [206].

Abietic acid may exist in two forms - as an uncharged carboxylic acid and with a negatively charged carboxylate ion (depending on the pH of the surrounding solution). Simulations were performed with both forms of the drug, (since a population of abietic acid molecules in the membrane, is likely to exist in equilibrium between the charged and uncharged forms). There appears however, to be little difference between the membrane locations and orientations of the two forms. Figure 4.36 shows a snapshot of the simulation of the negatively charged abietate ion in a POPC membrane of 128 lipids after 10 ns. Both forms of the toxin lie close to the surface of the membrane with the longest axis of the molecule lying approximately parallel to the plane of the membrane.

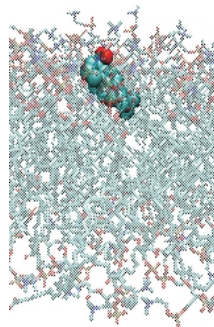


FIGURE 4.36: *Snapshot of the negatively charged form of abietic acid in a POPC bilayer after a 10 ns equilibrium simulation*.

Figure 4.37 shows the distribution of numbered atoms of abietate across the membrane throughout the simulation (see also figure 4.35). Despite the spacing of the different groups in the toxin molecule, most of the atoms lie at approximately the same height as the glycerol backbones of the bulk lipid.

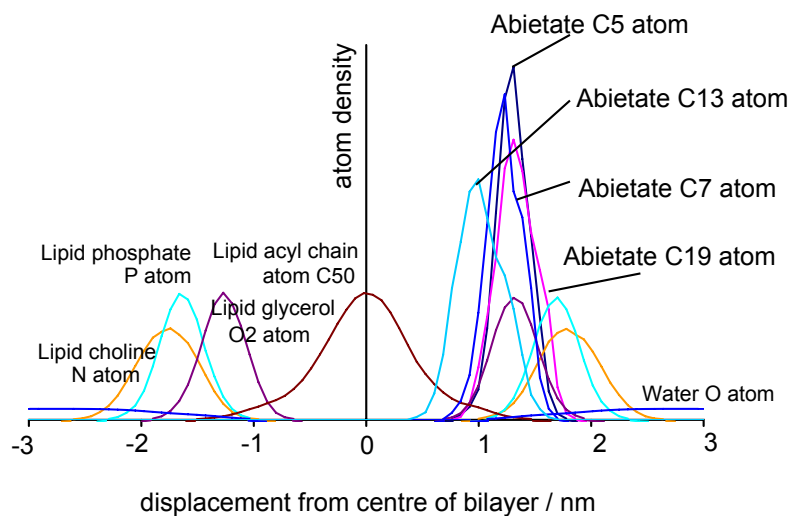


FIGURE 4.37: *Distribution of atoms of the negatively charged form of abietic acid across the bilayer.*

Table 4.1 compares the measured distance between the top of the bilayer and specific groups within the toxin molecule as measured by solid state NMR [206], and by the MD simulations reported in this chapter. The results of the simulations with both abietic acid and abietate are given, however the solid state NMR measurement presumably include populations of both the charged and uncharged forms. The top of the bilayer in the MD simulations was defined as the mean height of the lipid phosphorus atoms. The table shows clearly that in the MD simulations, the neutral form of the toxin lies 0.02 nm closer to the centre of the bilayer than the negatively charged abietate ion. There is some discrepancy between the absolute heights of the toxin in the membrane, however the angle of the drug appears to be consistent with the MD simulations of the two forms.

TABLE 4.1: Table showing the distances of abietic acid atoms from the surface of the bilayer, as determined by solid state NMR and simulation studies.

Atom number	Distance below top of bilayer / nm		
	NMR	MD (abietate)	MD (abietic acid)
C13	0.60	0.80	0.82
C7	0.22	0.43	0.45
C19	0.20	0.40	0.43
C5	0.18	0.38	0.41

4.3.3.1 Conclusion

The MD simulations performed with abietic acid were intended to act as control simulations to assess the validity and reliability of the simulations involving HMA, DMA and amiloride reported in section 4.3.1. Abietic acid was proven to be a useful control molecule, since the angle that the toxin adopts in the membrane is approximately perpendicular to that adopted by HMA-stiff, despite the fact that there is little flexibility in the two molecules. The position of the toxin in the membrane, predicted by MD simulations of both the charged and uncharged forms of the molecule, were consistent with solid state NMR measurements of abietic acid in egg yolk lipid membranes.

4.3.4 Interaction between HMA and Vpu

Previous computational studies have suggested that HMA is able to bind directly to Vpu, and have generally considered a binding site in the channel lumen, consistent with an *inhibition-by-occlusion* mechanism, as the most plausible [76, 77]. Docking simulations have also suggested that HMA may be able to bind to the side chain of Trp23, a residue which, although not essential for ion conduction, is highly conserved across HIV-1 subtypes and is predicted to lie on the outside of the Vpu oligomer (see figure 4.2) [76, 193]. These docking simulations have been in the absence of lipid and water, with a fully flexible HMA (analogous to the HMA-flex model defined in figure 4.8). However it has been suggested that the Trp23 sidechain is fully accessible to lipid-solubilised HMA and amiloride [77, 193]. 5 ns equilibrium MD simulations were therefore performed to determine whether the HMA-stiff was able to bind and remain bound to the aromatic sidechain of Trp23, when embedded in fully-solvated POPC bilayer, as a new sophistication of the HMA-Vpu interaction.

4.3.4.1 Generation of starting structures

The accuracy of simulations which attempt to dock drug molecules to short peptides such as Vpu₁₋₃₂ has been challenged [221]. Attempts to generate suitable starting structures for this series of simulations using the docking programs AutoDOCK 4.0 and MOE [222], were unsuccessful (data not shown) and so both HMA-stiff and amiloride were placed adjacent to the aromatic rings of the Trp23 sidechain, so as to ensure a maximum overlap between the two groups. The perpendicular separation between the aromatic systems was set as the sum of the van der Waals radii of two adjacent non-bound carbon atoms. The 'bound' structures were then embedded in a POPC bilayer of 128 lipid molecules and solvated.

4.3.4.2 Differences in the interactions of the drugs and Trp23

Figure 4.38 shows snapshots of the systems at the start and end of the equilibrium simulation production runs, after the processes of energy minimisation and equilibration. The snapshots show that amiloride does not remain bound to the Trp23 sidechain, however HMA does remain bound throughout the simulation. The difference in the tilt angle of the helix is also pronounced, and in the presence of HMA, the Vpu_{1-32} helix begins to bend over, whereas the helix in the amiloride simulation remains more or less straight. Also visible in figure 4.38 is the pronounced difference between the angle of the Tyr30 sidechain in the two simulations.

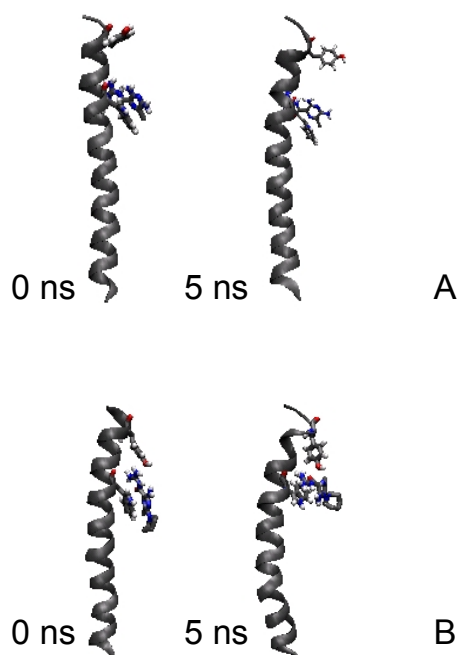


FIGURE 4.38: Snapshots of simulations with the amiloride (A) and HMA (B) and Vpu_{1-32} **A:** Vpu_{1-32} monomer with amiloride bound to residue Trp23 after 0 ns and 5 ns. **B:** Vpu_{1-32} monomer with HMA bound to residue Trp23 after 0 ns and 5 ns. The drug molecules and residues Tyr30 and Trp23 are shown in stick modus, with CPK colour coding. Lipids and water molecules are omitted for clarity. Images prepared using VMD [223].

Figure 4.39 shows the displacement between the centre of the Trp23 side chain and the aromatic system of the drug. HMA-stiff remains bound to the sidechain of Trp23 throughout the course of all simulations, however amiloride was unable to bind stably to Trp23 in any simulation.

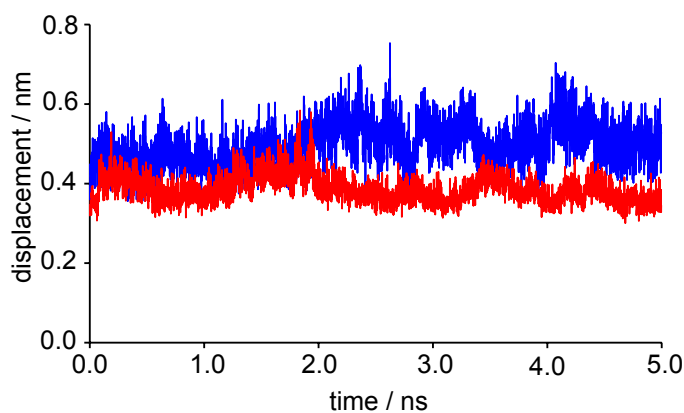


FIGURE 4.39: *Distance between the centre of the drug molecules and Trp23*
Amiloride (blue) and HMA-stiff (red).

The binding of HMA to residue Trp23 has a profound affect on the interaction between the lipid and the protein. Figure 4.40 shows the a snapshot of the simulation taken after 2.5 ns. Although the drug molecule is located below the average position of the phospholipid headgroups in the simulations, the guanidium head group remains strongly bound to the phosphate group of the adjacent lipid molecule. The guanidium group pulls the phospholipid head group both downwards towards the centre of the bilayer and also outwards away from the α helix of the peptide, which in turn creates a water pocket around the C-terminal end of the peptide. (The water pocket around residue Val25 is clearly visible in figure 4.40.)

4.3.4.3 Affect of HMA binding on Tyr30

Figure 4.41 shows the difference in the radial distribution function for all lipid phosphate groups in both the presence and absence of HMA around the Tyr30 sidechain. In the absence of HMA, the aromatic ring of Tyr30 interacts strongly

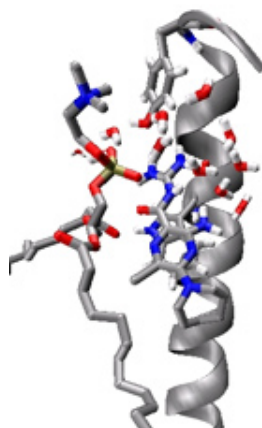


FIGURE 4.40: *Snapshot of HMA bound to residue Trp23 after 2.5 ns.* The guanidinium head group of HMA remains bound to the phosphate group of the adjacent lipid molecule, creating a water pocket around the C-terminal end of the peptide. Bulk lipids and water molecules are omitted for clarity. Image prepared using VMD [223].

with the phosphate group of an adjacent lipid to which it is bound throughout much of the simulation, appearing to form an anion- π interaction of 0.4 nm in length. The radial distribution function changes dramatically when HMA is bound to Trp23, and the interaction between the phosphate group and Tyr30 is abolished.

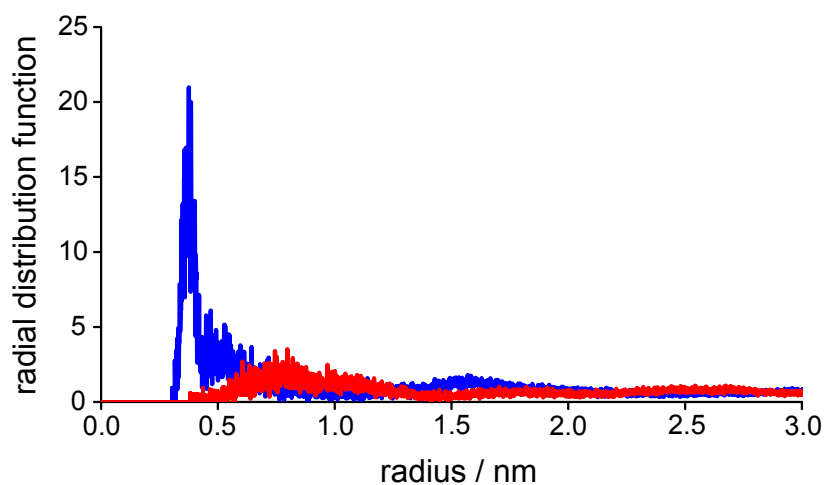


FIGURE 4.41: *Radial distribution function for the lipid phosphate groups around the Tyr30 side chain.* When HMA is absent (blue), when HMA is present (red).

4.3.4.4 Affect of HMA binding on helix secondary structure

The secondary structure of the Vpu₁₋₃₂ helix appears to be little affected by the presence of the HMA drug bound to Trp23. The binding of HMA to side chain Trp23 appears to have little affect on the stability of the Vpu₁₋₃₂ α helix. Figure 4.42 compares the root mean square deviation of the peptide in the presence of HMA and amiloride from an ideal helix. This is somewhat surprising, since it might be expected that the C-terminal end of the helix would unwind in the simulation with HMA.

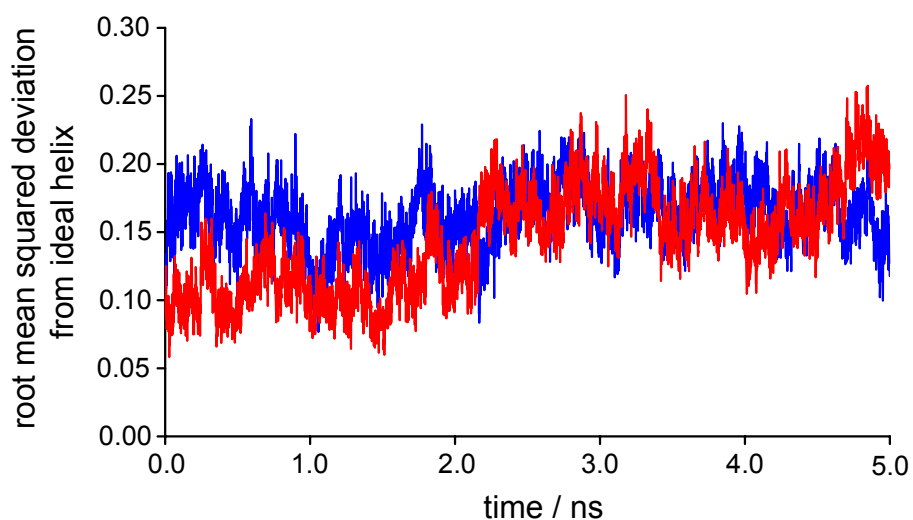


FIGURE 4.42: *Root mean square deviation of the Vpu₁₋₃₂ helix throughout the simulation.* in the absence of HMA(blue), in the presence of HMA (red).

4.4 Discussion

The mode of inhibition of the Vpu ion channel by 5-(*N,N*-hexamethylene) amiloride (HMA) has been investigated by in this chapter by molecular dynamics (MD) simulations. Earlier computational studies (without lipids or hydration) have suggested a pore occlusion mechanism, in which the drug binds to the channel lumen, thus preventing ion flux [76, 77].

Like many inhibitors of eukaryotic ion channels (see section 1.7.3), drugs of the amiloride family are amphipathic and their structure suggests that they should be able to partition into phospholipid bilayers and to be able to reach integral membrane proteins by lateral diffusion in the membrane. This property presents two alternative mechanisms of inhibition: that HMA inserts into the phospholipid bilayer and affects the order and dynamics of the lipid, reducing the probability of channel formation and/or opening and that HMA binds to residues on the outside of the channel, either destabilising the tertiary structure of the protein or reducing the probability of channel opening. A similar mechanism has been suggested previously for the inhibition of ion flux through the nAChR by general anaesthetics [131]. The simulations presented throughout this chapter have aimed to detect differences in the ways in which amiloride (which does not inhibit Vpu channel activity) and HMA interact with a model membrane and Vpu₁₋₃₂.

4.4.1 Interaction of drugs with model membrane

Equilibrium MD simulations have been used to investigate the interaction between three members of the amiloride family of drugs and a model bilayer. A series of 10 ns simulations were performed to observe the insertion of the drug molecules into a POPC bilayer, and to determine the equilibrium position within the membrane (sections 4.3.1 and 4.3.2). The simulations predict that the drug

molecules are able to insert into a pure POPC bilayer and reside at the interface between the hydrophilic and hydrophobic regions, (in common with many other lipophiles [150, 206, 224, 225]). A strong electrostatic interaction between the lipid phosphate group and the positively charged guanidium group of the drugs was observed, and the presence of the drug appears to restrict the motion of the phospholipid headgroups. There also appears to be a greater penetration of water molecules into the lipid headgroup region than into the bulk lipid. There appears to be little difference between the interactions of HMA and amiloride with the model membrane, suggesting that HMA does not inhibit Vpu by altering the biophysical properties of the bulk lipid.

4.4.2 Interaction of drugs with Trp23

The interaction between the drugs and the aromatic residue Trp23 of Vpu was also investigated by MD simulation. The residue is predicted to lie on the external face of the pentameric channel, facing the lipid membrane [76, 193]. Simulations performed with a single Vpu₁₋₃₂ α helix embedded in a POPC bilayer, predict that whilst HMA binds strongly to Trp23, amiloride does not (section 4.3.4). The binding of HMA to Trp23 has a profound effect on the organisation of the lipids immediately surrounding the helix. The phosphate group of the lipid bound to the guanidium group of the drug, is pulled towards the centre of the bilayer, residing ~ 7 Å from the expected position, creating a water-filled pocket around residue Val25. Although it has not been possible to simulate these results with a pentameric Vpu₁₋₃₂ bundle, it is likely that the development of an aqueous pocket destabilises the tertiary structure of the channel, thus preventing ion flux. Water is known to penetrate the annular lipid region surrounding the nAChR to a lesser degree than that of bulk lipid [123]. If Vpu has a similar requirement for an annular lipid region, which HMA is capable of disrupting, then this may also provide a mechanism of inhibition.

It is highly likely that the binding of HMA to the outside of the Vpu channel would affect the channel kinetics. The dramatic change in the position of the phospholipids and the increase in the depth of water penetration into the bilayer, which these simulations suggest occurs on the HMA to Trp23, may also destabilise the oligomeric state of the channel, and since Trp23 is likely to help to anchor Vpu within the bilayer [20], the positioning and stability of the monomer within the bilayer might also be affected.

4.4.3 Evaluation of proposed mechanisms of inhibition

Several well characterised inhibitors of ion channels are able to partition into phospholipid bilayers (see section 1.7.3). Rimantidine, the inhibitor of the M2 ion channel from Influenza A has been shown by solid state NMR to bind to the outside of the tetrameric channel, in close proximity to residues Asp44 and Arg45, creating a polar patch in a highly hydrophobic region of the protein [89] (although it appears that the adamantane binds within the channel lumen [226]). Hanatoxin, an amphipathic allosteric inhibitor of voltage-gated K^+ channels also binds to an external site [227, 228]. Many of the inhibitors of the n-acetyl choline receptors described in section 1.7.3 also appear to bind to the outside of the channel. The composition and dynamics of the immediate lipid environment of nAChR receptors appears to be important for the correct functioning of the channel and the addition of a drug molecule with the ability to perturb that environment affects the channel gating [119, 131].

There are implications for drug binding to the outside of the channel on the mechanisms of channel opening and closing discussed in section 2.4.1. Unlike the nAChR receptor which has twenty TM α helices per channel, of which only five line the pore [117], current models of Vpu suggest that the pore-lining helices are also exposed to the bulk lipid of the membrane [70] and so a change in the environment

on the outside of the channel is likely to be rapidly communicated to the inside of the channel, however in the simulations reported in this chapter, the binding of HMA to Vpu₁₋₃₂ did not appear to have a significant effect on the helix secondary structure.

Several mechanisms of channel opening and closing have been proposed and discussed in section 2.4.1. The different mechanisms are likely to be affected by the binding of HMA to residue Trp23. The helix-rotation mechanism of channel opening (in which simultaneous rotation of the TM α helices occurs to move the bulky Trp23 residues into and out of the centre of the pore) is likely to be impaired, although the binding of the drug to Trp23 would appear to favour and prolong the open state of the channel (with Ser24 residues lining the lumen) (see figure 2.18). It is difficult to assess the affect of HMA binding on the helix straightening mechanism of channel opening, however the binding of HMA may alter the lateral pressure profile of the membrane, and thus affect the rate of closure. The models which envisage a more transient oligomeric bundle, which breaks apart to stop ion flow are likely to be more seriously affected, since the increased water penetration around the helices is likely to affect the kinetics and thermodynamics of bundle formation.

4.5 Conclusion

The interactions between HMA, DMA, amiloride and a model phospholipid bilayer were investigated by MD simulations. Two different parameter sets were used for HMA, the first in which all single bonds were allowed to rotate freely and a second in which the delocalised electron system was extended from the six-membered aromatic ring to the guanidium group, thus rendering the molecule rigid. The drug molecules were observed to partition into the membrane unaided and to adopt a stable position within the bilayer. In simulations which employed the HMA-flex parameter set, the molecule was observed to lie almost exclusively within the lipid headgroup region, orienting its long axis parallel to the plane of the membrane. In simulations which employed the HMA-stiff parameter set, the molecule remained in the extended conformation, with its long axis perpendicular to the plane of the bilayer.

Simulations of amiloride and DMA embedded in a POPC bilayer were also performed using a similar parameter set to that of HMA-stiff. A key feature of the interaction of all four drug models with the membrane is the strong electrostatic interaction between the positively charged guanidium group and the negatively charged lipid phosphate groups. Control MD simulations were performed with abietic acid. The predicted membrane locations of these drugs closely matched their experimentally determined positions [206].

The four drug models were all observed to partition into the membrane from the aqueous phase within 1 ns of the start of the simulations. A model for the insertion of an amphipathic molecule into a lipid bilayer has been developed.

The interaction between HMA and the Trp23 side chain of Vpu was investigated using the HMA-stiff parameter set, following earlier docking simulations which had used a HMA parameter set analogous to HMA-flex [76]. HMA is able to bind to

residue Trp23, which is predicted to lie on the outside of the Vpu bundle. Binding of HMA to Trp23 has a profound effect on the immediate lipid environment of the Vpu monomer, and exposes residue Val27, which is normally in intimate contact with the lipid acyl chains, to water. It is proposed that this effect is responsible for destabilising the Vpu oligomer and reducing the favourability of the open channel state. Amiloride, which does not inhibit Vpu, was shown in this research to be unable to bind to Trp23.

The simulations performed in this research suggest that HMA is able to partition into model phospholipid membranes from the aqueous phase and that the drug is able to profoundly change the local organisation of the surrounding lipids when it is bound to residue Trp23. These experiments do not exclude the possibility that HMA inhibits the ion channel activity of Vpu by occluding the pore, however they do suggest that the major part of the drug population is present in the lipid at any one time, and that if the occlusion model is correct, diffusion of drug molecules into the lumen of the channel is likely to occur from the relatively small pool of drug molecules in the aqueous phase. The next chapters of this thesis will attempt to further investigate the interactions between the amilorides and model phospholipid bilayers to experimentally verify the predictions made by MD simulation in this chapter.

Chapter 5

Spectroscopic studies of the location of HMA in model membranes

SUMMARY

The position of HMA within a model membrane was analysed using a combination of spectroscopic techniques. The ^1H MAS NOESY NMR spectra of HMA reconstituted into DMPC membranes, show prominent cross peaks between lipid and drug resonances and suggest that the hexamethylene ring of HMA is located close to the lipid acyl chains, while the guanidium group is positioned within the headgroup region. ^{31}P MAS NMR was used to show that in a mixed membrane of 2:1 DMPC:DMPG, the positively charged HMA associates preferentially with the negatively charged DMPG, restricting the motion of the lipid headgroups. Raman spectroscopy was used to demonstrate that HMA was able to lower the phase transition temperature of DMPC vesicles. These experimental observations confirm that HMA partitions into bilayers, as proposed in the previous chapter.

5.1 Introduction

5.1.1 The Nuclear Overhauser Effect (NOE)

The Nuclear Overhauser Effect (NOE) is a relaxation phenomenon which is widely used in solution state NMR to provide structural information for organic molecules [229]. The effect is observed when the intensity of the resonance of one nucleus

changes in response to the perturbation of a second resonance. The effect is dependent on the transfer of magnetisation through dipolar coupling between nuclei. The cross-relaxation is distance dependent and the magnitude of the effect is inversely proportional to the sixth power of the distance between the two nuclei. NOEs are typically only observable between nuclei which are less than 5 Å apart [230].

5.1.1.1 A 1D NOE experiment

The energy level diagram for a two nuclei I and S is shown in figure 5.1A. The 1D NMR spectrum of the system consists of two lines, one arising from each nucleus. At equilibrium, the lowest energy state will be the most highly populated and if the system is perturbed, it will return to its equilibrium position via any pathway, a zero-quantum jump (W0), single-quantum jump (W1) or a double quantum jump (W2). W0 and W2 jumps (which are not normally detectable) may occur during the process of relaxation.

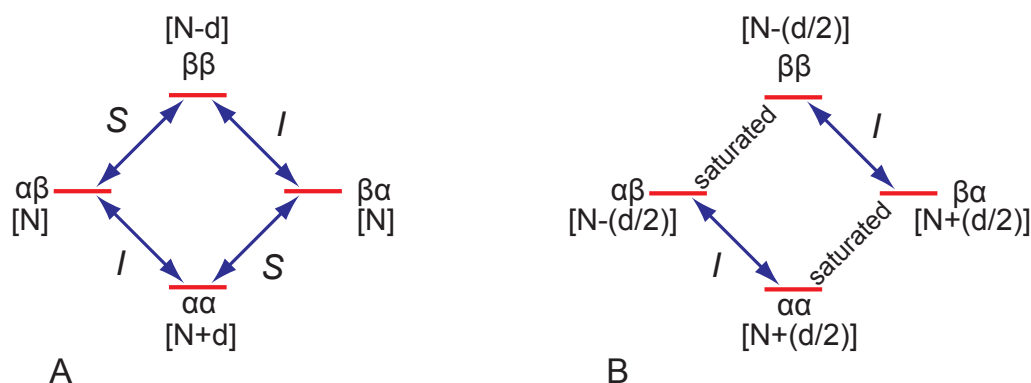


FIGURE 5.1: Energy level diagram for a two spin system: at equilibrium (A); after saturation of S transition (B) The populations of each state are given in square brackets. Figure reproduced from [230].

If the system is perturbed by irradiating the sample at the frequency of the S nucleus, the s transition will become saturated and the populations of nuclei in the upper and lower energy states will be equalised (figure 5.1B). The intensity of

the signal from nucleus I will be unaffected unless the nuclei are sufficiently close that relaxation can take place via the W_0 or W_2 pathways. If relaxation occurs fastest via the W_0 pathway, then the population of the highest energy level will increase and that of the lowest energy level will decrease, resulting in the decrease in intensity of the I resonance (a negative NOE) (figure 5.2A). If relaxation occurs fastest via the W_2 pathway, then the population of the highest energy level will decrease and that of the lowest energy level will increase, resulting in the increase in intensity of the I resonance (a positive NOE) (figure 5.2B) [230].

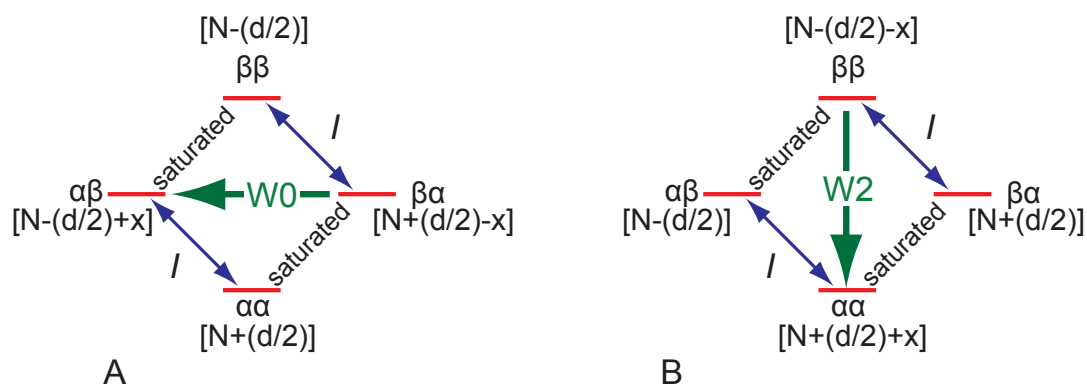


FIGURE 5.2: *Energy level diagram for a two spin system after the saturation of S transition. Relaxation may occur via the W_0 (A) or W_2 (B) pathways. The populations of each state are given in square brackets. Figure reproduced from [230].*

5.1.2 Nuclear Overhauser Effect Spectroscopy (NOESY)

The two dimensional NOESY experiment, which exploits the NOE phenomenon was first performed by Ernst and coworkers in 1980 [231].

5.1.2.1 Pulse sequence

The NOESY pulse sequence consists of three 90° pulses followed by the collection of a free induction decay signal (FID). Such experiments are routinely performed

as either homonuclear or heteronuclear experiments.

The first 90° pulse is responsible for converting the longitudinal z magnetisation into transverse magnetisation (figure 5.3). During the subsequent τ_1 period, the magnetisation precesses around the z axis, so that at the end of τ_1 , each nucleus has precessed through an angle of $\omega \cdot \tau_1$, where ω is the angular frequency of the nucleus compared to the reference frequency.

The second 90° pulse rotates the magnetisation around the pulse axis, so that an x pulse, produces magnetisation in the xz plane. The phases of the first two pulses are cycled in such a way that any residual transverse magnetisation remaining after the second pulse is cancelled (see section 5.1.2.3). The only magnetisation which is added constructively is that which is parallel to the z axis after the second pulse. This magnetisation has a magnitude $-\cos(\omega \cdot \tau_1)$. The first two pulses have therefore achieved a *frequency labelling* in which the magnetisation vectors of each nuclear spin, have an intensity dependent on both the length of τ_1 and the angular frequency ω .

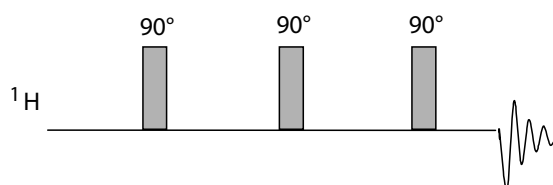


FIGURE 5.3: *Pulse sequence for homonuclear ^1H NOESY Nuclear Magnetic Resonance.* The sequence consists of three 90° pulses followed by the collection of an FID.

5.1.2.2 NOE development during (τ_m)

The mixing time (τ_m) is the period between the second and third 90° pulses in which the NOE develops. During this time, the nonequilibrium z magnetisation

which was generated by the first two pulses, produces a cross relaxation to other neighbouring nuclei. The remaining z magnetisation is converted into transverse magnetisation by the final 90° pulse, which is immediately followed by the collection of the free induction decay (FID).

Consider a nucleus I in the presence of another nucleus S , which relaxes at a rate:

$$\frac{dI_z}{dt} = -R_1(I_z - I_z^0) - \sum_S (S_z - S_z^0) \sigma_{IS} \quad (5.1)$$

where R_1 is the longitudinal relaxation rate for spin I ; I_z^0 is the equilibrium value of I_z and S_z^0 is the equilibrium value of S_z . σ_{IS} is the cross-relaxation rate between I and S given by:

$$\sigma_{IS} = \frac{1}{10} K^2 \left[\frac{6 \tau_c}{1 + (\omega_I + \omega_S)^2 (\tau_c)^2} - \frac{\tau_c}{1 + (\omega_I - \omega_S)^2 (\tau_c)^2} \right] \quad (5.2)$$

where

$$K = \frac{\mu_0}{4\pi} \hbar \gamma_I \gamma_S (r_{IS})^{-3} \quad (5.3)$$

and ω_I and ω_S are the Larmor frequencies for I and S respectively as measured in radians s^{-1} , which is proportional to $2\pi\nu$, where ν is the spectrometer frequency measured in Hz. τ_c is the correlation time for the molecule (a measure of the amount of time taken for it to reorient) given by

$$\tau_c = \frac{\frac{4}{3} \pi r^3 \eta}{kT} \quad (5.4)$$

where r is the radius of the particle and η is the viscosity of the surrounding fluid [232].

5.1.2.3 Phase Cycling

The phases of the three 180° pulses and the receiver phase must be cycled to allow the NOE relaxation signals to add and spurious signals to cancel out. The CYCLOPS phase cycling is used to eliminate quadrature images, which are the reflections of large signals about the central axis of the spectrum. The CYCLOPS scheme requires the pulse and receiver phases to be simultaneously cycled through the sequence $x, y, -x, -y$ [233]. In the NOESY sequence however, it is necessary only to cycle the final pulse and the receiver.

The CYCLOPS phase cycling is combined with the $x, -x$ cycle for the first pulse to suppress axial peaks. The addition of these phases produces an eight stage phase cycle scheme. A second set of eight stages must be added, which differ from the first set only in that the phase of the second pulse is increased by 90° to select for the $\Delta p = 1$ and $\Delta p = -1$ coherence pathways, thereby allowing NOE signals to add and other corelaxation signals to cancel [234]. Table 5.1 shows the full 16 stage CYCLOPS phase cycling used in this study.

5.1.2.4 Time-Proportional Phase Incrementation (TPPI)

In most NMR experiments, the carrier frequency of the RF pulse is usually placed in the centre of the spectrum. A given resonance may therefore have a positive offset from the carrier frequency or a negative offset. In a 1D spectrum, both the x and y components of the magnetisation and the complex time-domain function are constructed in the form:

$$e^{(i\Omega t)}e^{(-Rt)} \quad (5.5)$$

the Fourier transformation of which gives, in the real part of the spectrum, an absorption mode peak at frequency Ω . In the spectrum generated by the Fourier

Step	ϕ_1	ϕ_2	ϕ_3	ϕ_R
1	0°	0°	0°	0°
2	0°	0°	180°	180°
3	0°	0°	90°	90°
4	0°	0°	270°	270°
5	180°	0°	0°	0°
6	180°	0°	180°	180°
7	180°	0°	90°	90°
8	180°	0°	270°	270°
9	0°	90°	0°	0°
10	0°	90°	180°	180°
11	0°	90°	90°	90°
12	0°	90°	270°	270°
13	180°	90°	0°	0°
14	180°	90°	180°	180°
15	180°	90°	90°	90°
16	180°	90°	270°	270°

TABLE 5.1: Sixteen scan NOESY phase cycling (reproduced from [234]). Stages 1 to 4 show the cycling of the phase of the third pulse (ϕ_3) and the phase of the receiver (ϕ_R). Stages 5 to 8 are a repeat of the first four stages, except that the phase of the first pulse (ϕ_1) is increased by 180°. Stages 9 to 16 are a repeat of the first eight, except that the phase of the second pulse (ϕ_2) is increased to 90°.

transformation of the complex time domain function, the positive and negative frequencies are well separated.

In a 2D NMR spectrum however, an additional method is required to distinguish positive from negative offsets. If the two cannot be distinguished, then the spectrum will be reflected about its centre. These reflections can be removed by a process of quadrature detection which simultaneously collects data from both x and y channels. The TPPI method eliminates the quadrature reflections, by making it appear as if the RF carrier frequency lies at one side of the spectrum [235]. In a NOESY experiment, every time t_1 is increased, the phase of the first pulse is increased by 90° (the phases of the other pulses are unaffected). This means that the phase cycle used for the first t_1 condition is not repeated until the fifth t_1 condition. In this study TPPI was used in combination with the CYCLOPS phase cycling for all spectra acquired at a ^1H frequency of 500 MHz.

5.1.3 Raman Spectroscopy

Infra-red (IR) radiation may interact with organic molecules in a number of different ways (see figure 5.4). Incident photons may be absorbed (resulting in the promotion of the molecule to a higher vibrational energy level), or scattered (resulting in the promotion of the molecule to a virtual energy state from which it immediately relaxes by emitting a second photon). Of the light which is scattered, most is scattered elastically, meaning that the emitted photon has the same frequency as that of the absorbed photon. Approximately one photon in 10^7 is scattered inelastically, giving rise to the Raman Effect, in which the emitted photon may have either a lower or higher energy than the incident photon [236].

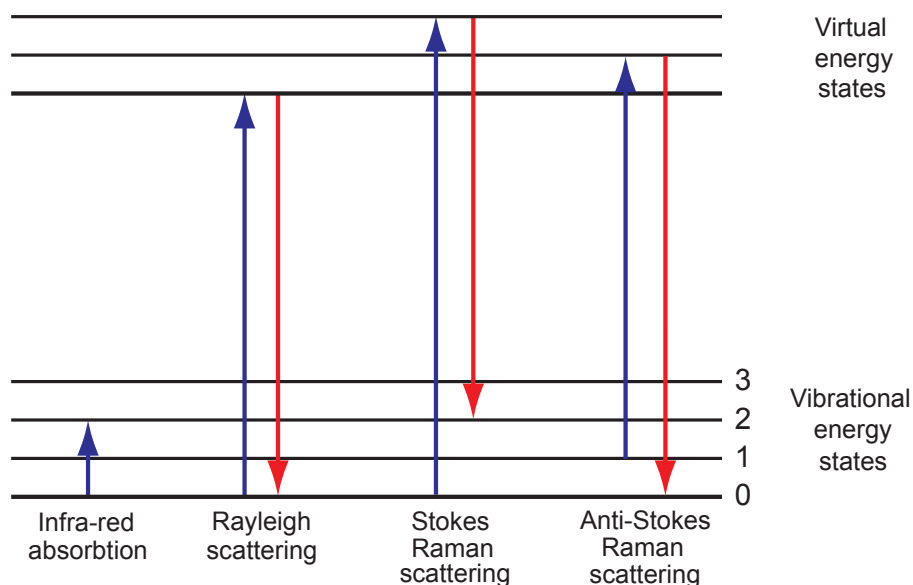


FIGURE 5.4: *Energy level diagram showing to compare the transitions involved in IR absorption and Rayleigh and Raman scattering.*

For a transition between vibrational or rotational energy levels to give rise to inelastic scattering of IR light, there must be a change in the polarisability of the molecule or group concerned. When the electromagnetic field of the incident radiation E_i interacts with a molecule or group, it induces a dipole p :

$$\Delta p = \alpha E_i \quad (5.6)$$

where α is the polarisability of the molecule or group. The strength of the electrical field of the radiation oscillates in a time-dependent manner:

$$E_i = E_0 \cos(2\pi\nu_i t) \quad (5.7)$$

where E_0 is the maximum electrical field strength of the incident radiation of frequency ν_i . For a vibrating molecule, the polarisability (α) is dependent on the vibrational frequency of the molecule ν_{vib} :

$$\alpha = \alpha_0 + \alpha_{vib} \cos(2\pi\nu_{vib} t) \quad (5.8)$$

Multiplication of E_i and α gives rise to the cross product:

$$E_i \alpha = \left(\frac{\alpha_{vib} E_0}{2} \right) (\cos 2\pi t(\nu_i + \nu_{vib}) + \cos 2\pi t(\nu_i - \nu_{vib})) \quad (5.9)$$

which gives rise to the anti-Stokes Raman scattering (when the energy of the emitted photon is greater than that of the incoming photon) or Stokes Raman scattering (when the energy of the emitted photon is less than that of the incoming photon) (see also figure 5.4) [236, 237].

Raman spectroscopy has been used to study a wide range of biological systems, usually in combination IR spectroscopy. The technique is able to provide secondary structural information for peptides and proteins, since the shifts of the amide I and III bands are sensitive to the hydrogen bonding pattern [238], and it can also be used to determine whether specific amino acids are accessible to water [239].

It has also been used to determine the conformational state of nucleic acids in different solvent environments [240].

Raman spectroscopy has also been used to study thermotropic lipid phase changes which may occur when proteins and drug molecules are inserted into phospholipid systems. Phospholipid bilayers may exist in various distinct phases: a more ordered gel phase and the liquid crystal phase, in which considerable lateral diffusion is possible.

The temperature at which the transition between the two phases occurs is dependent on the length of the phospholipid acyl chains and the character of the headgroups [241]. As the lipid disorder increases the percentage of the C-C bonds of the lipid acyl chains in the *gauche* configuration increases (see figure 5.19). Since the change in polarisability which occurs when a C-C bond in the *gauche* conformation is stretched, is different to that of the *anti* conformation, this change can be detected by Raman spectroscopy [242].

Previous studies have used infra-red spectroscopy to study the mobility of the lipid in the presence and absence of the anaesthetics halothane and chloroform [243]. These studies have been hindered by the requirement for large, dilute samples, leading to long acquisition times and the potential for the sample conditions to change. The integration of Raman spectroscopy with an optical trap allows the sample volume to be restricted to the volume of a single 1 μm diameter DMPC vesicle, allowing the sample temperature to be more accurately controlled and acquisition times to be reduced relative to a larger dispersed sample. The two techniques have been used in this study to follow changes in lipid phase which occur when amiloride and HMA are added to DMPC liposomes, and to determine whether perturbation of the lipid bilayer by the drugs might result in inhibition of Vpu (see Chapter 2).

5.1.4 Aims of this study

The aim of this chapter is to test the predictions made by MD simulations (in Chapter 4), which suggest that amiloride and its derivatives HMA and DMA are able to insert into a phospholipid bilayer. ^1H MAS NOESY NMR experiments give the opportunity to determine the location of the drug molecules within the membrane and cross-peaks would be expected to be observed between lipid and drug resonances if direct interactions occur. 1D ^{31}P MAS NMR will be used to test the suggestion also made in Chapter 4 that the positively charged guanidium group of the drug forms a strong electrostatic interaction with the negatively charged phosphate group of the lipid. A perturbation in the chemical shift of the lipid phosphate group is expected to be observed. This chapter will also attempt to characterise the effect of adding the amiloride derivative to DMPC vesicles on the lipid dynamics by Raman spectroscopy using vesicles trapped in optical tweezers, to demonstrate a possible direct drug-lipid interaction.

5.2 Materials and Methods

5.2.1 Determination of the partition coefficient of HMA

The octanol-water partition coefficient of the charged and uncharged forms of HMA was determined by isocratic high performance liquid chromatography (HPLC) using the method described in [244]. Anisole, toluene, bromobenzene, benzyl bromide, benzyl chloride and benzene were used as standards.

5.2.2 NOESY spectra

Sample preparation Dimyristoylphosphatidylcholine (DMPC), HMA, DMA, amiloride and deuterated solvents were purchased from Sigma. Chain-deuterated dimyristoylphosphatidylcholine (DMPC-d54) was purchased from Avanti Polar Lipids. All chemicals were used without further purification.

DMPC and DMPC-d54 were solubilised in ethanol, to which the HMA was added. The preparation was dried under N₂ gas and the solvent was removed under vacuum for 16 hours. Lipid and drug mixture (15 mg) was rehydrated with 40 μ l D₂O, and sonicated (4 °C;15 minutes). Since amiloride, HMA and DMA are light sensitive, vacuum drying and sonication were performed in darkness so far as practicable.

¹H MAS NOESY measurements A solution state NMR spectrum of HMA solubilised in a 1:1 mixture of MeOD/CDCl₃ was collected on a 500 MHz narrow bore Bruker spectrometer to assist the assignment of drug peaks in the 2D spectra.

Solid state NMR measurements were performed on a Varian Infinityplus 500 MHz spectrometer or Bruker 600 MHz spectrometer. Both were equipped with 4 mm MAS HXY probes. The experiments were performed at 300 K to ensure that the

sample was above the phase transition temperature of DMPC. ^1H experiments were performed at resonance frequencies of 500.11245 MHz or 600.1321 MHz with a spectral width of 8 kHz.

2D NOESY experiments performed at 500 MHz were acquired with TPPI phase cycling (see table 5.1) with 90° pulses of $3 \mu\text{s}$ [245]. 512 complex data points were collected in the indirect dimension and a 4 s pulse delay was used. Since no standard Chemagnetics NOESY pulse sequence was available, the Bruker NOESY pulse sequence was adapted and TPPI phase cycling added for use on Varian Infinityplus spectrometers. A sinebell-squared function was applied to the data prior to processing. All ^1H were referenced with respect to the terminal methyl group of the lipid chains at 0.89 ppm of DMPC in the absence of drug molecules.

Data processing Data were processed using NMRpipe and Sparky [246].

5.2.3 MAS ^{31}P measurements

Sample preparation DMPC and dimyristoylphosphatidylglycerol (DMPG) were purchased from Sigma and used without further purification (see figure 5.5 for structures). DMPC and DMPG in a molar ratio of 2:1 were solubilised in a 2:1 v/v mixture of methanol and chloroform, to which the HMA was added, dissolved in the same solvent mixture. The preparation was dried under N_2 gas and the solvent was removed under vacuum for 16 hours. The lipid-drug mixture (15 mg) was rehydrated by adding $40 \mu\text{l}$ buffer (10 nM HEPES, 10 mM NaCl, 1 mM EDTA in D_2O at pH 7.2) and sonicating at 4°C for 15 minutes. The samples were then loaded into a 4 mm zirconium oxide rotor with Kel-F spacer inserts for MAS NMR measurements.

^{31}P spectra were acquired at 202 MHz using a Varian 500 MHz InfinityPlus spectrometer equipped with a 4 mm MAS HX probe at 300 K. A single $4 \mu\text{s}$ 90° pulse

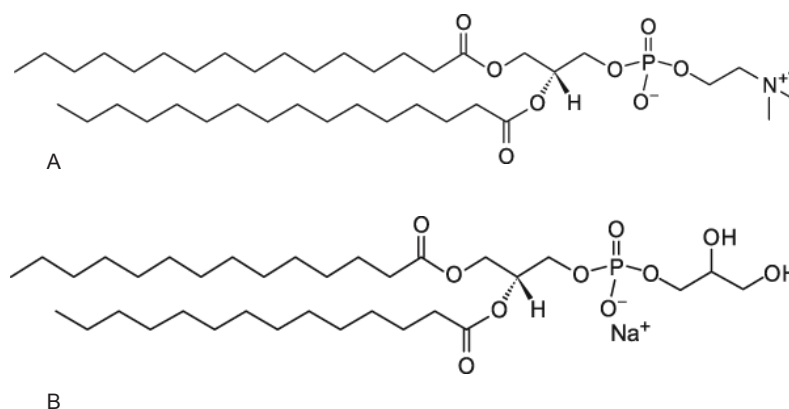


FIGURE 5.5: Structural formulae of A: DMPC and B: DMPG. DMPG has a net negative charge and is most commonly supplied as a sodium salt. DMPC has no net charge.

was used to directly excite the ^{31}P nuclei, and broad-band proton decoupling of 20 kHz was applied during the acquisition period (see figure 5.6). Samples were rotated at 8 kHz MAS at 30 °C. 5120 scans were collected and the pulse delay was 4 s. Spectra were referenced to adamantane and $\text{NH}_4\text{H}_2\text{PO}_4$.

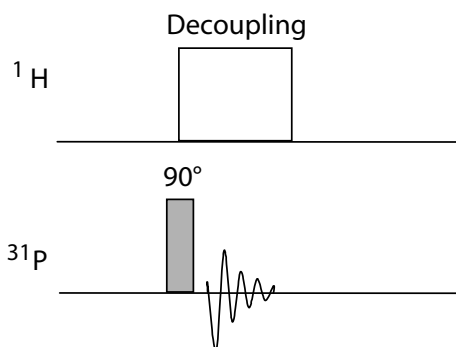


FIGURE 5.6: Pulse sequence for ^{31}P Nuclear Magnetic Resonance. TPPM ^1H decoupling was applied on the ^1H channel during the acquisition of the FID.

5.2.4 Raman spectroscopy

Sample preparation Solutions of DMPC and HMA or amiloride in a 1:1 mixture of chloroform and methanol were dried under vacuum for 16 hours to form a thin film, which was rehydrated with 1 ml MilliQ water to a concentration of 10 mg/ml and vortexed for five minutes. The suspension was subjected to five freeze-thaw cycles, further diluted to a lipid concentration of 1 mg/ml, then extruded through a 1 μm filter ten times to form vesicles.

Equipment and instrumentation A continuous-wave Argon ion laser of wavelength 514.5 nm and maximum power 2.0 W, (Innova 90-5-UV, Coherent). The beam was passed through two sets of lenses and reflected from a 1:2 beam-splitter into the microscope. Light was directed through the objective lens (x63 NA 1.2, Leica Microsystems) by a dichroic mirror and the optical trap was formed in the sample cell. (See also Appendix B.5.1.)

Raman light scattered back from the focal point was focussed by the objective lens and passed back along the same pathway to the beam splitter. A holographic notch filter (HNF-514, Kaiser Optical Systems) placed after the beam-splitter allowing only Raman light shifted above 514.5 nm to enter the spectrometer (SpectraPro-500 Acton Research Company) and detector (LN/CCD-1024, Princeton Instruments). (See Appendix B.5.1 for a diagram of the experimental apparatus.)

5.3 Results and discussion

5.3.1 Octanol-water partition coefficient

The partition coefficient P is a measure of the hydrophobicity of a molecule (see section 1.7.2) [111]. The octanol-water partition coefficient of an organic compound may be determined by isocratic HPLC, since the retention time of the molecule on the column can be used as a measure of hydrophobicity [244]. The retention times of seven standard compounds were determined, the partition coefficients of which had been previously published. The retention times of amiloride, DMA and HMA at physiological pH were then determined and converted to the partition coefficient using the standard curve.

5.3.1.1 Results

Table 5.2 shows the partition coefficients determined for HMA, DMA and amiloride at physiological pH. The results indicate that for a 1:1 v/v mixture of phospholipids and water, for every molecule expected to reside in the aqueous phase, 400 are expected to reside within the membrane.

TABLE 5.2: Partition coefficients for HMA, DMA and amiloride determined by isocratic HPLC, using the methodology of Griffin *et al.* [244].

Molecule	$\log(P)$
HMA	2.63
DMA	1.28
Amiloride	0.66

These results are consistent with the results of the MD simulations performed in Chapter 4, which suggest that HMA, DMA and amiloride are able to partition into phospholipid bilayers from the aqueous phase.

5.3.2 ^1H MAS NOESY

5.3.2.1 Assignment of HMA ^1H chemical shifts

A 1D solution ^1H spectrum of HMA solubilised in a 1:1 mixture of CDCl_3 and MeOD was acquired to facilitate the assignment of peaks in the 2D MAS NOESY (see figures 5.7 and 5.8). The peaks arising from the CH_2 protons on the hexamethylene ring of HMA fall as expected between 1.5 ppm and 1.8 ppm, in the same region as those of the DMPC acyl chain CH_2 groups. The chemical shifts of the guanidinium -NH groups differ considerably from the values for the comparable groups in the amino acid arginine [247]. Indeed, it might be expected that the NH and NH_2 protons would not be visible in the spectrum, since they could potentially exchange with deuterium atoms present in the solvent. Since H/D exchange does not appear to occur with the solvent, it is likely that the delocalised electron system extends from the six-membered ring to the guanidinium headgroup and that the nature of this aromatic system is responsible for the downfield position of the chemical shifts of the -NH and NH_2 resonances. The spectrum includes two additional peaks at 2.14 ppm and 4.82 ppm, which do not arise from HMA, but correspond to the expected values for chloroform and methanol protons respectively.

5.3.2.2 Assignment of DMPC ^1H chemical shifts

The chemical shifts of resonances from DMPC have been previously determined by a number of authors and are shown in figure 5.8 [225]. The chemical shifts of the HMA protons in a solid lipid sample are expected to be similar to those of the solution state values, however some variation is expected to account for the differences in the chemical environment of the groups.

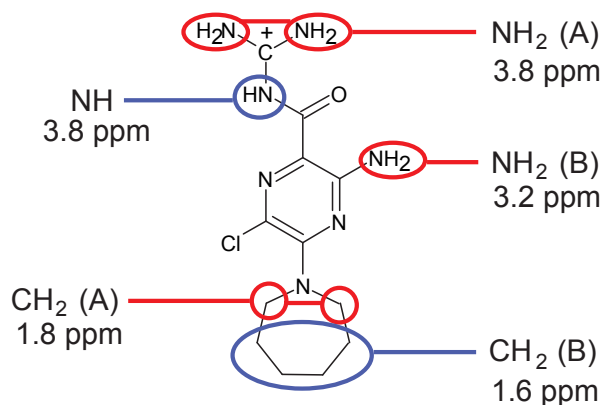


FIGURE 5.7: Key to assignment of ^1H resonances arising from HMA see also figure 5.8.

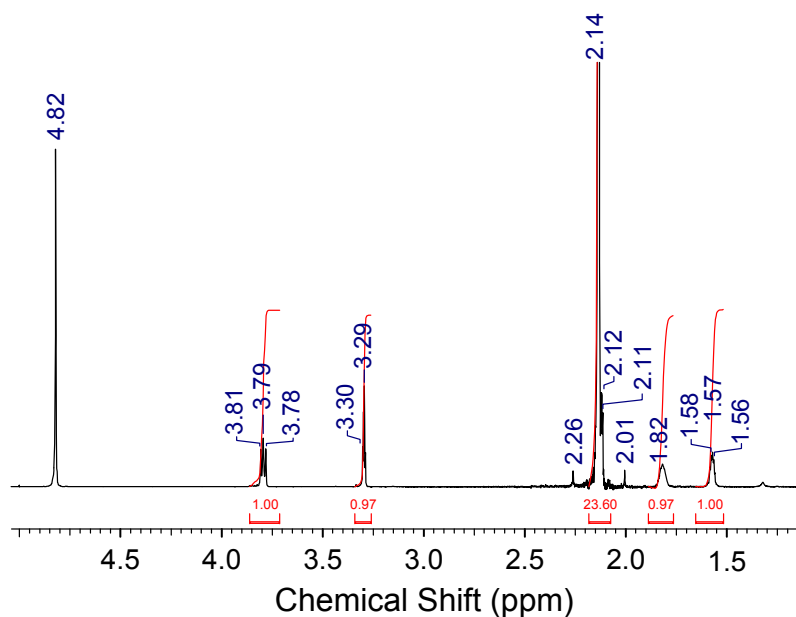


FIGURE 5.8: $1\text{D } ^1\text{H}$ solution spectrum of HMA in $\text{CDCl}_3:\text{MeOD } 1:1$ taken on Bruker 600 MHz narrow bore solution state NMR magnet by Dr Richard Ferguson (Oxford). Integrated peak areas shown in red and peak chemical shifts given in blue. For assignment of peaks see figure 5.7. Resonances at 2.14 ppm and 4.82 ppm correspond to the chloroform and methanol solvent peaks respectively.

5.3.2.3 2D MAS NOESY spectrum of DMPC:HMA 7:1

Cross-peaks between lipid and drug resonances are observed, indicating that an interaction occurs between the two species. Figure 5.9 shows the 2D MAS NOESY spectrum of a 7:1 ratio of DMPC to HMA in D₂O acquired at 600 MHz with a mixing time of 200 ps. Peaks arising from both HMA and DMPC are visible along the diagonal, and there appears to be only a limited difference between the HMA ¹H chemical shifts in the MeOD/CDCl₃ solution spectrum and the solid state sample. One additional intense peak at 4.62 ppm is visible, which corresponds to the expected chemical shift of H₂O protons. Although the lipid and drug mixture was rehydrated with D₂O, a limited amount of H₂O and HDO is expected to be present. The presence of the drug in the lipid induces the splitting of the C2 peaks from a single sharp resonance at 2.4 ppm in DMPC only spectra, to produce three separate peaks at 2.23 ppm, 2.60 ppm and 2.8 ppm. A similar C2 peak splitting, induced by ring currents in the extended aromatic system is observed when the amino acid tryptophan is added to DMPC membranes [248].

Cross-relaxation between two proton spin systems, corresponding to the amount of magnetisation transfer between the two, gives rise to off-diagonal cross peaks in the 2D spectrum. Intense cross peaks are observed between the lipid acyl chain CH₂ peak at 1.38 ppm and most of the other lipid ¹H peaks, including the choline γ CH₃ groups at 3.22 ppm. Cross peaks between lipid and drug resonances are also observed and will be discussed in detail in the next sections. The water resonance at 4.62 ppm does not form any cross peaks.

CH₃ and CH₂ spectral region Figure 5.11 shows the 0.5 ppm to 2.0 ppm region of the same spectrum. The resonances from the CH₂ and CH₃ groups of the lipid acyl chains fall in this region in addition to the CH₂ groups from the hexamethylene ring of HMA. The spectrum clearly shows cross peaks between

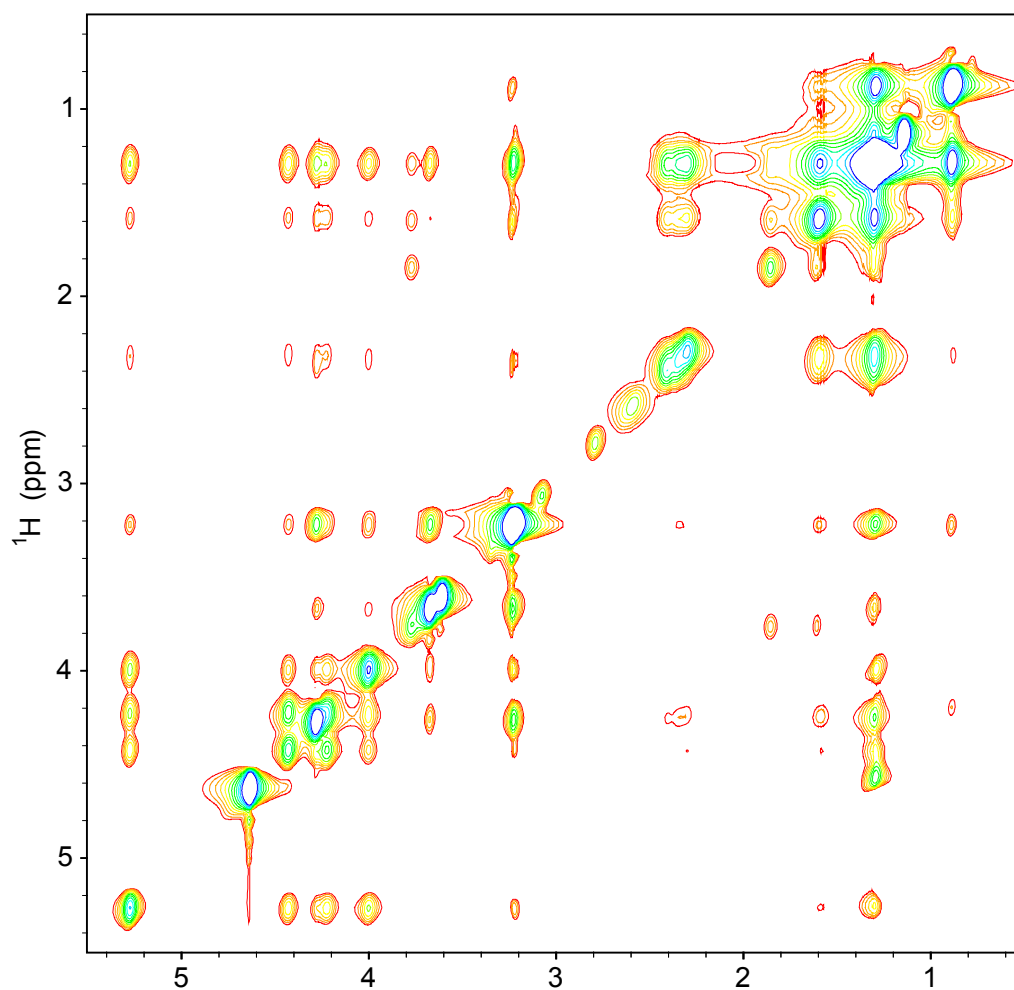


FIGURE 5.9: ^1H NOESY spectrum of HMA in DMPC 1:7 taken on Bruker 600 MHz wide bore magnet with a mixing time of 200 ms. Figure prepared using Sparky [246].

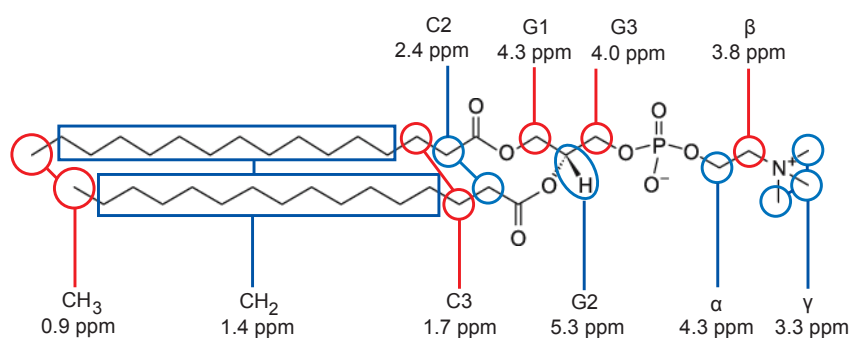


FIGURE 5.10: Key to assignment of ^1H resonances arising from DMPC adapted from [225].

the lipid and the drug resonances. The HMA CH₂ (A) protons (positioned below the aromatic ring of the drug) give a particularly well resolved diagonal signal at 0.82 ppm which forms cross peaks to the CH₂ and C3 peaks of the lipid. The HMA CH₂ (B) proton peak falls slightly downfield of the lipid CH₂ peak and because of this it is difficult to determine with certainty whether the resonance gives rise to drug-lipid cross peaks. Some τ_1 noise is present between 1.55 ppm and 1.60 ppm, although this does not affect the interpretation of the spectrum. The CH₂ (A) proton peaks also forms a cross peaks with the HMA -NH and -NH₂ resonances (see figure 5.9) .

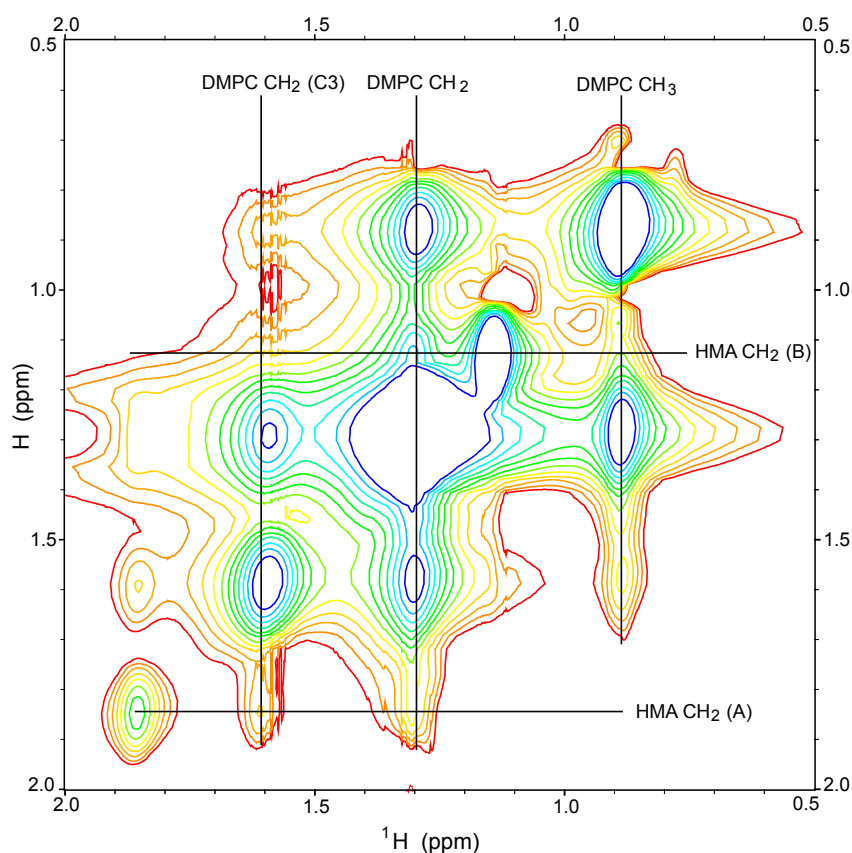


FIGURE 5.11: CH₂ and CH₃ region of NOESY spectrum from figure 5.9. Contours cut at seven times noise level. Figure prepared using Sparky [246].

Lipid headgroup spectral region Figure 5.12 shows the 0.5 ppm to 2.0 ppm region of the same spectrum. The HMA ^1H resonances which arise in this region are from the NH and $-\text{NH}_2$ groups and are expected to be less intense than the CH_2 and CH_3 peaks (find ref). Cross peaks between the lipid and drug resonances are again detected in this region, although the HMA resonances lie close to those of the lipid peaks. The DMPC β choline CH_2 resonance at 3.7 ppm has a clear cross peak with the HMA NH_2 (A) peak at 3.78 ppm. The HMA NH_2 (A) resonance also has cross peaks with the HMA CH_2 (A) resonance and the DMPC C3 resonance (see figure 5.9).

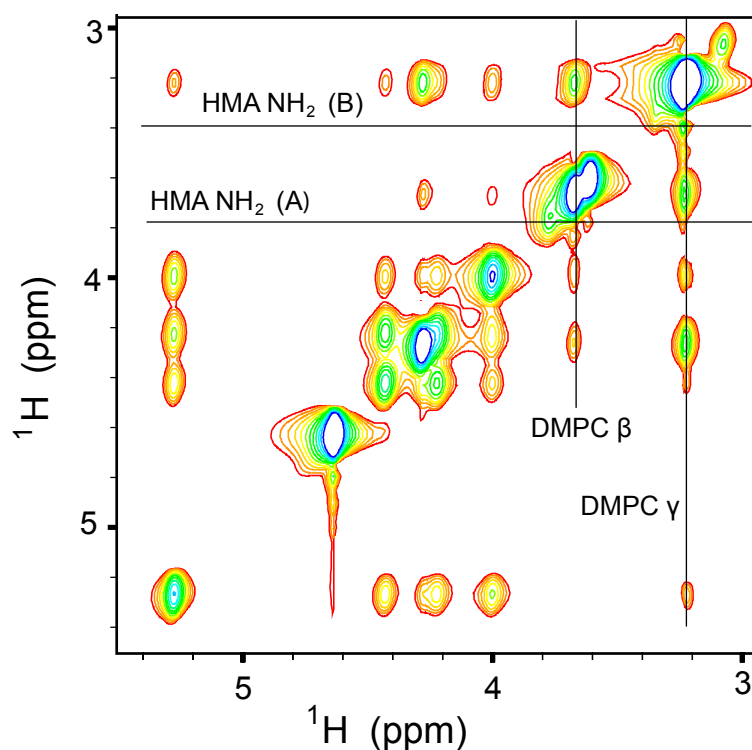


FIGURE 5.12: lipid headgroup region of NOESY spectrum from figure 5.9 Contours cut at seven times noise level. Figure prepared using Sparky [246].

The position of the HMA NH_2 (B) resonance is uncertain. From the solution state spectrum, the peak is expected to lie at 3.2 ppm close to the DMPC choline γ peak at 3.3 ppm. A peak is visible at this point in the spectrum, however the same

peak is also visible with approximately the same intensity in a pure DMPC solid state spectrum (see figure 5.14). Further comparison with a pure DMPC spectrum suggests that the HMA NH₂ (B) resonance may be visible as a side peak of the choline γ peak at 3.4 ppm. The difference in chemical shift between the solution state and solid state spectra, may reflect the proximity of the group to the charge cloud of the lipid phosphate groups in the solid state sample. The peak at 3.3 ppm is unlikely to be caused by ring current splitting of the DMPC γ CH₃ choline peak, because it is able to form a cross peak with the neighbouring resonance [248].

Given that the guanidium group of HMA was predicted by the MD simulations performed in the previous chapter to form a strong electrostatic interaction with the lipid phosphate group, it is surprising that no cross peaks are observed between the HMA peaks and the DMPC G1, G2 and G3 resonances, since the lipid phosphate group is covalently bound to the G3 carbon atom of the DMPC.

5.3.3 Comparison of MAS NOESY spectra acquired at 600 MHz and 500 MHz

Figure 5.13 shows two NOESY spectra of DMPC:HMA 7:1 acquired at 600 MHz and 500 MHz. (All other experimental parameters were the same.) As expected, the resolution of the 500 MHz spectrum is worse than that of the 600 MHz spectrum and the line widths of CH₂ proton chemical shifts increase from 0.5 ppm in the 600 MHz spectrum to 0.9 ppm in the 500 MHz spectrum. The most obvious effect of the poorer resolution of the 500 MHz spectrum, is the disappearance of the CH₂ (B) peak, which has possibly become buried under the lipid CH₂ peak. The 500 MHz spectrum appears however, to have less T₁ noise.

Although the crosspeak intensity between lipid and drug resonances is generally lower in the 500 MHz spectrum, there are some features which are not visible in the 600 MHz spectrum. A cross peak is visible between the lipid CH₃ group and

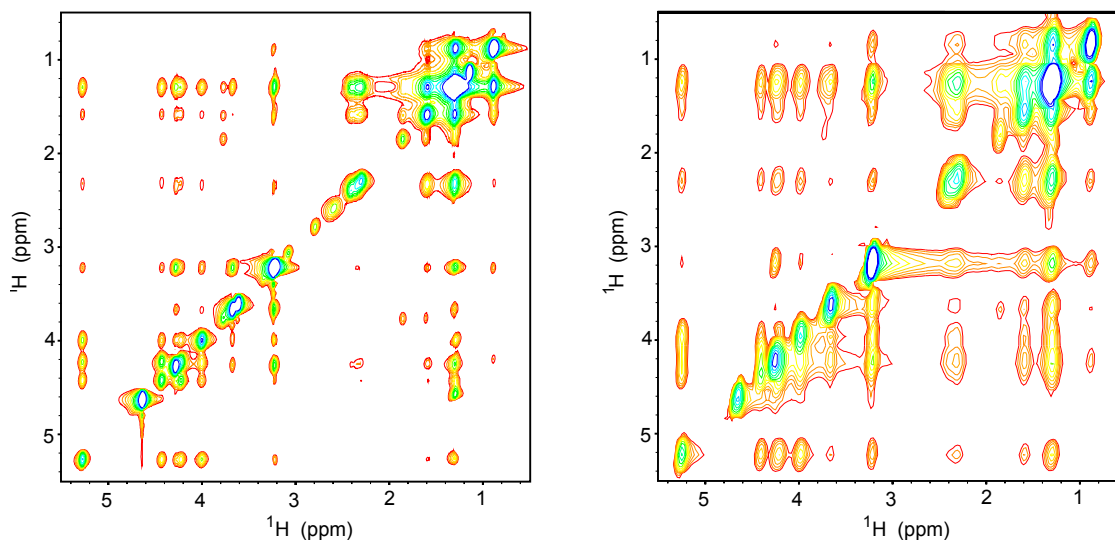


FIGURE 5.13: Comparison of NOESY spectra of HMA:DMPC 1:7 solubilised in D_2O acquired at 600 MHz (left) and 500 MHz (right) Contours cut at seven times noise level. Figure prepared using Sparky [246].

HMA CH_2 (A) groups, which probably does not represent a lower vertical height for the drug in the membrane, but instead means that under the conditions of the 500 MHz experiment, that lipids are able to extract themselves vertically from the membrane [249]. Additional cross peaks are also visible between the HMA CH_2 (A) resonance of the hexamethylene ring and the C2 resonance at 2.4 ppm, although the C2 diagonal peak itself does not show any evidence of ring current splitting. There also appears to be a very weak cross peak between the HMA CH_2 (A) and the γ choline CH_3 resonance at 3.2 ppm.

5.3.4 Comparison of DMPC only and DMPC:HMA 7:1 at 500 MHz

Figure 5.14 compares the ^1H MAS NOESY spectra of DMPC:HMA 7:1 and pure DMPC acquired at 500 MHz. The most apparent difference between the two spectra is the disappearance of the HMA CH_2 (A) peak at 1.82 ppm, confirming that this group must arise from the drug. The spectrum of the sample containing HMA, has more lipid-lipid cross peaks than the pure DMPC sample (the CH_3 resonance at 0.89 ppm and the G2 resonance at 5.3 ppm are good examples). In general, the pure DMPC spectrum has better resolution than the sample containing the drug, however the lipid peak positions in the two spectra appear to be very similar.

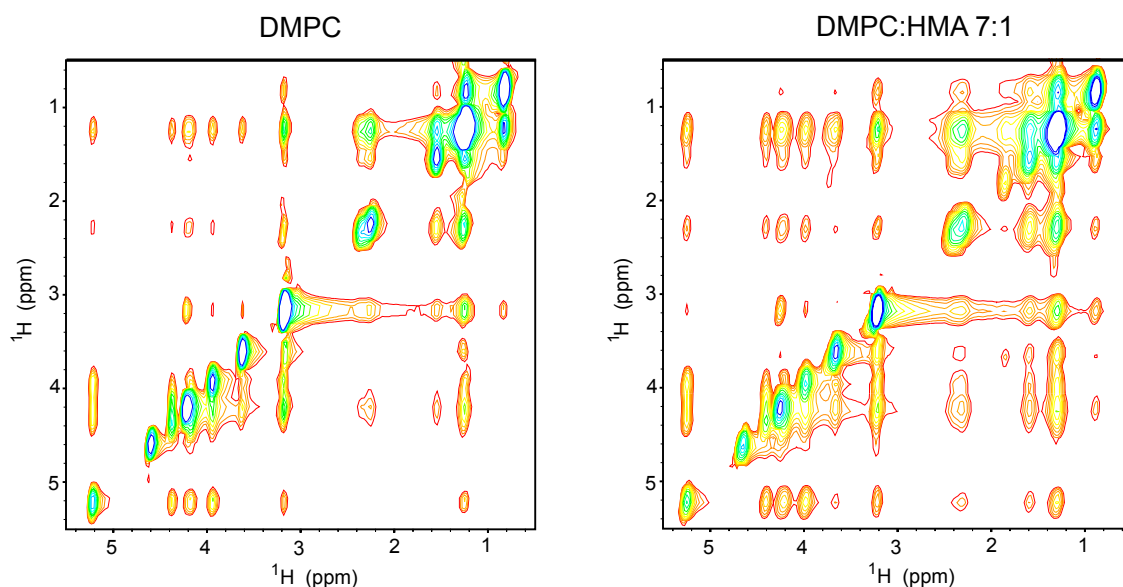


FIGURE 5.14: Comparison of NOESY spectra of HMA:DMPC 1:7 solubilised in D_2O acquired at 600 MHz (left) and 500 MHz (right) Contours cut at seven times noise level. Figure prepared using Sparky [246].

5.3.5 ^1H MAS NOESY spectra of DMA and amiloride in DMPC

Figure 5.15 shows the MAS NOESY spectra of DMA and amiloride in DMPC at a total lipid:drug ratio of 7:1. The DMA spectrum (figure 5.15) differs from the HMA spectrum in figure 5.13 in that the HMA CH_2 (A) peak at 1.75 ppm is missing, (a peak at this point is not expected since DMA lacks a hexamethylene CH_2 ring). An additional shoulder peak is visible at 1.12 ppm which is suggested to be the DMA CH_2 (B) peak, which has been shifted downfield from its position in the HMA spectrum due to the differences between the structures of the two drugs.

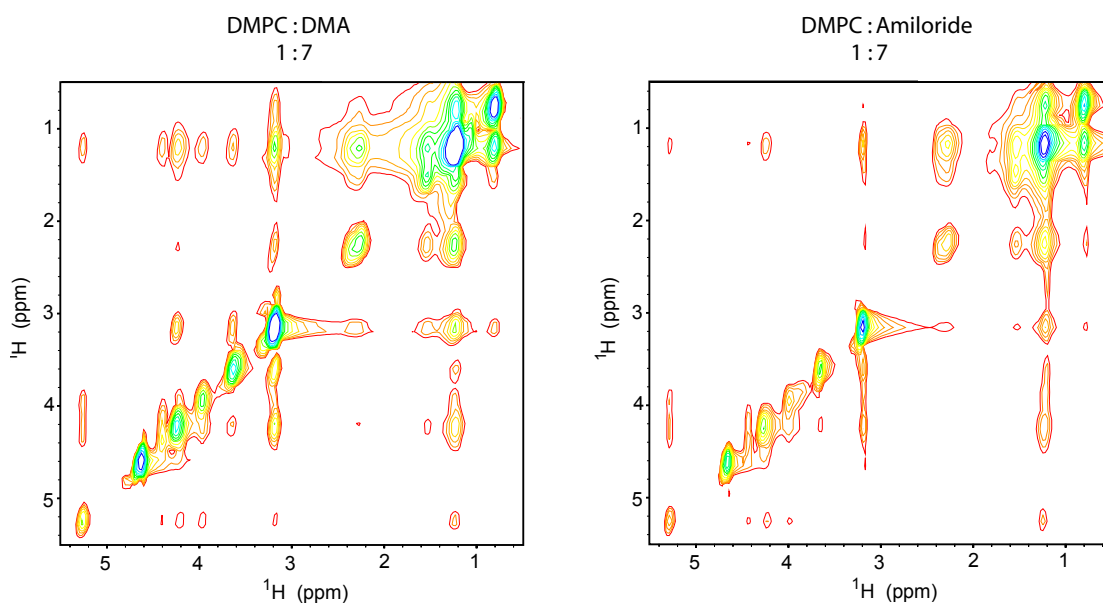


FIGURE 5.15: Comparison of spectra of DMA:DMPC 1:7 (left) and Amiloride:DMPC 1:7 (right) solubilised in D_2O acquired at 500 MHz. Contours were cut at seven times noise level and the figure prepared using Sparky [246].

Figure 5.15 also shows the ^1H MAS NOESY spectrum of amiloride in DMPC at a total lipid:drug molar ratio of 7:1. Both the HMA CH_2 (A) and (B) resonances are absent from the spectrum, since amiloride lacks both the methyl groups of

DMA and the hexamethylene ring of HMA. Since amiloride contains an additional aromatic -NH₂ group, which is not present in HMA and DMA, it is expected that the drug resonance at 3.4 ppm would be more intense than in either the DMPC and DMA or DMPC and HMA spectra. The overlap of this peak with the DMPC choline γ CH₃ groups at 3.3 ppm prevents a satisfactory comparison of the intensities from being made.

5.3.6 Substitution of DMPC by chain-deuterated DMPC

In order to determine the exact location of the HMA CH₂ (B) peak, which was absent from the 500 MHz spectrum in figure 5.13, 2D NOESY spectra were acquired in which a proportion of the lipids had been replaced by chain-deuterated DMPC. Since the fatty acid ¹H atoms are substituted with ²D, the lipid resonances in the 0.5 ppm to 2.0 ppm range are expected to be less intense relative to the HMA ¹H resonances. Figure 5.16 shows spectra of HMA:lipid molar ratio 1:7 in D₂O taken at 500 MHz. The fully chain-deuterated sample shows lipid ¹H resonances at 0.89 ppm, 1.27 ppm and 1.60 ppm, since the deuteration process is not 100% efficient. Cross peaks are formed between the HMA CH₂ (A) peak and the DMPC CH₂ C3 peak. The DMPC CH₂ peak at 1.27 ppm appears to be split in two, and it is proposed that the feature at 1.8 ppm corresponds to the HMA CH₂ (B) peak.

The right hand spectrum in figure 5.16 shows the 2D NOESY spectrum of a sample containing chain-deuterated and non-deuterated DMPC in equal proportion, with a total lipid:HMA molar ratio of 7:1. The HMA CH₂ (B) peak is not visible in this spectrum, and is proposed to be buried under the more prominent DMPC CH₂ peak at 1.27 ppm.

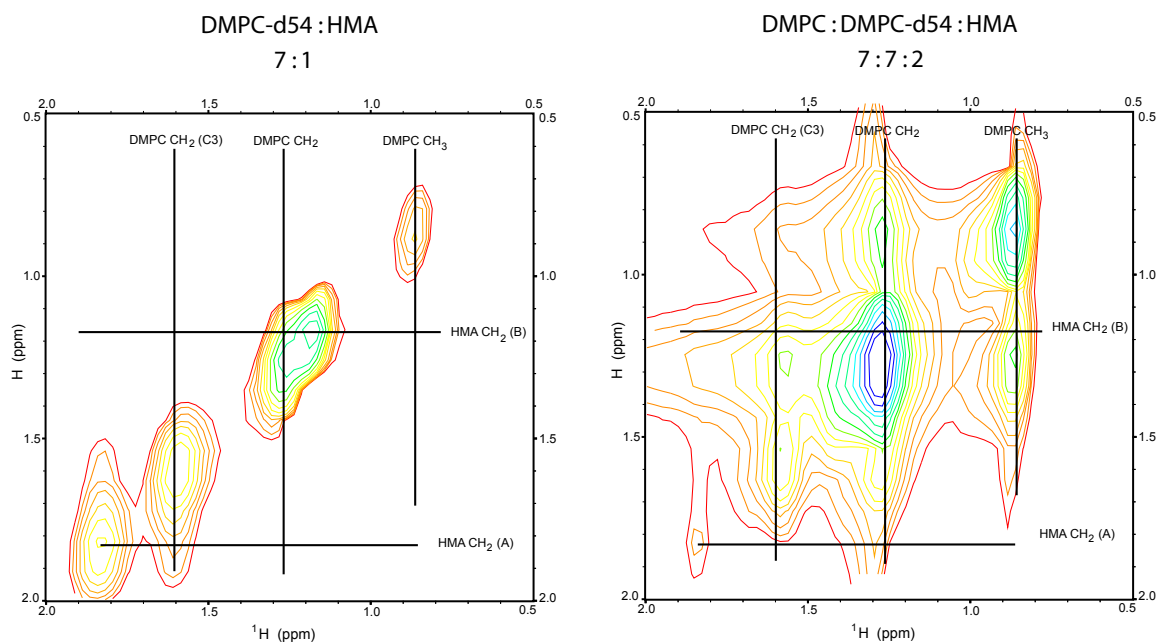


FIGURE 5.16: Comparison of NOESY spectra of HMA:DMPC- d_{54} 1:7 (left) and HMA:DMPC- d_{54} :DMPC 2:7:7 (right) solubilised in D_2O acquired at 500 MHz. Contours were cut at seven times noise level and the figure prepared using Sparky [246].

5.3.7 Discussion

The membrane location of the amiloride derivative HMA was investigated using 1H MAS NOESY NMR spectroscopy. Spectra of a lipid:drug 7:1 (molar ratio) mixture were obtained at 1H frequencies of both 500 MHz and 600 MHz. Peaks arising from all of the HMA protons are visible on the diagonal of the two spectra (see figure 5.13), indicating the H/D exchange with the solvent does not occur and suggesting that the aromatic character of the drug extends from the six-membered ring to the guanidium group. The two spectra (figure 5.13) show cross peaks produced by NOE relaxation between drug and lipid resonances, indicating that HMA is able to enter and remain within a model lipid membrane, with residency period which is significantly longer than the rate of exchange between the populations of the drug in the lipid and aqueous phases. The presence of a

cross peak between the two molecule types indicates that they must be within 5 Å of one another [230].

The spectra also allow the orientation and location of the drug in the bilayer to be determined. The resonances arising from the CH₂ groups of the hexamethylene ring form cross peaks with the lipid fatty acid chain CH₂ and CH₃ groups and the HMA guanidium group -NH and -NH₂ ¹H resonances form cross peaks to the DMPC choline and glycerol CH₂ and CH₃ resonances. The ring-current splitting of the C2 glycerol peak, indicates that the aromatic system of the drug lies nearby, and the change in the chemical shift of the HMA NH₂ (B) resonance suggests that this group lies close to the negatively charged lipid phosphate group. The experimentally determined membrane location therefore agrees well with the predictions made by MD simulations in Chapter 4.

A disadvantage of using the NOESY technique to determine the membrane location of drugs of the amiloride family is that all of the drug resonances fall in within the range occupied by peaks arising from the DMPC. The technique has been more successfully applied to drug molecules with aromatic protons, since these resonances typically fall in the range 6 ppm to 9 ppm (outside the range occupied by the lipid resonances) [225]. The NOESY cross-peak volume analysis is of limited use in defining the position of HMA across the hydrophobic region of the membrane, given that the majority of the DMPC acyl chain CH₂ protons have identical chemical shifts. Other spectroscopic techniques including wide line ²H NMR on selectively chain-deuterated lipids or ¹³C MAS would be able to locate the position of the drug within the hydrophobic region of the membrane, and these approaches have previously been used to determine the membrane locations of the antidepressants desipramine and imipramine [250].

The high concentrations of drugs used in the ¹H NOESY study are required to enable the observation of cross-peaks between lipid and drug molecules and the

total drug:lipid ratio in a cellular membrane would clearly be significantly lower. The full-width-half-heights (fwhh) and chemical shifts of the lipid ^1H resonances did not appear to change significantly on addition of drug and similar studies have used comparable lipid:drug ratios [225, 251]. Nevertheless there is the potential for the drug insertion to be an artefact of the high concentration of HMA used. Further spectroscopic techniques will be used to investigate the interaction between model membranes and HMA at lower drug concentrations.

5.4 HMA-lipid interactions by ^{31}P MAS NMR

^{31}P has a natural abundance of 100% and a nuclear spin of $I = \frac{1}{2}$ and a high gyromagnetic ratio of ^{31}P ($\gamma = 1.083 \times 10^4 \text{ gauss}^{-1} \text{ s}^{-1}$) making it highly suitable for NMR spectroscopy [252]. MAS ^{31}P NMR has been previously used to investigate the interaction between charged peptide molecules and model bilayers since the isotropic chemical shifts, chemical shift anisotropy and full-width-half-heights (fwhh) of the phosphate resonances are sensitive to changes in their chemical environment [253–255]. ^{31}P MAS NMR was used in this study to test whether there is a strong electrostatic interaction between the negatively charged lipid phosphate groups and the positively-charged guanidium moiety of HMA, as predicted by the MD simulations described in section 4.3.1.1 .

5.4.0.1 Chemical shift perturbation

Table 5.4.0.1 shows the effect of the addition of HMA to the ^{31}P MAS chemical shifts of DMPC, which results in an upfield shift in the peak position (spectra not shown). The fwhh of the spectra is initially doubled on addition of HMA to a drug:lipid ratio of 15:1, however further addition of HMA a molar ratio of 7:1 resulted in a decrease of the fwhh. The results suggest that HMA is able to alter the chemical environment of the phosphate groups, possibly by polarising the phosphate electron cloud, resulting in a deshielding of the ^{31}P nucleus and the upfield shift of the DMPC resonance.

Sample composition	σ_i	fwhh / ppm
DMPC	-0.90	1.10
DMPC:HMA 15:1	-0.88	1.91
DMPC:HMA 7:1	-0.87	1.09

TABLE 5.3: ^{31}P isotropic chemical shifts (σ_i) and line widths (fwhh) for DMPC model membranes at 6 kHz MAS and 30 °C recorded at 500 MHz after 8k scans.

5.4.0.2 DMPG:DMPC 2:1 model membrane

Figure 5.17A shows the MAS ^{31}P NMR spectrum of a 2:1 molar ratio of DMPC and DMPG at pH 7.2. The resonances at -0.9 ppm and 0.2 ppm arise from the DMPC and DMPG respectively. The intensity of the DMPG peak accounts for approximately 35% of the total spectral intensity, which reflects the fraction of DMPG in the mixture. Figures 5.17B-E show the effect of adding increasing concentrations of HMA to the same lipid mixture. As the concentration of HMA in the sample increases, the apparent intensity of the DMPG peak decreases relative to that of the DMPC, suggesting that the drug is binding preferentially to the negatively charged lipid (see also figure 5.18). The observed decrease in the DMPG signal, is as a result of an enhanced transverse relaxation rate and may reflect a reduction in the motional freedom of the lipid phosphate groups in the presence of the drug [255].

5.4.0.3 Discussion

The interaction between HMA and a model lipid membrane was further investigated by 1D ^{31}P MAS NMR spectroscopy. The results of the MD simulations presented in Chapter 4 and the MAS NOESY spectra discussed in section 5.3.2, suggest that the positively charged guanidium group of HMA is able to interact with the negatively charged phosphate groups of naturally occurring lipids. Changes in the anisotropic chemical shift and fwhh of the DMPC ^{31}P resonance were observed on the addition HMA, supporting the suggestion that the drug is able to partition into membranes from the aqueous phase. The drug was also added to model membranes containing a molar ratio of DMPC:DMPG 2:1 and resulted in a decrease in the intensity of the DMPG ^{31}P resonance relative to that of DMPC (figures 5.17 and 5.18), suggesting that HMA interacts preferentially with the negatively charged DMPG. The drug concentrations used in this study

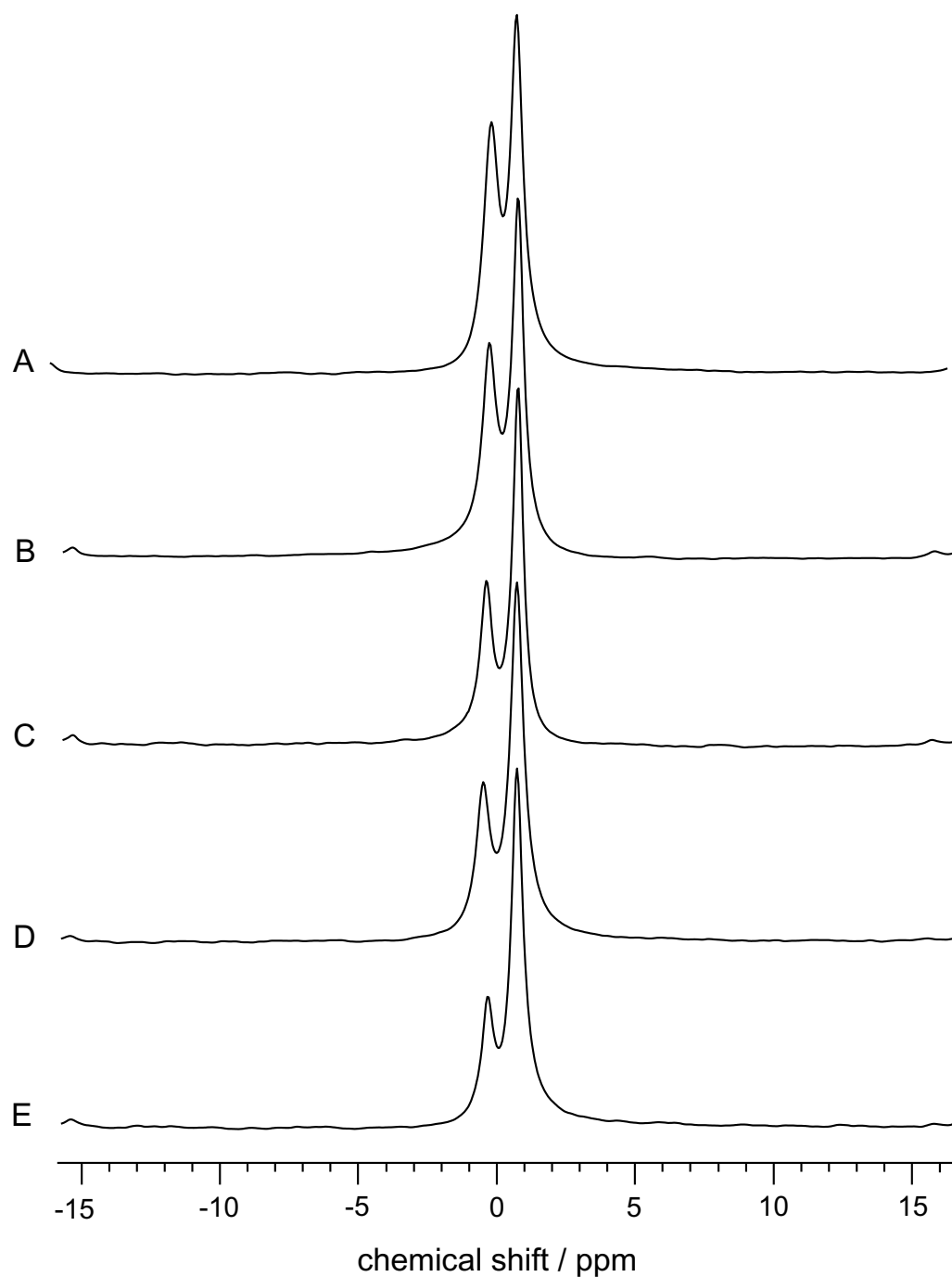


FIGURE 5.17: $1D$ ^{31}P MAS NMR spectra of DMPC:DMPG 2:1 in the presence of increasing HMA concentration. HMA/lipid molar ratios of 0.0 (A), 0.0067 (B), 0.025 (C), 0.050 (D) and 0.067 (E). Note the decrease in the height of the DMPG peak at 0.9 ppm relative to the DMPC peak at -0.2 ppm with increasing HMA concentration. Spectra taken on Varian Infinityplus 500 MHz spectrometer and referenced to $NH_4H_2PO_4$.

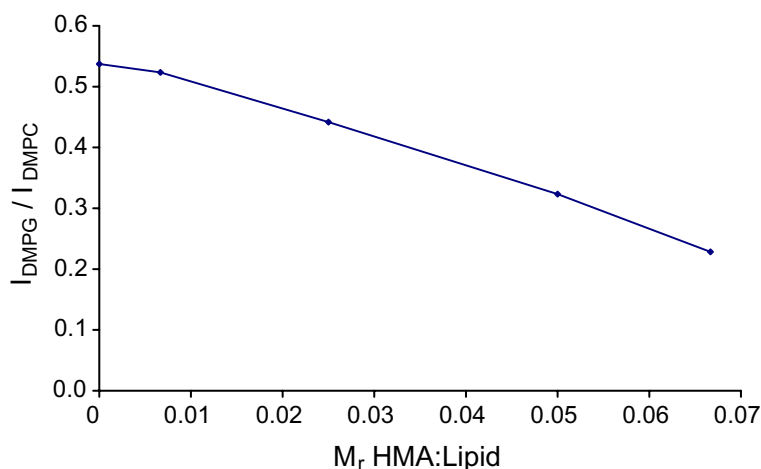


FIGURE 5.18: Ratio of the relative intensities of the DMPG and DMPC peaks against HMA/lipid ratio For spectra see figure 5.17.

are lower than those in the earlier ^1H MAS NOESY experiments, (a maximum lipid:protein ratio of 1:15) and there is evidence of a decrease in the intensity of the DMPG ^{31}P peak at lipid:drug molar ratios as low as 1:150 and 1:80.

In a study by Bonev *et al.*, the interaction between the positively charged l-antibiotic nisin and a DMPC:DMPG 2:1 model membrane, the authors also observed a decrease in the intensity of the DMPG resonance on addition of the peptide. Nisin has a +3 positive charge and it is clear from the published data that there is a strong association between nisin and DMPG. The authors also report the appearance of an additional broad resonance and suggest that the motion of a proportion of the lipids is restricted [255]. Nisin has a molecular weight approximately twenty times greater than HMA [256], and the DMPG peak almost disappears at a peptide/lipid ratio of 0.067 [255], whereas at the same lipid/HMA ratio, the DMPG peak height is only half that of its original intensity. There is some evidence from the MD simulations reported in the previous chapter (see section 4.3.1.1) that the motion of the lipid headgroups within 10 nm of HMA are restricted relative to those of the bulk bilayer. This results of the ^{31}P NMR reported here, therefore favour a similar membrane location for HMA.

5.4.1 Raman Spectroscopy

Laser tweezer Raman spectroscopy was used to determine the effect of the addition of HMA to a unilamellar vesicle of DMPC. Spectra from the near IR were taken, since the C-C and P-O lipid stretching vibration peaks fall in this region. Lipid phase transitions can be followed by observing changes in the positions and prominence of these peaks as the relative proportion of *gauche* and *anti* C-C bonds and the H bonding pattern at the phospholipid-water interface varies [257–259] (see figure 5.19).

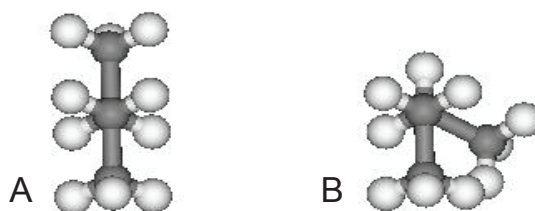


FIGURE 5.19: *Anti and gauche forms of butane as viewed looking along the C2-C3 bond*

The optical tweezers apparatus enables the sample size to be restricted to a single vesicle, of typical diameter $1\ \mu\text{m}$ (see figure 5.20), improving the signal to noise ratio, reducing the acquisition time, eliminating temperature gradients through the sample and allowing a background spectrum to be taken from the solution surrounding the vesicles [260]. The technique has previously been used to analyse the composition of aerosol droplets and liposomes [260, 261].

The Raman spectra of DMPC vesicles at $20\ ^\circ\text{C}$ (figure 5.21) clearly show that the lipid is in the gel phase. The C-C stretch region is dominated by peaks at $1060\ \text{cm}^{-1}$ and $1128\ \text{cm}^{-1}$, and the presence of the $1091\ \text{cm}^{-1}$ peak shows that the H bonding pattern at the phospholipid-water interface is consistent with the lipids being in the gel phase. (For assignment of additional peaks, see table 5.4.)

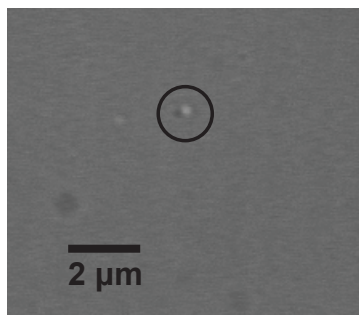


FIGURE 5.20: A DMPC vesicle (circled) held in the optical trap by the Ar^+ ion laser as viewed through a Leica DM-IRB light microscope (objective lens $\times 63$). Other vesicles floating free in the buffer above and below the plane of focus of the light microscope are also visible. The position of the trapped vesicle was sufficiently stable that spectrum acquisition times of upwards of 10 minutes were possible.

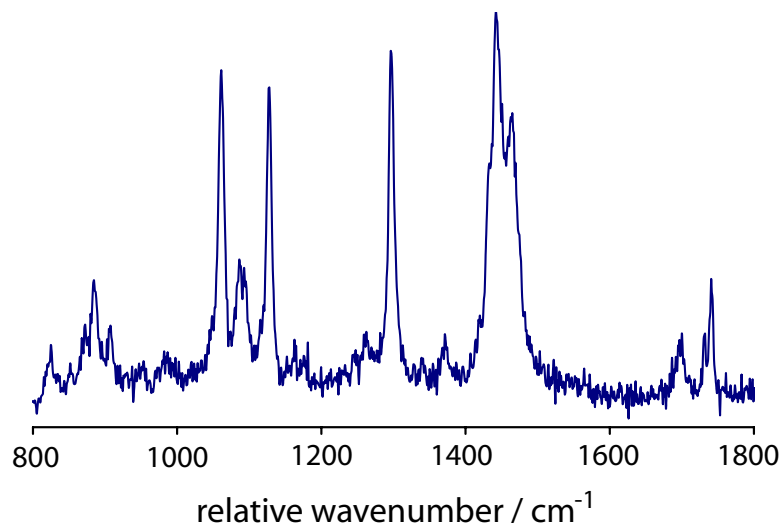


FIGURE 5.21: Raman spectrum of a DMPC vesicle in water. 60 s acquisition time at 200 W.

32 mM HMA solution spectra show a broad fluorescence peak, which covers all Raman scattering except for peaks at 964 cm^{-1} , 1040 cm^{-1} , 1326 cm^{-1} , 1386 cm^{-1} and 1419 cm^{-1} , (see table 5.4 for assignments) (data not shown). When HMA is added to DMPC before the freeze thawing and extrusion at molar ratios of 1:100 and 1:10 (see section 5.2), the fluorescence disappears, suggesting that the drug molecules enter the phospholipid bilayer instead of remaining in aqueous solution.

The spectrum of DMPC:HMA 50:1 (figure 5.22B) has many similarities to the pure DMPC spectra (figure 5.22A) and the HMA solution spectra peaks at 964 cm^{-1} , 1040 cm^{-1} (shoulder), 1139 cm^{-1} , are visible. Additional peaks at 915 cm^{-1} and 978 cm^{-1} are also observed. Compared to the DMPC-only spectrum, the ratio of the 1058 cm^{-1} , 1082 cm^{-1} and 1126 cm^{-1} peaks shows an increase in the proportion of gauche C-C bonds, suggesting that lipid disorder is induced by the presence of the drug. The DMPC:HMA 10:1 (figure 5.22C) spectrum shows an even greater change in this ratio and the complete disappearance of the 1090 cm^{-1} peak suggesting that a full phase change has taken place.

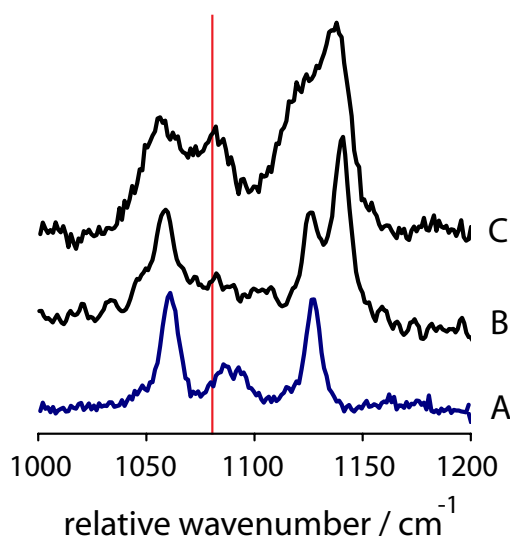


FIGURE 5.22: Effect of increasing HMA concentration on lipid phase for DMPC only (A), DMPC:HMA 1:50 (B) and DMPC:HMA 1:20 (C). The red line shows the expected position of the C-C gauche stretch at 1086 cm^{-1} . 60 s acquisition time at 200 W.

5.4.1.1 Conclusion

The effect on lipid dynamics of the addition of HMA to DMPC vesicles was investigated by Raman spectroscopy. The DMPC acyl chains appear to become more disordered on the addition of HMA, which would agree with the prediction made by MD simulations in the previous chapter, that HMA is able to enter lipid bilayers.

TABLE 5.4: Table of assignments for Raman spectra after [262].

Region / cm^{-1}	Intensity	DMPC	HMA
820-828	medium	P-O asym stretch	
915	medium		ring breathing
963	weak		ring breathing
970 - 980	medium	C-N asym stretch	
978	medium		ring breathing
1040 - 1050	weak & sharp	P-O-C sym stretch	
1060	strong	C-C gauche stretch	
1070	weak	CO-O-C sym stretch	
1085	strong	PO ₂ ⁻ sym stretch	
1086	strong	C-C cis stretch	
1091	strong	PO ₂ ⁻ sym stretch	
1128	strong	C-C gauche stretch	
1139	strong		C-C gauche stretch
1170	weak	CO-O-C asym stretch	
1296	strong	CH ₂ twist	
1359	medium		ring breathing
1370 - 1380	weak	CH ₃ sym bending	
1430 - 1480	strong	CH ₂ scissoring	
1690 -1750	medium	C=O stretch	

A similar increase in lipid disorder is observed when halothane and chloroform are added to DMPC and DPPC at five times above clinically relevant concentrations, although at clinically relevant concentrations there appears to be no observable effect on DMPC vesicles of halothane and chloroform at 37°C [243]. At 20° the phase change occurs at HMA concentrations below those that are reported required to achieve complete inhibition of the ion channel activity of Vpu [73]. The data presented in Chapter 2, suggest that the HMA concentrations used in this study are insufficient for complete inhibition of Vpu channel activity and it is therefore unlikely that HMA inhibits Vpu by altering the biophysical properties of the bulk lipid.

5.5 Conclusion

The interaction between HMA and model membranes has been investigated using a number of spectroscopic techniques. ^1H MAS NOESY spectra of HMA in DMPC membranes at a drug:lipid ratio of 1:7 were acquired at ^1H frequencies of 500 MHz and 600 MHz. Cross peaks are observed between the CH_2 protons of the hexamethylene ring of HMA and the lipid acyl chains of DMPC and between the HMA guanidium group and the DMPC choline and glycerol proton resonances. The experimental findings support the predictions made in the previous chapter by MD simulations, that HMA binds to the membrane and orients so that the hydrophilic guanidium group is located in the lipid headgroup region and the hexamethylene ring is close to the fatty acid chains. The spectra also suggest that the delocalised electron system of HMA extends from the six-membered ring to the guanidium group, supporting the HMA-stiff model proposed in the previous chapter.

1D ^{31}P spectra also support the proposed location for HMA within the lipid bilayer. The spectra show an upfield shift in the position of the DMPC resonance, possibly caused by the deshielding of the ^{31}P nucleus, due to the proximity of the positively charged guanidium group of HMA. The spectra also indicate that the positively charged drug interacts preferentially with the negatively charged DMPG over DMPC and is able to restrict the motion of the lipid headgroups.

Raman spectroscopy was used to examine the effect on lipid dynamics of the addition of HMA to DMPC vesicles. The spectra show a lowering of the phase transition temperature of the DMPC lipid at drug:lipid ratios of 1:20 and 1:50, confirming that HMA is able to partition into the lipid from the aqueous phase. However it is unlikely that HMA inhibits Vpu by altering the biophysical properties of the bulk lipid, since acyl chain disorder is produced at drug concentrations below those required for a complete inhibition of channel activity. It is however possible

that this mechanism is responsible for preventing the rapidly fluctuating trans-membrane currents, which have been reported by some as channel currents [21].

A variety of spectroscopic approaches have been used to determine the location of HMA within model membranes. The results of the experiments presented in this chapter confirm the predictions made by MD simulations that HMA is able to partition into the lipid from the aqueous phase. It has previously been suggested that HMA inhibits Vpu by binding to the interior of the channel and preventing ion flux [76, 77]. The results of these experiments do not exclude the possibility that ion flux is inhibited by a pore occlusion mechanism, however HMA molecules entering the Vpu channel must come from a relatively limited pool of drug molecules in the aqueous phase.

Chapter 6

REDOR Spectroscopy

SUMMARY

The interaction between HMA and Vpu was analysed by REDOR NMR spectroscopy. Vpu₁₋₃₂ labelled with ¹⁵N at the backbone nitrogen atom of Trp23 and HMA labelled with ¹³C at the guanidium carbon atom, were reconstituted into DMPC membranes. ¹³C spectra of the reconstituted system indicate that the prominence of the HMA guanidium carbon resonance was dependent on temperature. No dephasing of the same peak was observed in the REDOR spectra, indicating that, at this concentration of drug and temperature, there is no observable interaction between Vpu and the inhibitor.

6.1 Introduction

Rotational Echo Double Resonance (REDOR) is a solid state NMR experiment used to measure distances between nuclei. The technique reintroduces the heteronuclear dipolar coupling between two NMR-sensitive nuclei such as ¹³C and ¹⁵N, the magnitude of which is dependent both on the internuclear distance and on the gyromagnetic ratio of the two spins [263].

6.1.1 Applications

REDOR NMR has been used to determine precise internuclear distances between the glutamate and serine chemotaxis membrane receptors and their respective

ligands and the conformations of bound ligands. [264–266] The structure of ligands at their binding sites can also be determined by measuring intramolecular distances between NMR-sensitive nuclei. The structure TPMIM an analogue of SCH28080, a reversible inhibitor of the H^+ / K^+ -ATPase [267]. The structure of the ligand can in turn place constraints on the possible orientations of transmembrane helices and the proximity of key residues [268].

As discussed in section 4.1.2.3, a number of HMA-binding sites have been identified on the Vpu protein, both within the channel lumen and at the lipid-protein interface [76, 77], and ability to measure distances between the peptide backbone and HMA offers the ability to discriminate between these binding modes.

6.1.2 Outline of pulse sequence

The first step of the REDOR pulse sequence requires a 90° pulse on the 1H channel followed immediately by a cross polarisation step to transfer magnetisation to ^{13}C (the observed spin) (figure 6.1). For the remainder of the sequence, protons are decoupled at high power (typically > 80 kHz) with rapid phase alteration. The resulting transverse magnetisation of the ^{13}C nucleus begins to evolve by heteronuclear dipolar coupling, however the magnetisation is refocussed after each complete rotor revolution by MAS. The application of a train of 180° pulses on the ^{15}N (passive spin) channel, synchronised with the rotation of the rotor, interferes with the MAS averaging of the heteronuclear dipolar recoupling, resulting in a decrease in the intensity of the signal intensity of the ^{13}C in a manner dependent on the distance between the passive and observed spins. In addition a single 180° pulse, positioned half-way through the evolution time and also synchronised with the rotation of the sample, is used to refocus the isotropic chemical shifts.

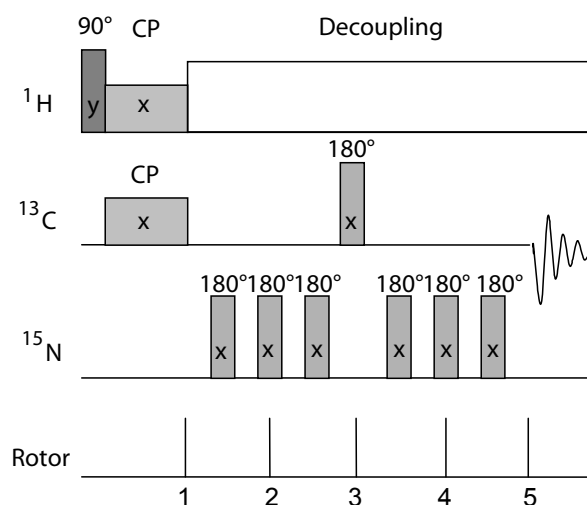


FIGURE 6.1: Pulse sequence for ^{15}N refocus, ^{13}C observe REDOR Nuclear Magnetic Resonance. Transverse carbon magnetisation is produced by the cross-polarisation (CP) transfer from dipolar-coupled protons. The ^{15}N 180° pulses prevent rotational refocusing of the dipolar interaction. Incomplete refocusing of magnetisation results in a decrease in signal intensity, S by the amount ΔS . The ^{13}C 180° pulse refocuses the isotropic ^{13}C chemical shift differences at the start of the data acquisition.

6.1.3 Cross polarisation

The sensitivity of spin species with low gyromagnetic ratios (such as ^{13}C and ^{15}N) can be enhanced by transferring magnetisation from abundant spin species (I -spins) with high gyromagnetic ratio, such as ^1H , ^{19}F and ^{31}P . In a CP experiment, the field strengths are set to the Hartmann-Hahn condition:

$$\gamma_H H_{1(H)} = \gamma_X H_{1(X)} \quad (6.1)$$

where γ is the gyromagnetic ratio and H_1 is the strength of the irradiation field. Polarisation is transferred when a spin-lock field is applied to both I and S simultaneously, during a period known as the contact time. MOIST (mismatch optimised I - S transfer) cross polarisation was used in this study [269–271].

6.1.4 Proton decoupling

The ^1H nucleus has a large gyromagnetic ratio and almost 100% natural abundance. The large number of protons in biomolecules and their spin interactions with the other low γ nuclei such as ^{13}C and ^{15}N complicate the spectrum. ^1H decoupling therefore is necessary to remove residual ^1H - ^{13}C dipolar couplings under MAS NMR and ^1H - ^{13}C residual J-couplings, which are not averaged with the sample spinning at the magic angle. Decoupling field strengths of 80-100 kHz are now commonly used. The simplest decoupling method involves continuous radio frequency irradiation of constant, phase during the acquisition of the FID and is called continuous wave (CW) decoupling [272]. Recently, more sophisticated methods have been introduced which significantly improve the decoupling efficiency [273]. Two-pulse phase modulation (TPPM) consists of two (pulses and their rapid phase switching. TPPM decoupling is sensitive to both pulse length and the phase angle [274].

6.1.5 REDOR pulses

The Hamiltonian which describes the heteronuclear dipolar coupling can be stated as:

$$H_D = \frac{\gamma_I \gamma_S}{r^3} \frac{(3 \cos^2 \theta - 1)}{2} (2I_z S_z) \quad (6.2)$$

Where γ_I and γ_S are the gyromagnetic ratios of spins I and S respectively and θ is the angle between the internuclear vector of length r and the external magnetic field. MAS rotation of the sample has the effect of removing the dipolar couplings, which are then reintroduced by applying a series of 180° radio pulses, synchronised to the rotation of the sample.

Rewriting equation 6.2 with the units of radians/sec, the heteronuclear dipolar interaction is:

$$H_D = d(t)S_Z I_Z \quad (6.3)$$

Since the sample is subjected to MAS, the dipolar coupling constant is time-dependent.

$$d(t) = d \left(\sin^2 \beta \cos 2(\alpha + \omega_r t) - \sqrt{2} \sin 2\beta \cos(\alpha + \omega_r t) \right) \quad (6.4)$$

where the dipolar coupling is d , the sample spinning rate is ω_r and α and β are the azimuthal and polar angles of the internuclear vector with respect to the spinning axis (figure 6.2).

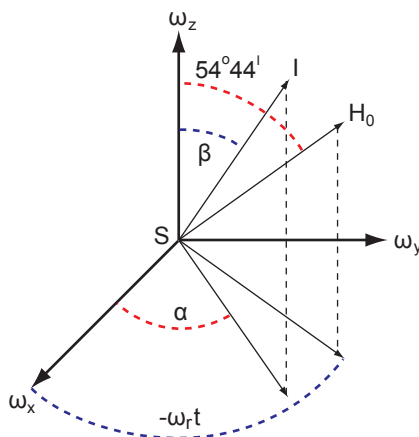


FIGURE 6.2: Definition of angles from equation 6.4 in the rotor frame rotating at the magic angle. I and S are the nuclei of interest.

The net dephasing angle ϕ can be calculated for each rotor period by:

$$\phi = \int_0^{\tau_r/2} \omega_d(t) dt. - \int_{\tau_r/2}^{\tau_r} \omega_d(t) dt. \quad (6.5)$$

where

$$\omega_d(t) = \pm \frac{d(t)}{2} \quad (6.6)$$

Without ^{15}N dephasing pulses, the accumulated phase in the first half of the rotor period would be cancelled in the second half. With dephasing there is non-zero phase accumulation. Rewriting equation 6.5 for N_c rotor periods, the total phase accumulation is given by:

$$\phi = \frac{N_c T_r d}{\pi} \sqrt{2} \sin 2\beta \sin \alpha \quad (6.7)$$

A reference spectrum (S_0) is obtained for each increment in the number of rotor periods, in which the ^{15}N dephasing pulses are omitted, completely refocusing the dipolar interaction. Since both the dephased (S) and non-dephased (S_0) spectra are susceptible to imperfections in the application of the π pulses and losses due to relaxation during the REDOR evolution periods, the ratio $\Delta S / S_0$ is used:

$$\frac{\Delta S}{S_0} = \frac{S_0 - S}{S_0} \quad (6.8)$$

For a single spin pair,

$$\frac{\Delta S}{S_0} = 1 - \cos(\phi) \quad (6.9)$$

For a powder sample, in which all internuclear orientations are included and all values of α and β intergrated,

$$\frac{\Delta S}{S_0} = \frac{1}{2\pi} \int_0^\pi \int_0^\pi \cos(\phi) \sin(\beta\alpha) d\beta. \quad (6.10)$$

where $\sin(\beta)$ is a geometric weighting factor [275].

Universal curves may be generated for this ratio for the purpose of comparing the experimental data to simulation predictions (see figure 6.3).

Systematic variation of the number of rotor cycles and observation of the signals

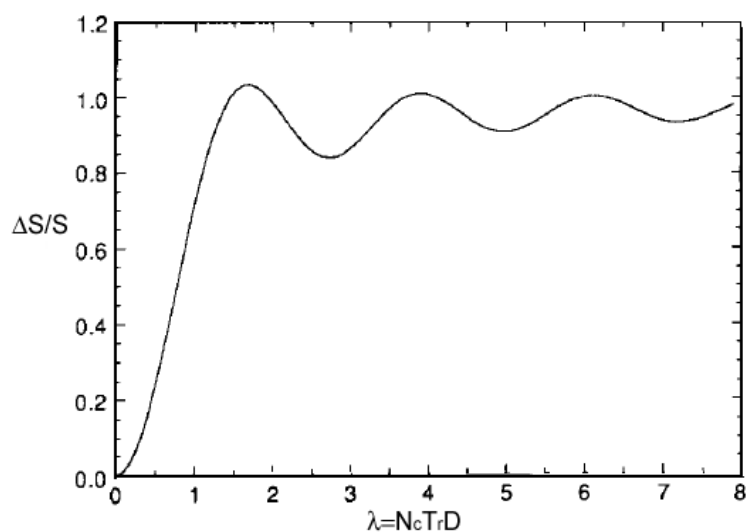


FIGURE 6.3: Variation of $\Delta S/S_0$ with the dimensionless parameter λ , a product of the number of rotor cycles (N_c) and the dipolar coupling (D). Reproduced from [275].

both with and without the application of π -pulse dephasing in the REDOR experiment, produces a time-domain REDOR dipolar dephasing signal from which internuclear couplings may be calculated directly.

The dipolar coupling:

$$d \propto \frac{\gamma_I \gamma_S}{2\pi r^3} \quad (6.11)$$

allowing the interatomic distance between NMR-sensitive nuclei to be measured [275].

6.1.6 Aims of this study

The dipolar coupling between two nuclei is dependent on the gyromagnetic ratios of and distance between the spins (see equation 6.11). The REDOR experiment exploits this phenomenon, allowing the distance between the two nuclei to be measured.

Docking and molecular dynamics simulations have previously been used to identify potential interactions between HMA and Vpu. Suggested binding sites for the drug include the interior of the channel lumen and the side chain of residue Trp23, which is predicted to lie on the outside of the oligomer [76, 77] (see also Chapter 4). In this study, a Vpu_{1–32} peptide, labelled with ¹⁵N at the backbone nitrogen atom of Trp23 and HMA labelled with ¹³C at the guanidium carbon atom, will be reconstituted into DMPC membranes. REDOR measurements are acquired to determine whether there is any interaction between Vpu and HMA could be detected.

6.2 Materials and methods

6.2.1 Sample preparation

Vpu₁₋₃₂ labelled with at the backbone N on residue Trp23 was synthesised by solid phase peptide synthesis by Matt Rosenberg (Australia National University, Canberra) and HMA, labelled with ¹³C on at the guanidium moiety was purchased from Biotron Ltd (Western Australia) (see figure 6.4). Both peptide and drug were in TFE and the solvent was evaporated under N₂ gas and dried under vacuum overnight, to a final molar ratio of 1:1. A lipid suspension of DMPC was rehydrated using D₂O and combined with the peptide and drug. The total lipid:peptide ratio was 1:50 and rehydrated with 40 μl D₂O. The lipid mixture was subjected to ten freeze thaw cycles and centrifuged prior to packing in the NMR rotor.

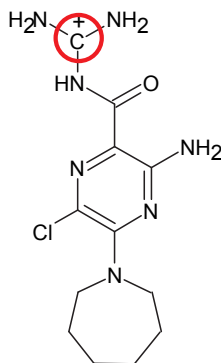


FIGURE 6.4: *Structural formula of HMA, showing the position of the ¹³C labelled guanidium group carbon atom.*

6.2.2 ¹H-¹³C cross polarisation experiments

¹H-¹³C cross polarisation experiments were performed to determine the optimum temperature to visualise the HMA guanidium group ¹³C resonance. The experiments were performed on a 500 MHz Varian spectrometer equipped with an HX

probe at temperatures of between $-10\text{ }^{\circ}\text{C}$ and $-30\text{ }^{\circ}\text{C}$. The sample was packed inside a 4 mm rotor with Kel-F inserts and rotated at an MAS frequency of 8 kHz.

6.2.3 REDOR experiments

REDOR experiments were performed on a 600 MHz Bruker spectrometer equipped with a low E field HXY probe at a temperature of $-35\text{ }^{\circ}\text{C}$. The sample was packed inside a 4 mm rotor with Kel-F inserts and rotated at an MAS frequency of 8 kHz. MOIST cross polarisation was used to transfer magnetisation from ^1H to ^{13}C with a contact time of 1.6 ms. The 180° pulse length for both ^{15}N and ^{13}C pulses was $5\text{ }\mu\text{s}$. 50 kHz TPPI ^1H decoupling was applied during the acquisition time. Data sets for the S and S_0 curves were acquired concurrently, so that the ^{15}N 180° pulses were omitted from alternate scans.

6.3 Results

6.3.1 Cross polarisation

HMA was synthesised with a ^{13}C label at the carbon of the guanidium group moiety. The chemical shift of the labelled carbon atom is 157 ppm, which falls in a region of the ^{13}C spectrum between the expected positions of the $^{13}\text{C}=\text{O}$ peaks of the lipid and Vpu peptide and the $^{13}\text{C}_\alpha$ resonances of the Vpu peptide. Figure 6.5 shows three 1D cross polarisation spectra of ^{13}C -HMA and ^{15}N -Trp23-Vpu₁₋₃₂ reconstituted at 1:1 ratio into egg phosphatidylcholine lipid (at a lipid:protein ratio of 50:1) acquired at different temperatures. The prominence of the HMA peak is dependent on temperature and lower temperatures are required to reduce the motion of the drug within the membrane, thereby facilitating the synchronisation of the ^1H and ^{13}C nuclear spins and increasing the efficiency of the cross polarisation.

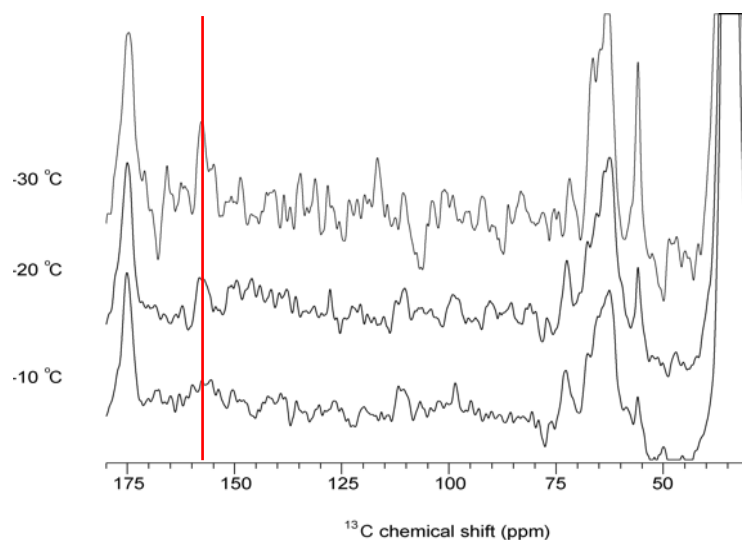


FIGURE 6.5: *Effect of decreasing temperature on the prominence of the HMA guanidium group ^{13}C resonance at 157 ppm (indicated by the red line) ^{13}C -HMA and ^{15}N -Trp23-Vpu₁₋₃₂ reconstituted at 1:1 ratio into egg phosphatidylcholine lipid. Spectra acquired on a 500 MHz Varian Infinityplus spectrometer equipped with an HX probe at 8 kHz MAS. All spectra were acquired for 1.4 ms contact time and with 80 kHz ^1H decoupling.*

A similar solid state NMR study of the phospholamban peptide reconstituted into DOPC membranes, found that temperatures of below $-40\text{ }^{\circ}\text{C}$ were required to visualise the labelled ^{13}C O and $^{13}\text{C}_{\alpha}$ labels [276].

6.3.2 REDOR spectra

Figure 6.6 shows the S and S_0 spectra acquired with 18 rotor periods between the initial cross polarisation and collection of the FID. Comparison of the S spectrum with the S_0 spectrum shows that the intensity of the HMA ^{13}C guanidinium carbon resonance is more intense in the dephased spectrum, indicating that despite the acquisition of 16k scans, the noise level of the spectrum is too great to allow dephasing to be observed under this condition.

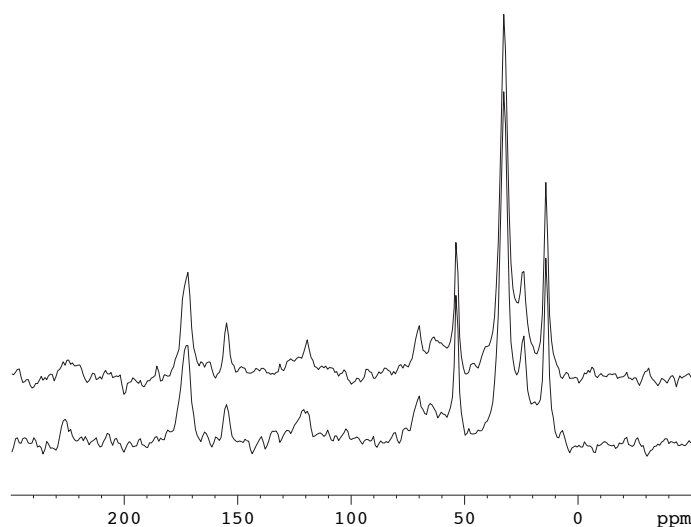


FIGURE 6.6: REDOR spectra of TR18 S (above) and S_0 (below). ^{13}C -HMA and ^{15}N -Trp23-Vpu₁₋₃₂ reconstituted at 1:1 molar ratio into egg phosphatidylcholine lipid. Spectra acquired on a 500 MHz Varian Infinityplus spectrometer equipped with an HX probe at 8 kHz MAS. All spectra were acquired for 1.4 ms contact time and with 80 kHz ^1H decoupling.

The experiment was repeated with a 34 rotor cycles between the initial cross polarisation and collection of the FID. 32k scans were collected (double the number of the previous experiment). Figure 6.7 shows the S and S_0 spectra acquired with

34TR. No difference in the intensity of the HMA ^{13}C guanidium carbon resonances was observed. Some of the lipid glycerol ^{13}C resonances showed some dephasing, indicating that the backbone nitrogen atom of residue Trp23 lies close to these groups (in agreement with the MD simulations presented in Chapter 4).

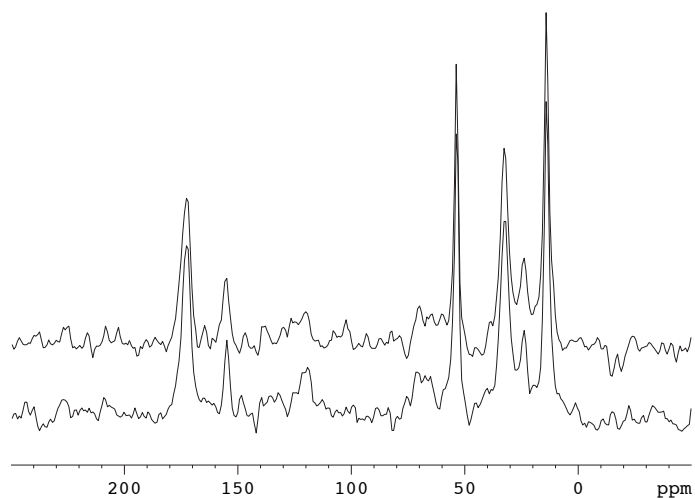


FIGURE 6.7: REDOR spectra of TR34 S (above) and S_0 (below). ^{13}C -HMA and ^{15}N -Trp23-Vpu₁₋₃₂ reconstituted at 1:1 ratio into egg phosphatidylcholine lipid. Spectra acquired on a 500 MHz Varian Infinityplus spectrometer equipped with an HX probe at 8 kHz MAS. All spectra were acquired for 1.4 ms contact time and with 80 kHz ^1H decoupling.

A further preliminary experiment to extend the number of rotor cycles to 40TR was abandoned because the ^{13}C signals were too weak for any useful data to be collected within the available experimental period.

6.4 Discussion

^{13}C - ^{15}N REDOR NMR spectroscopy was used to investigate the interaction between Vpu₁₋₃₂ and HMA. S and S_0 REDOR spectra with 18 and 34 rotor cycles were acquired of the drug and peptide reconstituted into DMPC membranes. No dephasing of the HMA ^{13}C guanidium carbon signal at 162 ppm was observed, suggesting that at this concentration, the interaction between the drug and peptide is too weak to be observed. Some dephasing of the lipid $^{13}\text{C}=\text{O}$ peaks by the ^{15}N -labelled peptide was observed in the spectrum acquired with 38 rotor cycles, indicating that the Trp23 backbone nitrogen atom lies close to the lipid headgroup regions. This is consistent both with the MD simulations reported in Chapter 4 and with the predicted role of the Trp23 side chain as an anchor of the peptide within the membrane [20, 70].

Dephasing of the HMA guanidium carbon resonance would be expected if the drug binds to the lumen of the pentameric channel in the position suggested in [76], since in this position the guanidium head group of the drug lies within 1 nm of the Trp23 backbone amide group. An interaction between HMA and the Trp23 side chain would also be expected to show some dephasing, although the distance between the two labelled atoms is an average of 4.5 Å, which is approaching the upper limit for distances measurable by ^{13}C - ^{15}N REDOR. Since the signal to noise ratio of the abandoned preliminary experiment was prohibitively low for any meaningful data to be collected, it is unlikely that further experiments with this sample would yield any positive results.

6.5 Conclusion

The cross-polarisation magic-angle spinning NMR method REDOR was used to investigate the binding of the inhibitor HMA to the transmembrane domain of the viral ion channel Vpu. Although the spectra are dominated primarily by the resonances from the lipid, the ^{13}C resonance from the HMA guanidium group is visible at $-40\text{ }^{\circ}\text{C}$ although no dephasing of the HMA guanidium group peak was observed with up to 38 rotor cycles. Extension of the experiment beyond this point was not possible, because the signal decreased significantly. The low number of data points and relatively high signal to noise ratio also means that it was not possible to estimate a minimum distance by which the two groups are separated.

Although dephasing was not observed, the possibility remains that the drug interacts so weakly with the protein that it is in fast exchange equilibrium with the population of drug solubilised in the lipid headgroup region. The inhibition data presented in Chapter 2 also suggested that HMA was unable to completely block channel activity and this also suggests a weaker short lived interaction. The possibility also exists that HMA does not interact with Vpu and in fact inhibits on channel activity by altering the physical properties of the lipid which surrounds the ion channel as discussed in the previous chapter.

Chapter 7

Conclusions and future work

A wide variety of different biophysical methods have been employed in this thesis to characterise the ion channel activity of Vpu from HIV-1 and to investigate the mode of channel inhibition by the amiloride derivative, HMA.

7.1 Vpu channel kinetics

The *in vitro* channel activity of a peptide (Vpu₁₋₃₂), corresponding to the transmembrane portion of Vpu, was synthesised by solid phase peptide synthesis and purified by HPLC. The full length Vpu protein (Vpu₁₋₈₂) was expressed as a fusion protein with Glutathione-*S*-transferase in *E. coli* BL21 cells, and purified by GSTrap affinity chromatography and HPLC.

Both (Vpu₁₋₃₂) and (Vpu₁₋₈₂) were reconstituted into black lipid membranes and transmembrane currents were observed when both positive and negative voltages were applied. Contrary to earlier electrophysiological studies of the two proteins [59], discrete channel openings are observed and once open, the conductance of the channel remains constant. Vpu is a non-rectified Ohmic channel, and the transmembrane currents recorded are proportional to the magnitude of the applied voltage. A number of conductance states were observed for both proteins,

with a main conductance state of 17 pS for Vpu₁₋₈₂ and 17.5 pS for Vpu₁₋₃₂. The kinetics of channel opening and closing is similar for both proteins, supporting solid state NMR spectroscopy which have shown that the structure of the transmembrane portion of Vpu₁₋₈₂, is similar to that of the transmembrane domain alone [67, 277].

A key difference between the recordings made using Vpu₁₋₈₂ and Vpu₁₋₃₂ is the conductance of the principal subconductance state, which in Vpu₁₋₃₂ falls at 13.5 pS and Vpu₁₋₈₂ at 12 pS. It is possible that the principal subconductance state corresponds to the flow of Cl⁻ ions (instead of Na⁺) through the channel. The addition of the two cytoplasmic helices at the C-terminal end of the TM helix, could result in the disordering of this region as the protein, moving the ring of Arg31 and Lys32 residues further apart, reducing the ability of this part of the channel to stabilise Cl⁻ and leading to a lower conductance. Occasional channel openings from Vpu₁₋₈₂ do not conform to the regular square-wave shape. It may be that the presence of the C-terminal cytosolic helices helps to destabilise the membrane allowing some leakage of ions, in a manner similar to that suggested previously [21].

Four possible mechanisms for channel opening and closing have been discussed (see section 2.4.1). The model which appears to be most consistent with the data presented is that in which the oligomeric and monomeric forms of the protein are in a dynamic equilibrium, and that ion flux through the channel ceases when the helices dissociate. Other models have previously been proposed, in which a conformational changes are responsible for channel opening and closing, however the stability of the different conductance states appears to be inconsistent with the small energy differences between conformation states.

7.2 Inhibition of channel activity by HMA

The amiloride derivative, HMA, has been previously shown to inhibit the ion channel activity of Vpu and several other viral proteins [73, 157, 158]. Addition of the drug to the buffer solutions on either side of the black lipid membrane into which Vpu_{1–32} had been reconstituted, resulted in the incomplete inhibition of ion flux across the membrane. Channel open times were observed to decrease, however contrary to previously published experiments, it was not possible to abolish channel activity completely. It has previously reported that DMA is also an inhibitor of Vpu [73], and in the experiments reported in section 2.3.7 the mean channel open time was reduced by 50% in the presence of 100 μ M DMA.

It has previously been suggested that HMA inhibits ion channel activity by binding to the lumen of the channel and blocking ion flow by occluding the pore [76, 77]. Docking simulation studies have also suggested the side chain of Trp23, which is predicted to lie on the lipid-accessible face of the Vpu oligomer, as a potential binding site for the drug [76]. By analogy with eukaryotic ion channel inhibitors, (see section 1.7), the binding of a drug to the lipid accessible face of the channel could promote the adoption of a desensitised closed state. Molecular dynamics (MD) simulations were therefore used to investigate modes of inhibition which involve the initial partitioning of the drug into the lipid bilayer.

The octanol-water partition coefficient of HMA was determined by isocratic HPLC ($\log(P) = 2.63$). HMA was observed to partition into model lipid membranes from the aqueous phase by MD simulations and to remain within bilayer over the course of a series of 10 ns simulations. A particularly strong electrostatic interaction was formed between the positively charged guanidium headgroup of HMA and the negatively charged phosphate groups, and this interaction appears to restrict the motion of the headgroups of lipids within 10 Å of the drug relative to those of the bulk lipid. The presence of the drug also allowed water to penetrate further into

the bilayer around the HMA molecule than into the bulk bilayer. No significant differences were observed in the interactions between HMA, DMA, amiloride and the phospholipids, suggesting that HMA is unlikely to inhibit Vpu by altering the biophysical properties of the membrane.

The interaction between HMA and the sidechain of Trp23 was also investigated by MD simulations. HMA was able to bind stably over the course of six 5 ns simulations to the sidechain, however amiloride, which does not inhibit ion flux through the channel, was not able to remain bound to Trp23. Throughout the simulation, the aromatic system of HMA maintained a perpendicular distance of 0.4 nm from the double ring system of the Trp23 side chain, suggesting that a π bond stacking interaction between the two groups is possible (although not explicitly modelled by the simulation parameters). The binding of HMA to residue Trp23 had a dramatic impact on the conformation of the lipid surrounding the channel. The headgroup of the neighbouring phospholipid molecule was pulled downwards to maintain the electrostatic bond between its phosphate group and the HMA guanidium group, so that the choline moiety rested 5 nm below the mean height of the other choline groups in the bilayer. The displacement of the lipid enabled the permeation of water into the bilayer around residue Val25, and it is suggested that this results in a decrease in the stability of the channel and therefore a decrease in the channel openings and the lengthening of the closed channel duration observed in Chapter 2. Electrophysiological experiments with a Vpu₁₋₃₂ mutant, from which Trp23 has been deleted, would be able to verify whether this mechanism is correct.

Solid state NMR was used to test the predictions made by MD simulation, that HMA, DMA and amiloride are able to spontaneously insert into a phospholipid membrane from the aqueous phase. ¹H MAS NOESY spectra of the drugs solubilised in DMPC were acquired at 600 MHz and 500 MHz. Crosspeaks were

observed between the lipid and the drug resonances and indicate that the guanidinium group of HMA resides close to the phospholipid headgroups, that the aromatic system of the drug lies close to the glycerol backbone and that the hexamethylene ring of the drug lies close to the fatty acid chains.

The suggestion that a strong electrostatic interaction is present between the negatively charged phosphate group of the lipid and the positively charged drug guanidinium group, was supported by 1D ^{31}P NMR experiments. Increasing concentrations of HMA were added to a 2:1 molar ratio of the lipids DMPC:DMPG. As the concentration of the drug was increased, the intensity of the resonance arising from the DMPG phosphate group decreased, suggesting a preferential association between the drug and the negatively charged lipid. The decrease in the mobility of the phospholipid headgroups close to the HMA, as observed by MD simulation, is suggested to be responsible for the decrease in intensity of the DMPG peak [255].

HMA and amiloride were shown by Raman spectroscopy to be able to induce lipid acyl chain disorder in DMPC vesicles, in a similar manner to many anaesthetics [243]. Since this effect occurs at concentrations below which inhibition of the Vpu channel occurs, it seems unlikely that HMA inhibits Vpu by altering the biophysical properties of the bulk lipid.

Rotational-Echo Double Resonance solid state NMR spectroscopy was performed to determine whether there was any evidence for the binding of HMA to Vpu. HMA was synthesised and ^{13}C -labelled at the guanidinium group along with a Vpu_{1–32} helix ^{15}N -labelled at on the peptide backbone at position Trp23. No dephasing of the HMA signal was observed in the ^{13}C spectrum, indicating that if there is no evidence for an interaction between the two groups. The possibility remains that HMA is able to bind to Vpu, either in the lumen of the channel [76], or to residue Trp23, as predicted by the MD simulations in Chapter 4, but that

the interaction is relatively weak and that the drug at its binding site on the protein is equilibrium with the population of drug molecules solubilised in the lipid headgroup region.

Several different lipid types and sample preparation methods have been used in the experiments reported in this thesis. For example, although the ^1H MAS NOESY NMR experiments and the Raman spectroscopy were both performed using HMA inserted into DMPC vesicles, the NMR used sonication to rehydrate the drug and lipid mixture, whereas the freeze-thawing was used for the Raman spectroscopy. POPC was the used primarily in the MD simulations. The consistency of the conclusions drawn from a range of both biophysical techniques and sample preparation methods, indicates that the partitioning of HMA into membrane does not originate from an artefact.

There are many inhibitors of eukaryotic ion channels which are thought to prevent ion transport, by binding to the protein and stabilising an inactive or desensitised form of the channel (see section 1.7). Many of these compounds are widely used in medicine and are routinely prescribed for patients. It is possible that HMA inhibits the ion channel activity of Vpu in a similar way, partitioning in cell membranes, diffusing laterally across the bilayer to the channel protein. Annular lipid regions have been identified in several eukaryotic ion channels including the *Torpedo* nAChR [126]. Water has been shown to penetrate into the annular lipid domain to a lesser degree to than the bulk bilayer lipid, making the region more hydrophobic [123]. It is plausible that a similar annular lipid region surrounds Vpu. Since unlike eukaryotic ion channels, each Vpu monomer has only a single transmembrane helix and so changes in the lipid environment on the outside of the oligomeric channel, are likely to effect the channel architecture and therefore ion flux. The data from this thesis suggest that HMA is able to penetrate the inter-helical region and to change its character, by increasing its water content.

This could then lead to channel inhibition, by favouring a closed or inactive conformation.

7.3 Conclusion

Progress in the study of Vpu has been made in this thesis. The kinetics of channel activity and the mechanism of inhibition have been investigated using a combination of biophysical methods. Despite its simplicity, Vpu shares many characteristics with larger eukaryotic and prokaryotic channels. The mechanism of the inhibition of the channel by HMA appears to share some characteristics with the inhibition of the eukaryotic ligand-gated ion channels by amphipathic drugs (see section 1.7). The advances made in this thesis will inform the wider field of ion channel study and may also have implications for the design of inhibitors for Vpu and for novel anti-retroviral therapies against HIV-1 infection and AIDS.

Appendix A

List of Viral Ion Channels

TABLE A.1: Viral proteins which have been identified as having ion channel activity.

Protein	Virus	Family	
3a	SARS-CoV	Coronaviridae	[278]
E protein	SARS-CoV	Coronaviridae	[279]
E protein	Murine Hepatitis Virus	Coronaviridae	[280]
Vpr	HIV-1	Retroviridae	[281]
Vpu	HIV-1	Retroviridae	[59]
M2	Influenza A	Orthomyxoviridae	[88]
BM2	Influenza B	Orthomyxoviridae	[282]
NB	Influenza B	Orthomyxoviridae	[283]
CM2	Influenza C	Orthomyxoviridae	[284]
p7	Hepatitis C Virus	Flaviviridae	[95]
E2-p7	Bovine Viral Diarrhea Virus	Flaviviridae	[100]
p13-C	GB Virus B	Flaviviridae	[98]
DVM-C	Dengue Virus	Flaviviridae	[285]
2B	Coxsackie virus	Picornaviridae	[286]
SH	Human Respiratory Syncytial Virus	Paramyxoviridae	[287]
6k	Sindbis virus	Togaviridae	[288]
6k	Semliki Forest Virus	Togaviridae	[289]
6K	Ross River Virus	Togaviridae	[105]
6K	Barmah Forest virus	Togaviridae	[105]
Kcv	<i>Paramecium bursaria</i> Chlorella Virus 1	Phycodnaviridae	[290]

Appendix B

General Methods

B.1 Solid Phase Peptide Synthesis

Fmoc solid phase peptide synthesis was performed using a automated peptide synthesiser (Pioneer, Prospective Biosystems). Figure B.1 shows a general overview of solid phase peptide synthesis.

Coupling reagents (*N*-Hydroxybenzotriazole (HOBt), 2-(1-H-Benzotriazole-1-yl)-1,1,3,3-tetramethyluronium hexafluorophosphate (HBTU), Benzotriazole-1-yl-oxy-trispyrrolidino-phosphonium hexafluorophosphate (PyBOP)), Fmoc-protected amino acids, and solid support (Fmoc-PAL-PEG-PS resin, loading 0.25 mmol/g) were obtained from Novabiochem (Merck).

Prior to peptide-resin cleavage, the resin was washed with DCM, methanol and diethyl ether and dried for 24 hours in a dessicator under vacuum. The peptides were cleaved from the resin by agitation for 3 hours in cleavage solution (trifluoroacetic acid (TFA) (95%), triethylsilane (TES) (2.5%) and water (2.5%)). The resultant liquid was filtered and the resin washed with 95% TFA / 5% water. Excess TFA was then evaporated off under a stream of nitrogen until approximately

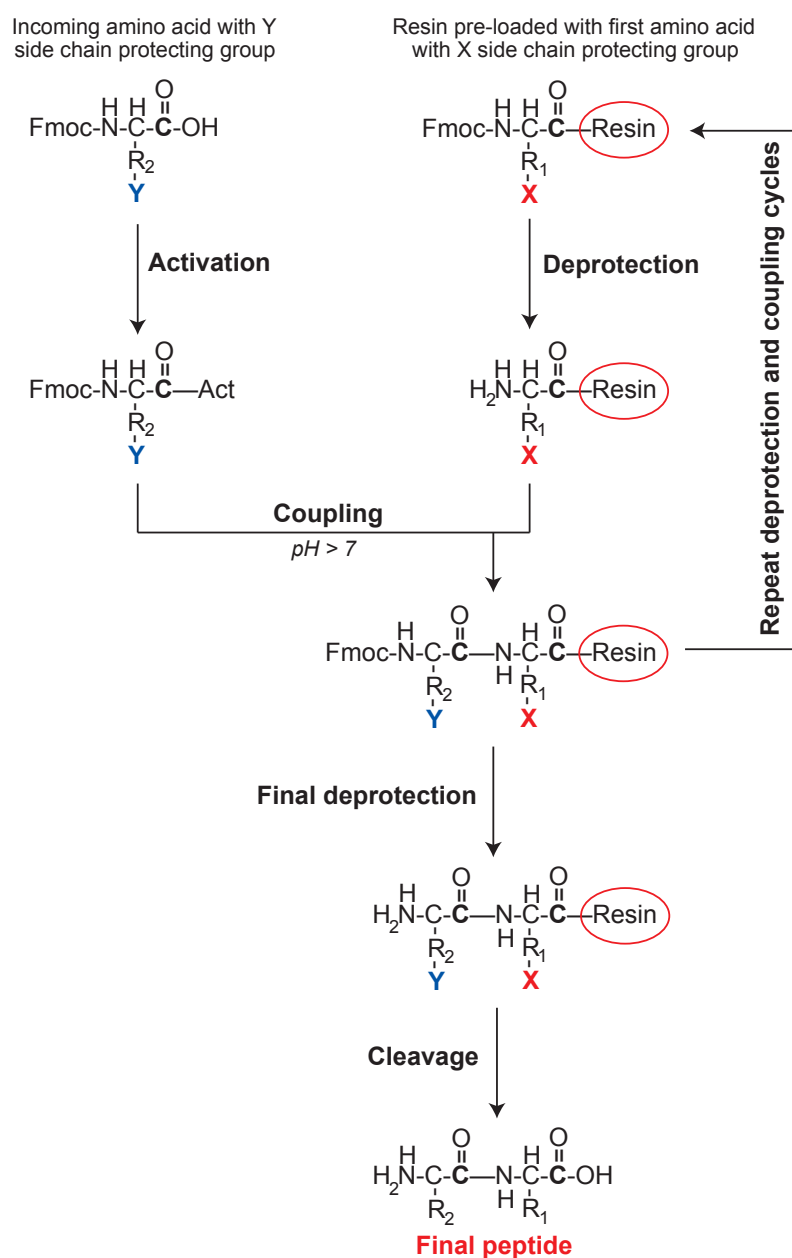


FIGURE B.1: *General scheme for Fmoc solid phase peptide synthesis.* Initially the first Fmoc amino acid is attached to an insoluble support resin via an acid-labile linker. Deprotection of the Fmoc protecting group is accomplished by treating the resin with a base (typically piperidine). The second Fmoc-protected amino acid is coupled using a pre-activated species or *in situ* activation. After coupling, excess reagents are removed by washing the resin. The process is repeated until the desired peptide sequence is assembled. In the final step, the resin-bound peptide is deprotected and then detached from the solid support using a trifluoroacetic acid (TFA) cleavage. Diagram adapted from Sigma Genosys technical bulletin.

1 ml remained. Ice cold diethyl ether (40 ml) was added, followed by centrifugation at 5000 g, 4 °C, 15 minutes. The supernatant was discarded and the ether extraction was repeated twice on the peptide pellet.

B.2 Heat shock transformation of competent cells

BL21 competent cells were obtained from Invitrogen. A 50 μ l aliquot of competent cells was thawed on ice, 1 μ l of plasmid DNA stock was added and the cells were incubated on ice for 30 minutes. The cells were then subjected to a heat shock 42 °C of 60 s duration and then returned to the ice for a further 10 minutes. SOC media (450 μ l) (see section C.1) was added and the culture agitated at 200 rpm for 60 minutes at 37 °C. The resulting culture was used to inoculate LB agar plates containing 100 μ g/ml ampicilin, which were incubated overnight at 37 °C.

B.3 SDS PAGE

Proteins were separated by SDS-PAGE using an X-cell Surelock minicell and pre-cast Tris-Glycine gels (Invitrogen). For Coomassie staining, gels were incubated for 2 hours at room temperature with agitation in Coomassie Brilliant Blue staining solution (Coomassie Brilliant Blue R250 (0.25% w/v), methanol (45% v/v), MilliQ H₂O (45% v/v), glacial acetic acid (10% v/v)), followed by destain solution (methanol (45% v/v), MilliQ H₂O (45% v/v), glacial acetic acid (10% v/v)). For Western blotting, proteins were transferred to nitrocellulose membrane (GE Healthcare) by semi-dry transfer (Biorad Transblot). Membranes were probed with mouse anti-Vpu antibody (Klaus Strebel) using WesternBreeze Chemiluminescent Western Blot Immunodetection Kit (Invitrogen).

B.4 Basic principles of solid state NMR

The nuclear spin Hamiltonian, (the energy operator containing the terms for the internal and external interaction of the spin system under consideration) is given by:

$$H = H_{ZN} + H_{CS} + H_J + H_D + H_Q \quad (\text{B.1})$$

The Hamiltonian for the Zeeman Interaction (H_{ZN}) measures the interaction between nuclear spin I and the magnetic field B_0 :

$$H_{ZN} = \gamma\eta B_0 I_Z \quad (\text{B.2})$$

where I_Z is the component of the macroscopic magnetisation operator aligned parallel to the direction of the B_0 field and γ is the gyromagnetic ratio.

The Hamiltonian for the chemical shift interaction (H_{CS}) is given by:

$$H_{CS} = \gamma\eta B_0 \sigma_{ZZ}^{labframe} I_Z \quad (\text{B.3})$$

where σ_{ij} , the chemical shift is a second rank tensor with principle elements σ_{11} , σ_{22} , σ_{33} . H_{CS} may be explicitly written as:

$$H_{CS} = \gamma\eta(\sigma_{11}\sin^2\theta \cos^2\phi + \sigma_{22}\sin^2\theta \sin^2\phi + \sigma_{33}\cos^2\theta)B_0 I_Z \quad (\text{B.4})$$

where θ and ϕ describe the angles formed between the principle axis and the laboratory fixed axis (see figure B.2).

The shielding anisotropy ($\Delta\sigma$), asymmetry parameter η and the isotropic chemical shift σ_{iso} can also be derived:

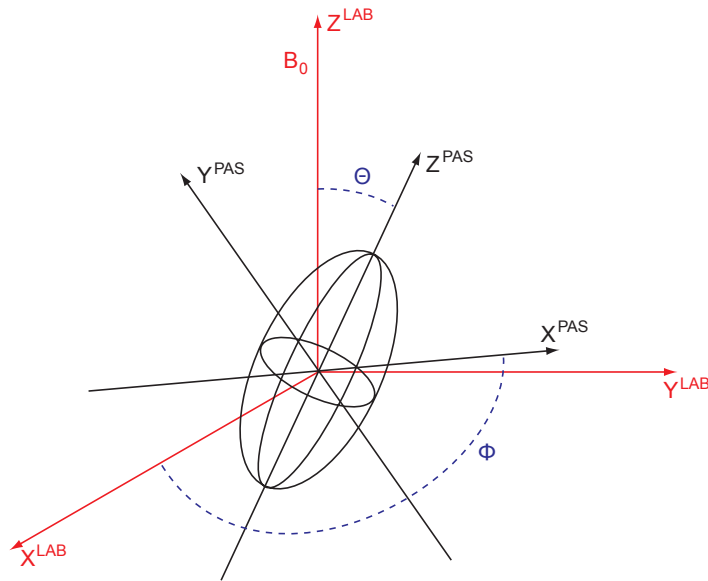


FIGURE B.2: *Chemical shielding ellipsoid with the geometric relationship between the Principal Axis System (PAS) of the nucleus and laboratory fixed axis (LAB).*

$$\Delta\sigma = \sigma_{33} - \frac{1}{2}(\sigma_{11} + \sigma_{22}) \quad (\text{B.5})$$

$$\sigma_{iso} = \frac{1}{3}(\sigma_{11} + \sigma_{22} + \sigma_{33}) \quad (\text{B.6})$$

$$\eta = \frac{\sigma_{22} - \sigma_{11}}{\sigma_{33} - \sigma_{iso}} \quad (\text{B.7})$$

Fermi-contact mediated interactions between nuclear spins give rise to the electron-mediated, J coupling Hamiltonian:

$$H_J = 2\pi I J I \quad (\text{B.8})$$

characterised by the indirect spin coupling tensor J . The Hamiltonian can be divided into the isotropic and anisotropic components:

$$H_J^{iso} = 2\pi J I_1 I_2 \quad (\text{B.9})$$

$$H_J^{aniso} = 2\pi J^{aniso} I_1 I_2 \quad (\text{B.10})$$

The homonuclear dipolar interaction can be approximated by the Hamiltonian H_D :

$$H_D = \frac{1}{2} \frac{\gamma_1 \gamma_2}{r^3} (1 - 3 \cos^2 \theta) (3I_Z S_Z - I \cdot S) \quad (\text{B.11})$$

and the heteronuclear dipolar interaction can be approximated by:

$$H_D = \frac{1}{2} \frac{\gamma_1 \gamma_2}{r^3} (1 - 3 \cos^2 \theta) (2I_Z S_Z) \quad (\text{B.12})$$

The Hamiltonian for the quadrupolar interaction of a nucleus having spin ≥ 1 , may be written in the form

$$H_Q = I Q I \quad (\text{B.13})$$

where Q can be expressed as a function of the electrical field at the nucleus (V):

$$Q = \frac{eQ}{2I(2I-1)\eta} V \quad (\text{B.14})$$

where eQ is the nuclear quadrupolar moment. Under the high field approximation, the Zeeman interaction is larger than the quadrupolar interaction and the non-secular terms may be ignored to give:

$$V_{zz}^{labframe} = \frac{1}{2}(3 \cos^2 \theta - 1)V_{xx}^{PAS} + \frac{1}{2}3 \sin^2 \theta \cos 2\phi(V_{xx}^{PAS} - V_{yy}^{PAS}) \quad (\text{B.15})$$

The asymmetry parameter η is given by

$$\eta = \frac{V_{xx} - V_{yy}}{V_{zz}} \quad (\text{B.16})$$

where by convention $V_{zz} \geq V_{xx} \geq V_{yy}$

$$V^{2,0} = \frac{1}{2}((3 \cos^2 \theta - 1) + \eta \sin^2 \theta \cos 2\phi) \quad (\text{B.17})$$

For an axially symmetrical deuteron, ($\eta = 0$), the quadrupolar contribution may be written as:

$$H_Q = \frac{e^2 q Q (3I_z^2 - I^2)}{4\eta} (3 \cos^2 \theta - 1) \quad (\text{B.18})$$

B.4.1 Magic Angle Spinning

NMR spectra of solid samples are typically more poorly resolved than those of liquid samples. Rapid rotation of a solid sample at the magic angle 54.73° reduces the line broadening caused by dipolar coupling to zero. The reduction occurs, because the dipolar interactions (D), indirect electron coupled interactions, chemical shift anisotropy (σ) and quadrupolar interactions are all affected in the same way.

Recalling equation B.11, the Hamiltonian for the homonuclear dipolar interactions (H_d) may be written:

$$H_D = \frac{1}{2} \frac{\gamma_1 \gamma_2}{r^3} (1 - 3 \cos^2 \theta) (3I_Z S_Z - I.S) \quad (\text{B.11})$$

If a sample is rotated about an axis inclined at β to the magnetic field (B_0), then the resulting spectrum will retain its shape, but be reduced in width by the scale factor $F(\beta)$:

$$F(\beta) = \frac{1}{2} (3 \cos^2 \beta - 1) \quad (\text{B.19})$$

so that when $\beta = 0^\circ$, 90° and 54.73° then $F(\beta) = 1$, 0.5 and 0 respectively. The angle 54.73° is commonly referred to as the *magic angle* [291, 292].

In theory, all anisotropic effects may be removed by rotation at the magic angle, but for most biological samples, this is not the case. Rapid isotropic motions within a solid may help to reduce linewidths, which are then further reduced by magic angle spinning (MAS), however slow and moderate isotropic motion may leave broadened lines. To narrow lines further which have already been narrowed by internal motions, may require MAS at a rate which exceeds the internal motion (technically impossible to achieve). Rapid molecular motion may therefore be a hindrance to achieving liquid state resolution [293].

B.5 Raman Spectroscopy

B.5.1 Apparatus

A continuous-wave Argon ion laser of wavelength 514.5 nm and maximum power 2 W, (Innova 90-5-UV, Coherent). The beam was passed through two sets of lenses and reflected from a 1:2 beamsplitter into the microscope. Light was directed through the objective lens (x63 NA 1.2, Leica Microsystems) by a dichroic mirror and the optical trap was formed in the sample cell (see figure B.3).

Raman light scattered back from the focal point was focussed by the objective lens and passed back along the same pathway to the beam splitter. A holographic notch filter (HNF-514, Kaiser Optical Systems) was placed after the beamsplitter allowing only Raman light shifted above 514.5nm to enter the spectrometer (SpectraPro-500 Acton Research Company) and detector (LN/CCD-1024, Princeton Instruments) [294]. The liposome was observed using filtered light (>700 nm) focussed onto a CCD array camera.

B.5.2 Calibration

The spectrometer was calibrated using toluene (spectroscopic grade, Aldrich). Recorded wavenumbers were accurate to 2 cm^{-1} . Background noise was eliminated by subtracting the Raman spectrum of the dispersion medium from the liposome spectrum. Peak ratios were calculated after the background spectrum had been subtracted.

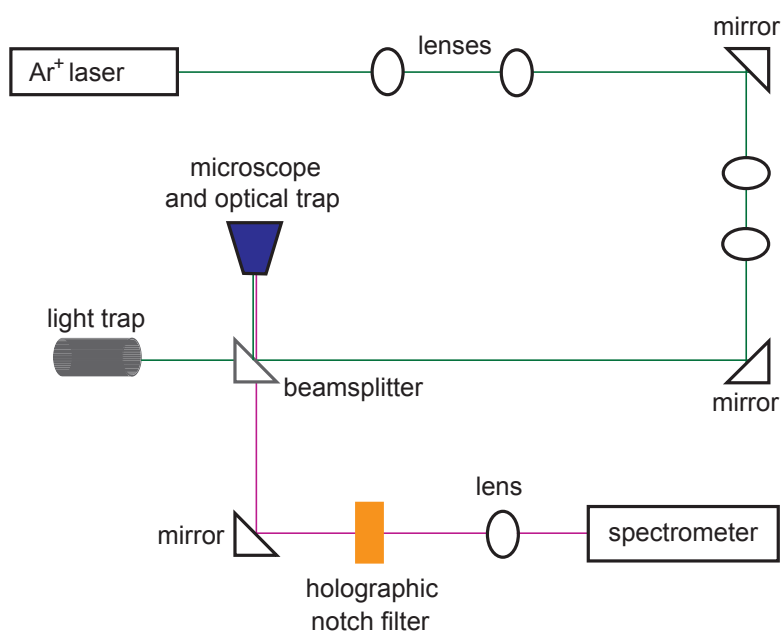


FIGURE B.3: *Diagram of Raman apparatus* All equipment was secured to an anti-vibration table (Newport Inc.)

Appendix C

Media and buffer compositions

C.1 Growth media

Luria-Betani (LB) liquid media Per litre ddH₂O: 10 g bacto-tryptone, 5 g yeast extract, 10 g NaCl, pH 7.0.

Luria-Betani (LB) agar Per litre ddH₂O: 16 g bacto-tryptone, 5 g yeast extract, 10 g NaCl, 15 g agar, pH 7.0.

SOC medium Per litre ddH₂O: 20 g bacto-tryptone, 5 g yeast extract, 0.5 g NaCl, 2.5 g KCl, 10 mM MgCl₂, 20 mM glucose, pH 7.0.

C.2 SDS PAGE

2x sample buffer 200 mM Tris-HCl (pH 8.8), 20% glycerol (v/v), 5 mM EDTA, 0.02% bromophenol blue (w/v). To a 700 μ l aliquot, add 200 μ l 20% SDS (w/v) and 100 μ l, 500 mM DTT before use.

Tris-Glycine SDS running buffer 25 mM Tris pH 8.3, 192 mM glycine, 0.1% SDS (w/v).

Tris-Glycine transfer buffer 12 mM Tris pH 8.3, 96 mM glycine.

C.3 Vpu₁₋₈₂ purification buffers

PBS buffer 150 mM NaCl, 16 mM Na₂HPO₄, 4 mM NaH₂PO₄

Buffer I 50 mM Tris/HCl pH 7.5, 5% glycerol v/v, 1 mM NaEDTA, 1 mM NaN₃, 10 mM DTT, protease inhibitor cocktail (complete EDTA-free, Roche)

Buffer II 50 mM Tris/HCl pH 7.5, 100 mM NaCl, 1 mM NaN₃, 10 mM DTT, protease inhibitor cocktail (complete EDTA-free, Roche)

Buffer III 50 mM Tris/HCl pH 7.5, 1% Na⁺ deoxycholate, 1% Triton X100, 1 mM NaN₃, mM DTT

GHB Buffer 6 M guanidium HCl, 0.5 mM NaCl, 20 mM Tris/HCl pH 7.5

TCB Buffer 50 mM Tris/HCl, 150 mM NaCl, 2.5 mM CaCl₂

C.4 HPLC Buffers

Buffer A 90% milliQ H₂O, 10% ACN, 0.1% TFA

Buffer B 10% milliQ H₂O, 90% ACN, 0.1% TFA

Bibliography

- [1] Deamer, D., J. P. Dworkin, S. A. Sandford, M. P. Bernstein, and L. J. Allamandola, 2002. The first cell membranes. *Astrobiology* 2:371–381.
- [2] Monnard, P.-A., and D. W. Deamer, 2002. Membrane self-assembly processes: Steps toward the first cellular life. *Anat Rec* 268:196–207.
- [3] Weiss, T., 1996. Cellular Biophysics: Transport, volume 1. MIT Press, Cambridge, MA., 1st edition.
- [4] Singer, S. J., and G. L. Nicolson, 1972. The fluid mosaic model of the structure of cell membranes. *Science* 175:720–731.
- [5] Nicholls, D. G., and S. J. Ferguson, 2002. Bioenergetics 3. Academic Press, 3rd edition.
- [6] Berry, S., 2002. The chemical basis of membrane bioenergetics. *J Mol Evol* 54:595–613.
- [7] Schäfer, G., M. Engelhard, and V. Müller, 1999. Bioenergetics of the Archaea. *Microbiol Mol Biol Rev* 63:570–620.
- [8] Matthews, C. K., and K. E. van Holde, 1990. Biochemistry. Benjamin Cummings Publishing Co.
- [9] Subczynski, W. K., L. E. Hopwood, and J. S. Hyde, 1992. Is the mammalian cell plasma membrane a barrier to oxygen transport? *J Gen Physiol* 100:69–87.
- [10] Ren, Q., and I. T. Paulsen, 2005. Comparative analyses of fundamental differences in membrane transport capabilities in prokaryotes and eukaryotes. *PLoS Comput Biol* 1:e27.
- [11] Hille, B., 2001. Ion channels of excitable membranes. Sinauer Associates, Inc, 3rd edition.
- [12] Zhorov, B. S., and D. B. Tikhonov, 2004. Potassium, sodium, calcium and glutamate-gated channels: Pore architecture and ligand action. *J Neurochem* 88:782–799.
- [13] Booth, I. R., M. D. Edwards, S. Black, U. Schumann, and S. Miller, 2007. Mechanosensitive channels in bacteria: signs of closure? *Nat Rev Microbiol* 5:431–440.

- [14] Ashcroft, F., 2000. Ion Channels and Disease. Academic Press.
- [15] Clare, J. J., and D. J. Trezise, 2006. Expression and analysis of recombinant ion channels: From structural studies to pharmacological screening. John Wiley and Sons.
- [16] Fischer, W. B., and M. S. P. Sansom, 2002. Viral ion channels: Structure and function. *Biochim Biophys Acta* 1561:27–45.
- [17] Pinto, L. H., and R. A. Lamb, 2006. The M2 proton channels of Influenza A and B viruses. *J Biol Chem* 281:8997–9000.
- [18] Clarke, D., S. Griffin, L. Beales, C. S. Gelais, S. Burgess, M. Harris, and D. Rowlands, 2006. Evidence for the formation of a heptameric ion channel complex by the Hepatitis C Virus p7 protein in vitro. *J Biol Chem* 281:37057–37068.
- [19] Liu, W., E. Crocker, D. J. Siminovitch, and S. O. Smith, 2003. Role of side-chain conformational entropy in transmembrane helix dimerization of glycophorin A. *Biophys J* 84:1263–1271.
- [20] de Planque, M. R. R., B. B. Bonev, J. A. A. Demmers, D. V. Greathouse, R. E. Koeppe, F. Separovic, A. Watts, and J. A. Killian, 2003. Interfacial anchor properties of tryptophan residues in transmembrane peptides can dominate over hydrophobic matching effects in peptide-lipid interactions. *Biochemistry* 42:5341–5348.
- [21] Gonzalez, M. E., and L. Carrasco, 2003. Viroporins. *FEBS Lett* 552:28–34.
- [22] Sanz, M. A., V. Madan, L. Carrasco, and J. L. Nieva, 2003. Interfacial domains in Sindbis virus 6K protein. Detection and functional characterization. *J Biol Chem* 278:2051–2057.
- [23] Griffin, S. D. C., L. P. Beales, D. S. Clarke, O. Worsfold, S. D. Evans, J. Jaeger, M. P. G. Harris, and D. J. Rowlands, 2003. The p7 protein of Hepatitis C virus forms an ion channel that is blocked by the antiviral drug, Amantadine. *FEBS Lett* 535:34–38.
- [24] Beitz, E., 2000. T(E)Xtopo: shaded membrane protein topology plots in LAT(E)X2epsilon. *Bioinformatics* 16:1050–1051.
- [25] Piot, P., editor, 2006. 2006 Report on the global AIDS epidemic. UNAIDS.
- [26] Popovic, M., M. G. Sarngadharan, E. Read, and R. C. Gallo, 1984. Detection, isolation, and continuous production of cytopathic retroviruses (HTLV-III) from patients with AIDS and pre-AIDS. *Science* 224:497–500.
- [27] Zagury, D., J. Bernard, J. Leibowitch, B. Safai, J. E. Groopman, M. Feldman, M. G. Sarngadharan, and R. C. Gallo, 1984. HTLV-III in cells cultured from semen of two patients with AIDS. *Science* 226:449–451.

- [28] Gallo, R. C., 2002. Human retroviruses after 20 years: A perspective from the past and prospects for their future control. *Immunol Rev* 185:236–265.
- [29] Buchbinder, S. P., M. H. Katz, N. A. Hessel, P. M. O’Malley, and S. D. Holmberg, 1994. Long-term HIV-1 infection without immunologic progression. *AIDS* 8:1123–1128.
- [30] Narayan, O., and J. E. Clements, 1989. Biology and pathogenesis of *Lentiviruses*. *J Gen Virol* 70 (Pt 7):1617–1639.
- [31] Narayan, O., and M. C. Zink, 1988. Role of macrophages in *Lentivirus* infections. *Adv Vet Sci Comp Med* 32:129–148.
- [32] Narayan, O., D. E. Griffin, and A. M. Silverstein, 1977. Slow virus infection: Replication and mechanisms of persistence of Visna virus in sheep. *J Infect Dis* 135:800–806.
- [33] Gao, F., E. Bailes, D. L. Robertson, Y. Chen, C. M. Rodenburg, S. F. Michael, L. B. Cummins, L. O. Arthur, M. Peeters, G. M. Shaw, P. M. Sharp, and B. H. Hahn, 1999. Origin of HIV-1 in the chimpanzee *Pan troglodytes troglodytes*. *Nature* 397:436–441.
- [34] Keele, B. F., F. Van Heuverswyn, Y. Li, E. Bailes, J. Takehisa, M. L. Santiago, F. Bibollet-Ruche, Y. Chen, L. V. Wain, F. Liegeois, S. Loul, E. M. Ngole, Y. Bienvenue, E. Delaporte, J. F. Y. Brookfield, P. M. Sharp, G. M. Shaw, M. Peeters, and B. H. Hahn, 2006. Chimpanzee reservoirs of pandemic and nonpandemic HIV-1. *Science* 313:523–526.
- [35] Korber, B., M. Muldoon, J. Theiler, F. Gao, R. Gupta, A. Lapedes, B. H. Hahn, S. Wolinsky, and T. Bhattacharya, 2000. Timing the ancestor of the HIV-1 pandemic strains. *Science* 288:1789–1796.
- [36] Worobey, M., M. Gemmel, D. E. Teuwen, T. Haselkorn, K. Kunstman, M. Bunce, J.-J. Muyembe, J.-M. M. Kabongo, R. M. Kalengayi, E. Van Marck, M. T. P. Gilbert, and S. M. Wolinsky, 2008. Direct evidence of extensive diversity of HIV-1 in Kinshasa by 1960. *Nature* 455:661–664. <http://dx.doi.org/10.1038/nature07390>.
- [37] Reeves, J. D., and R. W. Doms, 2002. Human Immunodeficiency Virus Type 2. *J Gen Virol* 83:1253–1265.
- [38] Robertson, D. L., J. P. Anderson, J. A. Bradac, J. K. Carr, B. Foley, R. K. Funkhouser, F. Gao, B. H. Hahn, M. L. Kalish, C. Kuiken, G. H. Learn, T. Leitner, F. McCutchan, S. Osmanov, M. Peeters, D. Pieniazek, M. Salmiinen, P. M. Sharp, S. Wolinsky, and B. Korber, 2000. HIV-1 nomenclature proposal. *Science* 288:55–56.
- [39] Osmanov, S., C. Pattou, N. Walker, B. Schwardlander, and J. Esparza, 2002. Estimated global distribution and regional spread of HIV-1 genetic subtypes in the year 2000. *J Acquir Immune Defic Syndr* 29:184–190.

- [40] Hemelaar, J., E. Gouws, P. D. Ghys, and S. Osmanov, 2006. Global and regional distribution of HIV-1 genetic subtypes and recombinants in 2004. *AIDS* 20:W13–23.
- [41] Miller, R. H., and N. Sarver, 1997. HIV accessory proteins as therapeutic targets. *Nat Med* 3:389–394.
- [42] Pacyniak, E., M. L. Gomez, L. M. Gomez, E. R. Mulcahy, M. Jackson, D. R. Hout, B. J. Wisdom, and E. B. Stephens, 2005. Identification of a region within the cytoplasmic domain of the subtype B Vpu protein of Human Immunodeficiency Virus Type 1 (HIV-1) that is responsible for retention in the golgi complex and its absence in the Vpu protein from a subtype C HIV-1. *AIDS Res Hum Retroviruses* 21:379–394.
- [43] Strebel, K., T. Klimkait, and M. A. Martin, 1988. A novel gene of HIV-1, Vpu, and its 16-kilodalton product. *Science* 241:1221–1223.
- [44] Strebel, K., T. Klimkait, F. Maldarelli, and M. A. Martin, 1989. Molecular and biochemical analyses of Human Immunodeficiency Virus Type 1 Vpu protein. *J Virol* 63:3784–3791.
- [45] Willey, R. L., F. Maldarelli, M. A. Martin, and K. Strebel, 1992. Human Immunodeficiency Virus type 1 Vpu protein induces rapid degradation of CD4. *J Virol* 66:7193–7200.
- [46] Terwilliger, E. F., E. A. Cohen, Y. C. Lu, J. G. Sodroski, and W. A. Haseltine, 1989. Functional role of Human Immunodeficiency Virus Type 1 Vpu. *Proc Natl Acad Sci U S A* 86:5163–5167.
- [47] Marassi, F. M., C. Ma, H. Gratkowski, S. K. Straus, K. Strebel, M. Oblatt-Montal, M. Montal, and S. J. Opella, 1999. Correlation of the structural and functional domains in the membrane protein Vpu from HIV-1. *Proc Natl Acad Sci U S A* 96:14336–14341.
- [48] Greene, W. C., and B. M. Peterlin, 2002. Charting HIV’s remarkable voyage through the cell: Basic science as a passport to future therapy. *Nat Med* 8:673–680.
- [49] Margottin, F., S. Benichou, H. Durand, V. Richard, L. X. Liu, E. Gomas, and R. Benarous, 1996. Interaction between the cytoplasmic domains of HIV-1 Vpu and CD4: role of Vpu residues involved in CD4 interaction and *in vitro* CD4 degradation. *Virology* 223:381–386.
- [50] Kimura, T., M. Nishikawa, and A. Ohyama, 1994. Intracellular membrane traffic of Human Immunodeficiency Virus type 1 envelope glycoproteins: Vpu liberates Golgi-targeted gp160 from CD4-dependent retention in the endoplasmic reticulum. *J Biochem* 115:1010–1020.
- [51] Singh, D. K., D. M. Griffin, E. Pacyniak, M. Jackson, M. J. Werle, B. Wisdom, F. Sun, D. R. Hout, D. M. Pinson, R. S. Gunderson, M. F. Powers,

- S. W. Wong, and E. B. Stephens, 2003. The presence of the casein kinase II phosphorylation sites of Vpu enhances the CD4+ T cell loss caused by the Simian-Human Immunodeficiency Virus SHIV(KU-1bMC33) in pig-tailed macaques. *Virology* 313:435–451.
- [52] Bour, S., C. Perrin, and K. Strebel, 1999. Cell surface CD4 inhibits HIV-1 particle release by interfering with Vpu activity. *J Biol Chem* 274:33800–33806.
- [53] Hill, M. S., A. Ruiz, E. Pacyniak, D. M. Pinson, N. Culley, B. Yen, S. W. Wong, and E. B. Stephens, 2008. Modulation of the severe CD4(+) T-cell loss caused by a pathogenic Simian-Human Immunodeficiency Virus by replacement of the subtype B Vpu with the Vpu from a subtype C HIV-1 clinical isolate. *Virology* 371:86–97.
- [54] Larkin, M. A., G. Blackshields, N. P. Brown, R. Chenna, P. A. McGettigan, H. McWilliam, F. Valentin, I. M. Wallace, A. Wilm, R. Lopez, J. D. Thompson, T. J. Gibson, and D. G. Higgins, 2007. Clustal W and Clustal X version 2.0. *Bioinformatics* 23:2947–2948.
- [55] Bour, S., and K. Strebel, 1996. The Human Immunodeficiency Virus (HIV) type 2 envelope protein is a functional complement to HIV type 1 Vpu that enhances particle release of heterologous retroviruses. *J Virol* 70:8285–8300.
- [56] Bour, S., U. Schubert, K. Peden, and K. Strebel, 1996. The envelope glycoprotein of Human Immunodeficiency Virus Type 2 enhances viral particle release: A Vpu-like factor? *J Virol* 70:820–829.
- [57] Abada, P., B. Noble, and P. M. Cannon, 2005. Functional domains within the Human Immunodeficiency Virus Type 2 envelope protein required to enhance virus production. *J Virol* 79:3627–3638.
- [58] Varthakavi, V., R. M. Smith, S. P. Bour, K. Strebel, and P. Spearman, 2003. Viral protein U counteracts a human host cell restriction that inhibits HIV-1 particle production. *Proc Natl Acad Sci U S A* 100:15154–15159.
- [59] Ewart, G. D., T. Sutherland, P. W. Gage, and G. B. Cox, 1996. The Vpu protein of Human Immunodeficiency Virus type 1 forms cation-selective ion channels. *J Virol* 70:7108–7115.
- [60] Hsu, K., J. Seharaseyon, P. Dong, S. Bour, and E. Marban, 2004. Mutual functional destruction of HIV-1 Vpu and host TASK-1 channel. *Mol Cell* 14:259–267.
- [61] Abbott, G. W., F. Sesti, I. Splawski, M. E. Buck, M. H. Lehmann, K. W. Timothy, M. T. Keating, and S. A. Goldstein, 1999. MiRP1 forms IKr potassium channels with HERG and is associated with cardiac arrhythmia. *Cell* 97:175–187.

- [62] Coady, M. J., N. G. Daniel, E. Tiganos, B. Allain, J. Friberg, J. Y. Lapointe, and E. A. Cohen, 1998. Effects of Vpu expression on *Xenopus* oocyte membrane conductance. *Virology* 244:39–49.
- [63] Neil, S. J. D., T. Zang, and P. D. Bieniasz, 2008. Tetherin inhibits retrovirus release and is antagonized by HIV-1 Vpu. *Nature* 451:425–430.
- [64] Hout, D. R., M. L. Gomez, E. Pacyniak, L. M. Gomez, B. Fegley, E. R. Mulcahy, M. S. Hill, N. Culley, D. M. Pinson, W. Nothnick, M. F. Powers, S. W. Wong, and E. B. Stephens, 2006. Substitution of the transmembrane domain of Vpu in Simian-Human Immunodeficiency Virus (SHIVKU1bMC33) with that of M2 of Influenza A results in a virus that is sensitive to inhibitors of the M2 ion channel and is pathogenic for pig-tailed macaques. *Virology* 344:541–559.
- [65] Hout, D. R., L. M. Gomez, E. Pacyniak, J.-M. Miller, M. S. Hill, and E. B. Stephens, 2006. A single amino acid substitution within the transmembrane domain of the Human Immunodeficiency Virus Type 1 Vpu protein renders simian-human immunodeficiency virus (SHIV(KU-1bMC33)) susceptible to rimantadine. *Virology* 348:449–461.
- [66] Schubert, U., S. Bour, A. V. Ferrer-Montiel, M. Montal, F. Maldarell, and K. Strebel, 1996. The two biological activities of Human Immunodeficiency Virus type 1 Vpu protein involve two separable structural domains. *J Virol* 70:809–819.
- [67] Park, S. H., A. A. Mrse, A. A. Nevzorov, M. F. Mesleh, M. Oblatt-Montal, M. Montal, and S. J. Opella, 2003. Three-dimensional structure of the channel-forming trans-membrane domain of virus protein "u" (Vpu) from HIV-1. *J Mol Biol* 333:409–424.
- [68] Park, S. H., and S. J. Opella, 2007. Conformational changes induced by a single amino acid substitution in the trans-membrane domain of Vpu: implications for HIV-1 susceptibility to channel blocking drugs. *Protein Sci* 16:2205–2215.
- [69] Cordes, F. S., A. Kukol, L. R. Forrest, I. T. Arkin, M. S. Sansom, and W. B. Fischer, 2001. The structure of the HIV-1 Vpu ion channel: Modelling and simulation studies. *Biochim Biophys Acta* 1512:291–298.
- [70] Fischer, W. B., 2003. Vpu from HIV-1 on an atomic scale: experiments and computer simulations. *FEBS Lett* 552:39–46.
- [71] Tiganos, E., J. Friberg, B. Allain, N. G. Daniel, X. J. Yao, and E. A. Cohen, 1998. Structural and functional analysis of the membrane-spanning domain of the Human Immunodeficiency Virus Type 1 Vpu protein. *Virology* 251:96–107.

- [72] Schubert, U., A. V. Ferrer-Montiel, M. Oblatt-Montal, P. Henklein, K. Strebel, and M. Montal, 1996. Identification of an ion channel activity of the Vpu transmembrane domain and its involvement in the regulation of virus release from HIV-1-infected cells. *FEBS Lett* 398:12–18.
- [73] Ewart, G. D., K. Mills, G. B. Cox, and P. W. Gage, 2002. Amiloride derivatives block ion channel activity and enhancement of virus-like particle budding caused by HIV-1 protein Vpu. *Eur Biophys J* 31:26–35.
- [74] Ismailov, I. I., V. G. Shlyonsky, O. Alvarez, and D. J. Benos, 1997. Cation permeability of a cloned rat epithelial amiloride-sensitive Na⁺ channel. *J Physiol* 504 (Pt 2):287–300.
- [75] Kleyman, T. R., and E. J. J. Cragoe, 1988. Amiloride and its analogs as tools in the study of ion transport. *J Membr Biol* 105:1–21.
- [76] Kim, C. G., V. Lemaitre, A. Watts, and W. B. Fischer, 2006. Drug-protein interaction with Vpu from HIV-1: proposing binding sites for amiloride and one of its derivatives. *Anal Bioanal Chem* 386:2213–2217.
- [77] Lemaitre, V., R. Ali, C. G. Kim, A. Watts, and W. B. Fischer, 2004. Interaction of amiloride and one of its derivatives with Vpu from HIV-1: a Molecular Dynamics simulation. *FEBS Lett* 563:75–81.
- [78] Ewart, G. D., N. Nasr, H. Naif, G. B. Cox, A. L. Cunningham, and P. W. Gage, 2004. Potential new anti-Human Immunodeficiency Virus Type 1 compounds depress virus replication in cultured human macrophages. *Antimicrobial Agents and Chemotherapy* 48:2325–2330.
- [79] Castrucci, M. R., M. Hughes, L. Calzoletti, I. Donatelli, K. Wells, A. Takada, and Y. Kawaoka, 1997. The cysteine residues of the M2 protein are not required for Influenza A virus replication. *Virology* 238:128–134.
- [80] Mould, J. A., J. E. Drury, S. M. Frings, U. B. Kaupp, A. Pekosz, R. A. Lamb, and L. H. Pinto, 2000. Permeation and activation of the M2 ion channel of Influenza A virus. *J Biol Chem* 275:31038–31050.
- [81] Sakaguchi, T., G. P. Leser, and R. A. Lamb, 1996. The ion channel activity of the Influenza virus M2 protein affects transport through the Golgi apparatus. *J Cell Biol* 133:733–747.
- [82] Wang, C., R. A. Lamb, and L. H. Pinto, 1995. Activation of the M2 ion channel of Influenza virus: A role for the transmembrane domain histidine residue. *Biophys J* 69:1363–1371.
- [83] Venkataraman, P., R. A. Lamb, and L. H. Pinto, 2005. Chemical rescue of histidine selectivity filter mutants of the M2 ion channel of Influenza A virus. *J Biol Chem* 280:21463–21472.

- [84] Pinto, L. H., G. R. Dieckmann, C. S. Gandhi, C. G. Papworth, J. Braman, M. A. Shaughnessy, J. D. Lear, R. A. Lamb, and W. F. DeGrado, 1997. A functionally defined model for the M2 proton channel of Influenza A virus suggests a mechanism for its ion selectivity. *Proc Natl Acad Sci U S A* 94:11301–11306.
- [85] Lear, J. D., 2003. Proton conduction through the M2 protein of the Influenza A virus; a quantitative, mechanistic analysis of experimental data. *FEBS Lett* 552:17–22.
- [86] Mould, J. A., H. C. Li, C. S. Dudlak, J. D. Lear, A. Pekosz, R. A. Lamb, and L. H. Pinto, 2000. Mechanism for proton conduction of the M2 ion channel of Influenza A virus. *J Biol Chem* 275:8592–8599.
- [87] Smondyrev, A. M., and G. A. Voth, 2002. Molecular Dynamics simulation of proton transport through the Influenza A virus M2 channel. *Biophys J* 83:1987–1996.
- [88] Sugrue, R. J., and A. J. Hay, 1991. Structural characteristics of the M2 protein of Influenza A viruses: Evidence that it forms a tetrameric channel. *Virology* 180:617–624.
- [89] Schnell, J. R., and J. J. Chou, 2008. Structure and mechanism of the M2 proton channel of Influenza A virus. *Nature* 451:591–595.
- [90] Jing, X., C. Ma, Y. Ohigashi, F. A. Oliveira, T. S. Jardetzky, L. H. Pinto, and R. A. Lamb, 2008. Functional studies indicate amantadine binds to the pore of the Influenza A virus M2 proton-selective ion channel. *Proc Natl Acad Sci U S A* 105:10967–10972.
- [91] Miller, C., 2008. Ion channels: coughing up flu’s proton channels. *Nature* 451:532–533.
- [92] Bright, R. A., M.-j. Medina, X. Xu, G. Perez-Oronoz, T. R. Wallis, X. M. Davis, L. Povinelli, N. J. Cox, and A. I. Klimov, 2005. Incidence of adamantane resistance among influenza A (H3N2) viruses isolated worldwide from 1994 to 2005: a cause for concern. *Lancet* 366:1175–1181.
- [93] Wang, C., K. Takeuchi, L. H. Pinto, and R. A. Lamb, 1993. Ion channel activity of influenza A virus M2 protein: characterization of the amantadine block. *J Virol* 67:5585–5594.
- [94] Hatta, M., and Y. Kawaoka, 2003. The NB protein of Influenza B virus is not necessary for virus replication *in vitro*. *J Virol* 77:6050–6054.
- [95] Carrere-Kremer, S., C. Montpellier-Pala, L. Cocquerel, C. Wychowski, F. Penin, and J. Dubuisson, 2002. Subcellular localization and topology of the p7 polypeptide of the Hepatitis C virus. *J Virol* 76:3720–3730.
- [96] Lohmann, V., F. Korner, J. Koch, U. Herian, L. Theilmann, and R. Bartenschlager, 1999. Replication of subgenomic Hepatitis C virus RNAs in a hepatoma cell line. *Science* 285:110–113.

- [97] Patargias, G., N. Zitzmann, R. Dwek, and W. B. Fischer, 2006. Protein-protein interactions: Modeling the Hepatitis C Virus ion channel p7. *J Med Chem* 49:648–655.
- [98] Takikawa, S., R. E. Engle, S. U. Emerson, R. H. Purcell, M. St Claire, and J. Bukh, 2006. Functional analyses of GB virus B p13 protein: Development of a recombinant GB virus B Hepatitis virus with a p7 protein. *Proc Natl Acad Sci U S A* 103:3345–3350.
- [99] Premkumar, A., X. Dong, G. Haqshenas, P. W. Gage, and E. J. Gowans, 2006. Amantadine inhibits the function of an ion channel encoded by GB virus B, but fails to inhibit virus replication. *Antivir Ther* 11:289–295.
- [100] Harada, T., N. Tautz, and H. J. Thiel, 2000. E2-p7 region of the Bovine Viral Diarrhea Virus polyprotein: Processing and functional studies. *J Virol* 74:9498–9506.
- [101] Loewy, A., J. Smyth, C. H. von Bonsdorff, P. Liljestrom, and M. J. Schlesinger, 1995. The 6-kilodalton membrane protein of Semliki Forest virus is involved in the budding process. *J Virol* 69:469–475.
- [102] Gonzalez, M. E., and L. Carrasco, 2001. Human Immunodeficiency Virus Type 1 Vpu protein affects Sindbis virus glycoprotein processing and enhances membrane permeabilization. *Virology* 279:201–209.
- [103] Sanz, M. A., L. Perez, and L. Carrasco, 1994. Semliki Forest virus 6K protein modifies membrane permeability after inducible expression in *Escherichia coli* cells. *J Biol Chem* 269:12106–12110.
- [104] Antoine, A.-F., C. Montpellier, K. Cailliau, E. Browaeys-Poly, J.-P. Vilain, and J. Dubuisson, 2007. The alphavirus 6K protein activates endogenous ionic conductances when expressed in *Xenopus* oocytes. *J Membr Biol* 215:37–48.
- [105] Melton, J. V., G. D. Ewart, R. C. Weir, P. G. Board, E. Lee, and P. W. Gage, 2002. Alphavirus 6K proteins form ion channels. *J Biol Chem* 277:46923–46931.
- [106] Yamakura, T., E. Bertaccini, J. R. Trudell, and R. A. Harris, 2001. Anesthetics and ion channels: molecular models and sites of action. *Annu Rev Pharmacol Toxicol* 41:23–51.
- [107] Meyer, H., 1899. Zur Theorie der Alkoholnarkose. Erste Mittheilung. Welche Eigenschaft der Anästhetica bedingt ihre narkotische Wirkung? *Arch. Exp. Path. Pharmacol.* 42:109–118.
- [108] Overton, E., 1901. Studien über die Narköse. Fischer, Jena, Germany.
- [109] Raines, D. E., and K. W. Miller, 1994. On the importance of volatile agents devoid of anesthetic action. *Anesth Analg* 79:1031–1033.

- [110] Alifimoff, J. K., L. L. Firestone, and K. W. Miller, 1989. Anaesthetic potencies of primary alkanols: Implications for the molecular dimensions of the anaesthetic site. *Br J Pharmacol* 96:9–16.
- [111] Langerman, L., M. Bansinath, and G. J. Grant, 1994. The partition coefficient as a predictor of local anesthetic potency for spinal anesthesia: evaluation of five local anesthetics in a mouse model. *Anesth Analg* 79:490–494.
- [112] Koblin, D. D., B. S. Chortkoff, M. J. Laster, E. I. n. Eger, M. J. Halsey, and P. Ionescu, 1994. Polyhalogenated and perfluorinated compounds that disobey the Meyer-Overton hypothesis. *Anesth Analg* 79:1043–1048.
- [113] Brehm, P., and L. Henderson, 1988. Regulation of acetylcholine receptor channel function during development of skeletal muscle. *Dev Biol* 129:1–11.
- [114] Wonnacott, S., 1997. Presynaptic nicotinic ACh receptors. *Trends Neurosci* 20:92–98.
- [115] Alkondon, M., and E. X. Albuquerque, 2001. Nicotinic acetylcholine receptor α_7 and $\alpha_4\beta_2$ subtypes differentially control GABAergic input to CA1 neurons in rat hippocampus. *J Neurophysiol* 86:3043–3055.
- [116] Dilger, J. P., 2002. The effects of general anaesthetics on ligand-gated ion channels. *Br J Anaesth* 89:41–51.
- [117] Arias, H. R., P. Bhumireddy, and C. Bouzat, 2006. Molecular mechanisms and binding site locations for noncompetitive antagonists of nicotinic acetylcholine receptors. *Int J Biochem Cell Biol* 38:1254–1276.
- [118] Grassi, F., E. Palma, A. M. Mileo, and F. Eusebi, 1995. The desensitization of the embryonic mouse muscle acetylcholine receptor depends on the cellular environment. *Pflugers Arch* 430:787–794.
- [119] Barrantes, F. J., 2004. Structural basis for lipid modulation of nicotinic acetylcholine receptor function. *Brain Res Brain Res Rev* 47:71–95.
- [120] Marsh, D., A. Watts, and F. J. Barrantes, 1981. Phospholipid chain immobilization and steroid rotational immobilization in acetylcholine receptor-rich membranes from *Torpedo marmorata*. *Biochim Biophys Acta* 645:97–101.
- [121] Ellena, J. F., M. A. Blazing, and M. G. McNamee, 1983. Lipid-protein interactions in reconstituted membranes containing acetylcholine receptor. *Biochemistry* 22:5523–5535.
- [122] Marsh, D., and F. J. Barrantes, 1978. Immobilized lipid in acetylcholine receptor-rich membranes from *Torpedo marmorata*. *Proc Natl Acad Sci U S A* 75:4329–4333.
- [123] Antollini, S. S., and F. J. Barrantes, 2002. Unique effects of different fatty acid species on the physical properties of the *Torpedo* acetylcholine receptor membrane. *J Biol Chem* 277:1249–1254.

- [124] Zingsheim, H. P., D. C. Neugebauer, J. Frank, W. Hanicke, and F. J. Barrantes, 1982. Dimeric arrangement and structure of the membrane-bound acetylcholine receptor studied by electron microscopy. *EMBO J* 1:541–547.
- [125] Miyazawa, A., Y. Fujiyoshi, and N. Unwin, 2003. Structure and gating mechanism of the acetylcholine receptor pore. *Nature* 423:949–955.
- [126] Mantipragada, S. B., L. I. Horvath, H. R. Arias, G. Schwarzmann, K. Sandhoff, F. J. Barrantes, and D. Marsh, 2003. Lipid-protein interactions and effect of local anesthetics in acetylcholine receptor-rich membranes from *Torpedo marmorata* electric organ. *Biochemistry* 42:9167–9175.
- [127] Miller, K. W., 2002. The nature of sites of general anaesthetic action. *Br J Anaesth* 89:17–31.
- [128] Watts, A., 1991. Molecular and cellular mechanisms of alcohol and anesthetics. *Annals of the New York Academy of Science* 625:653–669.
- [129] Szabo, G., A. Dolganiuc, Q. Dai, and S. B. Pruet, 2007. TLR4, ethanol, and lipid rafts: A new mechanism of ethanol action with implications for other receptor-mediated effects. *J Immunol* 178:1243–1249.
- [130] Gallagher, M. J., and J. B. Cohen, 1999. Identification of amino acids of the *Torpedo* nicotinic acetylcholine receptor contributing to the binding site for the noncompetitive antagonist ^3H tetracaine. *Mol Pharmacol* 56:300–307.
- [131] Fraser, D. M., S. R. Louro, L. I. Horvaath, K. W. Miller, and A. Watts, 1990. A study of the effect of general anesthetics on lipid-protein interactions in acetylcholine receptor enriched membranes from *Torpedo nobiliana* using nitroxide spin-labels. *Biochemistry* 29:2664–2669.
- [132] Zhang, J., T. Hadlock, A. Gent, and G. R. Strichartz, 2007. Tetracaine-membrane interactions: Effects of lipid composition and phase on drug partitioning, location, and ionization. *Biophys J* 92:3988–4001.
- [133] Bottner, M., and R. Winter, 1993. Influence of the local anesthetic tetracaine on the phase behavior and the thermodynamic properties of phospholipid bilayers. *Biophys J* 65:2041–2046.
- [134] Middleton, R. E., N. P. Strnad, and J. B. Cohen, 1999. Photoaffinity labeling the *Torpedo* nicotinic acetylcholine receptor with ^3H tetracaine, a nondesensitizing noncompetitive antagonist. *Mol Pharmacol* 56:290–299.
- [135] Valenzuela, C. F., J. A. Kerr, and D. A. Johnson, 1992. Quinacrine binds to the lipid-protein interface of the *Torpedo* acetylcholine receptor: A fluorescence study. *J Biol Chem* 267:8238–8244.
- [136] Arias, H. R., E. A. McCardy, M. J. Gallagher, and M. P. Blanton, 2001. Interaction of barbiturate analogs with the *Torpedo californica* nicotinic acetylcholine receptor ion channel. *Mol Pharmacol* 60:497–506.

- [137] Green, S. A., D. J. Simpson, G. Zhou, P. S. Ho, and N. V. Blough, 1990. Intramolecular quenching of excited singlet states by stable nitroxyl radicals. *Journal of the American Chemical Society* 112:7337–7346. http://pubs3.acs.org/acs/journals/doilookup?in_doi=10.1021/ja00176a038.
- [138] Matko, J., K. Ohki, and M. Edidin, 1992. Luminescence quenching by nitroxide spin labels in aqueous solution: studies on the mechanism of quenching. *Biochemistry* 31:703–711.
- [139] Arias, H. R., C. F. Valenzuela, and D. A. Johnson, 1993. Quinacrine and ethidium bind to different loci on the *Torpedo* acetylcholine receptor. *Biochemistry* 32:6237–6242.
- [140] Arias, H. R., C. F. Valenzuela, and D. A. Johnson, 1993. Transverse localization of the quinacrine binding site on the *Torpedo* acetylcholine receptor. *J Biol Chem* 268:6348–6355.
- [141] Yu, Y., L. Shi, and A. Karlin, 2003. Structural effects of quinacrine binding in the open channel of the acetylcholine receptor. *Proc Natl Acad Sci U S A* 100:3907–3912.
- [142] Arias, H. R., W. R. Kem, J. R. Trudell, and M. P. Blanton, 2003. Unique general anesthetic binding sites within distinct conformational states of the nicotinic acetylcholine receptor. *Int Rev Neurobiol* 54:1–50.
- [143] Chiara, D. C., L. J. Dangott, R. G. Eckenhoff, and J. B. Cohen, 2003. Identification of nicotinic acetylcholine receptor amino acids photolabeled by the volatile anesthetic halothane. *Biochemistry* 42:13457–13467.
- [144] Giess, F., M. G. Friedrich, J. Heberle, R. L. Naumann, and W. Knoll, 2004. The protein-tethered lipid bilayer: a novel mimic of the biological membrane. *Biophys J* 87:3213–3220.
- [145] Wiese, A., M. Munstermann, T. Gutschmann, B. Lindner, K. Kawahara, U. Zahringer, and U. Seydel, 1998. Molecular mechanisms of polymyxin B-membrane interactions: Direct correlation between surface charge density and self-promoted transport. *J Membr Biol* 162:127–138.
- [146] Winterhalter, M., 2000. Black lipid membranes. *Current Opinion in Colloid & Interface Science* 5:250–255. <http://www.sciencedirect.com/science/article/B6VRY-43W6052-F/1/b6d38b299e51173e347949b8c7eb8aef>.
- [147] Miller, C., and E. Racker, 1976. Fusion of phospholipid vesicles reconstituted with cytochrome c oxidase and mitochondrial hydrophobic protein. *J Membr Biol* 26:319–333.
- [148] Krishna, G., J. Schulte, B. Cornell, R. Pace, L. Wiczorek, and P. Osman, 2001. Tethered Bilayer Membranes Containing Ionic Reservoirs: The Interfacial Capacitance. *Langmuir* 17:4858–4866. http://pubs3.acs.org/acs/journals/doilookup?in_doi=10.1021/1a001480a.

- [149] Naumann, R., S. Schiller, F. Giess, B. Grohe, K. Hartman, I. Karcher, I. Koper, J. Lubben, K. Vasilev, and W. Knoll, 2003. Tethered Lipid Bilayers on Ultraflat Gold Surfaces. *Langmuir* 19:5435–5443. http://pubs3.acs.org/acs/journals/doi/lookup?in_doi=10.1021/la0342060.
- [150] Li, C., M. Yi, J. Hu, H.-X. Zhou, and T. A. Cross, 2008. Solid-state NMR and MD simulations of the antiviral drug amantadine solubilized in DMPC bilayers. *Biophys J* 94:1295–1302.
- [151] Steinmann, E., T. Whitfield, S. Kallis, R. A. Dwek, N. Zitzmann, T. Pietschmann, and R. Bartenschlager, 2007. Antiviral effects of amantadine and iminosugar derivatives against Hepatitis C virus. *Hepatology* 46:330–338.
- [152] Thuluvath, P. J., A. Maheshwari, J. Mehdi, K. D. Fairbanks, L. L.-W. Wu, L. G. Gelrud, M. J. Ryan, F. A. Anania, I. F. Lobis, and M. Black, 2004. Randomised, double blind, placebo controlled trial of interferon, ribavirin, and amantadine versus interferon, ribavirin, and placebo in treatment naive patients with chronic Hepatitis C. *Gut* 53:130–135.
- [153] Becker, C. F. W., M. Oblatt-Montal, G. G. Kochendoerfer, and M. Montal, 2004. Chemical synthesis and single channel properties of tetrameric and pentameric TASP (template-assembled synthetic proteins) derived from the transmembrane domain of HIV Virus Protein U (Vpu). *J Biol Chem* 279:17483–17489.
- [154] Benos, D. J., and B. A. Stanton, 1999. Functional domains within the degenerin/epithelial sodium channel (Deg/ENaC) superfamily of ion channels. *J Physiol* 520 Pt 3:631–644.
- [155] Horisberger, J. D., 1998. Amiloride-sensitive Na⁺ channels. *Curr Opin Cell Biol* 10:443–449.
- [156] Pena, F., E. Neaga, B. Amuzescu, A. Nitu, and M.-L. Flonta, 2002. Amitriptyline has a dual effect on the conductive properties of the epithelial Na⁺ channel. *J Pharm Pharmacol* 54:1393–1398.
- [157] Wilson, L., P. Gage, and G. Ewart, 2006. Hexamethylene Amiloride blocks E protein ion channels and inhibits *Coronavirus* replication. *Virology* 353:294–306.
- [158] Premkumar, A., L. Wilson, G. D. Ewart, and P. W. Gage, 2004. Cation-selective ion channels formed by p7 of Hepatitis C virus are blocked by hexamethylene amiloride. *FEBS Lett* 557:99–103.
- [159] Matzke, A. J., C. Behensky, T. Weiger, and M. A. Matzke, 1992. A large conductance ion channel in the nuclear envelope of a higher plant cell. *FEBS Lett* 302:81–85.

- [160] Macdonald, R. L., C. J. Rogers, and R. E. Twyman, 1989. Kinetic properties of the GABAA receptor main conductance state of mouse spinal cord neurones in culture. *J Physiol* 410:479–499.
- [161] Mehnert, T., Y. H. Lam, P. J. Judge, A. Routh, D. Fischer, A. Watts, and W. B. Fischer, 2007. Towards a mechanism of function of the viral ion channel Vpu from HIV-1. *J Biomol Struct Dyn* 24:589–596.
- [162] Kruger, J., and W. Fischer, 2008. Exploring the conformational space of Vpu from HIV-1: A versatile adaptable protein. *J Comput Chem* .
- [163] Busath, D., and G. Szabo, 1981. Gramicidin forms multi-state rectifying channels. *Nature* 294:371–373.
- [164] Urry, D. W., S. Alonso-Romanowski, C. M. Venkatachalam, T. L. Trapane, and K. U. Prasad, 1984. The source of the dispersity of gramicidin A single-channel conductances. The L X Leu5-gramicidin A analog. *Biophys J* 46:259–265.
- [165] Woolley, G. A., and B. A. Wallace, 1992. Model ion channels: gramicidin and alamethicin. *J Membr Biol* 129:109–136.
- [166] You, S., S. Peng, L. Lien, J. Breed, M. S. Sansom, and G. A. Woolley, 1996. Engineering stabilized ion channels: Covalent dimers of alamethicin. *Biochemistry* 35:6225–6232.
- [167] Smith, D. B., and K. S. Johnson, 1988. Single-step purification of polypeptides expressed in *Escherichia coli* as fusions with glutathione-S-transferase. *Gene* 67:31–40. <http://www.sciencedirect.com/science/article/B6T39-47PH71T-1FD/1/d1922dcac44dbbdd3bb512c0f87544c6>.
- [168] Kaelin, W. G., D. C. Pallas, J. A. DeCaprio, F. J. Kaye, and D. M. Livingston, 1991. Identification of cellular proteins that can interact specifically with the T/E1A-binding region of the retinoblastoma gene product. *Cell* 64:521–532. <http://www.sciencedirect.com/science/article/B6WSN-4CF6DM3-10/1/43008014b8ab15412ffb8add785eab7>.
- [169] Buck, M., 1998. Trifluoroethanol and colleagues: cosolvents come of age. Recent studies with peptides and proteins. *Q Rev Biophys* 31:297–355.
- [170] Ma, C., F. M. Marassi, D. H. Jones, S. K. Straus, S. Bour, K. Strebler, U. Schubert, M. Oblatt-Montal, M. Montal, and S. J. Opella, 2002. Expression, purification, and activities of full-length and truncated versions of the integral membrane protein Vpu from HIV-1. *Protein Sci* 11:546–557.
- [171] Karplus, M., 2002. Molecular Dynamics simulations of biomolecules. *Acc Chem Res* 35:321–323.
- [172] Karplus, M., and J. A. McCammon, 2002. Molecular Dynamics simulations of biomolecules. *Nat Struct Biol* 9:646–652.

- [173] Lindahl, E., and M. Sansom, 2008. Membrane proteins: Molecular dynamics simulations. *Curr Opin Struct Biol* .
- [174] Knecht, V., and S.-J. Marrink, 2007. Molecular Dynamics simulations of lipid vesicle fusion in atomic detail. *Biophys J* 92:4254–4261.
- [175] Scott, K. A., P. J. Bond, A. Ivetac, A. P. Chetwynd, S. Khalid, and M. S. P. Sansom, 2008. Coarse-grained MD simulations of membrane protein-bilayer self-assembly. *Structure* 16:621–630.
- [176] Psachoulia, E., P. Fowler, P. Bond, and M. Sansom, 2008. Helix-Helix Interactions in Membrane Proteins: Coarse-Grained Simulations of Glycophorin A Helix Dimerization. *Biochemistry* .
- [177] Efremov, R. G., D. E. Nolde, A. G. Konshina, N. P. Syrtcev, and A. S. Arseniev, 2004. Peptides and proteins in membranes: What can we learn via computer simulations? *Curr Med Chem* 11:2421–2442.
- [178] Forrest, L. R., and M. S. Sansom, 2000. Membrane simulations: Bigger and better? *Curr Opin Struct Biol* 10:174–181.
- [179] Tieleman, D. P., I. H. Shrivastava, M. R. Ulmschneider, and M. S. Sansom, 2001. Proline-induced hinges in transmembrane helices: Possible roles in ion channel gating. *Proteins* 44:63–72.
- [180] Forrest, L. R., D. P. Tieleman, and M. S. Sansom, 1999. Defining the transmembrane helix of M2 protein from Influenza A by Molecular Dynamics simulations in a lipid bilayer. *Biophys J* 76:1886–1896.
- [181] Tieleman, D. P., H. J. Berendsen, and M. S. Sansom, 2001. Voltage-dependent insertion of alamethicin at phospholipid/water and octane/water interfaces. *Biophys J* 80:331–346.
- [182] Allen, T. W., T. Bastug, S. Kuyucak, and S.-H. Chung, 2003. Gramicidin A channel as a test ground for Molecular Dynamics force fields. *Biophys J* 84:2159–2168.
- [183] Forrest, L. R., A. Kukol, I. T. Arkin, D. P. Tieleman, and M. S. Sansom, 2000. Exploring models of the Influenza A M2 channel: MD simulations in a phospholipid bilayer. *Biophys J* 78:55–69.
- [184] Fischer, W. B., L. R. Forrest, G. R. Smith, and M. S. Sansom, 2000. Transmembrane domains of viral ion channel proteins: A molecular dynamics simulation study. *Biopolymers* 53:529–538.
- [185] Federau, T., U. Schubert, J. Flossdorf, P. Henklein, D. Schomburg, and V. Wray, 1996. Solution structure of the cytoplasmic domain of the Human Immunodeficiency Virus Type 1 encoded Virus Protein U (Vpu). *Int J Pept Protein Res* 47:297–310.

- [186] Willbold, D., S. Hoffmann, and P. Rosch, 1997. Secondary structure and tertiary fold of the Human Immunodeficiency Virus protein U (Vpu) cytoplasmic domain in solution. *Eur J Biochem* 245:581–588.
- [187] Wray, V., R. Kinder, T. Federau, P. Henklein, B. Bechinger, and U. Schubert, 1999. Solution structure and orientation of the transmembrane anchor domain of the HIV-1-encoded Virus Protein U by high-resolution and solid-state NMR spectroscopy. *Biochemistry* 38:5272–5282.
- [188] Henklein, P., R. Kinder, U. Schubert, and B. Bechinger, 2000. Membrane interactions and alignment of structures within the HIV-1 Vpu cytoplasmic domain: Effect of phosphorylation of serines 52 and 56. *FEBS Lett* 482:220–224.
- [189] Wray, V., T. Federau, P. Henklein, S. Klabunde, O. Kunert, D. Schomburg, and U. Schubert, 1995. Solution structure of the hydrophilic region of HIV-1 encoded Virus Protein U (Vpu) by CD and ^1H NMR spectroscopy. *Int J Pept Protein Res* 45:35–43.
- [190] Kukol, A., and I. T. Arkin, 1999. Vpu transmembrane peptide structure obtained by site-specific Fourier Transform Infrared Dichroism and global Molecular Dynamics searching. *Biophys J* 77:1594–1601.
- [191] Park, S. H., and S. J. Opella, 2005. Tilt angle of a transmembrane helix is determined by hydrophobic mismatch. *J Mol Biol* 350:310–318.
- [192] Khattari, Z., E. Arbely, I. T. Arkin, and T. Salditt, 2006. Viral ion channel proteins in model membranes: A comparative study by X-ray reflectivity. *Eur Biophys J* 36:45–55.
- [193] Mehnert, T., A. Routh, P. J. Judge, Y. H. Lam, D. Fischer, A. Watts, and W. B. Fischer, 2008. Biophysical characterization of Vpu from HIV-1 suggests a channel-pore dualism. *Proteins* 70:1488–1497.
- [194] Chew, C. F., A. Guy, and P. C. Biggin, 2008. Distribution and dynamics of adamantanes in a lipid bilayer. *Biophys J* 95:5627–5636.
- [195] Vijayan, R., and P. C. Biggin, 2008. A steroid in a lipid bilayer: localization, orientation, and energetics. *Biophys J* 95:L45–7.
- [196] Norman, K. E., and H. Nymeyer, 2006. Indole localization in lipid membranes revealed by molecular simulation. *Biophys J* 91:2046–2054.
- [197] Newton, I., 1686. *Philosophiæ Naturalis Principia Mathematica*. Edmund Halley.
- [198] Leach, A. R., 2001. *Molecular Modelling: Principles and Applications*. Longman, 2nd edition.
- [199] Lindahl, E., B. Hess, and D. van der Spoel, 2001. GROMACS 3.0: a package for molecular simulation and trajectory analysis. *J Mol Mod* 7:306–317.

- [200] Van Der Spoel, D., E. Lindahl, B. Hess, G. Groenhof, A. E. Mark, and H. J. C. Berendsen, 2005. GROMACS: fast, flexible, and free. *J Comput Chem* 26:1701–1718.
- [201] Tieleman, D. P., S. J. Marrink, and H. J. Berendsen, 1997. A computer perspective of membranes: Molecular Dynamics studies of lipid bilayer systems. *Biochim Biophys Acta* 1331:235–270.
- [202] Berendsen, H. J. C., J. P. M. Postma, W. F. van Gunsteren, A. DiNola, and J. R. Haak, 1984. Molecular Dynamics with coupling to an external bath. *The Journal of Chemical Physics* 81:3684–3690. <http://link.aip.org/link/?JCP/81/3684/1>.
- [203] Lennard-Jones, J. E., 1931. Cohesion. *Proc Phys Soc* 43:461–482.
- [204] Tieleman, D. P., B. Hess, and M. S. P. Sansom, 2002. Analysis and evaluation of channel models: Simulations of alamethicin. *Biophys J* 83:2393–2407.
- [205] Darden, T., D. York, and L. Pedersen, 1993. Particle mesh Ewald: An $N \log(N)$ method for Ewald sums in large systems. *The Journal of Chemical Physics* 98:10089–10092. <http://link.aip.org/link/?JCP/98/10089/1>.
- [206] Villalain, J., 1997. Location of the toxic molecule abietic acid in model membranes by MAS-NMR. *Biochim Biophys Acta* 1328:281–289.
- [207] Vemparala, S., L. Saiz, R. G. Eckenhoff, and M. L. Klein, 2006. Partitioning of anesthetics into a lipid bilayer and their interaction with membrane-bound peptide bundles. *Biophys J* 91:2815–2825.
- [208] van Aalten, D. M., R. Bywater, J. B. Findlay, M. Hendlich, R. W. Hooft, and G. Vriend, 1996. PRODRG, a program for generating molecular topologies and unique molecular descriptors from coordinates of small molecules. *J Comput Aided Mol Des* 10:255–262.
- [209] Roux, B., and M. Karplus, 1991. Ion transport in a model gramicidin channel. Structure and thermodynamics. *Biophys J* 59:961–981.
- [210] Hess, B., H. Bekker, H. J. C. Berendsen, and J. G. E. M. Fraaije, 1997. LINCS: A linear constraint solver for molecular simulations. *Journal of Computational Chemistry* 18:1463–1472.
- [211] Berendsen, H. J. C., J. R. Grigera, and T. P. Straatsma, 1987. The missing term in effective pair potentials. *Journal of Physical Chemistry* 91:6269–6271. http://pubs3.acs.org/acs/journals/doi/lookup?in_doi=10.1021/j100308a038.
- [212] Williams, M. L., and J. E. Gready, 1989. Guanidinium-Type resonance stabilization and its biological implications: The guanidine and extended-guanidine series. *Journal of Computational Chemistry* 10:35–54.

- [213] Gross, K. C., and P. G. Seybold, 2000. Substituent effects on the physical properties and pK_a of aniline. *International Journal of Quantum Chemistry* 80:1107–1115.
- [214] Brookeman, J. R., and F. A. Rushworth, 1975. Nuclear magnetic resonance in solid cycloheptane. *J Phys C Solid State Phys* 9:1043–1054.
- [215] Tolkmith, H., 2006. Electron group polarizability and molecular properties of organophosphorus compounds. *Annals of the New York Academy of Sciences* 79:189–232.
- [216] Hristova, K., C. E. Dempsey, and S. H. White, 2001. Structure, location, and lipid perturbations of melittin at the membrane interface. *Biophys J* 80:801–811.
- [217] Saiz, L., and M. Klein, 2001. Electrostatic interactions in a neutral model phospholipid bilayer by Molecular Dynamics simulations. *J. Chem. Phys.* 116:3052–3057.
- [218] Raffa, K., A. Berryman, J. Simasko, W. Teal, and B. Wong, 1985. Effects of grand fir monoterpenes on the fir engraver *Scolytus ventralis* and its symbiotic fungus. *Environ Entomol* 14:552–556.
- [219] Villeneuve, D. C., A. P. Yagminas, I. A. Marino, and G. C. Becking, 1977. Toxicity studies on dehydroabietic acid. *Bull Environ Contam Toxicol* 18:42–47.
- [220] Burge, P. S., M. G. Harries, I. O’Brien, and J. Pepys, 1980. Bronchial provocation studies in workers exposed to the fumes of electronic soldering fluxes. *Clin Allergy* 10:137–149.
- [221] Hartmann, C., I. Antes, and T. Lengauer, 2007. IRECS: a new algorithm for the selection of most probable ensembles of side-chain conformations in protein models. *Protein Sci* 16:1294–1307.
- [222] Morris, G., D. Goodsell, R. Halliday, R. Huey, W. Hart, R. Belew, and A. Olson, 1998. Automated docking using a Lamarckian genetic algorithm and an empirical binding free energy function. *Journal of Computational Chemistry* 19:1639–1662.
- [223] Humphrey, W., A. Dalke, and K. Schulten, 1996. VMD: Visual molecular dynamics. *J Mol Graph* 14:33–38.
- [224] Frey, H. H., and W. Loscher, 1978. Distribution of valproate across the interface between blood and cerebrospinal fluid. *Neuropharmacology* 17:637–642.
- [225] Siarheyeva, A., J. J. Lopez, and C. Glaubitz, 2006. Localization of multidrug transporter substrates within model membranes. *Biochemistry* 45:6203–6211.

- [226] Stouffer, A. L., R. Acharya, D. Salom, A. S. Levine, L. Di Costanzo, C. S. Soto, V. Tereshko, V. Nanda, S. Stayrook, and W. F. DeGrado, 2008. Structural basis for the function and inhibition of an Influenza virus proton channel. *Nature* 451:596–599.
- [227] Swartz, K. J., and R. MacKinnon, 1997. Hanatoxin modifies the gating of a voltage-dependent K⁺ channel through multiple binding sites. *Neuron* 18:665–673.
- [228] Lee, S.-Y., and R. MacKinnon, 2004. A membrane-access mechanism of ion channel inhibition by voltage sensor toxins from spider venom. *Nature* 430:232–235.
- [229] Overhauser, A. W., 1953. Paramagnetic Relaxation in Metals. *Phys. Rev.* 89:689–700.
- [230] Rattle, H., 1995. An NMR primer for Life Scientists. Partnership Press.
- [231] Macura, S., and R. R. Ernst, 1980. Unknown. *Molecular Physics* 41:95.
- [232] Hsu, S.-T. D., E. Breukink, G. Bierbaum, H.-G. Sahl, B. de Kruijff, R. Kaptein, N. A. J. van Nuland, and A. M. J. J. Bonvin, 2003. NMR study of mersacidin and lipid II interaction in dodecylphosphocholine micelles. Conformational changes are a key to antimicrobial activity. *J Biol Chem* 278:13110–13117.
- [233] Hoult, D. I., and R. E. Richards, 1975. Critical Factors in the Design of Sensitive High Resolution Nuclear Magnetic Resonance Spectrometers. *Proceedings of the Royal Society of London. Series A, Mathematical and Physical Sciences* 344:311–340. <http://links.jstor.org/sici?sici=0080-4630%2819750729%29344%3A1638%3C311%3ACFITD0%3E2.0.CO%3B2-V>.
- [234] Williamson, M. P., 2007. Encyclopedia of Magnetic Resonance, John Wiley and Sons, chapter NOESY. 4th edition.
- [235] Redfield, A., and S. Kunz, 1975. Quadrature Fourier NMR detection: Simple multiplex for dual detection and discussion. *Journal of Magnetic Resonance* 19:250.
- [236] Atkins, P., and J. de Paula, 2006. Atkins' Physical Chemistry. Oxford University Press, 8th edition.
- [237] Shoemaker, D. P., C. W. Garland, and J. W. Nibler, 2000. Experiments in Physical Chemistry. McGraw-Hill, 6th edition.
- [238] Petricolas, W. L., T. Cutrera, and G. R. Rodgers, 1981. Quantitative determination of the secondary structure of proteins in solution by laser Raman scattering. *Biomol. Struct. Conform. Funct. Evol. Int. Symp.* 2:45.
- [239] Yu, N.-T., C. S. Liu, and D. C. O'Shea, 1972. Laser Raman spectroscopy and the conformation of insulin and proinsulin. *J Mol Biol* 70:117–132.

- [240] Small, E. W., and W. L. Peticolas, 1971. Conformational dependence of the Raman scattering intensities from polynucleotides. *Biopolymers* 10:69–88.
- [241] Ichimori, H., T. Hata, T. Yoshioka, H. Matsuki, and S. Kaneshina, 1997. Thermotropic and barotropic phase transition on bilayer membranes of phospholipids with varying acyl chain-lengths. *Chemistry and Physics of Lipids* 89:97–105. <http://www.sciencedirect.com/science/article/B6T2N-3RC52PG-3/1/9aba50d0ec85f4942555386bc8f4a4b6>.
- [242] Chapman, D., B. A. Cornell, A. W. Elias, and A. Perry, 1977. Interactions of helical polypeptide segments which span the hydrocarbon region of lipid bilayers : Studies of the gramicidin alipid-water system. *Journal of Molecular Biology* 113:517–538. <http://www.sciencedirect.com/science/article/B6WK7-4DMNPBJ-1S/1/a64deb4c89603f71b1db47bb801f7b82>.
- [243] Lieb, W. R., M. Kovalycsik, and R. Mendelsohn, 1982. Do clinical levels of general anaesthetics affect lipid bilayers? Evidence from Raman scattering. *Biochim Biophys Acta* 688:388–398.
- [244] Griffin, S., S. G. Wyllie, and J. Markham, 1999. Determination of octanol-water partition coefficient for terpenoids using reversed-phase high-performance liquid chromatography. *J Chromatogr A* 864:221–228.
- [245] Bodenhausen, G., R. L. Vold, and R. R. Vold, 1980. Multiple quantum spin-echo spectroscopy. *Journal of Magnetic Resonance* 37:93–106. <http://www.sciencedirect.com/science/article/B7GXD-4CV99DJ-SW/2/ba9610530a49dc3b9f40f7ad931d8064>.
- [246] Goddard, T. G., and D. G. Kneller, 2001. SPARKY 3.
- [247] Tsikaris, V., M. Sakarellos-Daitsiotis, E. Panou-Pomonis, E. Detsikas, C. Sakarellos, M. T. Cung, and M. Marraud, 1992. ¹H-NMR studies on arginine tripeptides: Evidence for guanidinium-C-terminal carboxylate interactions. *Pept Res* 5:110–114.
- [248] Yau, W. M., W. C. Wimley, K. Gawrisch, and S. H. White, 1998. The preference of tryptophan for membrane interfaces. *Biochemistry* 37:14713–14718.
- [249] Georgallas, A., and M. J. Zuckermann, 1986. Lipid vertical motion and related steric effects in bilayer membranes. *Eur Biophys J* 14:53–61.
- [250] Santos, J. S., D.-K. Lee, and A. Ramamoorthy, 2004. Effects of antidepressants on the conformation of phospholipid headgroups studied by solid-state NMR. *Magn Reson Chem* 42:105–114.
- [251] Scheidt, H. A., A. Pampel, L. Nissler, R. Gebhardt, and D. Huster, 2004. Investigation of the membrane localization and distribution of flavonoids by high-resolution Magic Angle Spinning NMR spectroscopy. *Biochim Biophys Acta* 1663:97–107.

- [252] Yoshizaki, K., Y. Seo, H. Nishikawa, and T. Morimoto, 1982. Application of pulsed-gradient ^{31}P NMR on frog muscle to measure the diffusion rates of phosphorus compounds in cells. *Biophys. J.* 38:209–211. <http://www.biophysj.org/cgi/content/abstract/38/2/209>.
- [253] Pinheiro, T. J., and A. Watts, 1994. Resolution of individual lipids in mixed phospholipid membranes and specific lipid-cytochrome c interactions by magic-angle spinning solid-state phosphorus-31 NMR. *Biochemistry* 33:2459–2467.
- [254] Spooner, P. J., and A. Watts, 1992. Cytochrome c interactions with cardiolipin in bilayers: a multinuclear magic-angle spinning NMR study. *Biochemistry* 31:10129–10138.
- [255] Bonev, B. B., W. C. Chan, B. W. Bycroft, G. C. Roberts, and A. Watts, 2000. Interaction of the L-antibiotic nisin with mixed lipid bilayers: a ^{31}P and ^2H NMR study. *Biochemistry* 39:11425–11433.
- [256] Cheeseman, G. C., and N. J. Berridge, 1959. Observations on the molecular weight and chemical composition of nisin A. *Biochem J* 71:185–194.
- [257] Pink, D. A., T. J. Green, and D. Chapman, 1981. Raman scattering in bilayers of saturated phosphatidylcholines and cholesterol. Experiment and theory. *Biochemistry* 20:6692–6698.
- [258] Brown, K. G., W. L. Peticolas, and E. Brown, 1973. Raman studies of conformational changes in model membrane systems. *Biochem Biophys Res Commun* 54:358–364.
- [259] Spiker, R. C., and I. W. Levin, 1976. Phase transitions of phospholipid single-wall vesicles and multilayers. Measurement by vibrational Raman spectroscopic frequency differences. *Biochim Biophys Acta* 433:457–468.
- [260] Sanderson, J. M., and A. D. Ward, 2004. Analysis of liposomal membrane composition using Raman tweezers. *Chem Commun (Camb)* 5:1120–1121.
- [261] King, M. D., K. C. Thompson, and A. D. Ward, 2004. Laser tweezers Raman study of optically trapped aerosol droplets of seawater and oleic acid reacting with ozone: Implications for cloud-droplet properties. *J Am Chem Soc* 126:16710–16711.
- [262] Tu, A., 1982. Raman Spectroscopy in Biology: Principles and Applications. John Wiley and Sons.
- [263] Gullion, T., and J. Schaefer, 1989. Rotational-Echo Double-Resonance NMR. *Journal of Magnetic Resonance (1969)* 81:196–200.
- [264] Watts, A., 2005. Solid-state NMR in drug design and discovery for membrane-embedded targets. *Nat Rev Drug Discov* 4:555–568.

- [265] Klug, C. A., K. Tasaki, N. Tjandra, C. Ho, and J. Schaefer, 1997. Closed form of liganded glutamine-binding protein by Rotational-Echo Double-Resonance NMR. *Biochemistry* 36:9405–9408.
- [266] Wang, J., Y. S. Balazs, and L. K. Thompson, 1997. Solid-state REDOR NMR distance measurements at the ligand site of a bacterial chemotaxis membrane receptor. *Biochemistry* 36:1699–1703.
- [267] Watts, J. A., A. Watts, and D. A. Middleton, 2001. A model of reversible inhibitors in the gastric H^+/K^+ -ATPase binding site determined by Rotational Echo Double Resonance NMR. *J Biol Chem* 276:43197–43204.
- [268] Watts, A., 1999. NMR of drugs and ligands bound to membrane receptors. *Curr Opin Biotechnol* 10:48–53.
- [269] Levitt, M. H., D. Suter, and R. R. Ernst, 1986. Spin dynamics and thermodynamics in solid-state NMR cross polarization. *The Journal of Chemical Physics* 84:4243–4255. <http://link.aip.org/link/?JCP/84/4243/1>.
- [270] Zhang, S. M., B. H. Meier, and R. R. Ernst, 1994. Mismatch-Compensated Cross Polarization. W-MOIST, an Improved Pulse Scheme. *Journal of Magnetic Resonance, Series A* 108:30–37. <http://www.sciencedirect.com/science/article/B6WJY-45P0B00-5Y/1/36abe862af0758b4e721a19ea44c75fb>.
- [271] Zhang, S. M., B. H. Meier, S. Appelt, M. Mehring, and R. R. Ernst, 1993. Transient Oscillations in Phase-Switched Cross-Polarization Experiments. *Journal of Magnetic Resonance, Series A* 101:60–66. <http://www.sciencedirect.com/science/article/B6WJY-45PKPG5-82/1/e1177f6152b2c5db4b7bb9e86b066571>.
- [272] Bloch, F., 1958. Theory of line narrowing by double-frequency irradiation. *Physical Review* 111:841–853.
- [273] Bennett, A. E., C. M. Rienstra, M. Auger, K. V. Lakshmi, and R. G. Griffin, 1995. Heteronuclear decoupling in rotating solids. *Journal of Chemical Physics* 103:6951–6958.
- [274] Ernst, M., H. Zimmerman, and B. H. Meir, 2000. A simple model for heteronuclear spin decoupling in solid state NMR. *Chemical Physics Letters* 317:581–588.
- [275] Gullion, T., 1998. Introduction to Rotational-Echo, Double Resonance NMR. *Concepts in Magnetic Resonance* 10:277–289.
- [276] Ahmed, Z., D. G. Reid, A. Watts, and D. A. Middleton, 2000. A solid-state NMR study of the phospholamban transmembrane domain: local structure and interactions with Ca^{2+} -ATPase. *Biochim Biophys Acta* 1468:187–198.

- [277] Kochendoerfer, G. G., D. H. Jones, S. Lee, M. Oblatt-Montal, S. J. Opella, and M. Montal, 2004. Functional characterization and NMR spectroscopy on full-length Vpu from HIV-1 prepared by total chemical synthesis. *J Am Chem Soc* 126:2439–2446.
- [278] Lu, W., B.-J. Zheng, K. Xu, W. Schwarz, L. Du, C. K. L. Wong, J. Chen, S. Duan, V. Deubel, and B. Sun, 2006. Severe Acute Respiratory Syndrome-associated Coronavirus 3a protein forms an ion channel and modulates virus release. *Proceedings of the National Academy of Sciences* 103:12540–12545. <http://www.pnas.org/content/103/33/12540.abstract>.
- [279] Wilson, L., C. McKinlay, P. Gage, and G. Ewart, 2004. SARS Coronavirus E protein forms cation-selective ion channels. *Virology* 330:322–331.
- [280] Madan, V., M. d. J. Garcia, M. A. Sanz, and L. Carrasco, 2005. Viroporin activity of murine Hepatitis virus E protein. *FEBS Lett* 579:3607–3612.
- [281] Piller, S. C., G. D. Ewart, A. Premkumar, G. B. Cox, and P. W. Gage, 1996. Vpr protein of Human Immunodeficiency Virus Type 1 forms cation-selective channels in planar lipid bilayers. *Proc Natl Acad Sci U S A* 93:111–115.
- [282] Mould, J. A., R. G. Paterson, M. Takeda, Y. Ohigashi, P. Venkataraman, R. A. Lamb, and L. H. Pinto, 2003. Influenza B virus BM2 protein has ion channel activity that conducts protons across membranes. *Dev Cell* 5:175–184.
- [283] Sunstrom, N. A., L. S. Premkumar, A. Premkumar, G. Ewart, G. B. Cox, and P. W. Gage, 1996. Ion channels formed by NB, an Influenza B virus protein. *J Membr Biol* 150:127–132.
- [284] Betakova, T., and A. J. Hay, 2007. Evidence that the CM2 protein of Influenza C virus can modify the pH of the exocytic pathway of transfected cells. *J Gen Virol* 88:2291–2296.
- [285] Premkumar, A., C. R. Horan, and P. W. Gage, 2005. Dengue virus M protein C-terminal peptide (DVM-C) forms ion channels. *J Membr Biol* 204:33–38.
- [286] Aldabe, R., A. Barco, and L. Carrasco, 1996. Membrane permeabilization by Poliovirus proteins 2B and 2BC. *J Biol Chem* 271:23134–23137.
- [287] Gan, S. W., L. Ng, X. Lin, X. Gong, and J. Torres, 2008. Structure and ion channel activity of the human respiratory syncytial virus (hRSV) small hydrophobic protein transmembrane domain. *Protein Sci* 17:813–820.
- [288] Gaedigk-Nitschko, K., and M. J. Schlesinger, 1990. The Sindbis virus 6K protein can be detected in virions and is acylated with fatty acids. *Virology* 175:274–281.
- [289] Liljestrom, P., S. Lusa, D. Huylebroeck, and H. Garoff, 1991. *In vitro* mutagenesis of a full-length cDNA clone of Semliki Forest virus: the small 6,000-molecular-weight membrane protein modulates virus release. *J Virol* 65:4107–4113.

- [290] Plugge, B., S. Gazzarrini, M. Nelson, R. Cerana, J. L. Van Etten, C. Derst, D. DiFrancesco, A. Moroni, and G. Thiel, 2000. A potassium channel protein encoded by Chlorella virus PBCV-1. *Science* 287:1641–1644.
- [291] Andrew, E. R., A. Bradbury, and R. G. Eades, 1958. NMR spectra from crystals rotated at high speeds. *Nature* 182:1659.
- [292] Lowe, I. J., 1959. Free Induction Decays in Rotating Solids. *Phys. Rev. Lett.* 2:285.
- [293] Andrew, E. R., 1996. Magic Angle Spinning. Encyclopaedia of Nuclear Magnetic Resonance. Wiley.
- [294] Yang, B., M. Morris, and H. Owen, 1991. Holographic Notch Filter for Low-wavenumber Stokes and Anti-Stokes Raman Spectroscopy. *Appl. Spectrosc.* 45:1533–1536.